Cronfa
Swansea University's Research Repository

# Methods for the efficient utilisation of dynamic CAE solvers to derive appropriate optimisation loadings for complex problems.

PhD

**Ryan Thornhill**




Zienkiewicz Centre for Computational Engineering

Swansea University

Wales

2023

Copyright: The Author, Ryan Thornhill, 2023

# Abstract

Computer Aided Engineering (CAE) within the automotive sector is a constantly evolving area, with automotive manufacturers continuously seeking new techniques that will allow for an improved output within a shorter time frame, allowing them to keep up with the rapidly changing automotive market. This challenge is more evident than ever with the automotive industry facing one of the biggest changes in its history, as it begins to move away from conventional fossil fuel internal combustion engines (ICE) to battery electric vehicles (BEV). This change is leading to a much wider range of design options and new components to be considered, therefore the ability to asses new models rapidly and accurately is key to obtaining the optimal overall vehicle package. Therefore, this thesis details a number of investigations that have been carried out researching various options to allow for reducing simulation time, whilst simultaneously improving the quality of data that can be obtained and utilised in the design and lightweighting process of future vehicle components. Key areas of focus included the assement and optimisation of a planetary gear carrier, investigations into the load extraction from various sources to aid static part optimisations.

**Synopsis** The aim is to develop methods for the efficient utilisation of dynamic CAE solvers to derive appropriate topology loadings for complex problems. Typically, load conditions are known and for topology optimisation this then leads to the solution of a complex linear elastic problem. In realty however, loading is uncertain and varying, e.g. torque ripples in a drive train due to motor design and drive conditions, structural loading due to gust loading on for instance automotive car doors; This requires a mapping of the load space for these varied events onto the components of interest. For the first case mentioned above this leads to a very high number of simulations. The objective is to reduce the computational work for deriving the correct loading conditions in an efficient and robust manner.

# Declaration and Statements

**DECLARATION**

This work has not previously been accepted in substance for any degree and is not being concurrently submitted in candidature for any degree.

Signed [redacted] Date..01/12/2024.....

**STATEMENT 1**

This thesis is the result of my own investigations, except where otherwise stated. Other sources are acknowledged by footnotes giving explicit references. A bibliography is appended.

Signed [redacted]. Date..01/12/2024.....

**STATEMENT 2**

I hereby give consent for my thesis, if accepted, to be available for photocopying and for inter-library loan, and for the title and summary to be made available to outside organisations.

Signed [redacted]. Date.01/12/2024.....

**STATEMENT 3**

The Universitys ethical procedures have been followed and, where appropriate, that ethical approval has been granted.

Signed [redacted]. Date.01/12/2024.....

# Contents


**1 Introduction** **19**

1.1 Motivation . . . 19

1.2 Overview . . . 20

1.3 Aims and Objectives . . . 21

1.4 Computer Equipment . . . 22

**2 Literature Review** **23**

2.1 Vehicle Composition and BIW . . . 23

2.2 Introduction to Electric and Hybrid Vehicles. . . . 26

2.2.1 Overview . . . 26

2.2.2 Advantages and Disadvantages . . . 32

2.2.3 EV examples . . . 32

2.3 FE Modelling . . . 33

2.3.1 Meshing . . . 34

2.3.1.1 Overview . . . 34

2.3.1.2 Meshing Types . . . 34

2.3.1.3 1D Meshing . . . 35

2.3.1.4 2D Meshing . . . 35

2.3.1.5 Medial Axis Transformation . . . 36

2.3.1.6 MidMesh . . . 37

2.3.1.7 How it works . . . 37

2.3.1.8 Benefits and Uses . . . 37

2.3.1.9 3D Meshing . . . 37

2.3.1.10 TetraMesh . . . 38

2.3.1.11 Tetra Mesh Generation . . . 38

2.3.1.12 Benefits and Uses . . . 39

2.3.1.13 Time Step overview . . . 39

2.3.2 Low fidelity modelling . . . 40
2.4 Performance Testing . . . 45
2.4.1 Crash Testing . . . 45
2.4.1.1 History of crash testing . . . 45
2.4.1.2 Types of Crash Testing . . . 47
2.4.1.3 Computer Simulated Crash Testing . . . 49
2.4.2 EV crash testing . . . 49
2.4.2.1 Battery Testing . . . 51
2.4.2.2 EV Design stratergies . . . 53
2.5 E-Axles . . . 59
2.5.1 Torque Ripples . . . 60
2.5.2 E-Axle Modelling . . . 60
2.6 Chapter Summary . . . 62

**3 Practical Assessment and optimisation of planetary carrier. 63**
3.1 Introduction . . . 63
3.1.1 E-Axle . . . 64
3.2 Model Set Up . . . 66
3.2.1 Loads and Constraints . . . 68
3.2.1.1 Loadings . . . 68
3.2.1.2 Constraints . . . 70
3.2.1.3 Connections . . . 70
3.3 Results . . . 72
3.3.1 Initial Topology Results . . . 72
3.3.1.1 Model Set Up Adjustment . . . 72
3.3.2 Geometry Update . . . 73
3.3.2.1 Manufacturing Constraint - Draw . . . 74
3.3.2.2 Analysing Results . . . 75
3.3.3 Benchmarking . . . 80
3.3.4 Misalignment Results . . . 80
3.3.4.1 Park Lock Removal . . . 82
3.3.5 Material Investigation . . . 84
3.3.6 Manufacturing Exploration - Additive Manufacture . . . 85
3.4 Stiffness vs Mass . . . 86
3.5 Costing . . . 90
3.6 Design Selection . . . 91

3.7 Chapter Summary . . . 92

**4 Exploration of torque ripples and force distribution within key E-Axle transmission components. 94**

4.1 Introduction and background studies . . . 94
4.1.1 Chapter introduction . . . 94
4.1.2 Background Work . . . 95
4.2 Motionsolve Initial Investigations . . . 100
4.2.1 Initial Model Set-Up . . . 101
4.2.2 Initial Model Behaviour . . . 104
4.2.2.1 Forces and Penetration Depth Overview . . . 104
4.2.2.2 Contact force behaviour . . . 107
4.2.2.3 Force behaviour reviewed . . . 112
4.2.3 Steady Speed Analysis . . . 117
4.3 Timing Studies . . . 124
4.3.0.1 CPU run time consistency . . . 124
4.3.0.2 Input Speed effect on CPU time. . . . 125
4.3.0.3 Print times effect upon CPU run times. . . . 126
4.3.0.4 Print Time Accuracy Investigations. . . . 130
4.3.0.5 Loading Methods . . . 142
4.3.0.6 Acceleration Investigations . . . 149
4.3.0.7 Acceleration rates effect upon forces. . . . 149
4.3.0.8 Print Time Expression . . . 162
4.4 Chapter Summary . . . 168

**5 Utilisation of low fidelity models in crash scenarios to extract loadings for component and sub-system analysis. 169**

5.1 Chapter introduction . . . 169
5.1.1 Modelling . . . 170
5.1.2 Component Selection . . . 172
5.1.3 Dynamic Load Selection . . . 172
5.2 ESL Method . . . 173
5.3 Acceleration Method . . . 178
5.3.1 1D crush . . . 180
5.4 C2 Model Development . . . 181
5.4.1 Full vehicle C2. . . . 181

5.4.2 Localised C2 vehicle assessment. . . . . 182
5.5 Chapter Summary . . . . . 183

**6 Conclusion** **184**
6.1 Future Work . . . . . 185
.1 Misalignment Tables . . . . . 191
.1.1 Steel Benchmark Misalignments . . . . . 191
.1.2 Titanium Benchmark Misalignments . . . . . 192
.1.3 Misalignments for V4 steel castable model. . . . . 193
.1.4 Table displaying misalignments for v4 steel castable model with the park lock removed. . . . . 193
.1.5 Table displaying misalignments for adjusted v4 steel model, for no park lock instances. . . . . 193
.1.6 Table displaying misalignments for titanium version of v4 . . . . . 194
.1.7 Table displaying misalignments for v5 steel additive manufacture model. . 194
.1.8 Table displaying misalignments for titanium additive manufacture model. 194
.1.9 Table displaying misalignments for version four of titanium additive manufacture model. . . . . 195
.2 Costing . . . . . 196
.2.1 Table displaying estimated costs for various model options. . . . . 196

# Acknowledgements

I would like to firstly thank my thesis advisors Professor Johann Sienz and Dr Will Harrison, for all of their help throughout the project and guidance to ensure the project could fulfil its potential. Particular thanks to Professor Sienz for his assistance in ensuring this project was possible through multiple challenges which faced its continuation. I would also like to thank the Astute 2020 team for allowing me to have scope alongside my professional commitments to fulfil the work for this thesis, in particular Dr Dawn Morgan who aided in supporting this research.

Finally I would like to thank all of my friends and family who have supported me over the past few years. With continuous support and encouragement to get this thesis finished whilst furthering my career within the automotive industry. Alas, it would be unfair to not mention the real supporter of this thesis, Vernon who's incessance on multiple walks a day and trips to the beach provided a welcome break from the computer screens and confines of the office.

# List of Tables


2.1 Electric vehicle post-crash legal requirements [1] . . . . . 50

3.1 Steel material properties table . . . . . 64
3.2 Summary of key Load cases . . . . . 67
3.3 Prescribed Load cases . . . . . 68
3.4 Geometry comparison . . . . . 73
3.5 Material comparison . . . . . 84
3.6 Key summary of explored planetary carrier design options. . . . . 92

4.1 Details of the target vehicle performance. . . . . 99
4.2 Input speed, CPU run time comparison table, print time 1ms . . . . . 103
4.3 Print time, CPU run time comparison. . . . . 104
4.4 Key features of steady speed force waves for various tested speeds. . . . . 118
4.5 Key features of steady speed force waves for an extended range of tested speeds. 120
4.6 Repeat run timings for 10 rad/sec input speed. . . . . 125
4.7 Repeat run timings for 1000 rad/sec input speed. . . . . 125
4.8 Key timings attributes and variations at 10 and 1000 rad/sec . . . . . 125
4.9 Input speeds effect on CPU run time, with refined print time of 0.1 ms . . . . . 126
4.10 Print Times effect on CPU run time, at set input speed of 100 rad/sec . . . . . 127
4.11 CPU run times and corresponding result quality for various tested print times, at 10 rad/sec input speed. . . . . 130
4.12 CPU run times and corresponding result quality for various tested print times, at 100 rad/sec input speed. . . . . 131
4.13 CPU run times and corresponding result quality for various tested print times, at 50 rad/sec input speed. . . . . 132
4.14 CPU run times and corresponding result quality for various tested print times, at 200 rad/sec input speed. . . . . 132

4.15 CPU run times and corresponding result quality for various tested print times, at 500 rad/sec input speed. . . . 133
4.16 CPU run times and corresponding result quality for various tested print times, at 1000 rad/sec input speed. . . . 133
4.17 Suggested print times at various input speeds, for set number of sample points per force wave, determined from 10 rad/sec inspected result. . . . 136
4.18 Suggested print times at various input speeds, for set number of sample points per force wave, determined from 100 rad/sec inspected result. . . . 136
4.19 Suggested print times at various input speeds, for set number of sample points per force wave, determined from 10 rad/sec revisited result, utilising a larger print time. . . . 138
4.20 Suggested print times at various input speeds, for set number of sample points per force wave, determined from 1000 rad/sec inspected result. . . . 139
4.21 Summary of the suggested print times for various input speeds, derived from the four tested number of sample points per force wave. With there respective result quality and CPU run times. . . . 141
4.22 Tested acceleration rates, and corresponding acceleration periods. . . . 149
4.23 Extracted acceleration rates for the 1000rad/sec$^2$ run, with corresponding time stamps. . . . 152
4.24 Forces extracted at the midpoint of various acceleration periods, for a number of acceleration rates and both application methods. . . . 158
4.25 CPU run times, for a series of acceleration rates for both tested application methods. . . . 159

# List of Figures


1.1 Greenhouse gas emissions by sector *2020 data . . . . . 20

2.1 Vehicle mass breakdown by system and components [2] . . . . . 23
2.2 BIW of Ford Taurus . . . . . 24
2.3 Skateboard chassis of Tesla Model S [3] . . . . . 25
2.4 Monthly car registration by fuel type as a percentage of total registrations in Europe, for 2011-2020 . . . . . 27
2.5 Transition from internal combustion engine vehicles to full electric vehicles, with key BEV categories highlighted. . . . . 28
2.6 Overview of key parts within a conventional gasoline ICE vehicle [4] . . . . . 29
2.7 Overview of key parts within a Hybrid Electric Vehicle/Mild Hybrid [5] . . . . . 29
2.8 Overview of key parts within a Plug-in Hybrid Electric Vehicle [6] . . . . . 30
2.9 Overview of key parts within a Electrical Vehicle [7] . . . . . 30
2.10 Overview of key parts within a Fuel Cell Electric Vehicle [8] . . . . . 31
2.11 A 2D bracket and its medial axis. A maximal disc on the axis is also shown [9]. . 36
2.12 Depiction of testing method for tri-spring joint representations on vehicle B-pillar. 41
2.13 Frontal Crash Test Simulation of a Ford Taurus at 60 mph T=0.025 s [10] . . . . 48
2.14 Electric vehicle crash testing requirements Economic Commission for Europe (ECE) [1] . . . . . 50
2.15 Schematic diagram of impactor bench [11] . . . . . 53
2.16 Overview of primary and secondary safety zones for vehicles [12]. . . . . 54
2.17 Energy densities (kWh/litre) versus specific energy (kWh/kg) for various fuels [13]. . . . . 54
2.18 Comparison of force-displacement curves for different connection types in tensile test [14]. . . . . 56
2.19 Two different structures of battery model, denoted as S1 and S2, and the corresponding vehicle acceleration curves in the frontal impact simulations [15]. . . . . 58

2.20 Two different structures of battery model, denoted as S1 and S2, and the corresponding vehicle acceleration curves in the frontal impact simulations [12]. . . . . 58

3.1 Image highlighting the planetary gears location within the singular e-axle. . . . . 65
3.2 Image of the double e-axle . . . . . 65
3.3 Planetary Gear Schematic . . . . . 66
3.4 Planetary Carrier Design Spaces . . . . . 67
3.5 Planetary Gear Loads . . . . . 69
3.6 Park Lock loads . . . . . 70
3.7 Planetary Carrier cross section . . . . . 71
3.8 Topology result with stress response . . . . . 72
3.9 Stages of realising the topology results. . . . . 73
3.10 Draw direction for model. . . . . 74
3.11 Realising of result. . . . . 75
3.12 Stress contour of reverse PL loadcase . . . . . 76
3.13 Version four of the planetary carrier . . . . . 77
3.14 Stress contour of reverse park lock load case, with the carrier isolated. . . . . 78
3.15 Pin location numbers. . . . . 79
3.16 Exaggerated illustration of pin movement that is being captured and considered. 79
3.17 Loads displayed upon planetary assembly at 30deg. intervals. . . . . 80
3.18 Graph displaying the angular misalignments throughout the carriers 360 deg cycle for Load case one of version four of the planetary carrier. . . . . 81
3.19 Graph displaying the angular misalignments throughout the carriers 360 deg cycle for Load case two of version four of the planetary carrier. . . . . 82
3.20 Resultant topology iso surface, where the park lock load cases are not considered. 83
3.21 Version 4.2, displaying adapted version of the carrier for no park lock instances. . 84
3.22 Titanium version for additive manufacture inserted into full planetary carrier assembly . . . . . 86
3.23 Graph of mass saving vs misalignment increase, with version four cast steel as the benchmark point for a series of titanium versions. . . . . 87
3.24 Scatter graph of various iterations . . . . . 88
3.25 Titanium version four of the planetary carrier, mass 1.12 kg. . . . . 89
3.26 Graph displaying the angular misalignments throughout the carriers 360° cycle for Load case one of Titanium version four of the planetary carrier. . . . . 90
3.27 Pugh Matrix of key design options. . . . . 92

4.1 Labelled illustration of vehicle differentials parts [16] . . . . . 96
4.2 Visual of contact forces between pinion gear and crown wheel. . . . . 97
4.3 Contour plot displaying resultant stresses upon the differential crown wheel in MPa. . . . . 98
4.4 Plot of table 4.2, Input speed vs CPU time. . . . . 103
4.5 Plot of print times effect upon CPU run time. . . . . 104
4.6 Plot of print times effect upon CPU run time, for 10 rad/sec and 100 rad/sec . . 105
4.7 Plot of maximum forces observed at various input speeds. . . . . 106
4.8 Plot of maximum PD's observed at various input speeds. . . . . 106
4.9 Plot of contact forces observed at 10 rad/sec for all gear contacts, throughout 3.5 second analysis. . . . . 107
4.10 Plot of contact forces observed at 100 rad/sec for all gear contacts, throughout 3.5 second analysis. . . . . 108
4.11 Plot of contact forces observed at 950 rad/sec for all gear contacts, throughout 3.5 second analysis. . . . . 109
4.12 Pinion to Crown Wheel Contact Force wave over 0.5 seconds, at 10 ms print time 110
4.13 Pinion to Crown Wheel Contact Force waves over 0.5 seconds, comparing 10 and 1 ms print times . . . . . 110
4.14 Pinion to Crown Wheel Contact Force waves over 0.5 seconds, comparing 10,1 and 0.1 ms print times . . . . . 111
4.15 Force waves for 10,20 & 50 rad/sec input speeds. . . . . 111
4.16 Force waves for 10,50,100 & 200 rad/sec input speeds. . . . . 112
4.17 Force waves for 10,50 & 200 rad/sec input speeds. . . . . 112
4.18 Force waves for the full simulation duration, for a range of tested speeds from 10 to 200 rad/sec, supported by the velocity curves of the pinion gear at 10 and 100 rad/sec. . . . . 113
4.19 Force waves for the full simulation duration, for 1000 rad/sec, supported by the velocity curves of the pinion and bevel gear. . . . . 114
4.20 Plot of maximum forces observed between pinion gear and crown wheel contact at various speeds, for both original and refined print times. . . . . 115
4.21 Plot of maximum PD's observed between pinion gear and crown wheel contact at various speeds, for both original and refined print times. . . . . 115
4.22 Force Trend Comparison for pinion to crown wheel contact (contact 1) and bevel gear contact (contact 3), for 10 ms and 0.1 ms print times. . . . . 116

4.23 Steady state force wave amplitudes, across range of tested speeds. With anomalous result highlighted. . . . 118
4.24 Force waves for a range of speeds, over a 50ms time frame of the steady speed range. . . . 119
4.25 Steady speed force wave amplitudes for two series of tested speeds, with corresponding trend lines. . . . 120
4.26 Steady speed force wave amplitudes across a wide range of tested speeds, for all gear contacts within the differential. . . . 121
4.27 Steady speed force wave midpoints across a wide range of tested speeds, for pinion gear to crown wheel contact . . . 122
4.28 Steady speed force wave midpoints for two series of tested speeds, with corresponding trend lines. . . . 123
4.29 Force waves for a range of speeds, over a 50 ms time frame of the steady speed range. . . . 123
4.30 Varying print times, plotted against there corresponding CPU times at 100 rad/sec. 127
4.31 Force wave accuracy comparison between force wave generated at 0.6 ms and 0.1 ms print times. . . . 128
4.32 Force wave accuracy comparison between force wave generated at 0.8 ms and 0.1 ms print times. . . . 129
4.33 Force wave accuracy comparison between force wave generated at 15 ms and 0.1 ms print times. Highlighting disparity in accuracy at tested print time extremities. 129
4.34 Force wave accuracy comparison between force wave generated at 0.8 ms and 0.4 ms print times, for 10 rad/sec input speed. . . . 137
4.35 Force wave for 200 rad/sec input speed, using the linear loading option, with a significant rise in forces seen over a short time frame at the beginning of the simulation. . . . 142
4.36 Force wave for 200 rad/sec input speed, using the expression loading option, with the acceleration of the model over one second. . . . 143
4.37 Visualisation of the loading Curve utilised, to initially observe effect of curve loading the differential model. . . . 144
4.38 Visualisation of the loading Curve utilised, to observe the effect of an abrupt drop in the curve loading input. . . . 145
4.39 Comparison of force wave outputs for pinion gear contact, using both curve and standard loading methods. . . . 146

4.40 Comparison of force wave outputs for pinion gear contact, using both curve and standard loading methods, with the curve load taking loading inputs every 50 ms as opposed to Figure 4.39 which is every 0.1 ms. . . . . 147
4.41 Closer inspection of the pinion gear speed during the designated steady state region, comparing the standard expression loaded output with the curve loaded output. . . . . 147
4.42 Plot of maximum contact forces observed within differential model, for varying tested acceleration rates. . . . . 150
4.43 Plot of contact force plots for pinion gear/crown wheel contact, at varying acceleration rates. Supported by the tracked speed of the pinion gear for the corresponding rates. . . . . 151
4.44 Visualisation of results in table 4.23 . . . . . 152
4.45 Plot of acceleration rate against time, for the 1000 rad/sec$^2$ expression generated model. . . . . 153
4.46 Inspection of acceleration rates during steady speed region of the model displayed in Figure 4.45 . . . . . 154
4.47 Visualisation of forces for a linear acceleration at a rate of 1000 rad/sec$^2$, with reference plot of equivalent expression generated version. . . . . 155
4.48 Visualisation of forces for a capped linear acceleration at a rate of 1000 rad/sec$^2$ up to a speed of 500 rad/sec, with reference plot of equivalent expression generated version and previous linear version. . . . . 156
4.49 Comparison of maximum forces observed at various acceleration rates when using a linear accelertion and a expression derived curved acceleration. . . . . 156
4.50 Acceleration rates plotted for 1000 rad/sec$^2$ linear acceleration up to 500 rad/sec. 157
4.51 Forces plotted alongside pinion gear speed, for an exponentially increasing acceleration rate curve. . . . . 160
4.52 Forces plotted alongside pinion gear speed, for a model accelerating up to 500rad/sec and then decelerating back to zero, both at a rate of 1000 rad/sec$^2$ . . . . . 160
4.53 Forces and pinion gear speed, overlaid for two separate models one accelerating up to 500 rad/sec and the other decelerating from 500 rad/sec both at a rate of 1000 rad/sec$^2$ . . . . . 161
4.54 Forces plotted alongside pinion gear speed, for a model accelerating up to 500 rad/sec and then decelerating back to zero, both at a rate of 2000 rad/sec$^2$ . . . 162

4.55 Forces and pinion gear speed, overlaid for two separate models one accelerating up to 500 rad/sec and the other decelerating from 500 rad/sec both at a rate of 2000 rad/sec$^2$ . . . 162
4.56 Closer inspection of the pinion gear speed during the designated steady state region, comparing the standard expression loaded output with the curve loaded output. . . . 163
4.57 Comparison of force wave results during initial sharp acceleration period, for standard and expression print time application methods for a 200 rad/sec input speed. . . . 165
4.58 Comparison of force wave results during initial sharp acceleration period, for standard and expression print time application methods for a 10 rad/sec input speed. . . . 166
4.59 Comparison of force wave results during initial sharp acceleration period, for standard and expression print time application methods for a 10 rad/sec input speed, with a reduced print time of 2.00 ms. . . . 167

5.1 Key steps of Altairs C123 process . . . 171
5.2 Visual of the double crash scenario being assessed upon the Taurus model. . . . 173
5.3 Graph tracking body and tank displacements, with relative displacement calculated. . . . 174
5.4 Modal Assesment of the fuel tank,global modes depicted. . . . 175
5.5 Basic model set up for ESL assesment. . . . 176
5.6 Displacement contour plot for initial ESL assesment of the fuel tank. . . . 176
5.7 Left; Displaying deformed fuel tank post dynamic simulations. Right; Highlighted regions for individual ESL loading. . . . 177
5.8 (A) End deformed fuel tank, post dynamic test. (B) End deformed fuel tank post ESL test. . . . 178
5.9 Stress contour plot of the fuel tank post assessment. . . . 179
5.10 (A) Schematic of the initial 1D crush set-up. (B) Deformed result with 2D represented 1D beam. (C) Fuel tank 1D assessment pre-loading 3D mesh. (D) Fuel tank 1D assessment post-loading 3D meshed tank. . . . 180
5.11 (A) C2 skeleton from DFEM (B) 2D realised sections of C2 skeleton. . . . 181
5.12 (A) Front rigid crash DFEM T=0.25 ms (B) Front rigid crash reduced C2 T=0.0 ms(C)Front rigid crash reduced C2 T=0.25 ms . . . 182

# Acronyms

**1D** One Dimensional

**2D** Two Dimensional

**3D** Three Dimensional

**AM** Additive Manufacture

**BEV** Battery Electric Vehicle

**CAE** Computer Aided Engineering

**CFD** Computer Fluid Dynamics

**CFS** Crushable Frame Springs

**CPU** Central Processing Unit

**CVT** Continuously Variable Transmission

**DFEM** Detailed Finite Element Model

**DMM** Direct MidMesh

**DUT** Device Under Test

**ECE** Economic Commission for Europe

**ESL** Equivalent Static Loadings

**EU** European Union

**EV** Electric Vehicle

**FCEV** Fuel Cell Electric Vehicles

**FEA** Finite Element Analysis

**FEM** Finite Element Modelling

**FRP** Fibre Reinforced Plastic

**GBA** Granular Battery Assembly

**GM** General Motors

**HEV** Hybrid Electric Vehicle

**HP** High Performance

**HPC** High Performance Computer

**HSS** High Strength Steel

**HV** High Voltage

**IC** Internal Combustion

**ICE** Internal Combustion Engine

**KE** Kinetic Energy

**MAM** Maximum Authorised Mass

**MDO** Multi Disciplinary Optimisation

**NVH** Noise, Vibration and Harshness

**OEM** Original Equipment Manufacturer

**PD** Penetration Depth

**PL** Park Lock

**PHEV** Plug-in Hybrid Electric Vehicle

**RB** Rigid Body

**RESS** Rechargeable Energy Storage System

**SIMP** Solid Isotropic Material Penalisation

**SUV** Sports Utility Vehicle

**TE** Transmission Errors

$\mathbf{T_p}$ Print Time

**TPA**Transfer Path Analysis

**UMV** Urban Modular Vehicle

# Chapter 1

# Introduction

## 1.1 Motivation

The investigations and studies carried out within this thesis are driven by two main factors, the first of which is the transition away from fossil fuel powered vehicles, the second is the increasing demand for improved data and design, whilst ensuring reduced computational run times within the automotive industry. This prerequisite has become more prevalent in recent times, with Original Equipment Manufacturers (OEMs) developing fuel cell electric vehicles (FCEV), this is partly due to lack of previous data available to designers and OEM's for this type of vehicle.

The need for the automotive industry to respond to the current global climate crisis is well documented, with the use and source of energy used across the globe being one of the main contributors debated within the climate issue. With transportation responsible for over 15% of the overall greenhouse gas emissions, as shown in Figure 1.1. A key factor in this is the exclusive use of fossil fuels in many vehicles on the road, leading to a large portion of the fossil fuels generated energies to be consumed by transportation. As such using more economical vehicles that can utilise alternate fuel sources such as electricity offers the opportunity for the energy to be generated through more sustainable and renewable means, such as wind, tidal and solar.

This transition is a necessary step in ensuring OEM's futures within the transportation sector, and arguably the biggest change seen in the automotive industry since it's beginning in the late 1800s. Therefore, obtaining appropriate data and accurate loadings via Computer Aided Engineering (CAE), is crucial in allowing designers to achieve the best designs possible for the future of the automotive industry. With the ability to maximise weight savings within the designs through proper design exploration, being equally critical to ensure optimal fuel

efficiency for these future vehicles; In turn further aiding the industry in reducing it's carbon footprint. A secondary factor is using the reduced mass to improve vehicle performance, as within BEV's the vehicles weight as with other vehicles has an impact on the vehicle range, and given the fact the vehicle range is one of the key drawbacks of BEV's when compared with the conventional ICE vehicles when combined with refuelling times, this raises the importance of the vehicle mass. Therefore, a key driving force behind the project was to develop CAE techniques that would allow for improved data to be extracted, in the hope that with increased confidence in the computer generated loads; more accurate loadings could then be applied to components throughout the design process . In turn allowing designers the ability and confidence to design, to a much smaller tolerance and aid in the vehicle lightweighting process.

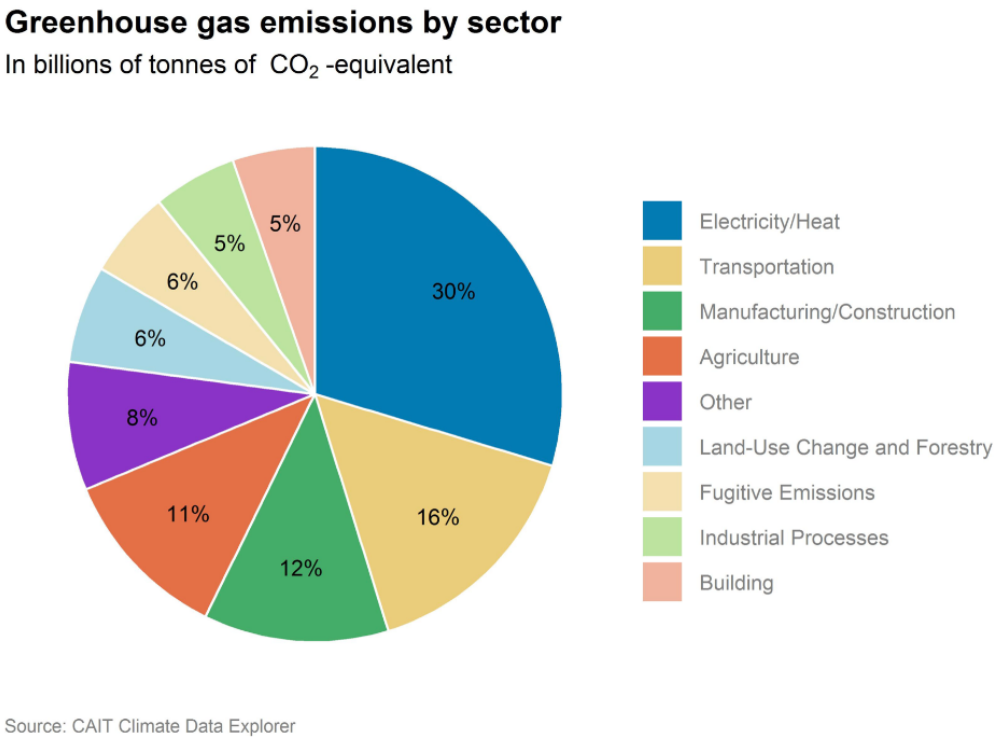



Figure 1.1: Greenhouse gas emissions by sector *2020 data

## 1.2 Overview

Studies within this thesis, cover investigations and utilisation of various CAE techniques which can be taken advantage of to enable improved component design activities; through the leveraging of rapid simulating large system models to provide improved inputs to sub-system and component level models. The two primary areas covered, each in turn offer new options for lightweighting of vehicles. The first two sections of the paper study areas in which dynamic solvers are utilised to capture and generate key static loadings, which can be utilised within

component design activities. The first of these two sections focusses upon the extraction of key static loadings from a dynamic solver which allows for real lifer transient loadings to be analysed within a shorter time frame and in turn offer the operator a clear overview of real life loadings. Therefore, allowing for the extraction of specific portions of the load to be applied within a static simulation, to further understand the loads implications and the necessary design requirements, allowing for a greater understanding and data set to be built and used in component level design.

Following the ideology of utilizing various FEA options to develop more accurate and meaningful loadings to aid in component design optimization, the area of dynamic crash loadings is explored, as crash scenarios often display the worst-case loadings for vehicles and their components. However, the typical draw back of crash analysis' is the computational intensity and time frame to successfully run them. However, the approach used within this thesis utilises a low fidelity model, to analyse the loadings passing through to key components in a much shorter time frame. This chapter investigates the difference in forces observed using the conventional detailed finite element model (DFEM), and the low fidelity counter part. As well as comparing these forces with the previously estimated forces and forces documented in guidelines. Allowing for a clearer understanding of the reliability of low fidelity models and the significance of extracting forces from real life events, to aid in the design and lightweighting process.

## 1.3 Aims and Objectives

The key aims for throughout the project are as follows:

- Utilise a variety of FEA techniques to extract more meaningful loads, which can be utilised to optimise component design.
- Leverage findings to provide an improved understanding of loads which may be experienced in real world scenarios.
- Prove forces and loadings generated via lighter modelling methods are accurate and reliable, when compared to more intensive conventional methods.
- Display weight saving opportunities for key e-axle components.
- Display clear comparison with standard design and optimisation methodology.

## 1.4 Computer Equipment

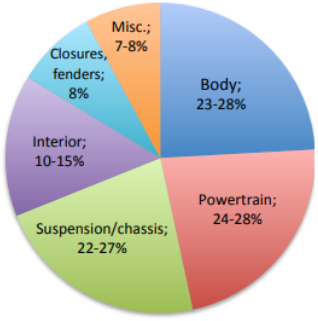
Throughout the following project all computational work has been carried out on the following system, unless otherwise stated. This should be considered when reading the resulting computational run times, and any other results regarding the computer use. The computer software used hosted a Intel(R) Core (TM) i7-6700K processor, at 4.00GHz, with an Installed Memory capacity (RAM) of 32.0GB, whilst running a Windows 64-bit operating system, with 4 active cores and 8 available threads.

# Chapter 2

# Literature Review

## 2.1 Vehicle Composition and BIW

Generally speaking all parts within a vehicle can be broken down into six key systems, these can be seen in Figure 2.1 with one of the major systems being the body in white (BIW), an example BIW is shown in Figure 2.2. The BIW typically makes up a quarter of the vehicle and is the core structure to which the remaining systems integrate and build around. One of the BIW's key roles within the vehicle, is the transfer of loads and as such in modern car build is often considered alongside the chassis, to improve the efficiency of these structures. Within high performance cars, the chassis and BIW are also sometimes combined to form a monocoque chassis, offering increased stiffness and weight reduction. Whether considered in isolation or with other key systems, the BIW is often an area targeted for both mass and stiffness design operations. An example BIW is shown in Figure 2.2.

| Approximate vehicle mass breakdown[a] | System | Major components in system |
|---|---|---|
|   | Body-in-white | Passenger compartment frame, cross and side beams, roof structure, front-end structure, underbody floor structure, panels |
| | Powertrain | Engine, transmission, exhaust system, fuel tank |
| | Chassis | Chassis, suspension, tires, wheels, steering, brakes |
| | Interior | Seats, instrument panel, insulation, trim, airbags |
| | Closures | Front and rear doors, hood, lift gate |
| | Miscellaneous | Electrical, lighting, thermal, windows, glazing |

[a] *Based on Stodolsky et al, 1995a; Bjelkengren, 2008; Lotus Engineering, 2010; the actual system definitions and system component inclusion can vary, and percentage weight breakdown can vary substantially by vehicle*

Figure 2.1: Vehicle mass breakdown by system and components [2]

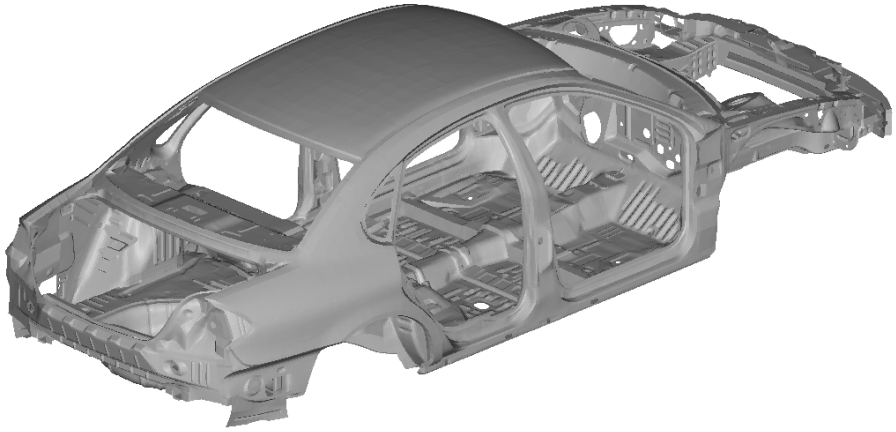


Figure 2.2: BIW of Ford Taurus

Body in White; as mentioned is a key system within the vehicle structure with the term originally stemming from coach building when the body work was constructed from wood and was unfinished, this was also commonly referred to as in white. However, the term BIW is slightly outdated as now it is less common for this stage to be isolated from the other manufacturing stages. As mentioned it is often best paired with the chassis when considering more modern vehicle compositions, with multiple vehicle designs combining them. Examples of the techniques include the aforementioned monocoque to older techniques such as ladder chassis'.

Beginning with one of the oldest and simplest combinations of both chassis and BIW; the ladder chassis or often coined the 'body on frame' approach. Typically construction is that of multiple steel tubular sections laid out in a ladder formation, with a body placed on top. This simple theory has been revisited and updated in recent years with multiple OEM's looking to utilise cross platform components, with various name plate bodies being placed upon the same chassis. In doing so removing the requirement to redevelop the whole car, in turn offering a more efficient manufacturing process and focus to be placed upon one key chassis which underpins multiple vehicle models. This carryover is also seen in instances where OEM's are owned by the same parent organisation, for example the VW group whereby sister companies can inherit the same chassis and adapt the body to suit there own model requirements.

An interpretation of the 'body on frame' has also been seen to be a popular option within EV development, with the incorporation of Energy Storage System (ESS) powertrain system into the chassis. This has been named the 'skateboard' chassis as seen in Figure 2.3, with Tesla being one of the first to use this method on the Tesla Model S in 2009. The 'skateboard' chassis utilises the ESS in the form of a flat battery at the centre of the vehicle, which can be lengthened or shortened based on requirements, with the vehicle body mounted on top [17].

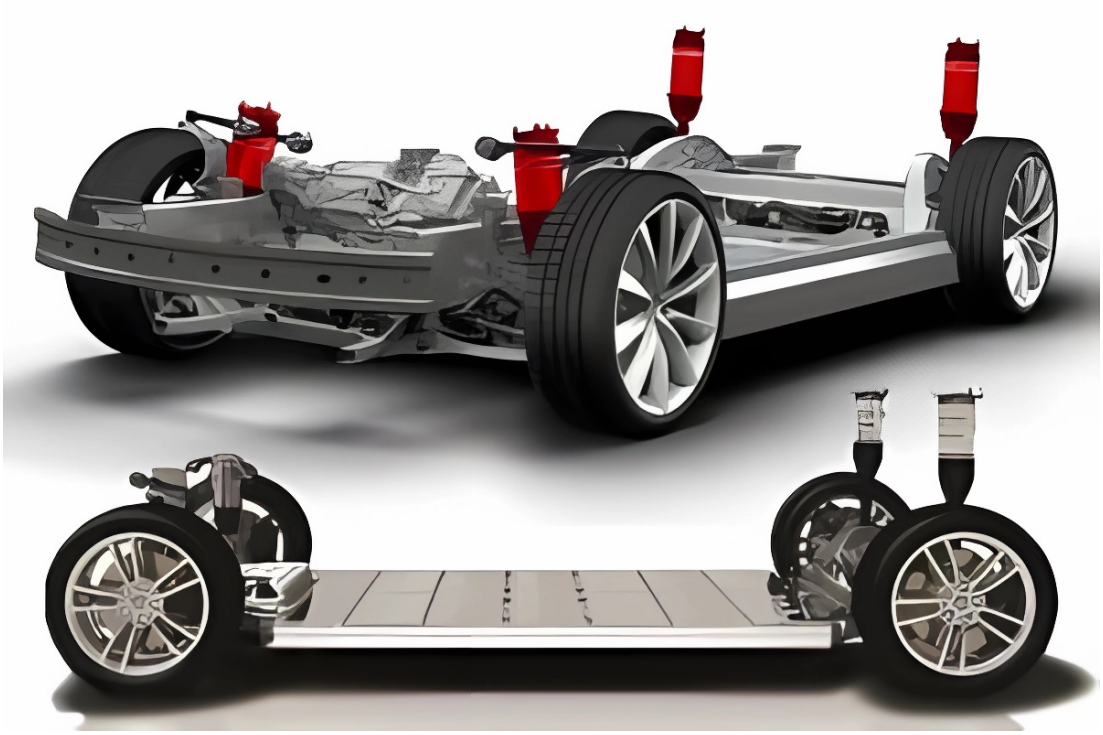


Figure 2.3: Skateboard chassis of Tesla Model S [3]

The monocoque or uni-body chassis, is often seen in motor sport or track day cars as its incorporation of the body and chassis as one structural component. Which are often built using carbon fibre, due to often being low production and highly mass driven. In addition to its light weight, it also has significant torsional stiffness. Monocoque's as the one main vehicle structure must therefore withstand all vehicle loads, including that of crash so must incorporate crumple zones. However, the draw back of utilising this one structure as a crash safety feature is that in the event of a collision, if a section of the monocoque is compromised through acting as a crumple zone. The whole monocoque may need replacing, as opposed to being repaired which is a possibility within other designs. Also, the merging of body and chassis to one single structure, removes the ability to be used as flexible architecture with each monocoque design being bespoke to a specific vehicle.

Across the various types of chassis with the exception of monocoques, the BIW and chassis can typically be broken down into three main groups, castings, extrusions and panels. With the majority of these parts being made from steel and aluminium, High Strength Steels (HSS) are often incorporated into key load paths with aluminium utilised in most panels and extrusions. Previously more low-carbon steel parts would of been present, however these have been replaced as material technology has advanced, with HSS offering improved strength and lower overall mass due to less material being used. Likewise, aluminium has replaced milder, low carbon steels due to it's lower density. Other materials which have increased their share in the chassis/BIW

composition include composites, plastics and lesser used metals such as magnesium.

Within the three main groups making up the chassis/BIW; Joints are a key subassembly often linking multiple extrusions and panels together. They are formed by several members intersecting, conventionally they are a thin walled structure of overlapping metal sheets fastened by spot weld. With the sheets coming from both panels and extrusions. Other key joints in the vehicles body are made using castings, particularly when it is a large number of intersecting components. The joints are key as they can deform locally, this flexibility can affect Noise Vibration and Harshness (NVH) characteristics for the vehicle, plus its structural performance. With any region of the automotive structure whereby two or more load carrying beam-like members intersecting, is categorised as a major compliance joint. With some OEMs incorporating multiple major compliance joints into one large structure, through the form of a large casting (mega casting), such as those seen on Tesla model Y with a single rear piece casting.

## 2.2 Introduction to Electric and Hybrid Vehicles.

### 2.2.1 Overview

Automotive technology has experienced numerous changes over the years but arguably the most significant change to date is the demand for an alternative fuel source, away from traditional fossil fuels. This demand for change has been driven by the increasing threat of global warming upon the planet, and the increased pressure to cut C02 emissions. In an effort to reduce the level of emissions numerous countries around the globe began a variety of green initiatives. One of which in Europe was the EU2020 targets, with the aim of cutting green house gas emissions from 1990 levels by 20% by 2020. [18] . A key area targeted for achieving this reduction, was the automotive sector through the planned implementation of new vehicle fuel and emission laws. Targeting a reduction within this area has became an even bigger challenge as the number of vehicles registered in Europe has seen continuous growth almost doubling from 163.628 million in 1990 to 312.7 million in 2018 [19] [20]. A big effort over this period has been made in developing vehicles with and alternative fuel source, which results in less C02 emissions, with BEV's proving to be the most significant. With OEMs beginning to modify popular vehicles into EVs. With the first modern mass produced EV being the EV1 made by General Motors in 1996 [21] , this was followed up by the successful launch of the Toyota Prius worldwide in 2000. The growth and popularity of the electric car remained steady throughout the early 2000's, with a more promising increase in the past decade. This has been largely due to a reduction in the cost of battery technology and a increased number of options within

the battery electric market. This rise has seen to continue with a sharp rise over the past two years, due to various governments increasing taxation of ICE vehicles , with diesels in particular being targeted, alongside government incentives for BEVs. A number of factors combined has led to a significant milestone within the automotive industry, with BEV new car registrations surpassing the number of diesel cars in September 2020. With BEV's taking up one in four new cars registered in Europe [22]. The transition and share of the automotive market over the past 9 years is illustrated in Figure 2.4. Overall in September 2020, 47% of the market was petrol, 24.8% and 25% BEV, this is a huge transition from a decade prior when diesels held 50% of the market and BEVs less than 1%. Within the 25% portion of BEVs, hybrids lead the way, making up 53% of the new registrations, with PHEVs and EVs 28% and 19% respectively. Also it is important to note that this percentile is not of a reduced Figure as a result of Covid-19, but instead the number of overall registrations was still seen to be 1.2% greater than September 2019. This growth of EV registrations has continued, growing from 24.5% in 2020 to 40.4% in 2021 [23]. This continual sharp rise is a by product of increased EV offerings from OEM's as they aim to match future new vehicle legislation in the UK and EU, banning the sale of all ICE vehicles in the uk by 2030, 2035 in the EU. With the UK also extending the ban to all hybrid vehicles by 2035 [24].

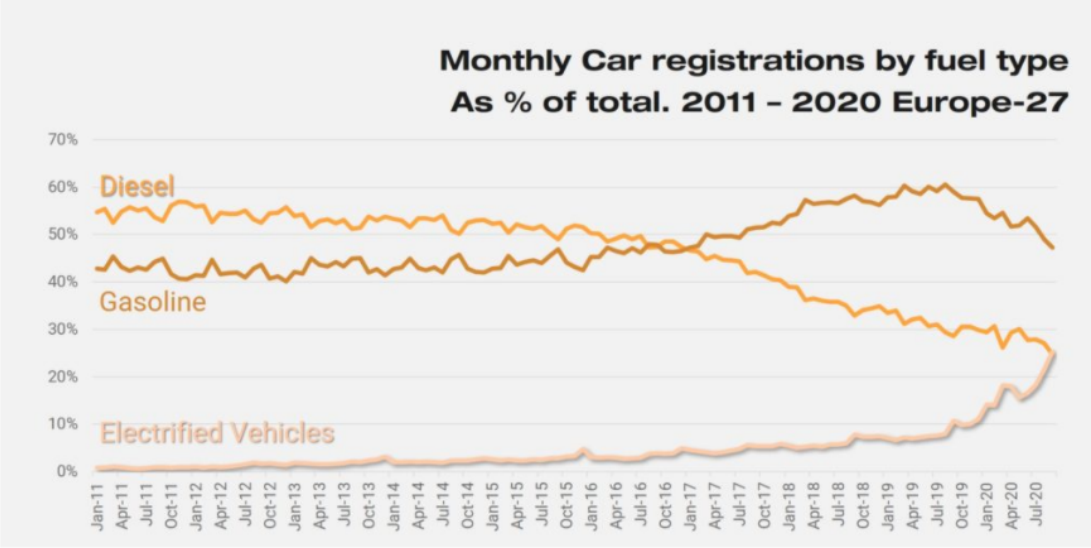



Figure 2.4: Monthly car registration by fuel type as a percentage of total registrations in Europe, for 2011-2020

Within the BEV sector the variety of options has increased, giving customers a much wider scope and allowing BEVs to cater for a larger range of customer requirements. The three main categories for BEV transitioning from conventional ICE vehicle can be seen in Figure 2.5. Each category offers different requirements to potential customers, the hybrid electric vehicle (HEV) also referred too as Mild Hybrid, function similarly to a conventional ICE vehicle, but has the

addition of batteries which are charged through regenerative braking and via the ICE. The fuel source for these vehicles remains as fossil fuel, with both petrol and diesel variants available. Typically the battery power supplements the conventional power unit lifting the typical mpg range to 50-85mpg, a marked increase on the standard diesel and petrol powered cars achieving around 28-45mpg [25] [26]. HEVs conventionally cannot operate on the battery power alone. However, when transitioning to the next level of electrification in plug-in hybrid electric vehicles (PHEV), they have the ability to function on just electricity. This category of BEV runs on a combined power of petrol/diesel, with an electric motor and larger rechargeable battery. The battery in this instance is charged in the same manner as HEVs by regenerative braking and the ICE but has the additional option of being plugged in to recharge. This increased electric capability allows the PHEVs to typically obtain 100-135mpg. The final category is the all electric vehicle, as the names suggests this vehicle type functions solely on electricity, with larger batteries storing the power and electric motors providing the power. The battery is charged again via various energy recovery systems, and primarily from the grid via plug in. With EVs typically offering a range of approximately 200 miles per full charge.

In addition to the these options, is the FCEV, similarly to the aforementioned options they utilise electricity to power electric motors. However, the mode of producing the electricity differs, as this is achieved using a fuel cell, typically fuelled by hydrogen, with other examples such as methanol and ethanol also utilised. They also often still contain smaller battery packs to recuperate braking energy, which can be deployed to smooth out the power delivery. Configurations highlighting the general key parts for these particular vehicle types can be seen in Figures 2.6 through to 2.10. Methods of maintaining the ICE have also been made through the exploration of alternative fuels, such as E-fuel. The idea being the fuels are created using clean renewable energy, wind, tidal etc. Although these options are currently expensive approximately 3-4 times the cost of conventional fuels. A significant positive is there high energy density, making them likely candidates for helping heavy duty, shipping and aviation become greener [27].

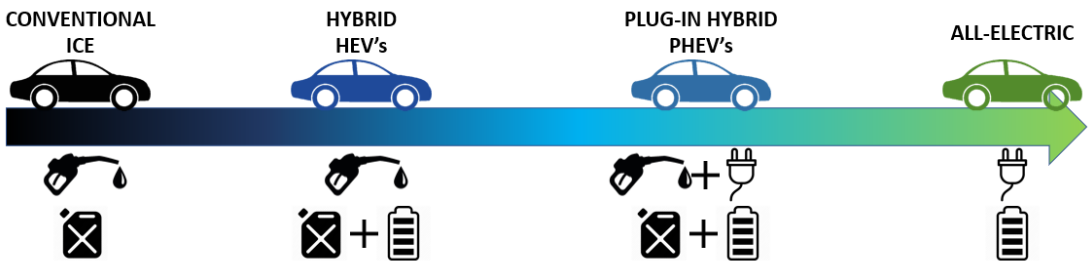



Figure 2.5: Transition from internal combustion engine vehicles to full electric vehicles, with key BEV categories highlighted.

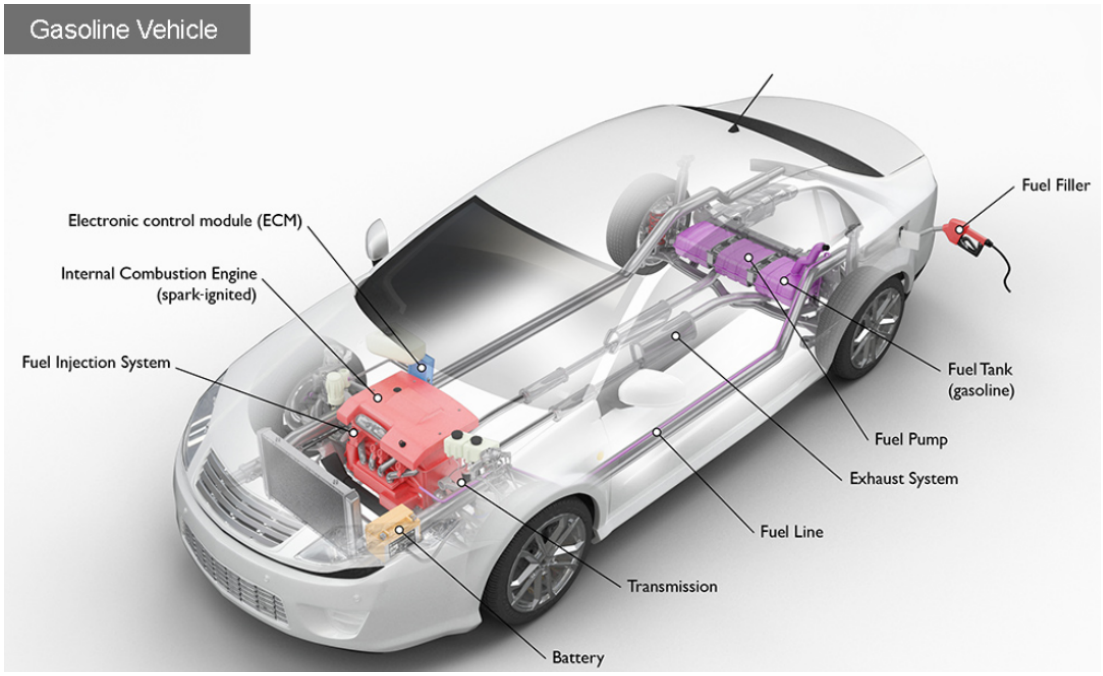



Figure 2.6: Overview of key parts within a conventional gasoline ICE vehicle [4]

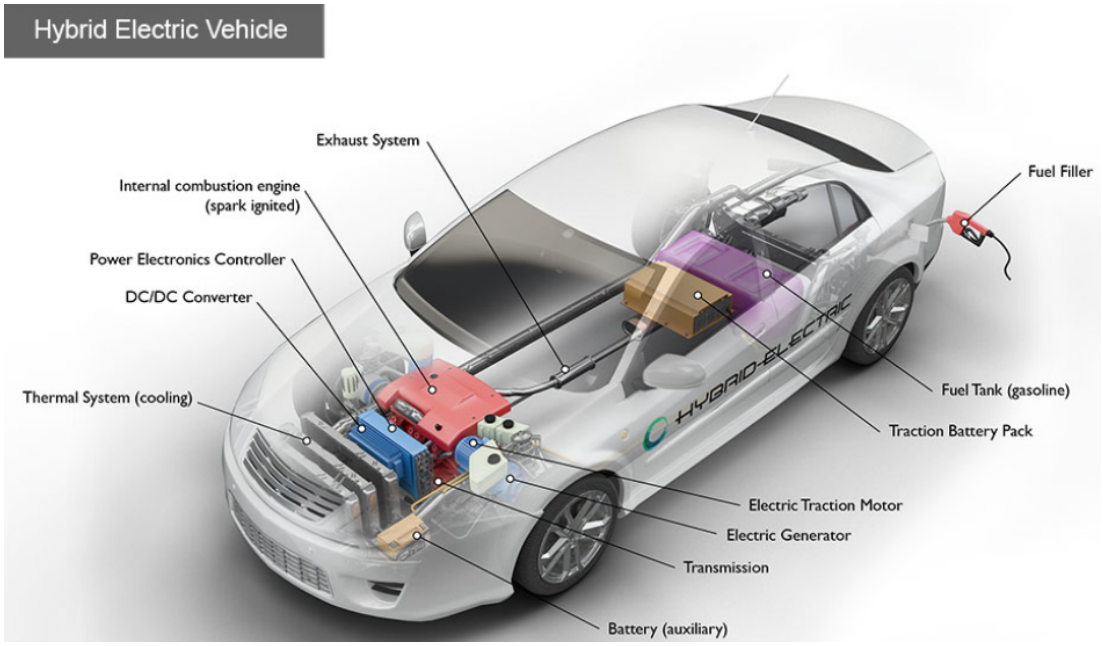



Figure 2.7: Overview of key parts within a Hybrid Electric Vehicle/Mild Hybrid [5]

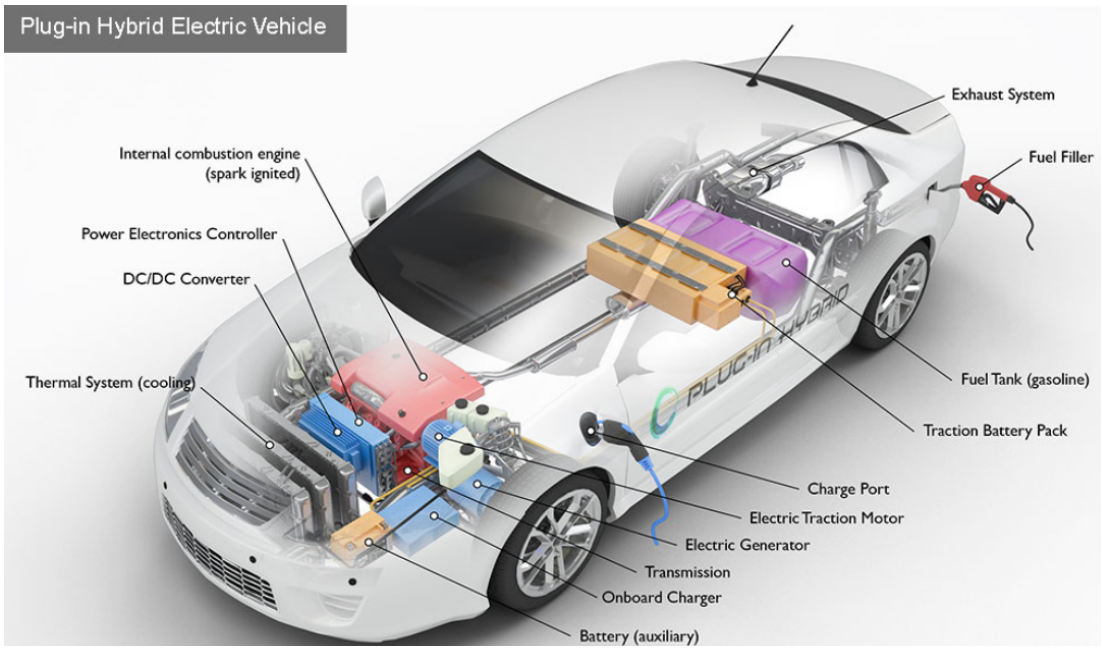



Figure 2.8: Overview of key parts within a Plug-in Hybrid Electric Vehicle [6]

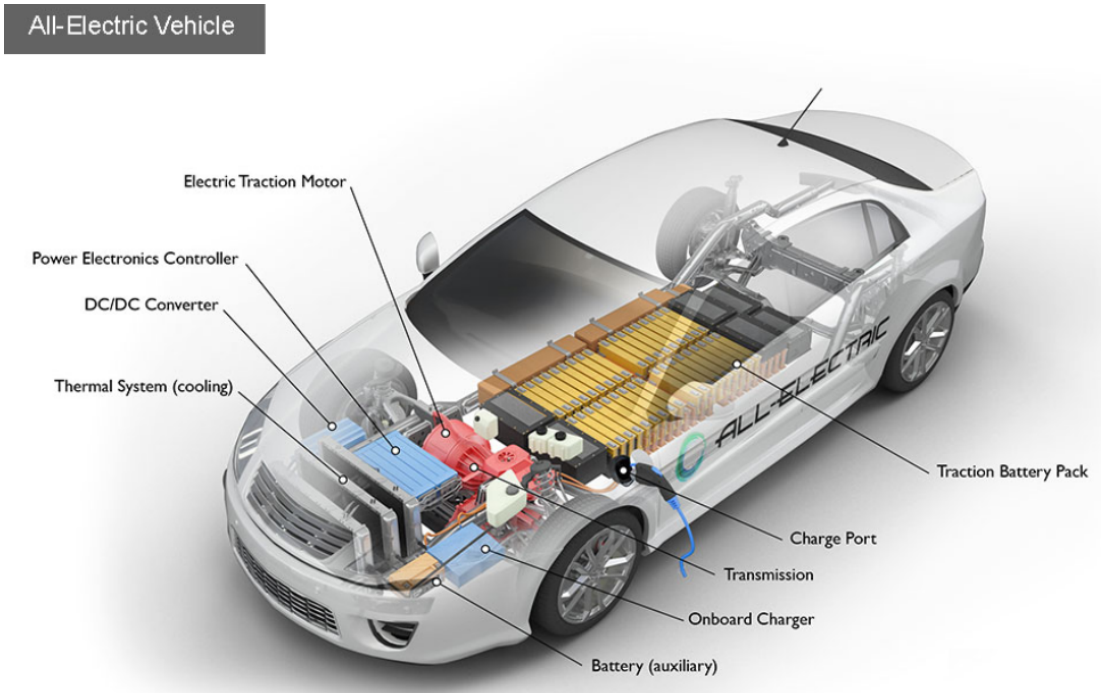



Figure 2.9: Overview of key parts within a Electrical Vehicle [7]

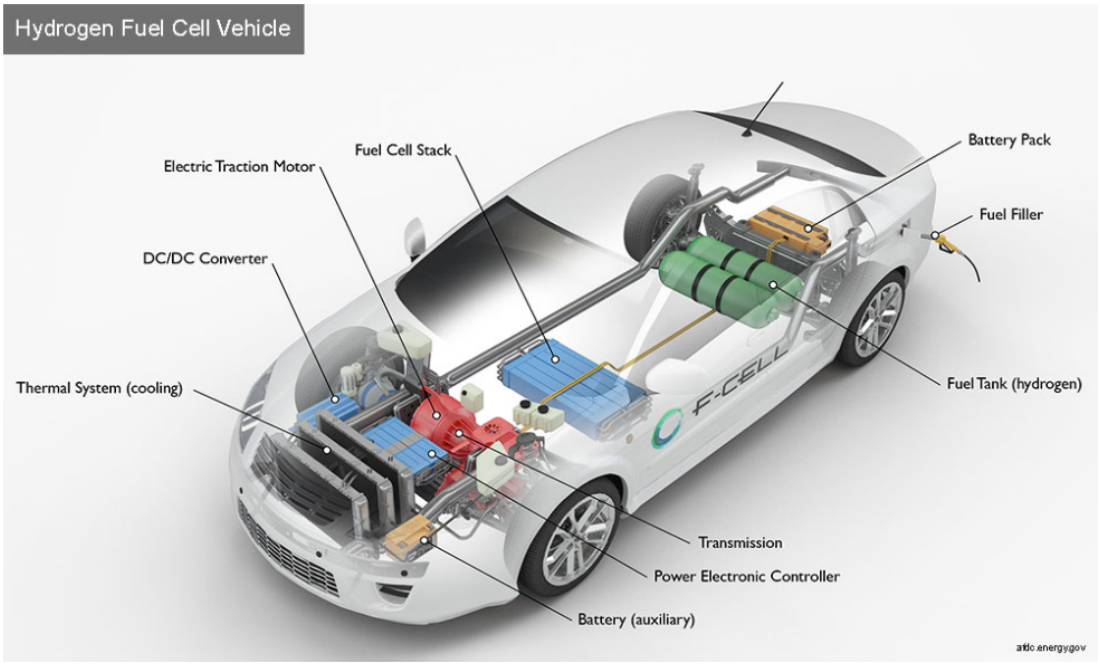



Figure 2.10: Overview of key parts within a Fuel Cell Electric Vehicle [8]

As mentioned the typical range of an EV is around 200 miles, this has been one of the biggest obstacles preventing the wider uptake in EVs. As when compared to the range of an ICE powered vehicle, the shortfall is clear. With a typical ICE vehicle averaging 38.8 mpg with a 45 gallon tank, providing a range of 465 miles, with a large portion of diesel cars capable of in excess of 600 miles [28]. However, battery technology has been improving along with EV design, over the years with the typical EV range growing from 100 miles in 2015 to 200 miles in 2020, with luxury models such as the Tesla Model S capable of in excess of 300 miles [29]. In addition to the improved technology companies have also been able to install more batteries to aid in extending range, however the batteries add significant weight in turn increasing the electrical consumption. Which is where the importance of weight saving becomes clear, which is why lightweighting is a key driving force for this thesis. Another factor limiting the practicality of pure EVs is the refuelling infrastructure, however, this is also rapidly becoming less of an issue with the number of public charging points constantly rising with a rise from 29,000 in 2019 to 34,488 as of $8^{th}$ October 2020. For perspective, there was 8385 conventional fuelling stations in the UK in 2019, providing approximately 61,210 fuelling points [30]. Whilst the infrastructure for EVs is rapidly catching up a key draw back is the refuelling/recharging time, with a conventional fuel pump taking a sixth of the time of a rapid charge point to refill/recharge. However, this doesnt account for the ability to charge BEVs at home as well as public charge points. Growth such as this has aided in consumer confidence in BEVs and the larger uptake resulting in the aforementioned surpassing of diesels in September 2020.

In addition to the environmental benefits of the EV market, battery electric offers a number

of other advantages. First of which is the reduced running costs for consumers and the ability to further enhance the environmental benefits by utilising renewable energies, they also offer cheaper maintenance due to the reduced number of moving parts, requiring less servicing. A number of driving benefits are also offered by EVs, these include instant torque, providing high and responsive acceleration, reduced engine noise and regenerative braking. Further benefits come from the electric powertrain, with the distribution of batteries allowing a low centre of gravity offering up handling and comfort benefits. The use of motors also aids handling and performance allowing for torque vectoring, varying the power at each wheel. This variety of benefits has influenced a growing number of consumers to move away from conventional fossil fuelled vehicles.

### 2.2.2 Advantages and Disadvantages

There are a number of key advantages which have been previously highlighted within this sections such as, environmental, economical and performance. However, there are a number of disadvantages which have been previously eluded to as causes for the delay in BEV development and uptake. Some of the issues facing the BEV area include practicality, safety concerns and economical factors. In the previous section the practicality issues and economical issues surrounding BEV, such as range and cost have been briefly discussed. However, one of the key disadvantages not yet highlighted is the safety concerns surrounding BEVs. This concern is a result of heavily documented BEV crashes, whereby the lithium ion batteries within the vehicles catching fire and being very difficult to extinguish once alight. The potential to combust is a known downside of battery technology, as is the ability for fossil fuels to combust also. Although there is an increased wariness of the less proven battery technology. As a result of this there are a large number of tight regulations and rules for BEV to adhere to, with regards to safety and in particular crash performance. This is covered in further detail in Section 2.4.2.

### 2.2.3 EV examples

In addition to the production models on the market, the past decade has also seen a number of show pieces generated, exploring the full capabilities of BEVs. A number of manufacturers have done this within a HEV platform, utilising the performance benefits of BEVs to complement, high end performance ICE vehicles. Examples of this include the McLaren P1, Ferrari La Ferrari, Porsche 918 and the Aston Martin Valkyrie. These models all utilise the electric motors to improve the flow of a standard engines torque curve, as well as aiding handling via torque vectoring, some also offer the ability to function solely on the electric power over a short range. Other manufacturers have displayed BEV potential via pure EV. Such as Rimac who

have created supercars such as the concept one in 2011, to display the performance potential of EVs for the future.

A showcase example was created by Williams Advanced Engineering in the form of the FW-EVX, which they referred to as the 'electric car platform for tomorrow'. The concept applied the companies motorsport knowledge in electrification, thermodynamics, aerodynamics and lightweight materials, to deliver a lightweight efficient concept. The showcase is based around a lightweight carbon fibre chassis encompassing the lithium-ion battery cells. The method delivers a crash resistant, scalable structure. The chassis is also designed to further aid the vehicles weight saving by incorporating numerous features into the design. Examples of this include the side sills of the chassis also designed to offer crash protection to the battery cells, channels within the chassis itself, to direct air flow for cooling to maintain batteries and power electronics at optimum temperature to aid performance and to reduce the need of radiators. An additional example from this showcase is the integration of the suspensions carbon fibre wishbones into the chassis. Overall this showcase is suggested to be able to save 40% (400 and 700kg) from conventional EV chassis, which would greatly aid the vehicles range and performance. The structure also accounts for manufacture ensuring its highly automated, using near zero waste processes, further boosting it's environmental benefits [31].

## 2.3 FE Modelling

A key for successful modern automotive design is the utilisation of efficient computer modelling, allowing engineers to examine various design options within a simulated environment, to make rapid adjustments to ensure optimal designs can be achieved to satisfy the desired criteria. Finite Element modelling/analysis (FEM)(FEA) is the most widely used method for solving the aforementioned engineering problems by generating accurate representations of components, which are often referred to as detailed finite element models (DFEM), whereby each component within the model is mapped as accurately as possible with current FEM techniques, this often results in large numbers of elements due to the refined meshes implemented within these models. When analysing and solving the required problems, the space is split into smaller simpler parts which are referred to as elements. The number of elements within a problem, directly affects the computational run time. As result of this, the method of meshing is key, with larger models generally including larger numbers of elements in turn creating larger problems to solve. Within the automotive industry full vehicle problems when are of significant size and therefore require a large amount of computational time to execute, reducing their effectiveness in the vehicle design stages and are often only utilised for validation. With smaller concept models for both

component and system level being utilised for design. However, a number of different modelling techniques have been developed and utilised to reduce the overall computational run time of large models to convert them to a low fidelity concept version.

DFEM's are often developed utilising both solid and shell elements for each individual part, which is a labour intensive process to develop. They also can be harder to utilise at the early vehicle design stages as they require detailed design information. Whilst developing detailed models is not as time consuming as it once was, due to the advancements in modelling techniques and software, the need for the component details is still a prevalent issue with utilising CAE for early design development. This shortcoming of using DFEM is another case where low fidelity models can be very useful as they can utilise approximations and simplified designs to generate meaningful design input at an earlier stage.

### 2.3.1 Meshing

#### 2.3.1.1 Overview

The decomposition of models using elements in the form of a mesh, underpins all FEA work. As such meshing is utilised throughout a range of engineering fields. Particularly within numerical simulations of models to supply validations. The solution of these broken down FEM's is an approximation of the original problem, whereby the accuracy of the solution is dependent on various factors when breaking the problem down into a discrete one. However, a major factor is the construction of a mesh of the computational domain, replacing the continuous regions with a finite union of elements from a range of geometries available, such as triangles, quadrilaterals, tetrahedral, prisms, etc. [32]. As a result of the importance of this stage of the modelling process, mesh generation can often become the bottleneck for numerical processes. Therefore, the importance of the mesh being executed correctly and appropriately is vital. The mesh size and type selected is also a key factor on the Central Processing Unit (CPU) run time.

#### 2.3.1.2 Meshing Types

There are a variety of meshing methods available each with its own merits, the various methods can have significant effects upon the simulations' computational demand and run time. The various meshes such as solid, shell, beam, axis symmetric etc. can be categorised into, one dimensional, two dimensional and three dimensional. Methods such as shell and mid thickness require the input of various properties and can be easily adjusted, however they only offer a 2D mesh of the component as opposed to a solid mesh which provides the more common 3D mesh.

#### 2.3.1.3 1D Meshing

One dimensional elements are commonly used when a structure's length is substantial greater than its cross section (L/r >20). They are often referred to as line elements as when modelling they can be simply represented as standard lines. There are two main types of one dimensional element, Beam and Bar (Sometimes referred to as a Rod). These two element types have a number of differences, with the beam elements being able to take both bending and shear loads, displaying deflections. Whereas, a bar element is primarily loaded axially for elongation and shortening. The mathematical principles behind these element types also differs, with the more complex beam element using Euler-Bernoulli or Timoshenko beam theory, to capture the shear and rotational [33]. Alternatively the bar element utilises simple axial deformation equations, using simple stress-strain relationships. Both of these beam representations require material properties as-well as section properties to be assigned for the elements. The three types each have their own restrictions as follows, the rod elements only undertake compression, bar elements can take both compression and tension forces, whilst a beam element is capable of absorbing a much wider range of forces including the same as a bar plus shear and moments. [34] One dimensional elements such as these allow for a better representation of long members in comparison to solids, whilst also being very simple to model. It is also useful when bending is the known route of failure and allows for much faster run times.

#### 2.3.1.4 2D Meshing

Two dimensional meshes within a three dimensional space are often selected when a component has a significantly larger length and width than its thickness. Once again there are multiple types of two dimensional element including surface and midsurface. These types of elements have no thickness, as the thickness is a property separately assigned. Two dimensional elements can often be referred to as shell elements due to their zero thickness. A significant feature of two dimensional elements is the fact they must have a constant thickness, which is not always desirable when dealing with complex geometries. Two dimensional elements when compared with three dimensional, has a key advantage again of its lower computational intensity.

Looking at both surface and mid surface in more detail however, displays their similarities as well as there difference within the two dimensional bracket. Surface meshing can be generated without a model and requires the parameter input to allocate a thickness to the two dimensional part. Where as when utilising midsurface, the midsurface shell model is generated from the original model. Doing this allows thickness properties to be generated from the original model. Shell meshes like these particularly lend themselves to iterative simulations due to the fact the thickness is just a mathematical property value, which can be simply modified. The reasoning

for the significant reduction in computational time is because a solid mesh requires multiple elements across its thickness which results in the large increase in elements and run time.

The shell meshes also offer more accurate results in some areas due to a solids' inability to model bending, depending on the coarseness of the solid mesh. Shell elements can sometimes provide overall more accurate stress results in all directions in a quicker time.

#### 2.3.1.5 Medial Axis Transformation

Medial Axis Transformation is a method in which geometry is represented by a by a skeleton. This method is an established way of simplifying geometries. It was first introduced by Harry Blum in 1967, to allow a user to capture a shapes properties, without the need for the whole geometry to be included.[35] This method of capturing geometries uses a code to extract the skeleton from a polygon, which can then be used to measure the distance between the skeleton and an unknown image. This can be used for reducing an images dimensions, shape matching as well as mesh generation.

When looking at mesh generation, it has been proven that one can use medial axis transformation to generate a mesh from a body, managing to recognise key shapes and features. Which can then be meshed with quadrilateral elements to a high standard [36]. Figure 2.11 displays a medial axis skeleton, it can be seen how the skeleton is generated through the centre of the object, through using locus of the centres of the balls which are maximal for within the object. A limitation displayed within these papers is the need to separate the 3D geometries into separate features to be used to generate the skeletons from, and the lack of ability to automatically generate a satisfactory representation of 3D problems, due to struggling to represent topological structure and shape accurately.

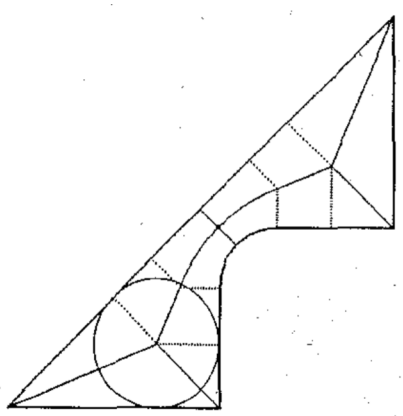


Figure 2.11: A 2D bracket and its medial axis. A maximal disc on the axis is also shown [9].

#### 2.3.1.6 MidMesh

#### 2.3.1.7 How it works

Midmeshing is a meshing ideology that is similar to medial axis transformation in its implementation of the plane through the centre of geometries, however it benefits from being able to allow the user to generate a mesh across the mid plane of a component without the requirement of a pre-existing surface to mesh. It also manages to do this without the need to break the component down into sections suitable for midplane selection, allowing for a continuous mesh flow around the entire 3D geometry. Formerly the only method of mid meshing within Hyperworks was through mid surface meshing, where by the user is required to generate a mid plane of the components first and the option to mesh the newly generated mid surface is available. However there are a number of issues with this methodology as the surface generated is often inadequate to allow the user to generate an accurate mesh representation.

However through the use of the Midmesh tool within Altair's hypermesh software, a mesh is directly extracted using the geometry as a reference. The elements are automatically mapped upon the mid plane of the component. With the use of various features within the tool such as Flatten connections and ignore flat edges, the mesh can automatically be manipulated to remove and adjust features as desired, without the need for post meshing amendments. The tool however does also offer tools designed to assist with the clean up of the initially generated Midmesh, along with a feature to allow for the re-meshing of elements to either improve quality within sections. In addition to coarsening or refining the whole mesh. The final feature within the tool allows for the thicknesses to be mapped to the elements to allow full representation of the initial component. The thickness mapper utilises the original component geometry and uses this to map the thickness either to the elements or nodes.

#### 2.3.1.8 Benefits and Uses

The key benefits of using a Direct Midmesh (DMM) is primarily the speed at which the mesh can be generated, whilst delivering a much lighter computational representation of the original component.

#### 2.3.1.9 3D Meshing

Three dimensional meshing is one of the most common mesh types, as it often delivers very accurate results. It has a significant drawback in comparison to the two and one dimensional types, that is its computational demand, with most good quality solid meshes requiring mutliple elements aross its thickness to help capture the stress variations within the component. Typically three to four elements are applied across the thickness, which causes a significant rise

in the number of elements comparatively therefore longer run times. However, solids do lend themselves to more complex geometries as they are not required to have a constant thickness throughout geometries.

Within three dimensional solid meshes a variety of element types are used for different geometries. The shapes include tetras/pentagons/hexagons and pyramids.[37] Tetrahedral's are the simplest and most common three dimensional element, otherwise known as simplex, due to the fact they can be mesh and three dimensional volume, regardless of shape. The other element types are generally only implemented when there is motivation to do so, as the element shape does not always lend itself to the models geometry as the tetrahedrals do [38]. For example hexahedron meshes will often supply more accurate results, due to the fact the elements are aligned with the flow, but due to this, hexahedron meshes will often struggle to mesh a whole geometry.

#### 2.3.1.10 TetraMesh

Tetra Mesh is one of the most common three dimensional element types, and consists of elements of a tetrahedral geometry with four triangular faces, which can successfully map any enclosed three dimensional volume. Tetrahedrals can also be used alongside adaptive mesh refinements, whilst allowing the user control of the mesh by specifying a tentative element size. [39]

Tetra mesh elements can be represented as either first or second order elements. First order elements have fewer nodes than second order elements. Second order are often preferred due to the larger number of nodes allowing them to have better mapping abilities across the area of the element, whilst also reducing integration, all of which together result in more accurate results, at the cost of run time. The first order elements also follow a linear interpolation where as second order follow a curved line, of a higher order interpolation [40].

#### 2.3.1.11 Tetra Mesh Generation

Tetra mesh generation is one of the more simple mesh types, where the mesh generator generates a mesh from a single closed volume [41] with no adjustments required allowing it to mesh from CAD geometry immediately. The mesh can be refined by the user to specify a target mesh size when generating. The generated mesh can then be altered using an array of refinement techniques, allowing adjustments to be made across the whole mesh or to local areas. Altair's volume mesh generation uses tetrahedrals to capture the geometry with additional features such as proximity and curvature options which allow for an improved geometry capture. With the proximity feature, generating smaller elements around the small features allows for smooth transitions, while the curvature option will place an increased number of elements along the

curved surfaces according to the user specified settings. [42]

Tetrahedral mesh elements are also split into two categories of 1st and 2nd order elements. These can be easily activated using a change of order function within the mesh generation software.

#### 2.3.1.12 Benefits and Uses

The key benefit of using a tetrahedral mesh is that it is often a very automated mesh generation system, which will allow the user to capture the geometry of any three dimensional closed volume very quickly, whilst also allowing mesh refinement of the whole model or local areas. Also the generation of a tetra mesh does not require a surface mesh, and delivers accurate and reliable results.

Due to the aforementioned benefits tetrahedral meshes are often implemented on complex geometries, where other mesh types typically struggle. The key down side of using a tetra mesh is it requires larger amounts of computational run time, in comparison to many other mesh types.

#### 2.3.1.13 Time Step overview

Time Steps are a significant feature of any computational simulation. This is due to the fact that the time step of the computational model is the driving point for the computational run time and therefore the computational intensity required. The time step is crucial to the computational run time, due to the fact the minimum time step throughout the model will drive the entire model's computational run time. The time step is driven by the minimum edge length of an element. The time step can be simply calculated from Equation 2.1, as a model can remain stable when a shock wave passing through the mesh, does not pass through more than one element per time step. This ensures that no nodes/elements are skipped during the analysis.

$$\Delta t \leq I_c/C$$

$I_c$ is Critical length of element, $C$ is Speed of Sound, $E$ is Youngs Modulus, $\rho$ is Material Density. (2.1)

$$C = \sqrt{E/\rho} \tag{2.2}$$

Along with the time step the type of element is a key part of a model's computational

run time. With current industrial knowledge and experience, it is known that a 3D mesh is much more computationally expensive than the preferred 2D shell elements, largely due to the increased number of elements within a 3D mesh. Hence, the motivation for the project being driven by finding a 2D replacement for the current 3D representation of castings within a crash model.

### 2.3.2 Low fidelity modelling

One of the methods commonly utilised to reduce computational run time is low fidelity (lo-fi) modelling. Lo-fi modelling, utilises approximations to simulate a physical system as opposed to detailed modelling of the system, creating DFEM of the problem. The transition to a lo-fi model is often regarded to be trading model accuracy for efficiency. However, more recent lo-fi methods have proven to be able to maintain accuracy and key characteristics of the system being represented, whilst still delivering significant time benefits. Within a vehicles BIW, various components are easier to convert to a lo-fi model than others. An example of this is the 1D representation of the BIW's beam sections. With parts such as joints proving much more difficult to accurately capture their stiffness and behaviour outside of DFEM.

A number of methods have been carried out for building a low fidelity vehicle model, with various methods being applied. For previously developed lo-fi models of a vehicles BIW, the system is often divided up into three key categories beams, panels and joints. It is often the modelling of the joints which sees a variety in techniques being implemented. A series of papers on low fidelity vehicle models have been investigated, to aid understanding of the benefits and potential issues of developing a lo-fi model of a vehicle. As mentioned the joint representation is a key area of difference across most papers, leading to a number of representations being introduced over the past 38 years. One of the various representations seen across the papers is the Tri-Spring representation which was introduced in 2006, by Kuo [43] in which the joints on the vehicle are simulated with three rotational springs which represent the three stiffness parameters of the actual joint from a static joint stiffness test. The three parameters being fore/aft, inboard/outboard and torsional stiffness. The method used to test the joint stiffness was the application of a force through a lever arm on the weakest leg of the joint. As when the joint is subjected to the bending or torsional load, the joint experiences a rotation in two perpendicular directions, the resistance to this rotation is categorised as the joint stiffness. An example is depicted within Figure 2.12. This method can be applied via CAE methods, analysing each of the vehicles joints in isolation, then applying the appropriate stiffnesses as three rotational spring elements within the low fidelity model. This method and representation has a number of key advantages, such as values can be obtained from pre-existing DFEM or

physical testing, also approximate values can be used from previously tested models for similar joint types. The design of the representation is useful to engineers to understand the physical strength of the joints and to carry out efficiency studies. In Kuo's initial proposal a test was also carried out whereby the stiffness of the joints was reduced by 25%, however this was observed to have a negligible effect on the overall body stiffness. Suggesting weight reductions could be made, such as down gauging of the panels making up the b-pillar joint or carrying out a sizing optimisation to reduce the overall size of the joint thus saving mass.

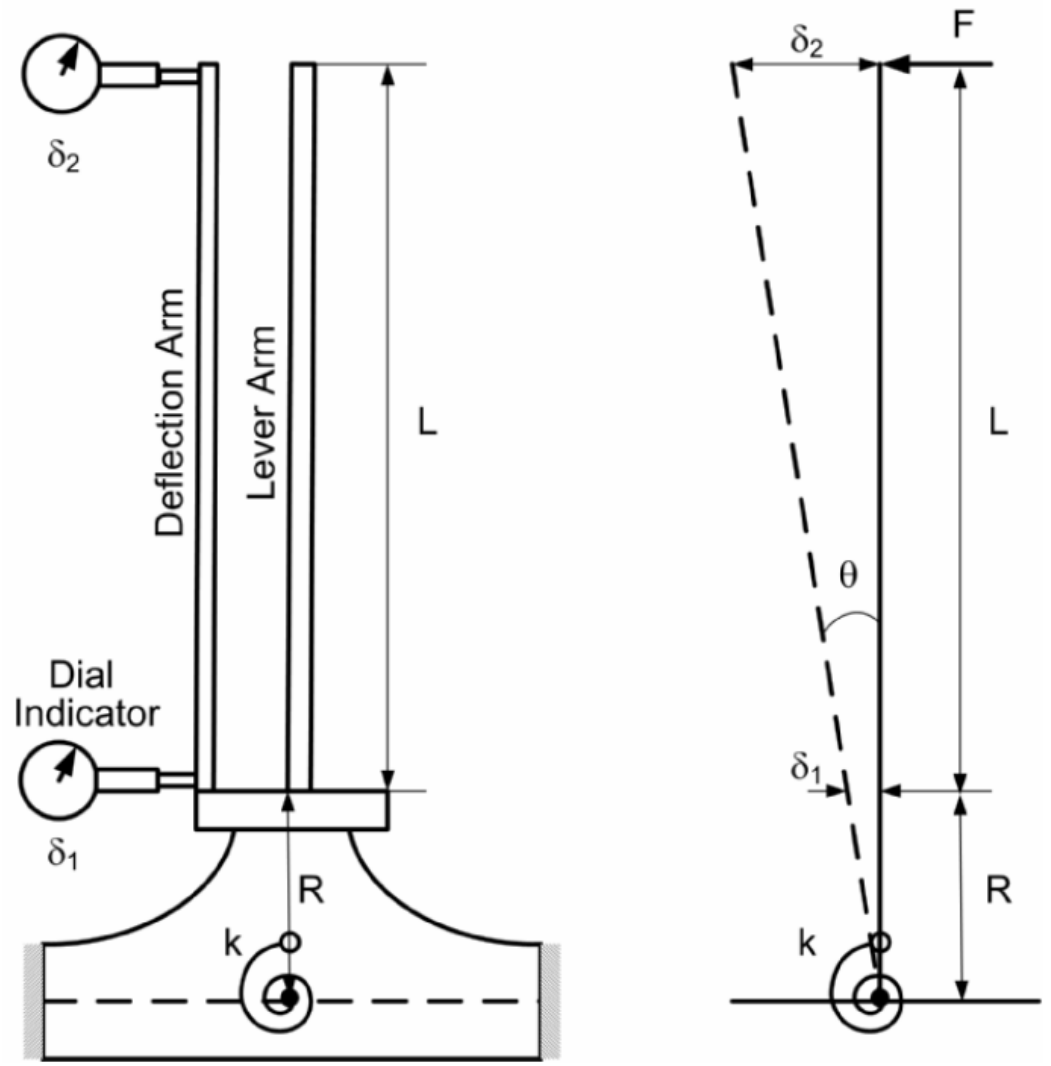



Figure 2.12: Depiction of testing method for tri-spring joint representations on vehicle B-pillar.

Following on from the tri-spring joint representation, another joint representation regularly discussed is a super-element representation. The super element, groups and processes a set of finite elements typically from a DFEM, and applying an optimisation procedure, that selects constants and beam lengths that relate to the selected DFEM elements mass, stiffness, modal and strain energy attributes. Allowing for an accurate lo-fi representation of the vehicles

joints and beams. The suggestion of super elements was first introduced by Wierzbicki and Abramowicz in 1983 [33] and 1989 [4] respectively, with the concept of a super-folding element and super-beam.

Shahhosseini [43] in 2010 reiterated how the main difference in various low fidelity models are the joint representations and the significance of accurately doing so, as the joints are key components within the vehicle bodies structure providing key stiffness to the model, which effects the static and dynamic behaviour of a model. Therefore compared the tri-spring representation with that of a super element. Within the paper the models were compared back to a DFEM. The paper in question favours the tri spring element as a result of it's following disadvantages associated with the super element; They add complexity to the overall model, reducing the overall computational efficiency, whilst also requiring a level of design detail to generate them, which may not be available during early design stages. Also the use of a super element that maintains its physical interpretation can limit the scope for optimisation.

The papers previously highlighted all utilised the low fidelity modelling options for static testing purposes only, as accurate capture for dynamic events when using a lo-fi representation is a much more significant challenge, with a larger disparity in result accuracy from a DFEM counterpart. However, in recent years there have been attempts made to accurately use lo-fi representations for dynamic simulations. In 2017 G Georgiou, looked at using macro-element methodology for full vehicle crashworthiness [44]. The paper looked at comparing an established DFEM crash model with a lo-fi version using macro elements, which was first introduced in the late eighties by T.Wiezerbicki and W Ambrowicz among others [45][46].

The method utilised items such as super-folding elements to represent the beams within the model and an approach similar to that of the tri-spring representation for joints, utilising intersecting load carrying beams, which are connected at a geometrical centre, X,Y,Z offsets can be applied to the start and end of the beams to modify their position and length and hence approximate more realistically the actual geometry of the structure and the rigid core of the joint. The joint representations were generated using a CAE simulation model, similar to the physical testing highlighted in "Major compliance joint modelling survey for automotive body structures." [43]. The super folding elements used for the beams are a foundation of the macro element method, capturing the crushing response of thin walled members, primarily extrusions. This method has known disadvantages such as the user is required to have an expert level structural and crashworthiness knowledge, and model build experience to be able successfully implement the super elements in the correct manner. Also the super beam elements do not have the capability to accurately predict all crash events, as they are only proven to be accurate in axial crushing. For this particular paper, connections between metal sheets are also an issue, as

they are considered rigid and therefore do not offer failure criteria and do not account for any energy dissipation within the model. The paper also offers a breakdown of the methods used to create a lo-fi version of the full vehicle model, including the sub-assemblies. For which the suspension was represented using a series of beams, with items such as dampers omitted from the representation. Thin surface parts (roof, floor etc.) and glass parts, which contribute to the vehicles response via shear deformation, these panels were replaced by super beams. Large rigid parts such as engine block etc. were replaced by simplified rigid body representations.

A series of models with increasing complexity were tested, a strong correlation for both versions was seen. With further experimental testing of a simple beam in isolation being represented by a super beam element was carried out, examining the effect of increasing the number of super beams by splitting the beam down, which had no effect on the accuracy of the lo-fi representation. However, a study of different time steps for the model displayed the importance of an appropriate time step, as studies with the larger time step resulted in the energy balance not being satisfied. The joint representations in isolation also yielded positive correlation for fore and aft loadings, although the correlation was not as strong for inboard and outboard directions. This was a result of the joint representation technique not providing adequate response during out of plane deformation. Improvement was suggested to be obtainable by using rotational springs. The full vehicle tests for roof crush and rigid wall showed good correlation, again displaying strong promise for the utilisation of lo-fi models within a dynamic environment. It appears the occasional loss of correlation on parts in isolation is overshadowed when built into a larger scale model. The time benefits highlighted were also clear with the roof crush taking 25s on 1 core to run for the lo-fi model, as opposed to 4hr 42mins on 16cores for the DFEM.

Another example of implementing a low fidelity model of a full vehicle, for crash and NVH was presented in 2019 by T Zeguer and S Bates [47]. The solution utilised the C2 stage of Altairs C123 design process to rapidly a convert 2.5million element DFEM to a 101 thousand element C2 low fidelity version. This rapid approach addresses an issue presented by previous papers on the volume of time required to develop an accurate low fidelity model. The low fidelity model generated uses a variation of the super folding element, referred to as a crushable frame spring (CFS) to accurately capture beam sections of the model, and uses super elements to capture the bodies joints. The theory also highlighted how a library of generic joints and beams can be created, allowing for users to use these parts during the early design stages of new vehicles before detailed CAD is generated, eradicating one of the negatives previously highlighted within Shahhosseini's paper [43]. The principal of a low-fidelity part library could greatly increase the amount of design direction supplied to engineers during preliminary vehicle

design, and in turn optimise the resultant product. The C2 low fidelity models created displayed positive correlation within both static NVH and dynamic crash environments.

## 2.4 Performance Testing

Performance testing is paramount in validating any new vehicles or design alterations of existing platforms, to ensure that key performance targets are met. The testing covers a range of sectors, the two which are most prevalent and are often carried out using CAE are crashworthiness and NVH. With some targets for the testing set based upon the car type and its specific aims, and other prescribed by national institutions with predefined criteria, the later being particularly true for crashworthiness testing. When using performance testing within the design and optimisation stage of vehicle development, multi disciplinary optimisation (MDO) can be utilised to evaluate various performance tests in conjunction with one another, to deliver an optimum result. Despite the overall optimum an optimisation strategy such as the aforementioned one would deliver, it is not always the option utilised. With OEM's often weighting designs to specific needs, an example of this would be an MDO study that prioritises crashworthiness above NVH qualities and weight, to ensure the safest car possible but not necessarily the lightest or most comfortable. Similarly the MDO study may be weighted to favour NVH performance but still contain key crashworthiness targets to ensure the vehicle does not under-perform against any set regulations or company standards.

### 2.4.1 Crash Testing

Crash testing is utilised to determine the crashworthiness of a structure, this being the ability of a structure and any of its components to protect its occupants in a survivable crash. The term was first used within the aerospace industry in the early 1950's [48]. In modern day vehicles the section of the definition referring to the structure and any of its components, now also encompasses technologies which aid crash avoidance, as naturally the ability to avoid a collision entirely is by far the safest option for the vehicles occupants.

#### 2.4.1.1 History of crash testing

The arrival of the automobile just after the mid 18th century in the form of steam vehicles, the first of which regarded to of been created in 1769 by French engineer Nicholas Joseph Cugnot. The arrival came with no current safety concerns, and continued in this manner as the number of various automobiles rose, until the first automobile fatality on the 31 August 1869 which saw Mary Ward fall from a steam carriage under one of its heavy iron wheels after rounding a street corner [49]. Further consequent events over the next 50 years, such as Henry Lingfield's fatal crash of his motorcar into a tree in 1898, led to the public beginning to have safety concerns around automobiles [50]. However, despite the concerns in the late 1800's it wasn't until 1922

that the first car safety feature was introduced, in the form of four wheel hydraulic brakes in Duesenberg Model A.

This first safety introduction was a catalyst in a significant rise in safety features and considerations for automobiles in the 1930's such as the addition of safety glass. With a significant milestone in a leading automotive company General Motors (GM) performing its first barrier crash test in 1934, [51]. At the same time as GM executing it's first barrier test. Claire Straight and C.J Strickland began a key movement for other car safety features, with the proposed use of seat belts and padded dashboards in 1930. With a law being passed in 1967, stating that front seat belts are to be installed in all vehicles sold in the UK, a consequent law making it compulsory to wear them was later introduced in 1983. Both of which have attributed to saving tens of thousands of lives a year. To support the increasing number of safety features and laws, as well as the increasing number of cars on the road in the UK, with the number seen to rise from 4.2millions in 1951 to 35.6 million in 2014 [52]. Organisations to govern vehicle safety began to form, the first of which in 1967 'The National Traffic Safety Administration'. With the leading organisation in Europe for crash testing being the European New Car Assessment Program (Euro NCAP),which was established in 1996. The Organisation has continued to adapt over the years becoming more stringent and thorough, introducing a stricter rating system in 2009, with the score being based upon previous measures such as adult and child occupant safety and pedestrian safety but also accounting for emerging safety assist features. The testing criteria has continued to be tightened with an overhaul of its ratings every two years with the latest taking place in 2020 [53].

As the section discusses, car safety is a key aspect in modern day car design, with a particular focus on the crashworthiness of the vehicle. This is a direct result of tighter laws and monitoring of car safety, in addition to a change in customers requirements with safety being a key consideration for many. Manufacturers have also become the leaders in the field often carving their own paths in automotive safety with new features being developed such as autonomous braking and blind spot monitoring. Causing for the testing organisations to adapt to encompass the rising technologies. Additionally to OEMs introducing new safety technologies, another area of improvement are based upon the chassis', with the introduction of crumple zones to help dissipate crash energy and ensure passenger safety. The crumple zones can be easily assessed via crash testing and edited accordingly, with large vehicles having softer crumple zones to absorb the additional energy associated with the mass of the larger vehicle [54]. Perfecting a crash structure via physical testing can be very costly, especially with high end vehicles, so the utilisation of computer simulations for this purpose can offer quick iterative designs, whilst allowing for checks pre production, saving OEMs large sums of money.

#### 2.4.1.2 Types of Crash Testing

A range of crash tests are routinely carried out on new-to-market cars. The tests are designed to ensure the safety of the car, during various scenarios which aim to replicate the most common crash scenarios. For testing purposes crash test dummies are used as substitutes for car occupants. The dummies are an Anthropomorphic Test Device (ATD) designed to simulate the dimensions, size and weight of a human body, which are typically fitted with sensors to record key data during the collisions from an occupants position. Key parameters which are monitored to gauge the success of the various crash tests are peak decelerations across the car, intrusions and energy absorption curves throughout the load case.

The five most common crash tests are:

- **1. Front Full Width Rigid Barrier** The front impact test is one of the most common tests as it utilises a non deformable barrier of a minimum height of 80mm, from the ground and running the full width of the vehicle, allowing for an overview of the whole frontal crash structure of the car to be analysed. The test is executed at an impact speed of 50km/h[55]. The frontal impact test can sometimes utilise additional vehicles to recreate vehicle on vehicle crashes, this form of test has most commonly been used by SUV's and vehicles with a higher ride height than normal. They can also be utilised to demonstrate old versus new crash situations, to demonstrate improvements in crashworthiness of varying models and the same model. An example of this test can be seen in Figure 2.13.

- **2. Front Offset Deformable Barrier** Amongst the offset tests, two key tests are used, first of which is a moderate overlap with 40% of the cars structure on the drivers side comes into contact with a deformable barrier at 64km/h. This simulation is designed to replicate a car-on-car head on collision, as it is most likely to occur. The second which is the most severe test is a small overlap test designed to simulate a corner of the car striking a tree or pillar. This simulation is the most severe as it loads the force at the smallest given area of all the tests, with the test area for the collision typically being 15% to 20% of the front of the car, with the impact speed being set at 50km/h into a non deformable barrier.

- **3. Side Pole** The side pole test is crucial due to it's replication of a side swipe collision, in which a fatality is most likely due to the lack of a material and crumple zone to absorb the energy of the collision before impacting the occupant. The testing procedure for the side impact utilises a trolley of mass 950kg, with a wheelbase of 3000mm and a track of 1500mm at both front and rear, which is directed perpendicular to the vehicle at 50km/h

[56].

- **4. Rear Deformable Impact / Whiplash Test** The rear impact test is used to replicate one of the most common crashes on the road, testing a vehicles crash performance when being rear ended. This scenario is one of the most minor rarely resulting in a fatality, however it does often result in injuries such as whiplash. The testing procedure uses a weighted sled once again, which strikes a stationary vehicle at approximately 32km/h. The test also provides insight into the robustness of the rear of the vehicle, which is crucial due to its housing of the fuel tank, providing insight into the possibility of a small collision escalating due to a fuel tank failure. As a result of the main resultant injury being whiplash, a whiplash testing procedure is also used whereby a seat and dummy are mounted to a testing sled which is accelerated and decelerated at a range of values, such as 60g [57].

- **5. Roof Crush** The fifth test that must be considered by manufacturers is the roof crush test, due to the large number of fatalities which occur during a roll over scenario. Electronic stability control helps to reduce the occurrence of car roll over, however roll overs still occur. Therefore the following testing procedure is used to asses the strength and integrity of the car's roof and supporting pillars, which are key components within the vehicles BIW. The test is carried out using an angled metal plate that is pressured against one side of the cars roof at a constant rate, typically one eighth of an inch a second until the roof is deformed by 5inches. The required force used to achieve this is then measured and tracked. More recently the test has been altered to a dynamic roll over test, which whilst providing a more representative set of results, is difficult to monitor parameters for the test but is instead often used for illustrative purposes as opposed to design guidance.

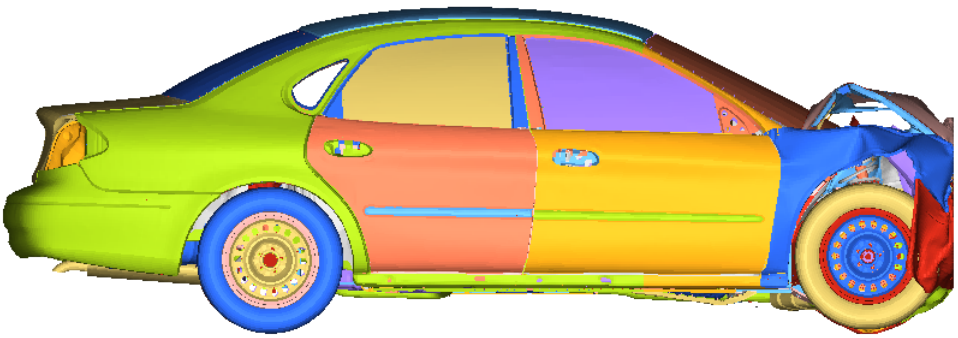


Figure 2.13: Frontal Crash Test Simulation of a Ford Taurus at 60 mph T=0.025 s [10]

#### 2.4.1.3 Computer Simulated Crash Testing

The expense of physical crash testing can be high, particularly for high end vehicles, as post testing the assessed vehicles require destroying. The tests can also be time consuming, both of these factors do not make physical crash testing a useful resource for iterative design development. Therefore, computer simulated crash testing is utilised, the process conventionally uses a DFEM of the focus vehicle. By using the FE model, reductions in the financial implications of crash testing can be made in addition to the time savings. Also the utilisation of simulations allows for more iterative designs to be assessed and a wider range of tests to be carried out, with alterations being easily made [58].

However, computer simulations for crash testing are computationally expensive and are therefore often executed on a high performance computer (HPC) to ensure an efficient run. The cause for the significant computational intensity is the highly non linear nature of crash test simulations. With non linear problems typically being defined by having large applied loads, resulting in large deformations and stresses and strains that exceed their linear relationships, as well as characteristically having large amounts of contact. As a result of this, specific computer software is utilised, with an increasing array of options available such as LS-Dyna, Abaqus and Altair's RADIOSS software which are all used for explicit time integration simulations. Additionally to the computational costs associated with the non-linear simulations, the mesh refinement and type generally required to accurately capture the results of the crash events is also a key contributor to the computational intensity. However, in recent years as highlighted by Bates [47], Georgiou [44] and others [59][60], various low fidelity modelling options are now being assessed as a suitable method to reduce the computational intensity of the model. Overall with advancements such as these and increased computing efficiency, FEA of crash testing has allowed OEM's to make significant financial savings during the design stages, with the reduction of the number of physical tests being executed and the number of associated vehicles being destroyed. Whilst also offering the ability for greater improved designs, as a result of the increased number of design iterations that can be carried out. The utilisation of simulations also offers the benefit of a offer a plethora of information which is not as easily obtained in practice, through 360 viewing, snipping and also energies absorbed across the whole car.

### 2.4.2 EV crash testing

From the standards and regulations for crash testing of EV's, two key areas can be defined for assessment; these are the crash performance of the battery itself, secondly the crash protection of the HV components within the vehicle. The rise in the number of these standards and

regulations for EV's, has resulted in new challenges for OEMs, due to the stringent nature of EV specific crash testing requirements. These requirements en-compass legal testing requirements defined for the battery packs and cells themselves. In addition to the structural safety of the electric drive train components, additional consideration has to be given to 'high voltage safety' and 'fire and explosion protection' particularly in post crash. A series of the regulations for post crash for various countries can be seen within table 2.1, with European and Japanese testing being far more detailed than the U.S market. The disparity in regulations indicates an issue in the current crash testing protocols for EV's.

| **Market** | **Regulation** | **Title** |
|---|---|---|
| Europe<br>ECE | ECE R94/12<br><br>ECE R95 | Uniform provisions concerning the approval of vehicles with regard to the protection of the occupants in the event of a frontal collision.<br>Uniform provisions concerning the approval of vehicles with regard to the protection of the occupants in the event of a lateral impact. |
| USA | FMVSS 305 | Electric powered vehicles: electrolyte spillage and electrical shock protection. |
| Japan | Trias 67-3<br><br>Art 17-2 Attach. 111 | Test procedure for protection of occupants against high voltage in electric and hybrid vehicles after collision.<br>Technical standard for protection of occupants against high voltage after collision in electric vehicles and hybrid electric vehicles. |
| China | GB/T 18384<br>GB/T 19751 | Electric vehicles - safety specifications.<br>Hybrid Electric Vehicles - safety specifications. |

Table 2.1: Electric vehicle post-crash legal requirements [1]

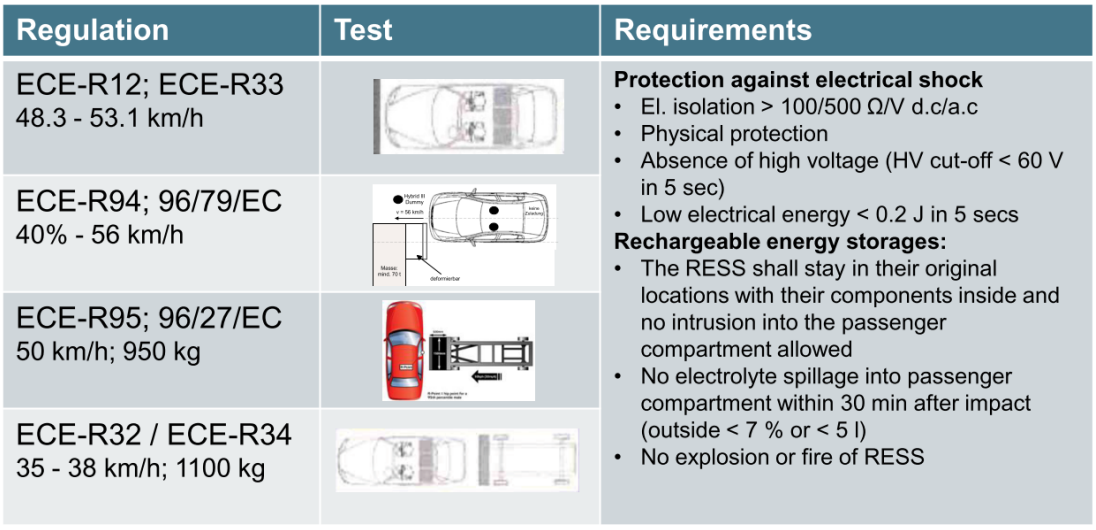



Figure 2.14: Electric vehicle crash testing requirements Economic Commission for Europe (ECE) [1]

A closer inspection of the detailed European regulations can be seen in Figure 2.14, from these it is clear that the battery packs will have to be highly protected in crash instances to ensure the Rechargeable Energy Storage System (RESS) stay in their original locations. Despite legal requirements such as these, further crash testing criteria are imposed upon the battery packs and cells themselves. This is a result of safety concerns surrounding new technologies such as high voltage (HV) lithium ion batteries being used, which aid in bridging the gap in vehicle range of EV's and ICE vehicles [61] . Once again within these standardised tests, differences in requirements and expectations from various regulators can be seen, which highlights the need for standardised testing, as enforced within ICE vehicles. However, co-operation and standardisation is starting to emerge between some regulators as the popularity of EV's continues to rise. These additional regulations can lead to enhanced complexity of the performance testing of vehicles. Particularly crash testing whereby some guidelines require monitoring for gas leakage from battery cells, which to include in a computational model would require the use of computational fluid dynamics (CFD), adding significant complexity to the simulations.

#### 2.4.2.1 Battery Testing

In addition to vehicle level testing for BEV's further component and pack level tests are outlined by a number of regulatory bodies for OEM's to meet. The stringent nature of some of the aforementioned regulations has resulted in, numerous articles and reports highlighting concerns surrounding the potentially excessive loads and overly stringent requirements being enforced upon OEM's, battery designers and vehicle engineers [61][62]. A key battery test which is discussed in multiple sources and proves a compelling example of the potentially excessive requirements; specifies an intrusion of 50% of the battery dimension. This test also highlights lack of continuity with some of the standards, as forces specified in current battery standards (SAE J2464) of a thousand fold of the weight of the battery is not sufficient to achieve the 50% stipulated crush. Whilst its agreed tests are crucial for HV-battery design a test such as the aforementioned 50% intrusion does not represent realistic loads which would be expected in crash testing or in severe real world accidents [63] . This is demonstrated by the fact a battery of 50 to 200 kg would be subject to 500 to 2000 kN, where as in a typical crash test, the vehicle loads are rarely seen to exceed 200 kN [62]. Which due to the vehicle level requirements forces observed at pack or ESS component level remain a further fraction of this value.

Alongside module level testing, a number of pack tests also exist for OEM's. Including but not exhaustive ; Penetration tests, drop tests, vibration tests, underfloor protection and water immersion tests, the combination of passing all of the tests adds to the complexity of ESS design often drives increased mass.

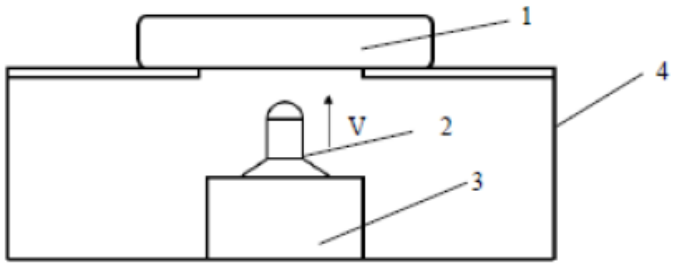
- **Penetration test** is a mechanical test whereby a steel rod/nail is forced through the base of the pack at a constant speed typically 8 $cms^{-1}$ , resulting in a short circuit and a rapid increase in temperature often leading to a thermal runaway event. This in turn tests the venting strategy applied to a pack, whereby venting gasses should exit the pack through a designated location through a pressure burst disc. Whilst the penetration test itself cannot be mitigated through design, the venting and thermal runaway event induced by the test can.

- **Drop tests** simulate a situation when a battery may be dropped during installation or removal from the vehicle, if the pack requires replacement or removal in it's lifetime, the test is repeated three times. The test drops the device under test (DUT) onto a rigid flat surface or cylindrical object made of steel. The test can also be carried out horizontally with the equivalent velocity being used. However, again variation for this test is seen in different standards with the specified height ranging from one to ten meters [64].

- **Vibration tests**, again vary across standards, with some using random excitation and others random and shock, SAE J2380 and ISO 19453-6 respectively. Although all aim to evaluate the effects of long term vibration profiles, representative of driving. Sine swept testing is also often a component of the vibration simulations alongside random vibrations to simulate everyday scenarios. The profiles used in these tests are derived from generic measurements from conventional vehicle locations appropriate for mounting traction batteries. These vibration profiles can also vary internally for OEM's based upon vehicle requirements from stiffer suspensioned sports cars to large offroad SUVs.

- **Water immersion** submerges the DUT at a state of full charge in ambient temperature salt water for a minimum of two hours. With the depth being sufficient to fully submerge the DUT. Both ISO 6469-1 and SAE J2464 utilise the same testing procedure. This test is a result of components within the pack being susceptible to damage and short circuiting if not appropriately protected, through dry sealing the pack. The sealing of the pack could also be affected by other driving loads, as a result of often being incorporated with the chassis as a design solution.

- **Underfloor protection** is a requirement under the CNCAP where an impactor is fired into the underside of the battery pack, a schematic of the test is shown in Figure 2.15, the impact energy is determined by the manufacture with options ranging from 80-120J (4-4.9 $ms^{-1}$ equivalent) categorised as benchmark to advanced. With the post test requirements being no housing cracking, leakage or fire. This requires adequate protection to be implemented into the pack design to provide this required underfloor protection.




Note:
1 - Battery system under test; 2 - Impact head;
3 - Launcher; 4 - Test bench.

Figure 2.15: Schematic diagram of impactor bench [11]

From the above tests at pack level, this may be resulting in larger loading than necessary when compared to realistic loadings from vehicle level analysis. Such as in the case of vibration testing, where the accuracy of the loads used in these simulations is key in the output. In turn further supporting this thesis' suggestion of the requirement for using rapid simulation techniques to identify and extract key loadings for component level testing, from vehicle tests. Additionally the examples also highlight variation in testing standards, which could benefit from clearer unambiguous testing guidelines to allow for improved design efficiency in the future, preventing OEMs having to cater for such a large range of tests.

#### 2.4.2.2 EV Design stratergies

Due to the rigorous EV regulations and the protection required for battery technology, alternate vehicle design strategies have to be considered to ensure adequate protection to the vehicles ESS; This is primarily enabled through the strategic placement of the ESS. The primary design strategy for EV's requires the ESS to be located outside of the primary intrusion zones of the vehicle. These areas house key crash energy absorption devices and therefore can often be severely degraded in the event of a collision. Leading to items housed within this region to be vulnerable to deformation in crash events. Similarly these key zones highlighted in Figure 2.16 as the primary and secondary safety zones, correspond to the intrusion areas. with the non-highlighted region being the primary intrusion zone in the event of a crash.

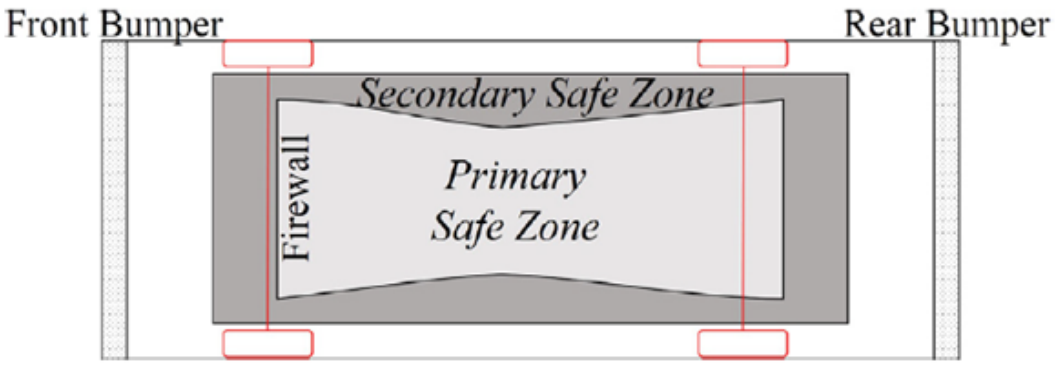



Figure 2.16: Overview of primary and secondary safety zones for vehicles [12].

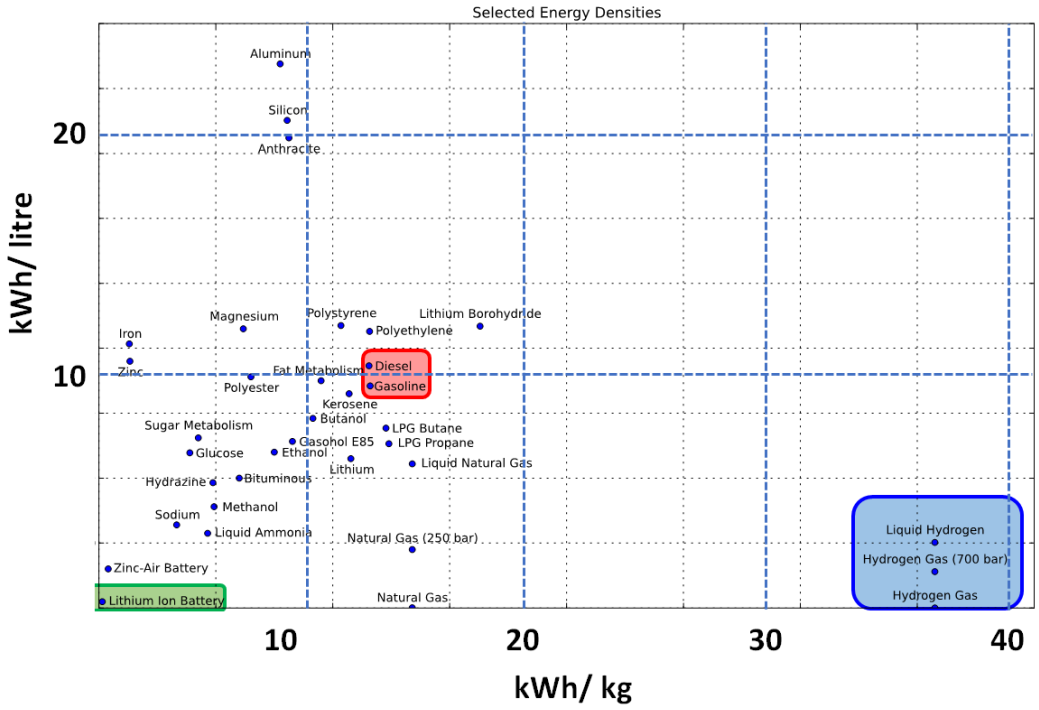



Figure 2.17: Energy densities (kWh/litre) versus specific energy (kWh/kg) for various fuels [13].

In addition to this, the challenge is amplified due to the size of the ESS; as a result of battery technology not being as efficient in both volumetric and gravimetric efficiency, typically supplying 0.1 to 0.27 kWh/kg in comparison to gasoline at 13 kWh/kg, therefore, requiring a larger quantity to offer a equivalent overall energy to ICE fuel options. This loss can be seen clearly in Figure 2.17 displaying a multitude of ESS and chemical options with their volumetric and gravimetric efficiencies; From this it is also clear to see why FCEV's utilising hydrogen is a desirable option as discussed in Section 2.2.

This combination of challenges in the past has inhibited EV range due to designers being limited to a safety zone, which follows the occupant space. However, as ever with engineering

when a new challenge is posed it often results in both new and sometimes novel approaches to overcome this; An example of this is designers attempting to push the previously conceived confines of the safety zone when packaging the ESS. This has been enabled via multiple avenues, one of which being through improvements in crash absorption devices; such as front longits which on EV's have been seen to grow in both height and width, offering equal or superior energy absorption to its predecessors in a decreased length. In turn reducing the size of the primary intrusion zone, offering an increased safety zone for ESS packaging.

However, when space is more limited such as that in a smaller vehicle, the appeal to place cells in this zone may be increased. Particularly due to the information highlighted in Section 2.4.2.1, reporting that cells can withstand significant loads. Although the previous section mentioned how they can withstand these loads without severe damage, it also discussed how equally high crash safety performance can be achieved by implementing an intelligent safety concept, some of the example targeted areas of this referred to by Justen et al. [62];

- Safety performance of materials, e.g chemistry of cells.
- Battery stability, enclosure material, interior expansion space, deformation zones,
- Battery protection, stiff cage around battery, reinforcements in surrounding vehicle structures.
- Battery integration, compliance in mounting, clearance for movement.
- Safety performance of the battery in crash.
- Ultimate mechanical loads to the battery , in static and dynamic tests.

Although a number of these areas mentioned would compromise weight and packaging space, which in some vehicle types is at a premium, such as mass on high performance vehicles. As such lightweighting remains a key aspect in vehicle design, as lighter vehicles require less cells to achieve a given range and in turn a smaller packaging volume. Another significantly growing sector of the automotive market alongside FEV's is SUV's (Sports Utility Vehicles.) Despite the advantages of a smaller vehicle size when transitioning from conventional ICE powertrains, this growing consumer desire for larger vehicles primarily SUVs, enhances manufacturers requirement for lightweighting. Particularly for the UK & European markets, where the maximum authorised mass of standard vehicle is 3,500 kg [65]; with a number of large conventional ICE SUV's weighing circa 3,300 kg and some PHEVs with MAM's just below the 3,500 kg limit such as the BMW XM and MercedesMaybach GLS600. This has been addressed in multiple works, one of which by [14] and ALIVE (Advanced High Volume Affordable Lightweighting for Future Electric Vehicles.) targeted a 30 - 40% mass saving for BIW, closures and chassis components,

whilst trying to maintain economical viability for mass production. Some of the materials selected in the BIW design included Aluminium alloys, high strength steels and FRP components. With Aluminium making up 65% of the BIW, and high strength steels being implemented in key load paths, with strengths up to 1800 MPa. Another key method of unlocking mass in this paper was the integration of the battery module. The bonding methods used within the construction indicated how welds in key areas could be reinforced by stronger adhesive bonds. Comparative joining techniques bond strengths can be observed in Figure 2.18.

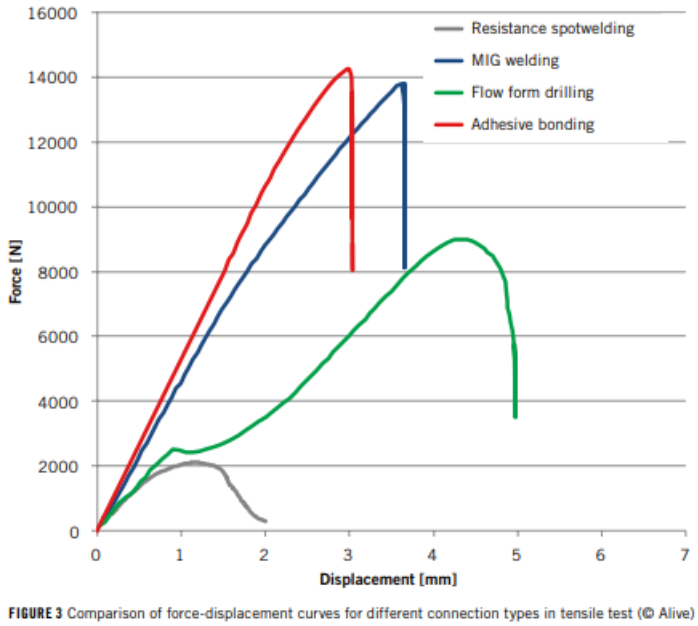



Figure 2.18: Comparison of force-displacement curves for different connection types in tensile test [14].

A challenge in designing these lightweight materials, such as FRP is the accurate material modelling of them for CAE analysis, which is imperative in correctly leveraging these materials in future EV body structures. Liu [66] reviewed a method of developing the CAE material models of composites, which is more challenging than that of it's metallic counterparts, due to its microstructural heterogeneity and behavioural sophistication. With the paper utilising a multiscale approach of;

- Microscale  Material characterization
- Mesoscale  Verification
- Macroscale  crashworthiness analysis.

This ability to accurately model composite materials has continued to develop up to the present day, allowing the materials to be leveraged in future EV body design concepts.[66] also displayed a 28% mass saving over the FRP option, which is extensively adopted for parts such

as roof, door, floor and body panels saving 40-60% over metallic components whilst maintaining or improving performance. An additional material gaining popularity within the application of crashworthiness is carbon fibre reinforced plastics (CFRP), due to it's energy absorption qualities. Steel-CFRP reported in Liu's work, offered improved specific energy absorption (SEA) over steel or CFRP alone.

Improvements of key components surrounding the primary safety zone have also been investigated, to improve protection of ESS items in close proximity. Such as Schaffer et al. [67] work on an improved side crash concept for a urban modular vehicle(UMV), with the improved side pole performance being achieved through the integration of energy absorbing panels within the door sills, reducing intrusion by 30% and boosting SEA by 24%. The approach taken in this paper touches on a key area of this thesis, with a key step in the documented work being the use of a crash concept model to highlight key load paths to aid appropriate down line design, through development techniques such as the Optimisation of crash absorber by morphing and Optimisation door sill: parametric geometry optimisation task'.

A final consideration under EV design strategy, is the investigation of the ESS becoming multifunctional through it's inclusion within the crash concept. A number of papers on the topic of altering battery packs to become energy absorption components can be found, such as those by J.Kukerja [12] and F.Hao et al. [15]. Hao uses plates within a simplified battery model, to provide a 'flexible battery structure', S2 shown in Figure 2.19 houses plates perpendicular to the crash direction, which is seen to reduce the peak acceleration in front crash by over 50% from 80g to 40g, and also below the previous ICE version of 46g; Hao concludes this decrease in acceleration is a result of the flexible structure, which buffers the frontal impact. This theory of batteries absorbing kinetic energy as well as just supplying the power to the vehicle is further covered by Kukerja et al.[12] where the inclusion of sacrificial tubes within the battery module is investigated, referred to as a granular battery assembly (GBA), example of which is seen in Figure 2.20. The mechanics of the GBA cell remain similar to the cell solid, with initial elastic response, then a plateau as the tubes collapse and dissipate energy within the module, proceeded by densification. Results showed that despite the increased volume of a GBA required to match a solid cells energy, GBA still performs better with regard to number of failed cells. This still remains true when the volume difference of the GBA and standard, is eradicated by supplying the standard cell block with a foam protection layer.

However, GBA does contribute to an increased ESS mass, which in turn will reduce the efficiency of the energy stored. Of course this can be traded off against the ability to place cells outside of the primary safety zone, and the ESS's dependency on other protective structures. However, placing modules within the front of the vehicle may help with larger packs and

increased energy requirements, but this does negate a positive of BEV's which is the low central mass of the ESS. Whilst ICE vehicles locate engines up front or to the rear which poses a similar issue, are not as mass dense as battery modules with average engines rarely weighing over 200 kg, also the fuel tank at the opposite end often aids in balancing the weight distribution.

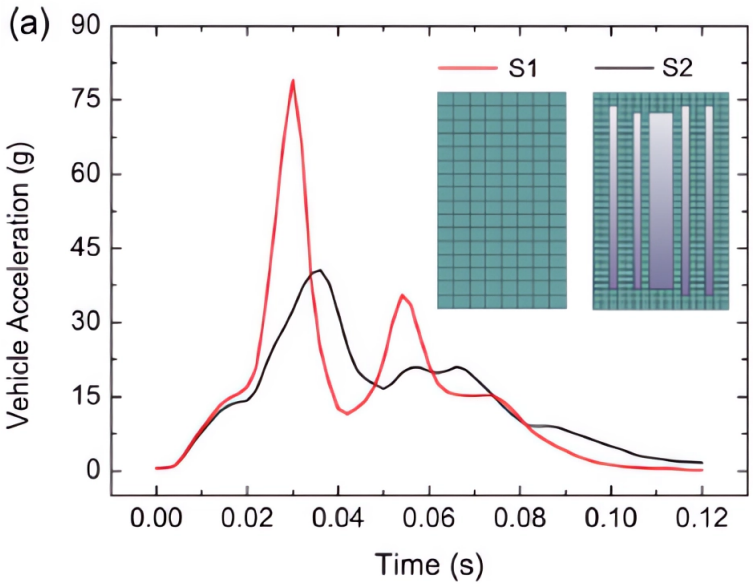



Figure 2.19: Two different structures of battery model, denoted as S1 and S2, and the corresponding vehicle acceleration curves in the frontal impact simulations [15].

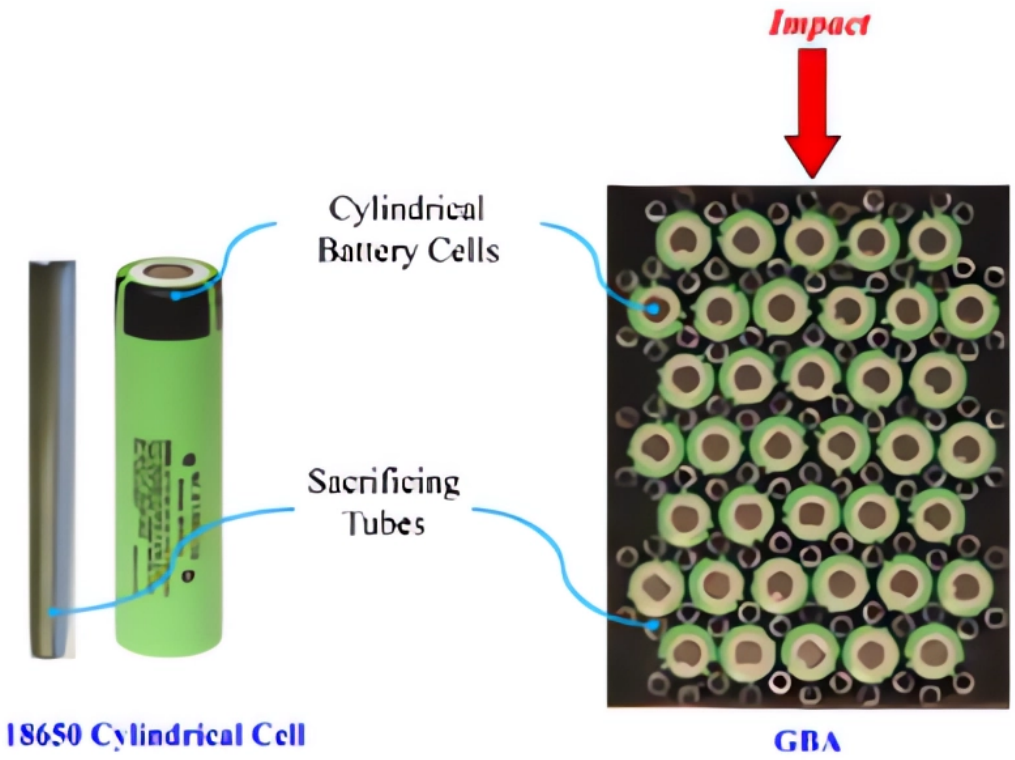



Figure 2.20: Two different structures of battery model, denoted as S1 and S2, and the corresponding vehicle acceleration curves in the frontal impact simulations [12].

## 2.5 E-Axles

E-Axles, are the primary propulsion system within BEVs, which combine multiple key components such as the electric motor, power electronics, transmission and differential. The advantages of an e-axle are the compact design and reduced complexity aiding packaging and integration. Other advantages include instant torque performance and efficiency with merged components allowing for designer to potentially increase efficiency of all components working in harmony. A key area aiding the efficiency is the transmission. Conventionally there are multiple options such as Fixed gear transmission, manual transmission and continuously variable transmission (CVT).

- **1.** Fixed Gear Transmission (Single-Speed Transmission): Uses a single gear ratio with no shifting. Often seen in early or small electric vehicles due to its simplicity.
- **2.** Manual Transmission: Typically associated with ICE vehicles, requiring the driver to manually engage different gears. However, this type of transmission is not commonly used in electric vehicles or e-axles due to the different torque delivery and driving characteristics of electric motors.
- **3.** Continuously Variable Transmission (CVT): CVTs offer a smooth, stepless transition between a range of gear ratios, providing an infinite number of gear ratios within a specific range. Often able to deliver improved efficiency over other methods by being kept at its peak rpm. While not as common in electric vehicles, it has many uses in ATVs, bikes and some cars.

In the context of e-axles, the most common transmission type is the fixed gear transmission. This is due to electric motors being able to deliver high torque across a wide RPM range, removing the need for multiple gears. As opposed to ICE which deliver high torque in much narrower RPM ranges. Whilst some research does indicate CVT may be more efficient by around 7% by keeping the motor at its optimal performing region more often [68].

Monitoring and understanding of loadings within components within the e-axle are key in delivering improved designs in the future. There are a number of items which can effect loadings within an e-axle system, these are primarily the torque and power requirements, operating conditions and thermal loading. However, additional items such as regenerative braking also have an effect with the motor switching from using electrical energy to generate Kinetic Energy (KE) to harvesting power from the KE back to electrical stored energy. With the switching from using electrical energy to generating it, requiring a sudden reversal of current which in turn can cause motor overload.

In a planetary gear system inequalities of load distribution arise on each planet gear, due to random errors in manufacture and assembly, this causes a loss in efficiency. Whilst operating at high speeds variations in the dynamic loads can be seen to increase. Even when distribution is equal, torque variation can still lead to dynamic tooth loads varying greatly. However published works show that dynamic tooth loads can not be estimated from only the mean load distribution and mean dynamic load factor [69]

### 2.5.1 Torque Ripples

Within the loadings generated a feature that can result in spikes in the forces of the system are torque ripples; which are a fluctuation in the output of torque of electric motor. With primary causes of this feature being imperfect motor design, electrical imbalances and magnetic saturation. With the reduction of torque ripples being crucial for applications where smooth and consistent torque is necessary. As large variations can result in spiking of forces and in turn peak and unwanted stresses upon components, in addition to causing additional noise and vibration to a vehicles NVH set up.

Due to torque ripples being a key aspect within loadings generated within the e-axle system a number of papers can be seen to research the modelling of the e-axle components with a number having a primary focus upon torque ripples. Wang et al. [70] examined the effect of random perturbation on the responses, with insight into other factors which could result in vibrations, such as manufacturing errors or gear tooth shape and imperfections. Another feature highlighted in this work was the effect of meshing stiffness, leading to fluctuations deviating from standard results, however, within the overall system these effects were not as substantial as those resulting from torque fluctuations. Attempts have been made by others in component design to reduce the torque pulsations ahead of it reaching the end transmission components, via a device which generates damping of the pulse in the same phase [71].

### 2.5.2 E-Axle Modelling

Transmission errors (TE) have previously been modelled in various works, with Du et al.[72] using both a 2d and 3d model to examine tooth deflections under torque loads. As the deflection is a primary contributor to TE, the models also expressed the ability to handle torque fluctuations. Although for the studies torque was kept constant. Modelling results supported that the TE arose from gears deflecting, with misalignment having minimal effect.

Mesh stiffness; refers to the rigidity of gear teeth when engaging with other gears in a system, with forces and torque being transmitted between teeth. Mesh stiffness is a key aspect in modelling and as the number of teeth in contact changes, this can result in excitation and gear

vibration and noise, with excitations occurring even in ideal systems with no manufacturing or assembly errors. With the mesh stiffness being a cause of TE within gear models. Typically within an analytical gear vibration model, time varying mesh stiffnesses is used, which excites the system. The excitation can lead to noise and increase in dynamic loads and potentially damage gear teeth and bearings [73]. From papers read, it is apparent that how the instability in the system from varying mesh stiffness can result in tooth separation and this non linearity can dramatically changes the dynamic response.

## 2.6 Chapter Summary

The literature review contained within this chapter covers a range of topics surrounding the design and testing processes commonly used in the automotive industry, emphasizing the shift towards FCEVs and the importance of meshing types for low fidelity models. Key focusses from this chapter with regards to the remainder of this thesis are the background into meshing types and how these can be used within low fidelity models. Along with research into the performance tests commonly used within the industry, for both vehicle level testing and component level testing, specifically surrounding the ESS of BEVs. The background research included is paramount in allowing for a fundamental understanding of the breadth of challenges that must be considered within a full vehicle design. With this thesis primarily focussing upon the structural assessments, with a mind in the future to using techniques and principals outlined for non-structural assessments such as some of those pertained in the vehicles NVH performance.

The performance testing topics covered also help to highlight the importance and motivation behind the work in this thesis. With regards to potentially over constrained testing of ESS systems which plausibly results in limited design scope and over engineered components for the tasks actual requirement.

# Chapter 3

# Practical Assessment and optimisation of planetary carrier.

This chapter contains a practical application study into the light weighting of an OEMs planetary gear carriers, a key component within their e-axle, designed for use within a high performance full electric vehicle. Within the e-axle two different planetary carriers are to be considered, one to function with a park lock the other without. With the content of the report investigating both the potential and practical weight savings, for both instances. With the potential weight savings explored through material and manufacturing investigations. Doing so whilst maintaining the carriers rigidity to ensure the gears alignment remains within prescribed limits, and the manufacturers misalignment constraints are adhered to. Whilst also maintaining commonality between the park lock and non-park lock instances, to ensure the most beneficial and practical design was achieved. With this passage of work being a key factor, in further investigating the loads and constraints which must be applied to components with limited vehicle level and real life load inputs available.

## 3.1 Introduction

The following study investigated both practical and potential weight loss of the planetary gear carrier, designed for integration within Aston Martin's AM10/11 projects. Two carriers have been designed to be fitted within the E-Drive system of the vehicle, with one at the front and two at the rear. The lone carrier housed at the front of the vehicle, will also be used in conjunction with the vehicle's park lock and therefore will exhibit significant loads, from the park lock. The other loads exhibited by the carrier will be due to the drive forces acting upon both the planetary and pinion gears.

| Steel GS42CrMo4 | |
|---|---|
| Youngs Modulus (E) | 210 GPa |
| Poisson's Ratio (Nu) | 0.3 |
| Shear Modulus | 80 GPa |
| Density | 7800kg/m$^3$ |
| Thru Hardened to... | |
| UTS | 900-1100 MPa |
| Rp0.2 | >800 MPa |

Table 3.1: Steel material properties table

The objective of this study was to minimise the mass of the carrier, for both park lock and non-park lock instances, whilst trying to ensure universality between the two versions to assist with production. Doing so whilst remaining within the prescribed gear misalignment values, to ensure the gear's functionality through all loadings. The study also considered various manufacturing options, such as casting, forging and additive manufacture. In addition to this, material options were also explored to exploit further potential weight savings. With all weight savings made from the studies executed within the report, assisting with the e-axles overall mass target of less than 60 kg, of which the three carriers currently in use comprise of over 20% of the axles target mass. Therefore, a key area for potential weight savings.

The initially supplied carrier design weighed 4.415 kg, with a foundation material of GS42CrMo4 carburising steel selected, the details of the material are seen within table 3.1.

### 3.1.1 E-Axle

The planetary gear carrier is a key part of the electric drivetrain being developed, for use within a series of future full battery electric HP vehicles. The e-axle system can be broken down into two subsystems, one at the front and one at the rear. The sub-system at the front features a singular planetary carrier, and at the rear the subs-system features two planetary carriers. An example of the double rear axle can be seen in Figure 3.2, with the carrier's location highlighted within the singular e-axle displayed in Figure 3.1. Both axles house motors with peak output speeds of approximately 20,000 rpm, with the single axle having a peak torque of 2800 Nm and the double 5600 Nm.

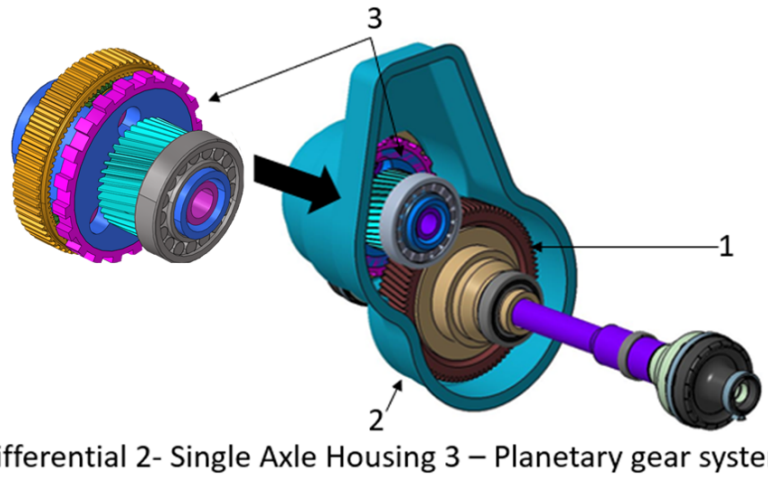



Figure 3.1: Image highlighting the planetary gears location within the singular e-axle.

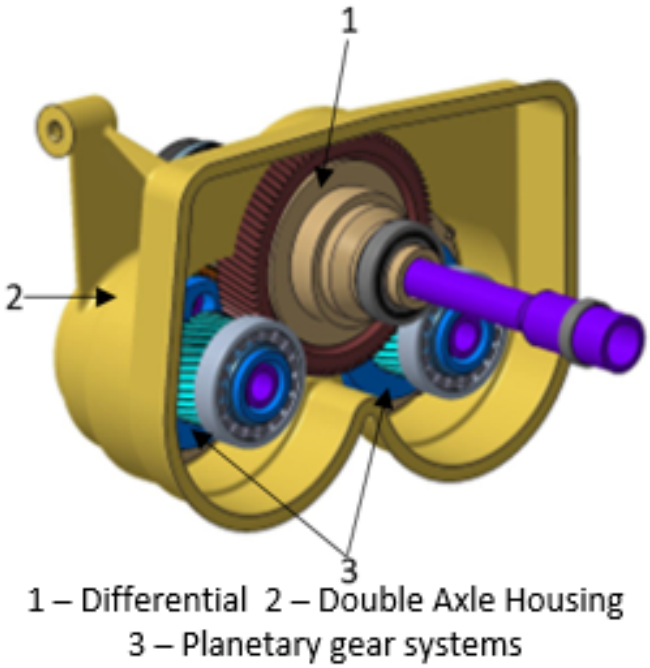



Figure 3.2: Image of the double e-axle

The planetary gear assembly however experiences maximum torque values of 1266 Nm along the carrier shaft under normal drive loadings. Although this is increased to 2700 Nm for the singular axle, which encounters the park lock loading. Both values are transmitted to the planetary carrier in which this chapter focussed upon. The carrier itself is a key component within the planetary gear system, as it acts as the output shaft with the pinion gear attached directly to it. A schematic for a typical planetary gear system can be seen in Figure 3.3, the planetary gear system is utilised to transfer large amounts of torque within a small region. The configuration within a HP e-axle is the drive side being the sun gear, the output being the carrier itself and in turn the pinion gear and the fixed aspect being the ring gear. This set up

allows for a reduction in speed from the input, and an increase in the torque being transferred in turn to the cars wheels. This is executed whilst utilising the smallest amount of space possible, with each of the three gear systems taking up a cylindrical envelope of just ⌀185 mm by 140 mm.

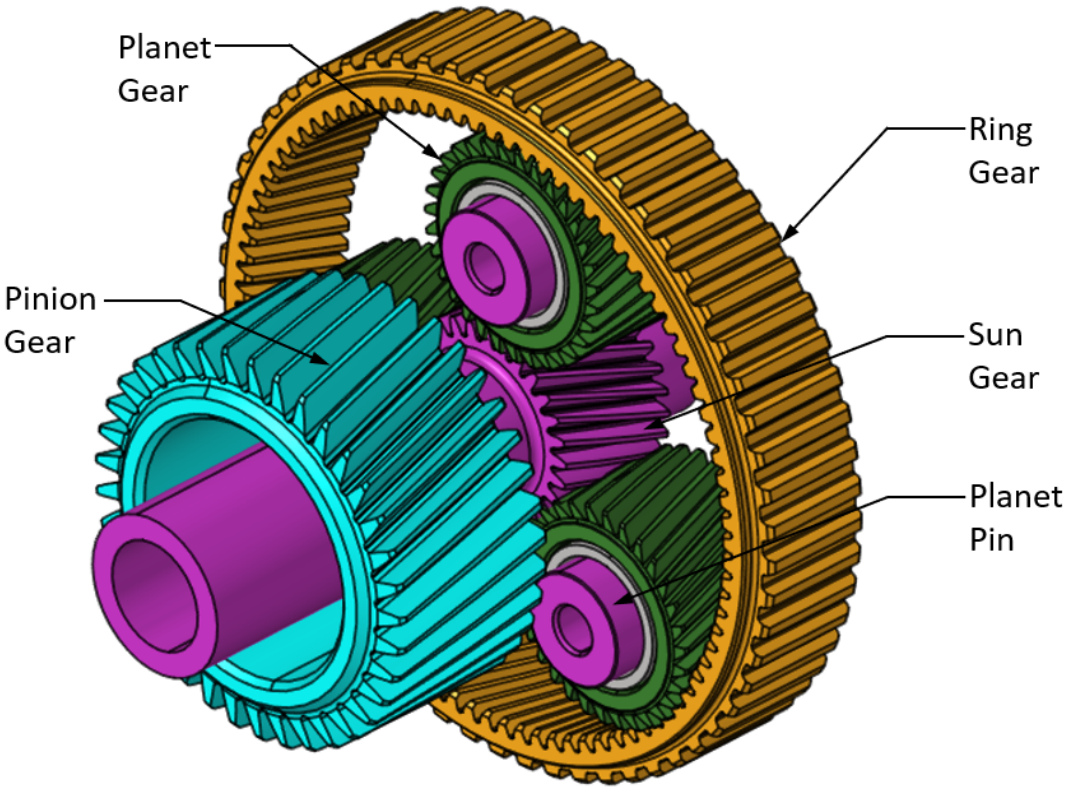



Figure 3.3: Planetary Gear Schematic

## 3.2 Model Set Up

The initial set up of the planetary carrier model was for the Topology Optimisation studies, to provide design direction to commence the reduction of the weight of the carrier. This is done through the use of a topology optimisation, whereby the material layout is optimised within a given design space whilst adhering to a series of given boundary conditions, and loads. This particular topology analysis was driven by the objective of mass reduction, and the constraint of the planet gears angular misalignment. The topology studies carried out within the chapter, utilised Altairs Hyperworks software and Optistruct as the solver for the topology analyses. Within Optistruct a gradient based method is used, the specific method used in this instance is a Solid Isotropic Material with Penalisation method (SIMP), utilised to predict the optimal material distribution for the prescribed design space, based upon the user's desired objective and constraints. In this example this is executed using a tetrahedral mesh to map the design space, with the solver algorithm adjusting the material distribution to converge upon an optimal

solution.

To allow for a successful topology optimisation the design spaces were defined. Therefore, the models geometry was defined with two properties, one allocated to the feasible design space, the second to highlight the regions of non-design space. In addition to the components categorised as non-design, sections of the carrier were also added to this classification. With the sections of the carrier which contacted with other non-design space components, added to ensure enough contact to these areas was maintained. A good example of this is the circle of geometry retained around each pin, to ensure the contact surface between the pin and the carrier are maintained. These spaces can be seen highlighted within Figure 3.4.

The final stage in defining the model's set up, was the allocation of the objective for the topology study. Which was defined as minimise the mass for the design space, whilst adhering to the misalignment constraint, for all present load cases.

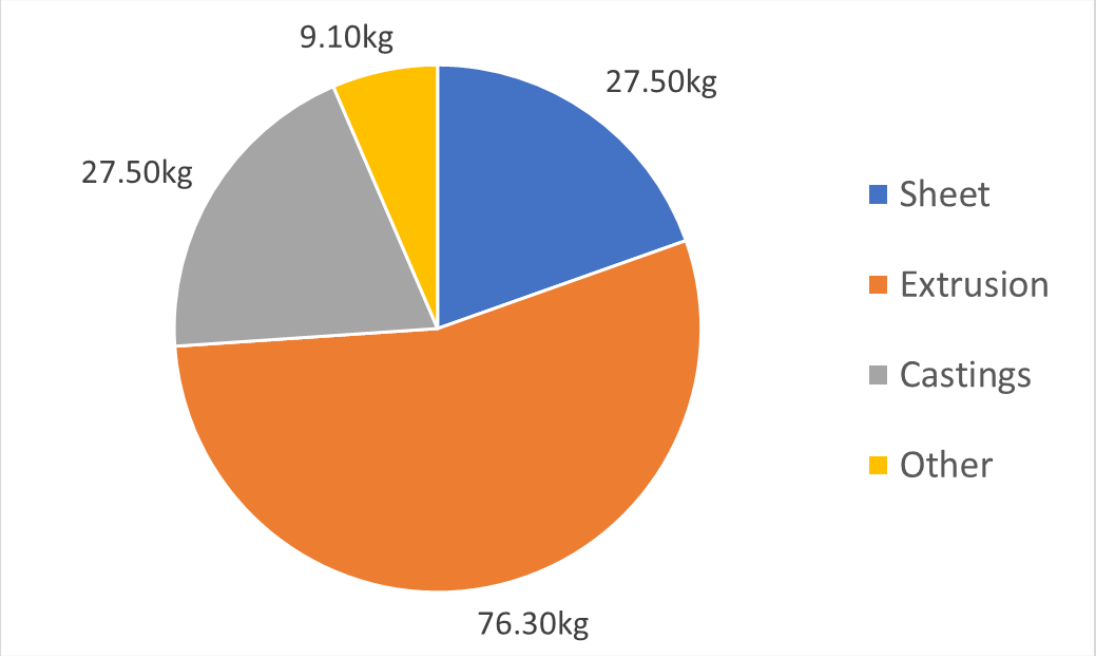



Figure 3.4: Planetary Carrier Design Spaces

| Loadings | |
|---|---|
| Load Case | Description |
| 1 | Forward driving load case, with key loads acting upon the three planetary pins, and the pinion gear. |
| 2 | Reverse driving load case, with key loads acting upon the three planetary pins, and the pinion gear. |
| 3 | Forward park lock load case, with key loads acting upon the park lock wheel and the pinion gear counteracting each other. |
| 4 | Reverse park lock load case, with key loads acting upon the park lock wheel and the pinion gear enhancing each other. |

Table 3.2: Summary of key Load cases

| Load Case | 1 | 2 | 3 | 4 |
|---|---|---|---|---|
| Loading Direction | Load Value | | | |
| Tangential Load at Annulus Mesh (Torque around Y) | +4638 N | -4638 N | - | - |
| Axial Load at Annulus Mesh (Y) | +1657 N | -1657 N | - | - |
| Tangential Load at Sun Mesh (Torque around Y) | 4638 N | -4638 N | - | - |
| Axial Load at Sun Mesh (Y) | -1657 N | +1657 N | - | - |
| Axial Load applied at small ball bearing (Y) | +4971 N | +4971 N | - | - |
| Tangential Load at Pinion Mesh, (Torque Around Y) | -31901 N | 31901 N | +68035 N | -68035 N |
| Axial Load at Pinion Mesh (Y) | -11398 N | +11389 N | +24308 N | -24308 N |
| Separating Load at Pinion Mesh (Z) | -11806 N | -11806 N | -25178 N | -25178 N |
| Tangential Load at Park Lock (Torque around Y) | - | - | -36986 N | +36986 N |
| Separating Load at Park Lock (Z) | - | - | +6522 N | +6522 N |

Table 3.3: Prescribed Load cases

### 3.2.1 Loads and Constraints

#### 3.2.1.1 Loadings

The loadings were specified and selected to ensure the worst case loading scenario for the topology run was utilised, ensuring a combination of maximum forces from those specified were utilised to ensure the highest level of fatigue within the studied part. The loadings comprised of a forwards and backwards planetary drive load case, as well as a forward and backwards park lock load case. The utilised loads and their purpose can be seen in table 3.2. Further details for these load cases can be seen in table 3.3. As the park lock geometry remained considered throughout the initial analysis. With load case one & two utilised during Section 3.3.4.1. These load cases were selected due to them being considered the worst-case loadings for each functional use.

All loads for the first two load cases were then applied directly to their respective parts via RB3's rigid elements, connecting the specified mesh points to which the load is applied to the adjacent surface of the pins. The setup of the planetary gear loads can be seen within Figure 3.5, with the red arrows displaying the drive load case and blue the reverse load case.

The second two load cases, representing the park lock load cases were applied in the same manner via RB3s. With the key loads applied only to the Pinion and Park Lock, with the park lock load applied at a prescribed 78 degree angle from the final drive (pinion) mesh point. These loads applied to the Pinion and the Park Lock can be seen within Figure 3.6, with the

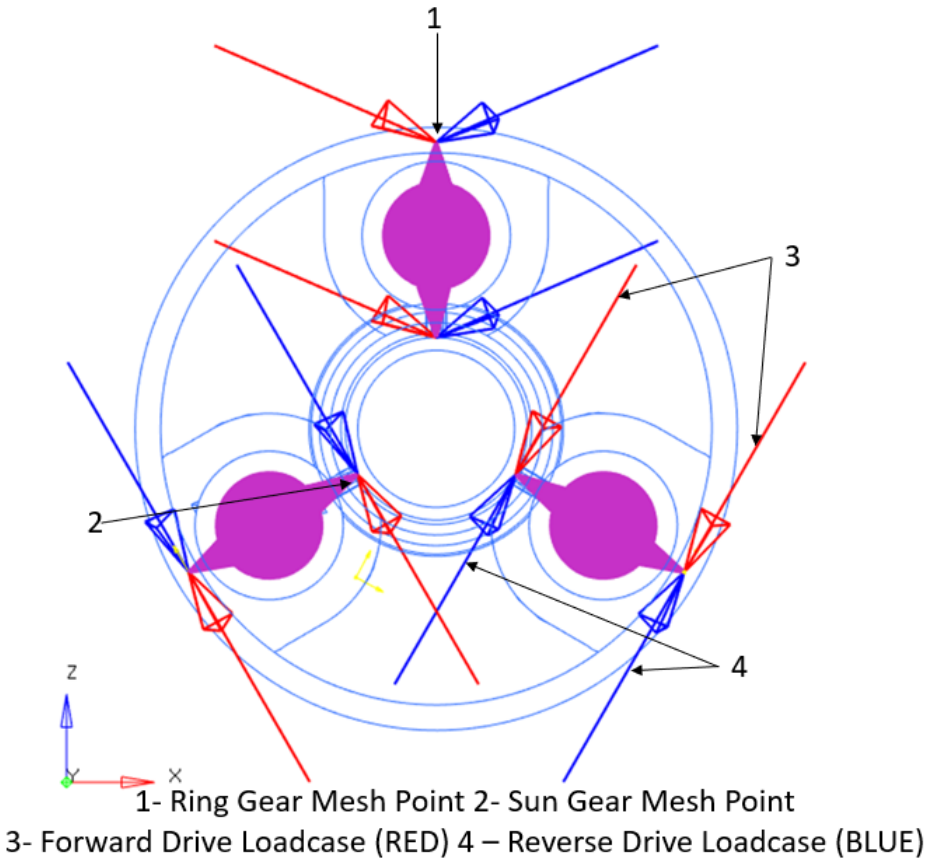



Figure 3.5: Planetary Gear Loads

green loads representing the forwards park lock load case and yellow the reverse.

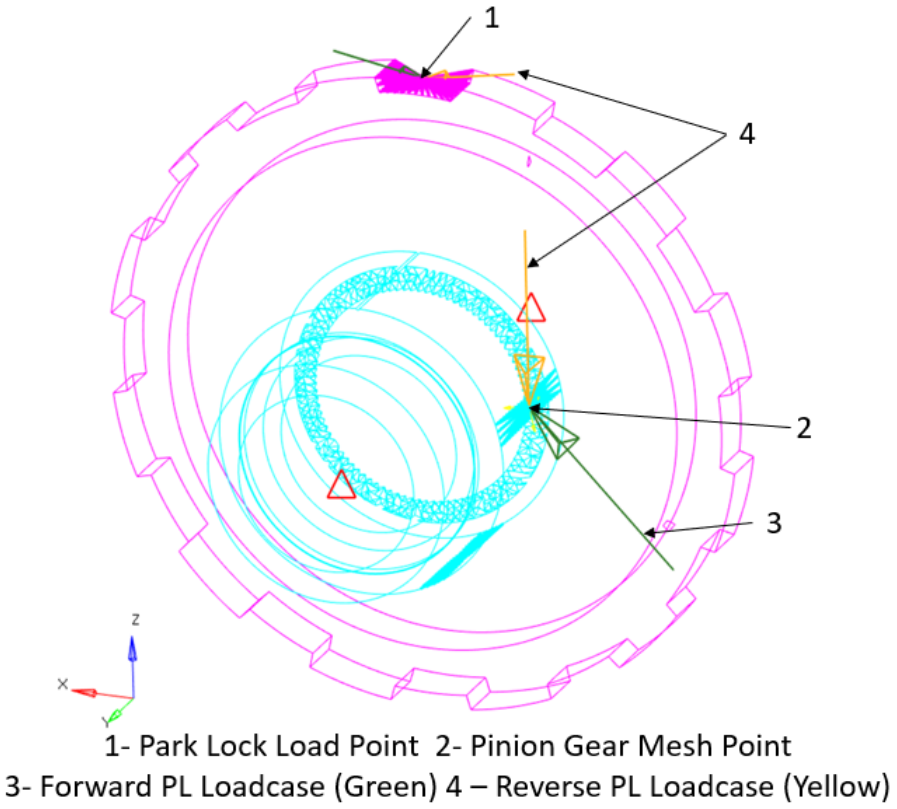



Figure 3.6: Park Lock loads

#### 3.2.1.2 Constraints

The constraints applied to the model, were set up to allow for the model to ensure all loads are dissipated throughout the carrier and not passing out of the carrier. This interpretation, whilst not being a direct representation of the carrier's actual performance, will ensure the carrier experiences similar loads and stresses to reality. The lead edge of the carrier (bearing end) is restrained in three degrees of freedom, one, two & three. The trail edge (Pinion Gear side) is also restrained in three degrees of freedom, one, three & five. These constraints are illustrated within Figure 3.7. Both constraints were set up utilising 1D element rigid webs, from calculated centre nodes to the outer faces of the carriers bearing contact faces.

#### 3.2.1.3 Connections

To enable the loads to be successfully transferred throughout the model, the connections between the different components remaining within the assembly have to be established and recreated. Both the pinion gear and park lock wheel are connected to the carrier via welded splines, giving a near solid connection. Therefore, the connections between these components was represented within the model by equivalencing the contacting faces, ensuring all forces are fully transferred between the two components. The pins however are shrink fitted, once again

when fitted the connection between the carrier and the pins is assumed rigid. Therefore, the pins were also equivalenced to the carrier. This representation assumption will result in slightly higher stress and energy transfer than reality, due to the lack of stress and energy losses at connection points. However, when looking to minimalize weight whilst adhering to the set constraints this assumption will only lead to a marginal penalty in weight saving but will ensure the function of the carrier is maintained.

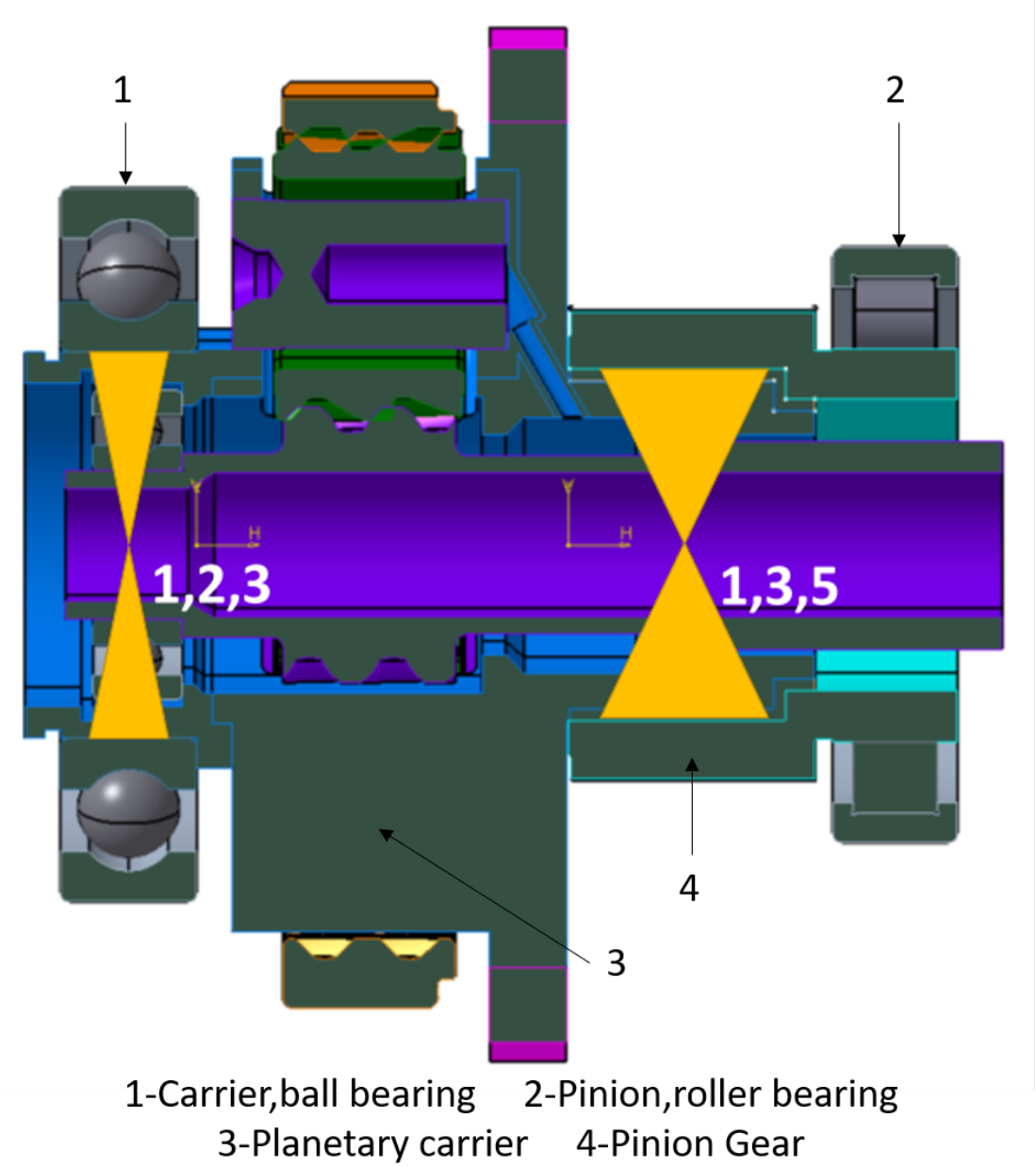



Figure 3.7: Planetary Carrier cross section

## 3.3 Results

### 3.3.1 Initial Topology Results

An initial series of topology runs were executed from these a series of issues were raised, these included the lack of supporting material retained for the park lock wheel and the outputted designs being non uniform. Due to the location of the pinion load having a slightly different effect on each of the three pins and segments.

#### 3.3.1.1 Model Set Up Adjustment

Therefore, before progressing from this model several adjustments were considered. First of which was the addition of a cyclic symmetry feature to the topology study, to ensure uniformity in each of the three 120deg segments. In addition to the cyclic symmetry an additional segment of the carrier was added to the non-design space, this being the region where the park lock connects to the carrier, to ensure this ring of material on the outer edge remains for assembly purposes.

The model was set to run with all four key load cases, with the output displaying a uniform design with material supporting the park lock wheel. Satisfied with the output an additional stress constraint of 180MPa was added to the model to accompany the misalignment constraint. The effect of this was a slight increase in retained material within the design space. The supporting structures became more profound and generated a more concise design. The mass was seen to increase by approximately 5% to 1.93kg for the carrier, a reduction of over 56% from the original mass of 4.415kg. The resultant iso surface can be seen within Figure 3.8.

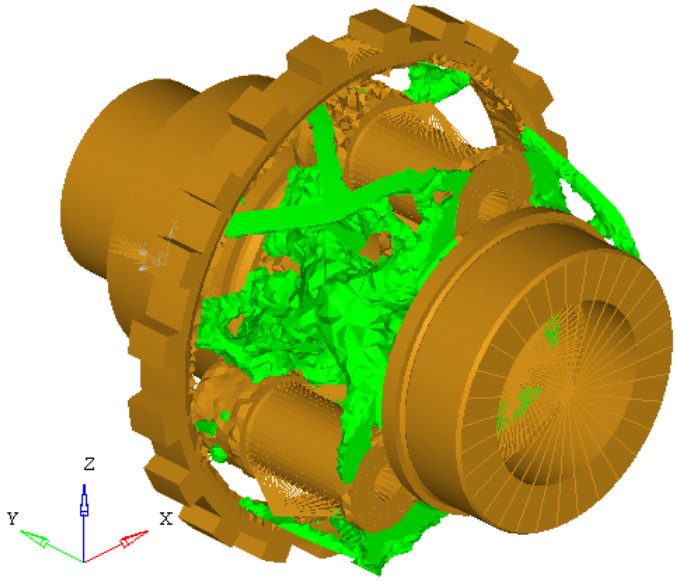



Figure 3.8: Topology result with stress response

The generated result was then taken to be realised within inspire, to ensure all parts are fully connected, and to smooth the geometry from the outputted elemental iso surface. The workflow of the realisation of the results can be seen within Figure 3.9. In doing so an increase in the structures volume was exhibited, causing a mass increase up to 2.848kg, resulting in a 47.5% increase. This realised result however still supplies, a substantial mass saving from the original carrier of 35.5%.

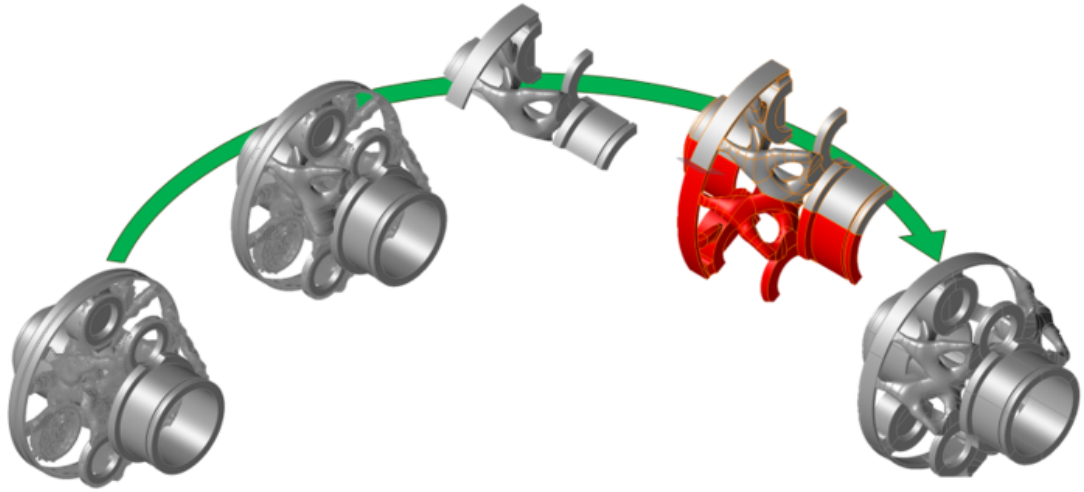


Figure 3.9: Stages of realising the topology results.

### 3.3.2 Geometry Update

Following the series of initial studies, a second version of the geometry was made available for study. This new geometry was then set up in the same manner as the previous. Key changes to the geometry included a series of diameter changes, as well as increased entry points for the planet gears, reducing the available design space. These adjustments led to some mass changes, as displayed in table 3.4. The new geometry assembly whilst being overall heavier than the original planetary carrier assembly, does supply a lighter carrier design, in turn providing less scope for weight reduction.

| Geometry Comparison | | |
|---|---|---|
| | Original Model V1 | New Geometry V2 |
| Pinion Gear | 0.845 kg | 1.032kg |
| Park Lock Wheel | 0.330 kg | 0.734 kg |
| Planet Pins | 0.497kg | 0.453kg |
| Carrier | 4.415 kg | 4.336 kg |
| Carrier's Non-Design Space | - | 0.598kg |
| Total Mass | 6.087 kg | 6.555 kg |

Table 3.4: Geometry comparison

#### 3.3.2.1 Manufacturing Constraint - Draw

An additional feature was added to the topology study to allow for the model to be utilised for production. As it would not be possible to manufacture the previous result by casting, though it could be produced by Additive Manufacturing (AM) Techniques though this would be impractical particularly for mass production. Therefore, a draw feature was added with a selected draw direction of 60 deg angle from the z axis, at the centre of the segment used for cyclic symmetry. The draw direction is depicted within Figure 3.11. This addition helps to ensure the designs generated are viable for casting as the selected manufacturing option.

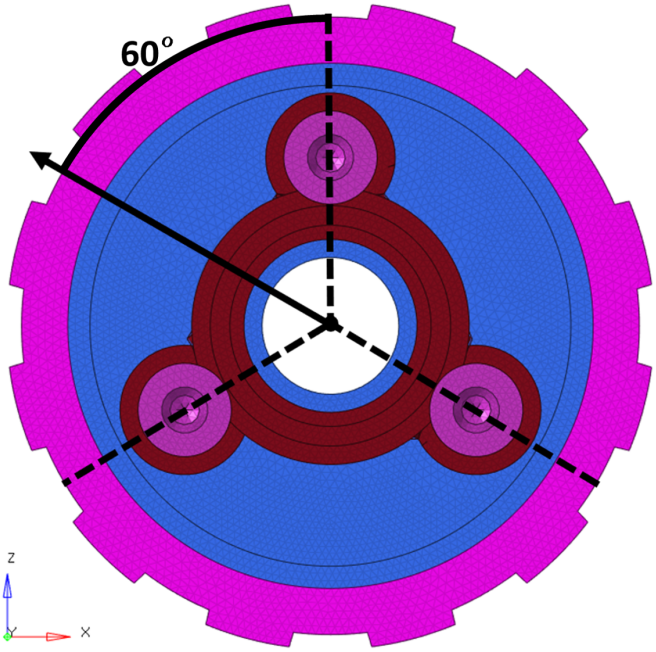



Figure 3.10: Draw direction for model.

#### 3.3.2.2 Analysing Results

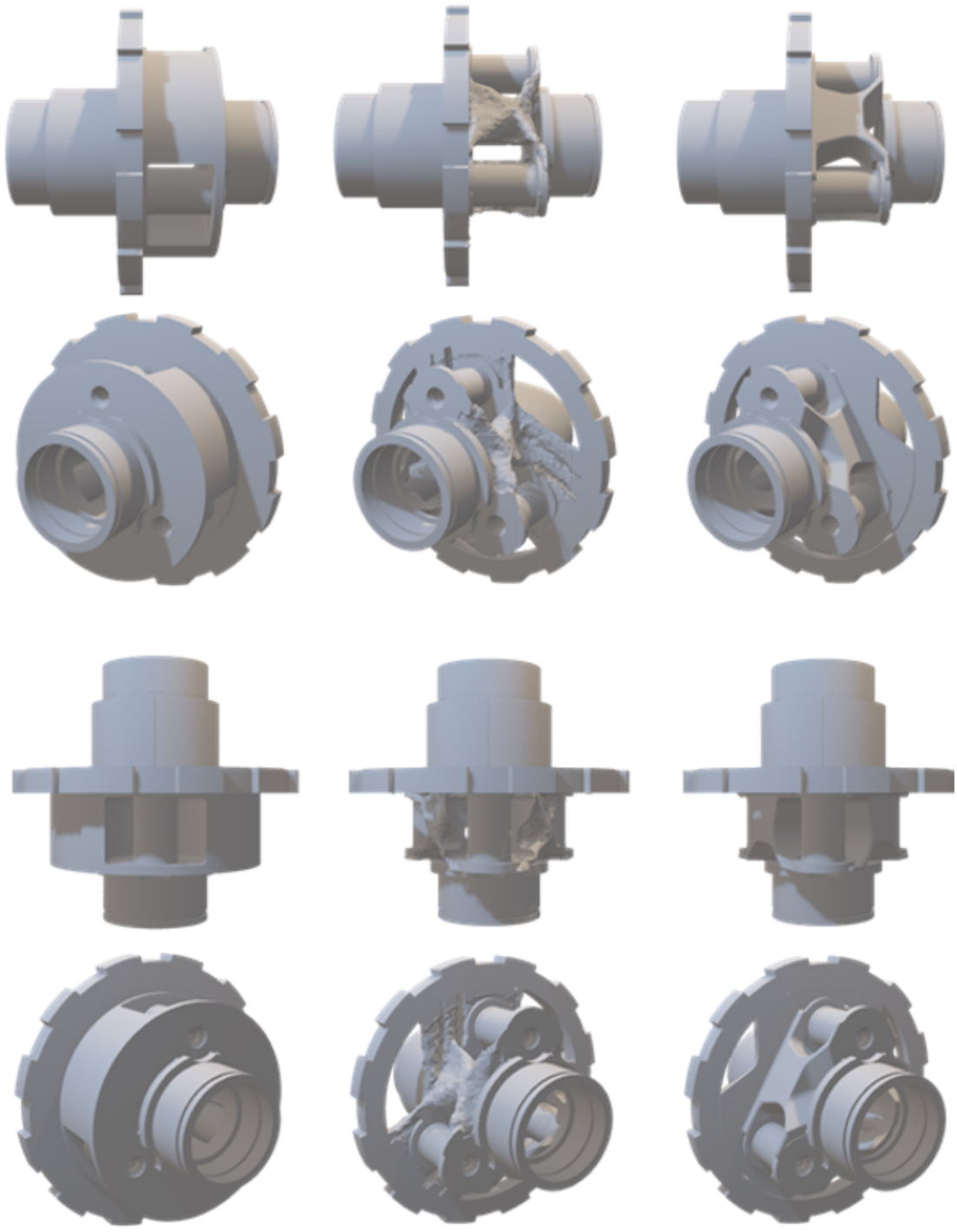


Figure 3.11: Realising of result.

The resultant topology model utilising the draw feature was realised into a viable design, with a weight of 2.801 kg, with a weight saving of 35.41 %. The iso output along with the realised design, are seen within Figure 3.11. This version of the carrier was then tested for its strength and functionality. The stresses were first investigated. The stress results highlighted peak stresses, that were exhibited under the park lock load cases, whilst the drive load cases yielded

insignificant stresses in comparison. Therefore, focusing upon the park lock load cases, the stress concentrations were investigated. The contour plot displayed in Figure 3.12 helped to highlight areas that required further design work, to reduce any stress concentrations. The key areas highlighted were the corners and the pins housings, it was also noted when analysing these regions, that the realised result had reduced the clearance surrounding the pins and therefore, the planet gears. Another key feature of the stresses was that whilst the maximum stress recorded was large at 1735 MPa, this is occurring upon the surface only and not propagating through the part and is likely a result of the connection point of the load application. These larger stresses also are only seen within the park lock wheel and pinion gear, due to being the location of the largest forces being applied.

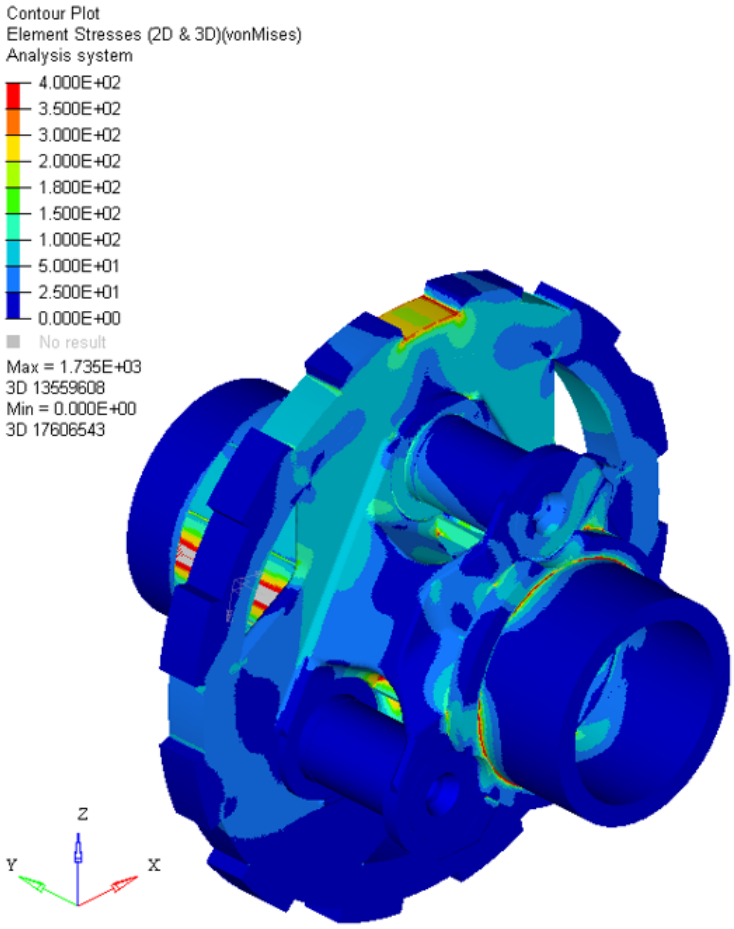



Figure 3.12: Stress contour of reverse PL loadcase

To progress the design the highlighted issues were addressed, and the carrier was modified, with the aim of decreasing stress concentrations and increasing assembly clearances. This was done through increasing edge fillet radii, and applying a smoother transition between areas of the geometry with significant differences to reduce the stress concentrations observed. As well as removing material that had been added within the realisation phase which encroached upon

the non-design space, to ensure clearance around the planetary gears. The resultant geometry from these adjustments can be seen in Figure 3.13. The key design adjustments in addition to the overall polishing of the design, include the full encapsulation around the planet pins on both sides, as well as increased openings for the planet gears. These adjustments led to a resultant carrier weight of 2.64 kg, which is a 39.1 % reduction, which was a further 3.7 % saving from version three.

Stresses were again checked, with the maximum stress exhibited being brought down to 721 MPa, and most of the stresses within the carrier itself remaining below 200 MPa. The stresses occurring in the carrier alone for the reverse park lock load case can be seen within Figure 3.14. The stresses are also seen to of become much more dispersed throughout the carrier, as opposed to the localised patches previously seen.



Figure 3.13: Version four of the planetary carrier

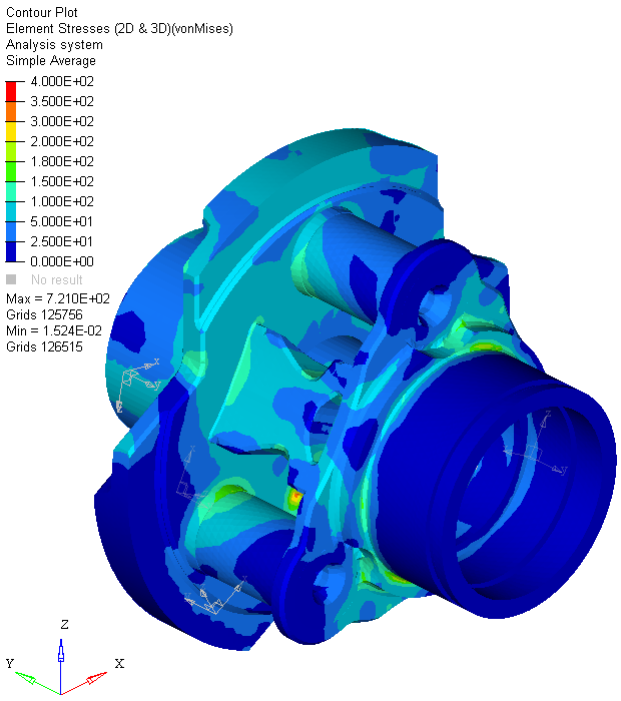



Figure 3.14: Stress contour of reverse park lock load case, with the carrier isolated.

Once satisfied with the stress results, the misalignments and rigidity of the model were tested, to ensure the 1mrad constraint was adhered too. To do this the displacement of the centre point at the end of each pin was monitored, along with the centre points at the end of the pinion gear. All these points were calculated and then connected to the relevant components via a rigid web, to ensure the overall motion of the pin is tracked and not just one node. The displacements occurring at these points was utilised to calculate the misalignment shift, by taking the resultant displacements, as depicted within Figure 3.16 for the parts local axes systems. Then utilising these displacements to calculate the misalignment with the below equation. Where the critical length of the pin utilised within the calculations was 46.00 mm and the critical length of the pinion gear used was 41.50 mm.

$$\begin{aligned} \theta(rad) &= tan^{-1}((x^2 + z^2)/(L + y)) \\ x &: Resultant\ x\ displacement, \\ y &: Resultant\ y\ displacement, \\ z &: Resultant\ z\ displacement, \\ L &: Critical\ length\ of\ component \end{aligned} \tag{3.1}$$

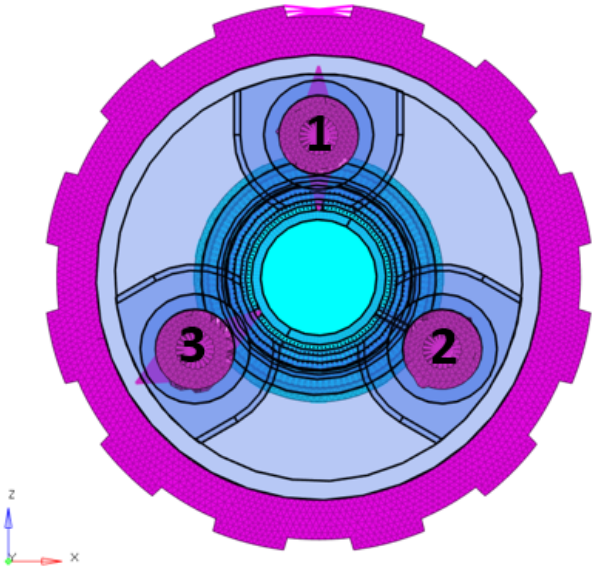



Figure 3.15: Pin location numbers.

Each of the pins was numbered, these can be seen within Figures 3.15. The misalignments were tracked for the two drive load cases (Load case one and two), as the drive gears shift is not critical during the PL loadings. However, the load cases utilised were tested for a series of pinion mesh point locations, to ensure functionality for the whole cycle of the part. Therefore, each of the two load cases h repeated 12 times, with the pinion load mesh point rotated around the circumference of the pinion gear at 30 degree intervals, as illustrated within Figure 3.17.

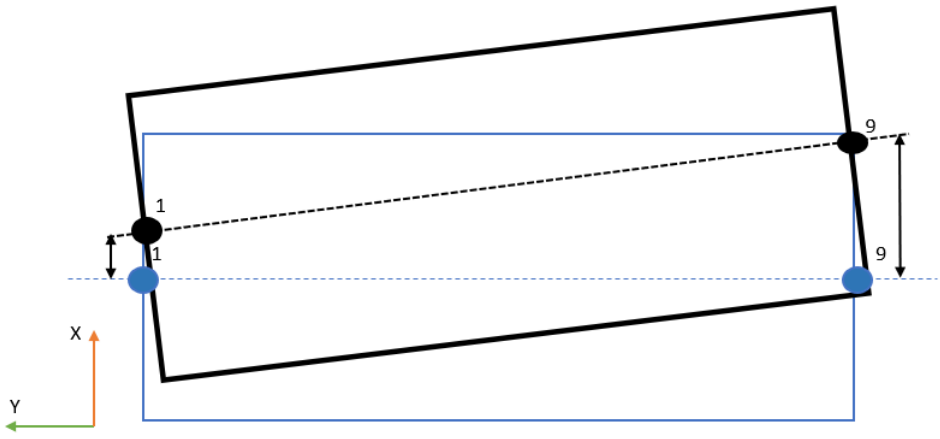



Figure 3.16: Exaggerated illustration of pin movement that is being captured and considered.

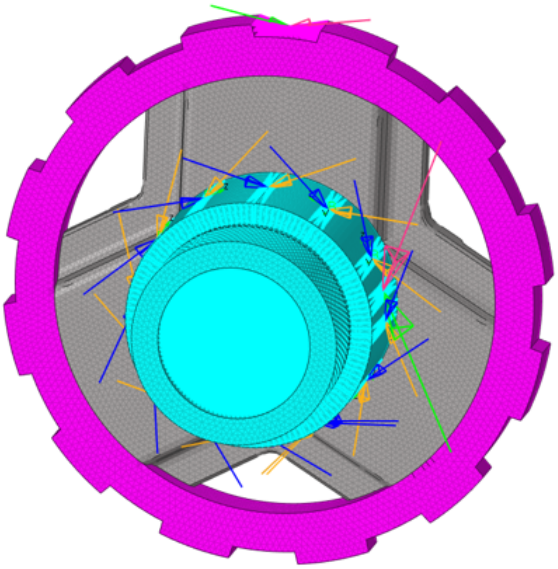


Figure 3.17: Loads displayed upon planetary assembly at 30deg. intervals.

### 3.3.3 Benchmarking

To help understand the newly generated results, a benchmark study was completed on the second version of the planetary carrier, to improve understanding of how this carrier design performed. The carrier was set up with both drive load cases one and two, with the pinion load mesh point rotated around the pinions circumference at 30deg intervals. The misalignments were then calculated from the displacements observed within the simulations. With the angular misalignments for all three pins and the pinion gear, for the Steel version of the carrier listed within Appendix .1.1 . The maximum misalignments seen were well within the prescribed 1mrad misalignment target. Providing ample scope for material removal, leading to a reduction in the carriers overall stiffness and therefore an increase in the angular misalignments.

### 3.3.4 Misalignment Results

Numerous studies were executed with a full list of misalignments available within Appendix .1. The angular misalignments for the cast version of the carrier (V3) were collated into a table, with the full table seen in Appendix .1.3. The results display the fact that the reverse load case (load case two), provides lower angular misalignment Figures with the pins shifting less than the forward drive load case (load case one), similarly to the original geometry. Nevertheless load case one still manages to adhere to the initial criteria and all the pins misalignment Figures remain below 1mrad, with a maximum misalignment of 0.613 mrad with load case two peaking at 0.528 mrad . The behaviour of the misalignments throughout the 360° rotation of the pinion gear mesh point, highlights appropriate carrier behaviour. With each of the three pins

misalignment results being 120° out of phase with each other, which is depicted within the graphs shown in Figure 3.18 and 3.19.

The average increase of the maximum angular misalignment for both load cases is 52.55 %, with a mass decrease of 39.11 %. Indicating that the percentage decrease in mass of the carrier has a profound effect on the rigidity. Although the proportionality of the mass decrease to the misalignment increase is a sensible portion. This was then monitored as the weight reduction progresses, to extract the point at which the weight saving is no longer viable, in relation to the misalignment increase. The proportionality factor for version four of the carrier is R=1.343, using equation 3.2 to calculate this.

$$R.\%Mass\ Reduction\ = \%Misalignment\ Increase \tag{3.2}$$

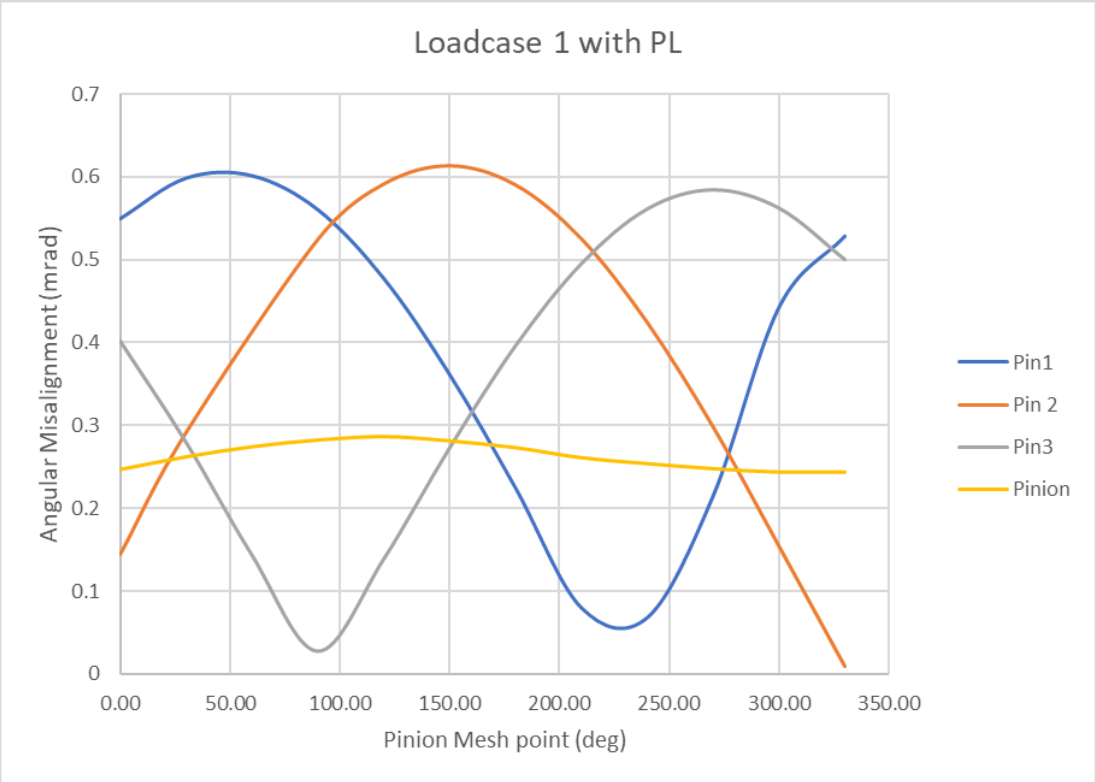



Figure 3.18: Graph displaying the angular misalignments throughout the carriers 360 deg cycle for Load case one of version four of the planetary carrier.

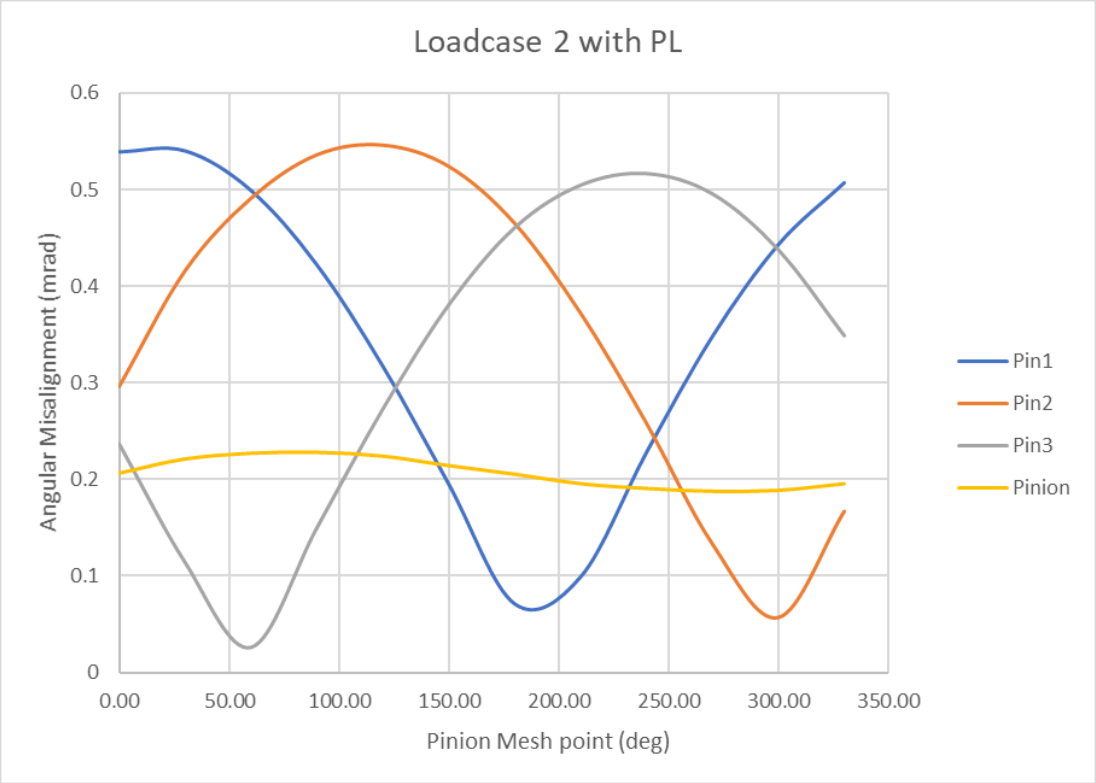



Figure 3.19: Graph displaying the angular misalignments throughout the carriers 360 deg cycle for Load case two of version four of the planetary carrier.

#### 3.3.4.1 Park Lock Removal

Once satisfied with the rigidity of the model, the carrier was then investigated for further weight savings for the instances where the Park Lock (PL) is not required. Therefore, the additional material supplied by the PL, is no longer available to absorb some of the stresses and reinforce the carrier. An initial study was carried out to examine the effect of leaving the carrier design the same but removing the park lock wheel from the outside of the part. The same load cases were tested, and the misalignments were once again recorded. These can be seen within Appendix .1.4. The removal of the PL wheel from the carrier has a mild effect upon the maximum misalignment's seen, the maximum misalignment shifts by 0.81% from 0.613mrad to 0.618mrad.

Due to the lack of change by removing the PL geometry, further design work was executed upon the carrier to remove the PL housing material. Then to examine how the part would look if the PL load cases were not required in the initial topology study. Therefore, by re-running the topology study without the two PL load cases, the iso surface output displayed a more compact version of the current version. With the same cross member geometry between pins, but with no disc connection outwards to the PL wheel. This output can be seen within Figure 3.20. Therefore, a redesign of the carrier was carried out on the PL capable version, with the

aim of trying to retain uniformity for the remaining central portion of the carrier for both park lock and non-park lock instances. Whilst also aiming to keep any modifications simple enough to be executed using an additional manufacturing machining process from the original version. The modified version of the carrier can be seen within Figure 3.21, with the adjustments to the design reducing the carriers mass down to 2.073 kg a further 21.48 % reduction from the PL capable carrier. Once again, this model was tested in the same manner as before with the misalignments monitored and listed within table in Appendix .1.5. Again, the increase in the maximum misalignment's exhibited is minimal due to the majority of the material providing support to the pins housing remaining unaffected. Therefore, this marginal increase of 5.5 % from 0.613 to 0.647, is outweighed by the 21.48 % weight decrease. For this model the scaling factor R decreasing to 1.085. This result along with the results with just the park lock removed provides a clear design direction, for designing for rigidity. The results highlight that the outer region of the part, is not constructive to supporting the pins and therefore the planetary gears. Due to this the material situated on the outer region causes mass increase, with a negligible effect upon the misalignment and functional rigidity of the carrier, when under driving load cases. However, the additional material is imperative when the park lock is required.

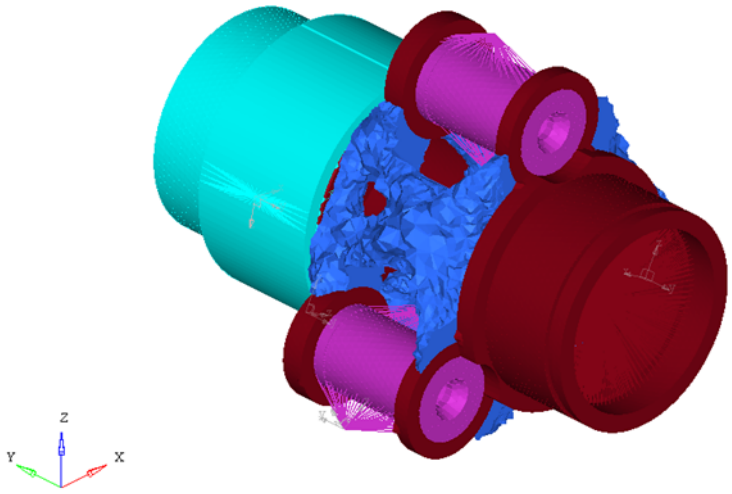



Figure 3.20: Resultant topology iso surface, where the park lock load cases are not considered.

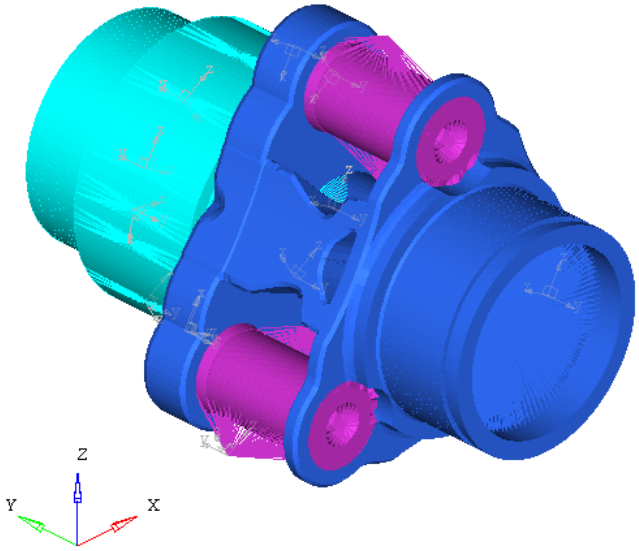



Figure 3.21: Version 4.2, displaying adapted version of the carrier for no park lock instances.

### 3.3.5 Material Investigation

Following on from the successful weight reduction of the steel component, an investigation into the planetary carrier's material was actioned. Initially the model's topology study was carried out with three different materials, to allow for an overview of potential weight savings for the model. These initial studies were carried out upon the original carrier model prior to the design changes. For each material the topology study was set up in the exact same manner with only the carriers material differing. The material info utilised for the studies is highlighted within the table 3.5.

| MATERIAL | E(GPa) | Nu | DENSITY (g/cc) |
|---|---|---|---|
| STEEL | 210 | 0.3 | 7.85 |
| TITANIUM | 220 | 0.34 | 4.5 |
| ALUMINIUM | 64 | 0.36 | 2.7 |

Table 3.5: Material comparison

The results extracted from these studies, assisted in highlighting potential materials for further investigation. It was seen that Aluminium due to its low density provided a low weight but with very little scope for material removal from the original design. Titanium however again showed a decreased part mass due to the reduction in density but a similar scope for material removal due to its similar strength to steel. Due to titaniums promising results it was investigated further, using the topology set up utilised for the generation of steel version

three of the carrier. This updated version of the carrier pre-optimisation had a mass of 2.486 kg. This model was tested to establish benchmark misalignment values in the same manner as Section 3.3.3, these values can be found within Appendix .1.2. With maximum misalignment values for load case one&two of 0.389&0.331 mrad respectively, both well within the 1mrad constraint, providing ample scope for mass reduction. The optimised titanium version provided a carrier weight of 1.514 kg, delivering a mass reduction of 39.09 % from the starting titanium carrier weight, and 65.08 % reduction from the original steel component. The titanium parts rigidity was also tested n the same manner and the results for this are seen in the table within Appendix .1.2, the misalignments are seen to decrease by around 5 %, due to the increased material properties, such as the 10 GPa ( 5%) rise in young modulus value.

### 3.3.6 Manufacturing Exploration - Additive Manufacture

In addition to material investigations, a series of manufacturing investigations were carried out. With the manufacturing constraints in place for casting being removed, with the aim to further investigate the potential weight savings that could be made. The designs generated without the manufacturing constraints lead to more organic free flowing structures, which lend themselves to being produced using modern manufacturing methods, such as additive manufacturing (AM).

A series of studies were executed without these manufacturing constraints limiting the design options. The version carried out using steel as the selected material yielded a resultant model weight of 1.6297 kg which is a saving of 62.41 % from the original carrier model. Which is a further 38.27 % lighter than the castable version four of the steel carrier. The peak misalignment was however seen to increase to by 200 % from the original version from 0.413 to 1.236. The sharp rise is an indication, that the weight saving has surpassed the point in which it remains profitable with regards to structural rigidity. Although when utilising titanium with no manufacturing constraints the AM suitable design had a resultant weight of just 1.105 kg, which displays a weight saving of 74.52 % from the original steel carrier. The displacements were again seen to increase but only by 75.06 % up to 0.723 mrad. Unfortunately, though this promising design displayed clearance issues when being integrated into the full assembly.

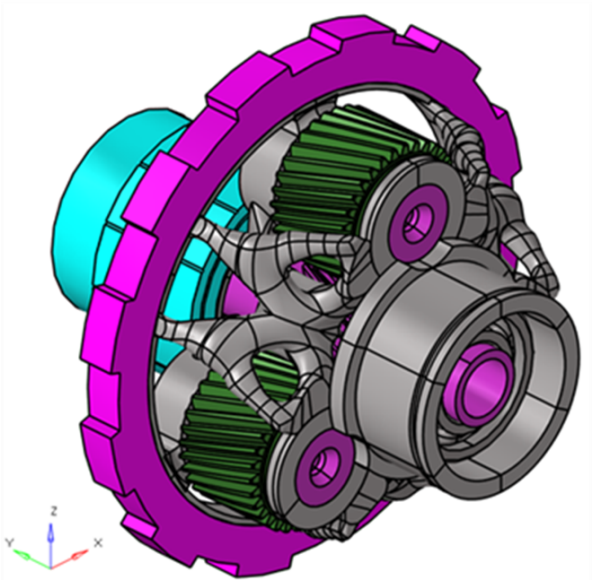


Figure 3.22: Titanium version for additive manufacture inserted into full planetary carrier assembly

Therefore, a second titanium version was created which ensured adequate clearance. The clearance was checked by inserting the model into the full assembly once realised, the updated assembly featuring this Ti AM version can be seen within Figure 3.22. This version sowed a further slight weight decrease down to 968 grams, however this additional reduction of 3.16 % from the last AM titanium version leads to a misalignment increase of 101.9 %, from 0.723 mrad to 1.46 mrad. This sharp rise indicates a clear drop off in structural rigidity, due to a fractional mass decrease. The rigidity of all mentioned designs were tested in the same manner as that previously documented with the misalignments collated within tables included in appendices .1.3 through to .1.9. Further detail for both the material and manufacturing investigations can be seen within the full-length report.

## 3.4 Stiffness vs Mass

To try and validate the aforementioned hypothesis and confirm the location of the optimum mass reduction for this model and study, an investigation was formulated based upon the ranging relationship between the models maximum misalignments percentage increase and the percentage mass saving. As following the completion of Titanium AM design version four, the results highlighted a clear drop in structural rigidity beyond a certain point, with a marginal mass gain.

Due to the hypothesis that version three of the AM titanium carrier being approximately at the optimum, the titanium version of the carrier was selected to investigate in further detail. With the aim of highlighting the point the optimisation and mass reduction becomes less

viable and highlighting the optimum mass reduction. The study was carried out utilising the steel cast optimised version of the carrier, as the benchmark, all previously completed versions were compared. The initial four points displayed within the graph, represented the titanium unoptimized model, the cast titanium version and two of the titanium AM versions. From the initial plot displayed in Figure 3.23 , plotting a series of titanium design iterations against percentage misalignment increase, with the 1mrad limit clearly indicated. A change in the gradient of the curve was observed, from a linear relationship up to 45 % mass saving, leading to a sharp rise beyond 58 % mass saving. Showing a relationship between the reduction in mass to the structural rigidity of the part. This relationship whilst providing a clear trend for this particular series of designs, it is not conclusive for all potential designs, as the number of options can be vast when using the SIMP topology method, each of which could result in a different average curve. However, confirmation of the overall trend for designs investigated within the study can be seen within Figure 3.24 where all tested models have been plotted, and the feasible design region and non feasible region have been highlighted, leaving the non highlighted region displaying results which do not surpass the misalignment target but do not achieve the desired mass target. Within this figure several best fit curves could be generated depending on which points are utilised, although for all of them it is clear that as the mass saving increases the misalignment value also tend to increase.

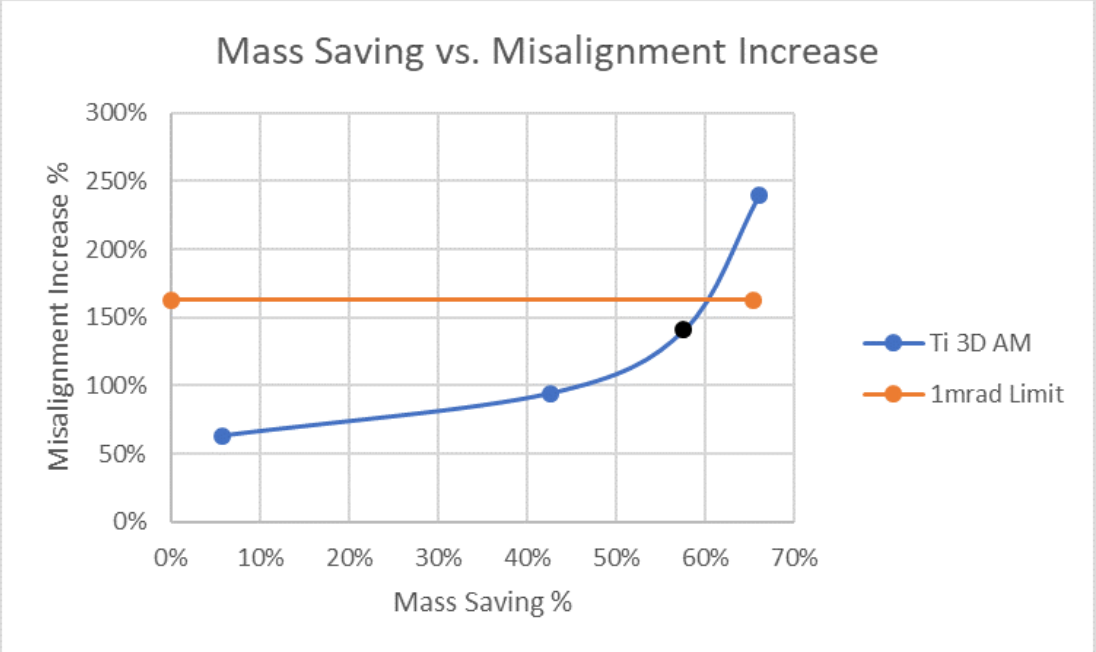



Figure 3.23: Graph of mass saving vs misalignment increase, with version four cast steel as the benchmark point for a series of titanium versions.

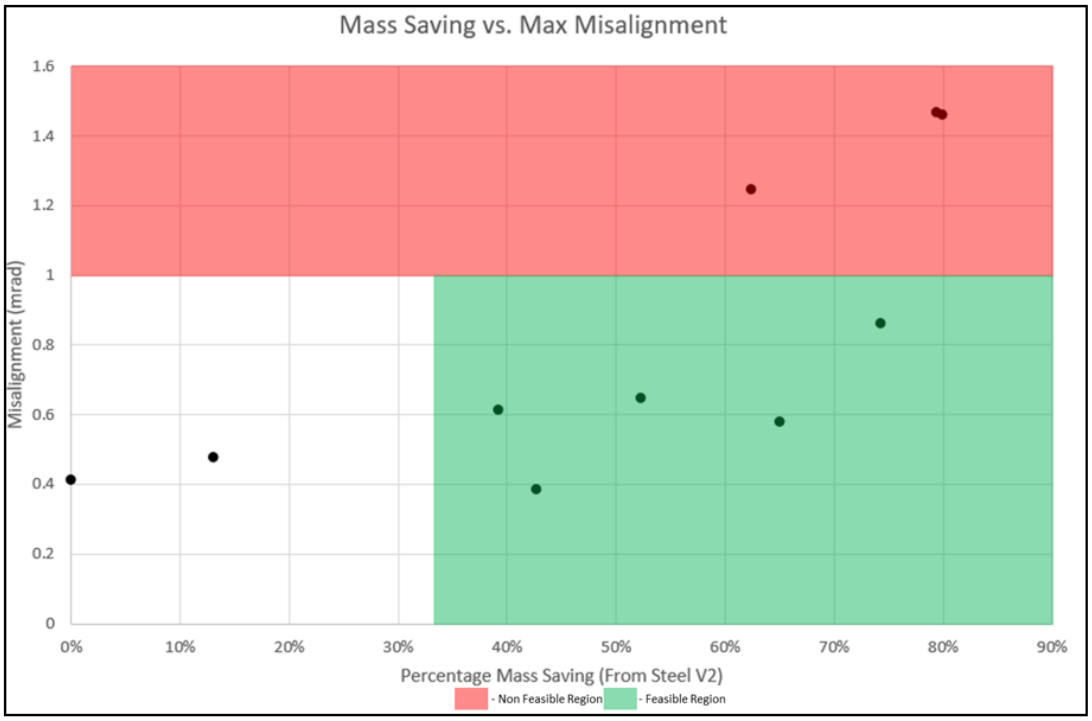



Figure 3.24: Scatter graph of various iterations

Therefore, using the guidance from the graphs in Figure 3.23 and 3.24, further design exploration was carried out with the aim of adding mass and reinforcing version two of the titanium additive manufactured design, to see the reaction the decrease in mass saving had upon the increase in misalignment. The curve was also utilised for design guidance, providing an indication to the maximum feasible mass reduction, whilst adhering to the misalignment constraint. This value can be calculated based on the 1mrad limit, which indicates a misalignment increase of 163 % from the benchmark result, which when examining Figure 3.23 equates to a maximum potential weight saving of 63 %. Although this point is displayed within the sharp rise of the mass misalignment relationship and therefore beyond the point in which the mass saving has proven to be beneficial. The scatter graph also indicates the regions deemed feasible and non-feasible with the region beyond 1mrad target constraint being classified as non-feasible, and the feasible section being below and beyond 33.3 % mass reduction, as across the three carriers this minimum percentage will ensure at least one whole carrier mass saving.

The next design generated based on the information above, resulted in a mass of 991grams, a marginal increase in mass of 23 grams. Although instead of reducing the misalignment, it increases by a further 2 %. This marginal change proves that depending on the approach and the location of mass removal, the behavioural effect may differ. In this example the lack of increase in misalignment is likely due to the increased element density material on the outer edge of the carrier, which has been previously proven when looking into transitioning the steel cast model to

a non-park lock version, to have minimal effect upon the misalignment performance. Therefore, a further design was generated with the aim of having a mass reduction of approximately 55 %, therefore final mass of around 1.2 kg. The newly generated design can be seen in Figure 3.25, the design itself to achieve this desired weight target needs to sit between the cast version and the AM version. Therefore to achieve this, the design took inspiration from two previous topology design outputs, the first being the same iso output used to generate version 3 of the titanium AM model, the second part of the design to add rigidity came from the cast version; which displayed a more solid base plate around the three pin bases on the pinion side. These adjustments lead to an end part mass of 1.12 kg, with a maximum misalignment of 0.86mrad, successfully back below the 1mrad cap. Figure 3.23 shows a gradual rise in the curve. With the point in which the mass reduction begins to become less profitable being between points two and three, 43 % and 58 % respectively. The black marker highlighting the latest design is also seen to be very close to the maximum misalignment limit. With only a potential further 2 % potential weight saving indicated, before raising the misalignment by approximately a further 23% and surpassing the misalignment constraint. From these results, it was concluded that the design currently generated was sufficiently optimised within the defined limits, and further design exploration and weight reduction, would not be profitable for the carriers overall stiffness. Therefore, all misalignment results were extracted for the aforementioned design, to allow for comparisons to be drawn with other investigated model versions.

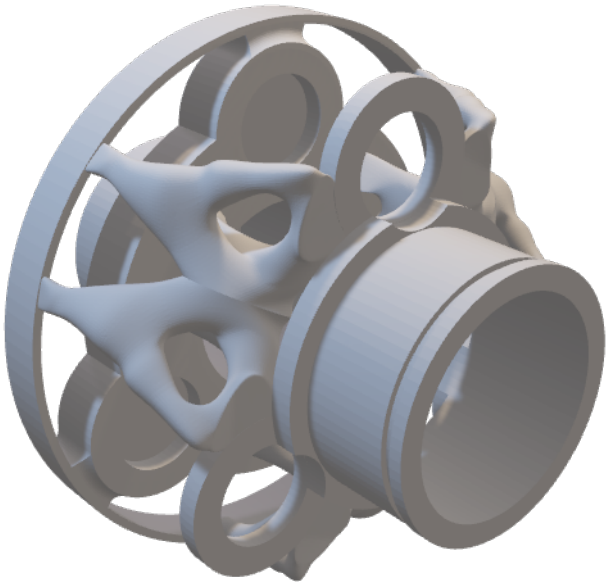


Figure 3.25: Titanium version four of the planetary carrier, mass 1.12 kg.

The misalignments for each load case for this version can be seen within appendix .1.9, with the corresponding graph for the driving load case one within Figure 3.26. The graph

displays the transition of the pins movement throughout the 360° cycle of the carrier, with the maximum misalignment ranging from 0.145 up to 0.860 but never surpassing the 1mrad target value. Using the misalignments collected from the various models and focusing upon the cycle of the misalignments for pin two for load case one a graph was generated. As the mass was decreased from the original titanium model, through to the AM versions the misalignments increased. However, it is seen that tested versions with a mass below 1kg therefore over 76 % mass decrease, yielded results with a misalignment beyond the prescribed constraints. These can be seen to fall within the Non-feasible red portion of the scatter graph shown in Figure 3.24. Therefore models with additional mass were then investigated for the final design option to ensure they fall within the green feasible portion.

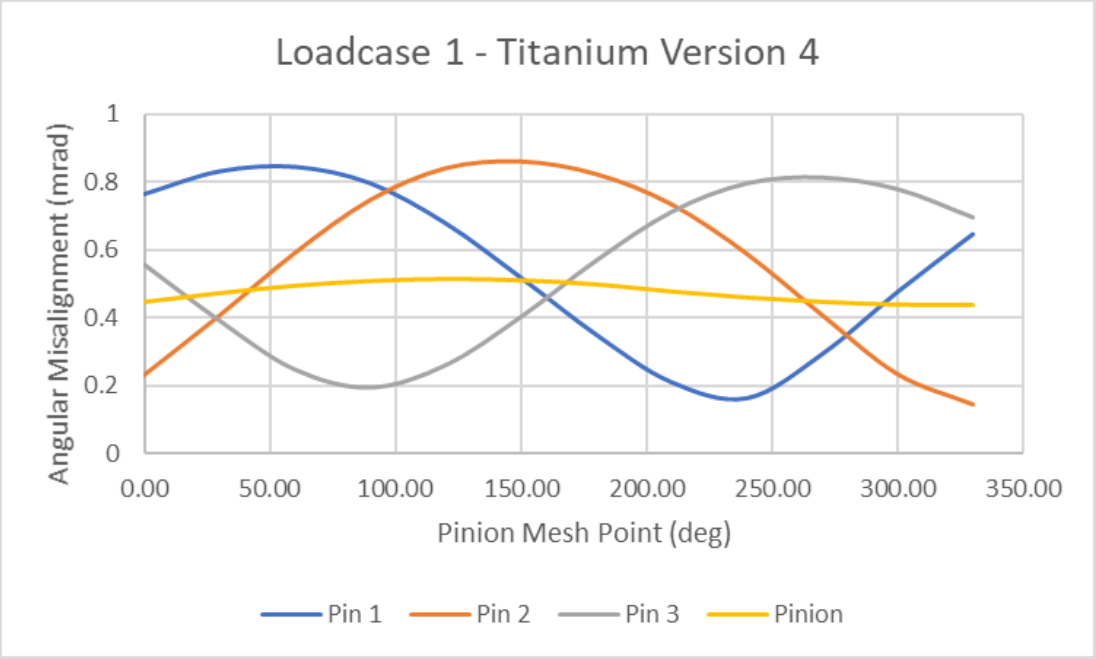



Figure 3.26: Graph displaying the angular misalignments throughout the carriers 360° cycle for Load case one of Titanium version four of the planetary carrier.

## 3.5 Costing

A key aspect in selecting the appropriate design is its feasibility and viability, whilst both manufacturing methods explored of casting and AM are potentially feasible, another aspect in selection is their financial viability. In addition to the financial costs associated with the various manufacturing techniques the material cost must also be considered. To fully understand the various costs of each design a costing study was carried out utilising a set of standardised costs. To provide context to the costing a sensible quantity must be considered as to offset the cost of tooling, for example, the die's required for casting. Therefore, a production rate of 800 cars per year was estimated based upon AML's current model production rate, the 800 cars require

2,400 planetary carriers based upon three per e-axle system, with two being non park lock and the third housing the park lock.

The assumed costs resulted in a net cost per carrier for both the titanium and steel cast versions of between 40 and 100 USD, whereas the rapid prototyped AM versions had a resultant unit cost of between 1,300 and 1,700 USD. A breakdown of these costs are shown within Appendix .2.1, from these it is clear that the AM versions are of a much higher cost, however if it was examined for a singular E-drive system during prototyping, the AM versions price remains constant whereas the unit cost of the cast versions would rise substantially, due to the cost of the tooling being spread across fewer units. Resulting in the AM options becoming more financially viable during the early stages of vehicle development and low volume vehicles.

Some key areas not considered in the above costings are as follows; firstly is the assumption that the designs with the draw constraints removed and more complex organic geometries must be manufactured via AM, whilst the designs lend themselves to this process, other methods of manufacture could be implemented such as casting, however if successful the tooling cost would be substantially higher due to the designs complexity, and may also lead to the mould not being reusable. Another aspect of the AM pricing is, the current price estimation does not fully account for part complexity, and only assumes cost for material used. Whereas it is common practice for material costs to be for the entire volume of the print bed as opposed to the end part volume, although the excess powder can in some cases be reused up to ten times. Also, the current price for titanium powder is between 300-500 USD and steel powder 80-120 USD per kg. Whereas solid steel is 1-5 USD/kg and titanium 35-70 USD/kg.

## 3.6 Design Selection

A number of key design's mass and misalignment values can be found summarised within table 3.6.

Figure 3.27, displays the final pugh matrix for these various design options for the planetary gear carrier. The pugh matrix is used as a criteria based matrix to compare the various design options in a simple way, whereby a simple postive, neutral and negative ranking is given to each design for each of the defined criteria, in turn giving each design an overall score and ranking. From this the suggested design is the cast steel version with adapted non park lock design. The selection of this design is due to its substantial weight saving from the initial carrier design of 39.1% for the park lock instance and for the two cases where the park lock is not required a 52.19% reduction, whilst simultaneously only resulting in an average misalignment increase across the three instances of 53.75%, which keeps the maximum misalignment well within the

| Planetary Carrier Exploration Summary | | |
|---|---|---|
| Version | Max Misalignment | Carrier Mass |
| Original Steel | 0.413 mrad | 4.336kg |
| Original Titanium | 0.389 mrad | 2.486kg |
| Steel Castable V4 | 0.613 mrad | 2.64kg |
| Steel Castable Adapted No PL | 0.647 mrad | 2.073kg |
| Titanium Castable V4 | 0.579 mrad | 1.514kg |
| Steel AM Version | 1.25 mrad | 1.629kg |
| Titanium AM Version | 0.86 mrad | 1.12kg |

Table 3.6: Key summary of explored planetary carrier design options.

1mrad target. Another aspect making the design preferable, is the material cost is lower than that of its Titanium counterparts. The final aspect in the design selection, was it proved to be one of the most manufacturable, with a simple casting procedure required, with a secondary machining process for the two non-park lock instances. However, if uniformity was desired between the park lock and non-park lock instances, the cast version in either steel or titanium would be suitable, with the selection between the two then being based purely upon material cost and weight. The AM designs also display potential for any lower volume instances, however their comparatively large cost along with their inability for mass production inhibit them from being utilised as the final selected design.

| Design | Weight | Manufacturability | Strength | Cost | Result |
|---|---|---|---|---|---|
| Original | -1 | 1 | 1 | 1 | 2 |
| Steel Cast | 0 | 1 | 1 | 1 | 3 |
| Steel Cast/Adapted | 1 | 1 | 1 | 1 | 4 |
| Steel AM | 1 | -1 | -1 | -1 | -2 |
| Ti Original | 1 | 1 | 1 | 0 | 3 |
| Ti Cast | 1 | 1 | 1 | 0 | 3 |
| Ti AM | 1 | -1 | 1 | -1 | 0 |

Figure 3.27: Pugh Matrix of key design options.

## 3.7 Chapter Summary

The selected design successfully fulfils the aims of the design brief, to reduce the overall mass of the planetary carrier whilst maintaining rigidity and not surpassing 1mrad of gear misalign-

ment, during both drive and reverse load cases. The combined mass reduction across all three carriers is 6.222 kg (2.263 kg per non PL carrier and 1.696 kg for PL instance) substantially aiding in the OEMs overall weight target for the e-axle system, of below 60 kg's. The weight saving represents just shy of one whole original planetary gear carrier assembly including park lock. This reduction comes at the cost of structural rigidity; however, the light-weighted design does not exceed the 1mrad misalignment target. The additional weight savings and investigations carried out within this chapter, assisted in displaying the behaviour of the model as the weight was reduced, with an optimum weight reduction to structural rigidity relationship indicated. The models to obtain results approaching the optimum, required the removal of the manufacturing constraints and therefore lend themselves to more advanced manufacturing methods such as AM, and therefore are not suitable for this particular instance but show the potential for any future developments of the HP e-axle system within lower production instances.

# Chapter 4

# Exploration of torque ripples and force distribution within key E-Axle transmission components.

## 4.1 Introduction and background studies

### 4.1.1 Chapter introduction

A key aspect of ensuring optimal results when designing components, is ensuring the loads applied are appropriate and as accurate as possible. To do this a detailed understanding of the macro scale problem is needed, with an understanding of the various loadings which may arise in the system, which should be used to drive the component level design; typically the worst case loadings. The focus within this chapter is upon the forces induced during driving loads for the e-axle transmission components, specifically the effects and spikes of torque ripples which is an exclusive feature of BEV vehicles.

Previous literature into the effects of torque ripples within e-axles, highlights a clear gap in the research, with no practical work being executed, to examine the effects of the varying torque, within an e-axle system and its effect upon components. Likewise, there is also a lack of research investigating the effect, the torque ripples generated by the e-motor have upon the components loadings. The research covered indicates that the varying torque during acceleration and deceleration, results in varied loadings across planetary drives. With this variation in loads resulting in vibrations being created, which in turn cause several issues, that could impact the efficiency of the system as well as affecting its longevity. There is also no regard to the effect these aforementioned issues would have when looking at optimising components, as often

to compensate for these spikes and variants in loadings a substantial safety factor is applied. However, this simplistic method could lead to over or under compensation of loadings, and in turn potentially impeding weight saving opportunities, or leading to insufficient designs.

Whilst the effects of varying loads has been discussed in previous literature, the combination of components working in sequence and the consequent effects have not been discussed or investigated fully. Also, all individual component-based investigations have been purely theoretical. Whereas, a proposed feasibility investigation was carried out to try to fill this gap in previous research, to see if the e-axle system can be fully modelled, to allow for the stresses and deflections on gear teeth to be monitored and observed. In turn, allowing for investigations to be carried out as to determine the worst loading conditions, and the effect of these conditions on the NVH performance of the components. The model would also allow for the user to determine the actual effect, if any, the torque ripples generated by the e-motor have upon the loadings within other components of the e-axle system. Allowing for clarification as to whether they require accounting for, to ensure any analysis on individual components takes this additional loading effect into account. (Such as Topology and light weighting studies.)

### 4.1.2 Background Work

The initial plan is to accurately model the e-axle system, including the e-motor, planetary gear and differential. Focusing on each section the aim will be for the e-motors to generate and provide the transient loading input to the planetary gears systems. With the aim of the e-motors taking the initial inputs for a lap of the Nrburgring, and accurately generating the output torque curves along with the torque fluctuations. However, this stage is not compulsory as the transient loadings for the planetary gear inputs are available. However, this is without the additional torque fluctuations, but the utilisation of both would allow for the comparisons to be made. As for the planetary carrier and the differential, these can both be assessed in the same manner. As the required output from both components is the deflections and loadings upon the gears, and in turn their impact on their respective casings. The final torque outputs are also required from the end of each part, to see if further fluctuations or drop offs in efficiency are seen, as the torque is transmitted throughout the system.

To establish a starting point for how best to execute the work, whilst doing so in a timely manner. A simple system was utilised, with the model comprising of a basic differential set up and focussing upon the first gear contact at the end of the prop shaft, with the pinion gear meshing with the ring gear. A simple depicition of the differential can be observed in Figure 4.1, whereby the input rpm for the model is applied upon the pinion gear through the prop shaft. This allowed for preliminary timings to be calculated and enable testing of the simulations. The

work was carried out using a multitude of Altairs Hyperworks softwares, including Motionsolve and Optistruct. First to be utilised was Motionsolve which modelled a single rotation of the ring gear, during this rotation the model was set to extract all forces generated upon the surface of the ring gear, from the driving pinion gear. This model set up constrained the ring gear in five degrees of freedom but allowed it to freely rotate around it's central Z axis, the pinion gear was similarly constrained in five degrees of freedom but left free to rotate around its Y axis, which was also the roation axis in which the input RPM load was applied to the pinion gear. The contact between the two gears was modelled using a impact based contact model. The Motionsolve software for this load case was executing a dynamic non-linear analysis, to provide a time history solution of the contact forces for the proposed problem. These forces could then be logged and utilised, as time variant loading within Optistruct, which could be applied directly to the surface of the crown wheel, relieving the need for any rotational movements within the simulations. This removal of dynamic movement aids significantly in reducing the complexity of the model, decreasing the computational run time. This broken down method as well as saving computational time, also allows for each stage to be checked. Assisting the user in identifying where any issues may be arising. The generated forces upon the face of the ring gear/crown wheel can be seen in Figure 4.2 which have been generated during the Motionsolve simulation. The stresses from the consequent Optistruct simulation are shown within Figure 4.3.

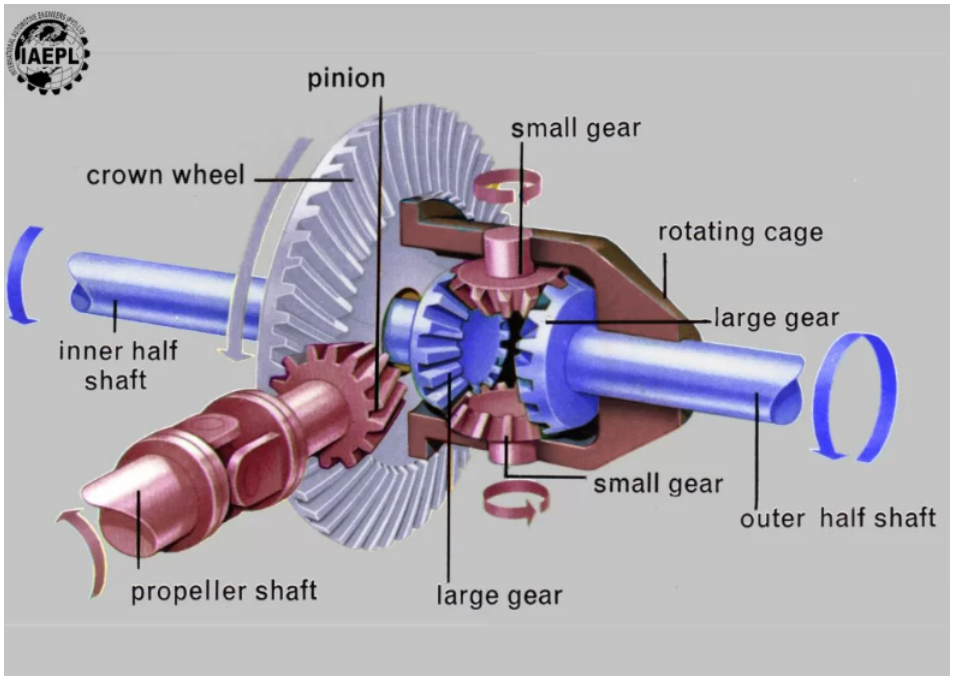



Figure 4.1: Labelled illustration of vehicle differentials parts [16]

This modelling set up takes approximately 360 minutes to run locally and is focussing

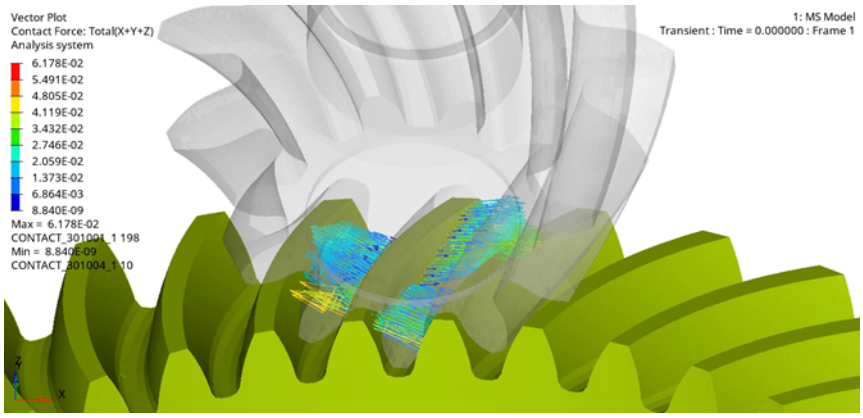



Figure 4.2: Visual of contact forces between pinion gear and crown wheel.

only upon one contact surface and a steady input torque. This simple system highlights the varying stresses and deflections as the ring gear begins to accelerate up to its desired operational speed. Providing a clear indication that when progressing from this basic model, to one with a transient loading as the input for the driving pinion gear. Stresses and deflections will vary as the input rpm ranges and the ring gears speeds differ. It was from simple outcomes like this, that peaked interest and gave indicative evidence that these variations may have a significant effect upon other components within the gear system. For example, how the loads on each of three planetary gears differs, as the sun gear speed changes.

However, the biggest issue raised from the initial testing was the timings, as the run took a substantial amount of computational time for just a single revolution of the ring gear. Whereas what would be required for the e-axle would be thousands of revolutions even if simplifying the model. As the sharpest acceleration or deceleration curve for the system spans across a much larger time period, in comparison to the 2.3second simulation tested. This is due to the fact that for full observations of how the systems performs across a range of varied loadings, a lap around the Nrburgring is utilised as a typical benchmark, due to covering a range of loading scenarios as it includes aggressive acceleration and deceleration points, along with prolonged acceleration periods. In addition to this issue, there is also the matter of contact faces simulated, as in the example model only one contact surface is considered, whereas the requirement for the planetary gear system alone is six, which rises when its contacts with the differential and the differentials internal contacts are considered, giving a total increase up to 11, for just a singular e-axle. With the twin motor containing 18 contacts points of interest. Due to the linear nature of the system, the simplest method of reducing computational run time cannot be utilised, as it cannot be parallelised to reduce computational run time. Therefore, an estimation of the run time was made, based upon the initial run timings. This estimation was for a model looking at inputting the torque to the planetary gear system directly, with the input loading being based

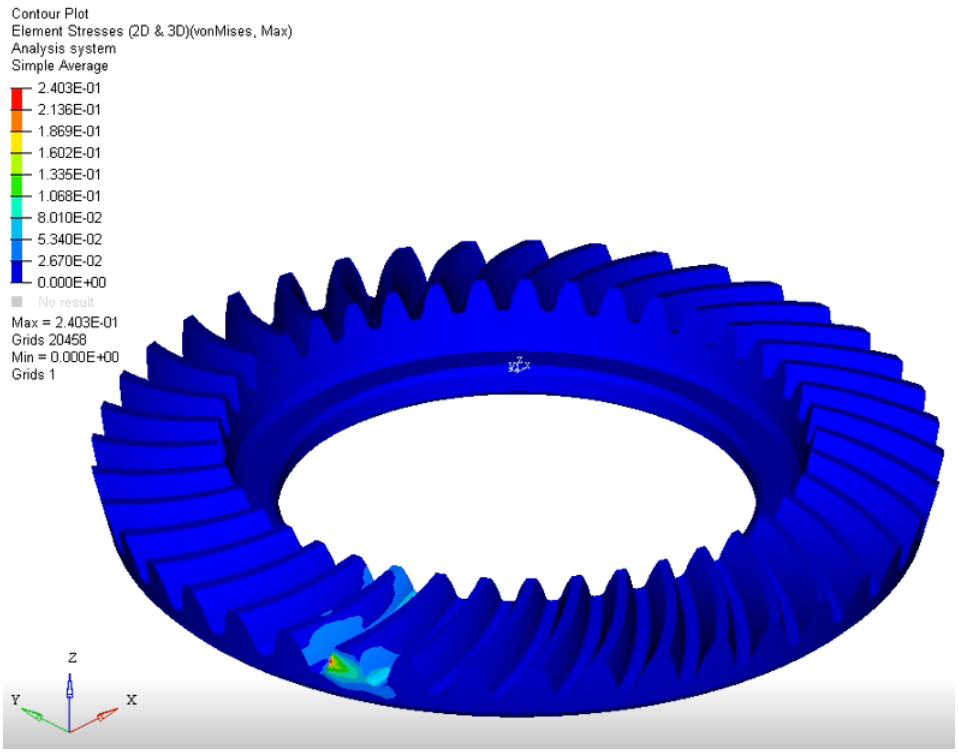



Figure 4.3: Contour plot displaying resultant stresses upon the differential crown wheel in MPa.

upon a single Nrburgring lap, with an estimated lap time of eight minutes, 480 seconds. This period of time for even the example differential system would increase the computation run time from 360 to 75,130 minutes (52days), due to this clearly being infeasible a shorter initial time period was to be considered.

The new time period was decided upon as it would allow for the steepest section of the ramp up curve, for the full ramp up of the system from 0 rpm up to 18000 rpm (the max rpm of the e-motor). As this curve will be utilised during aggressive acceleration periods, such as 0-100 kph. The e-motor itself will take approximately 10 seconds to reach its top rpm. Therefore, focussing upon the initial rise of the curve of the motor is accelerating up to running speed. As a 10 second simulation would again still be far too computationally expensive.

As the e-motors can supply maximum torque from low rpm, with the torque generated dropping off as the motor converges upon its maximum speed. Opting to focus on the target 0-100 kph time as the simulation input, provides a more reasonable time frame, with an estimated 0-100 kph time of between 3.8 and 3.9 seconds. Whilst this is still a 69.6 % increase in run time from the original simulation this will not be the key factor in the increase of computational run time. The key factor is the additional contact faces requiring modelling for just the singular e-axle, from 1 to 11. The combination of these two factors estimates that a run time of around 6,714 minutes would be realistic. Whilst a computational run time of around five days is not un-common it is certainly too large to supply quick feedback to designers when looking to check

for torque ripple effects when executing iterative modelling. Although it would supply a good benchmark point to work from.

As a result of the run time being comparatively long, and potentially prohibiting of iterative design processes, a number of time saving avenues could be explored for the model. Including supplementing 3D components for 2D, substantially increasing the time step, modelling all components bar contact faces as 1D and the contacts as 2D and also reducing the loading time as mentioned above. The options whilst posing potential time savings, may also result in a drop-in modelling accuracy. As to support the 2D contact faces in both instances, they would require rigid support which in turn would over strengthen the parts, making the results void. Unless the rigid supporting the 2D mesh, was dveloped to deliver a more accurate representation of the solid structure, allowing for a closer correlation to reality. Also, the increase in time step, depending on size may reduce the accuracy causing the ripples which are intended to be captured and studied to be missed. Therefore, careful consideration is required when taking this approach.

| Option | 0-100 kph | 0-200 kph | Max Cont. Speed (kph) |
|---|---|---|---|
| SUV Target | 3.90 s | 10.00s | 249.5 |
| SUV Actual | 3.87 s | 11.28 s | 252.7 |
| Sedan Actual | 3.82 s | 11.23 s | 249.5 |

Table 4.1: Details of the target vehicle performance.

It is also key to note that for all the possible models discussed, the benefit of a physical test validation and benchmark would be advantageous. As for in the instance of the computationally lighter models, the typical method for validation when researching new modelling techniques, is to utilise a pre-existing correlated dfem as the benchmark. Although, this still requires the correlation of the dfem model against a physical test. However, this would prove challenging when trying to capture any deflections of gears within their casings under physical testing. A simpler method for validation would be to extract the end torque curve, and observe the fluctuations seen on this in comparison to the comparative computational final output. A Validation of the time savings, may also be required to establish the initial run time of the conventional model utilising 3D meshed components.

The negative points and list of challenges previously led to the decision between myself and support, to think this may not be an achievable project. Although at this time of thinking, it was still believed that investigations would be based on a much more significant run time well into the months, as feasible time frame which would still supply us the details required has not been identified. However, the newly suggested time frame should show sufficient levels of detail required to see the effects of the varying loadings. Also, most importantly it would allow for a 3D benchmark to be generated, to be used as a reference point when trying to decrease

the computational run time through some of the suggested time saving options. Which were disregarded initially due to the uncertainty in obtaining models of note to reference results, to identify what sort of losses in accuracy were being caused by making these time saving adjustments. Additionally, the time frame again was still larger so even with a computationally lighter model, the investigations planned still projected any run times to be infeasible.

Although with the new time frame suggested, it is believed that the modelling of these gear systems could work, to fill the gap where assumptions are made with loadings and loose safety factors are applied to account for this varied loading across different gears, particularly within the planetary system. Therefore, getting the system working is achievable and if not the studies will provide data and baseline evidence, into a number of problems that could be solved to make it nearer to being achievable given faster computing in the future. However, it is clear for the time being a simulation as extreme as the full lap of the Nrburgring or another circuit wont be as feasible, simply due to the simulation having to span for the entirety of the lap time. In addition to the computational cost of this, the amount of data which would be generated would be significant and I do not believe the extensive range would be required to analyse and validate what effects if any torque ripples are having upon the system. Beyond getting the simulation set up and functioning as desired within a manageable timeframe, it would be prudent to utilise other skills to allow for the simulation to become seamless and automated. Below is an outlined draft work plan for how to get the studies to function and possible areas of investigation. If the workplan was successfully completed and resulted in a functioning model. It could be used to check behaviours under a range of loadings not just the sharp acceleration, which are being used a starting point. Therefore, the hope that if functioning, engineers could really utilise the tool to indicate possible areas which need further attention, or simply confirm that the effect of torque ripples and varied loadings is negligible and can be easily accounted for with a safety factor. It is key to note the drafted workplan was to give a loose framework and potential areas of investigation for reducing run time of the system, and has been included within the thesis to assist in illustrating the planned route ahead of further investigations which shaped the direction of the studies, as some areas may be applicable and assist in future work or for similar alternate studies.

## 4.2 Motionsolve Initial Investigations

To begin the investigation into getting the e-axle analysis functioning to allow for an improved understanding of torque fluctuations and ripples, the system was broken down as previously suggested. With the initial target of getting each section working as time efficiently and ac-

curately as possible. Therefore, the initial starting point was the Motionsolve analysis of the simplified model, in this case the focus is utilising just the differential from an e-axle system.

The aim of the Motionsolve region of the analysis system is to execute the multi-body system analysis of the differential system. Executing dynamic analyse of the model and exporting the contact forces observed within areas of interest for further analysis. The initial section of work to be carried out in this region is to improve the understanding of the systems behaviour and understand and highlight appropriate options for use for the analysis.

### 4.2.1 Initial Model Set-Up

The sole input for the differential model, is the input speed at the pinion gear. In the full e-axle simulation this input will be the output of the planetary gear system, which will in turn have their input from the e-motor. Therefore, the model needs to be assessed for its functionality at the speeds expected at this stage of the e-axle. As currently the model functions at a pinion gear input speed of 10 rad/sec, using the calculation shown in equation 4.1 this is simply converted to 95.49 rpm.

$$\begin{aligned} V_{rad/sec} * 30/\pi &= V_{rpm} \\ 10 rad/sec * 30/\pi &= 95.49 rpm \end{aligned} \tag{4.1}$$

The expected top motor speed is known to be 18,000 rpm and the gearing ratio for the planetary system provided is roughly 3 to 1 giving an input speed for the differential of 6,000 rpm. This equates to 628 rad/sec. Therefore, the model needs to be tested at a higher speed range as the initial tested speed is far too low.

Once the model was set up under the initial loadings, the input angular velocity of the pinion gear was doubled to 20 rad/sec to observe if the model still functioned as expected. Once the results were confirmed this was then increased again to 50 rad/sec and once again checked, these initial adjustments assisted in improving the understanding of how to control the models input. Satisfied the model was handling the changing angular velocity correctly, a significant jump in speed was made to 1000 rad/sec to ensure that the model can cope with any speed that is to be considered, including the overspeed. The print time for the model for this jump in speed was also adjusted by 100x from that used for 10 rad/sec. With it being reduced to 0.1 ms. The model once again handled the high speed, however the time as expected with the decreased print time increased significantly from 3minutes to 20 minutes. Therefore, the time step (from here on in reffered to as print time) was increased back to 2 ms to examine the effects, the first item noticed was an un-expected increase in computational run time, however the maximum forces for the model were seen to increase. However, from this it was hypothesised that this

could be due to the increased print time not capturing enough detail resulting in a spike in the observed forces, which in turn requires a greater computational intensity to compute.

Following on from this initial investigation it was clear that there was two key factors effecting the computational run time, first of which being the input speed, the second being the print time selected. Focusing upon the input speed first, a range of input speeds were investigated with a constant print time allocated, to examine the effect of the speed on the CPU run time.

The study tested at a range of speeds from 10 rad/sec through to 1,000 rad/sec with a print time of 1 ms. All settings were kept the same with a run time of 3.5 seconds and the simulation ran on the same local device on 4 threads. The resultant times from this can be seen in table 4.2, Figure 4.3.0.2 contains the results plotted upon a graph. Where it is clear to see a linear trend, with the CPU run time increasing as the motions input speed is increased and forces rise. However, there are some results on this curve which differ from the trend line slightly, this could be due to several factors, including forces seen within the study or if other tasks being calculated on the device is diverting power from the simulation. Overall though the behaviour is clear, that as the motion input speed is increased the user can in turn expect an extended CPU run time.

| Input Speed, CPU run time comparison | |
|---|---|
| Input Model Speed | CPU run time |
| rad/sec | Seconds |
| 10 | 144 |
| 20 | 165 |
| 50 | 207 |
| 100 | 221 |
| 200 | 331 |
| 500 | 558 |
| 750 | 751 |
| 850 | 875 |
| 900 | 757 |
| 1000 | 1196 |

Table 4.2: Input speed, CPU run time comparison table, print time 1ms

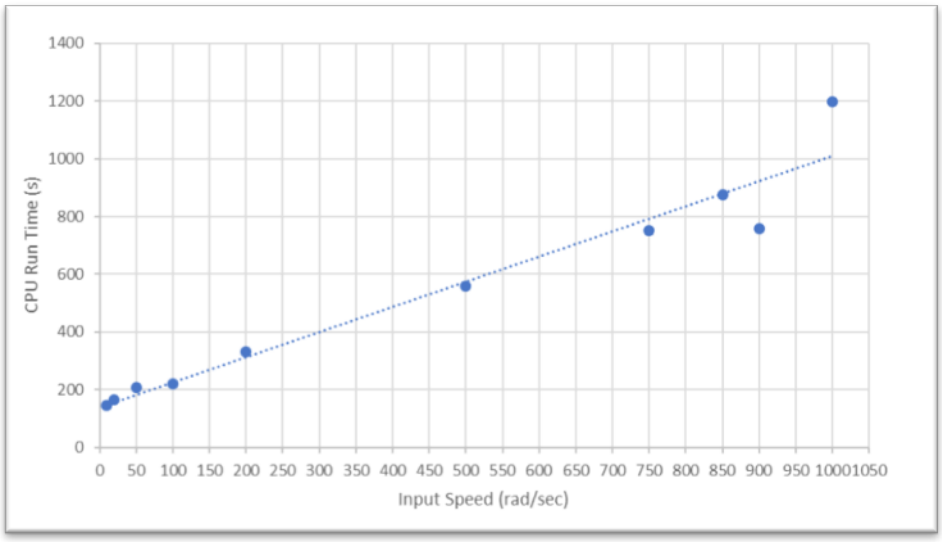



Figure 4.4: Plot of table 4.2, Input speed vs CPU time.

Continuing from the preliminary input speed investigation, the print time was also assessed to examine its effect upon the CPU run time, to assist in confirming if the print time could be a key area to save time when expanding the simulation. For that reason a study investigating a range of print times, at a constant input speed of 100 rad/sec was executed. The print times ranged from 150 ms down to 1ms, with the resulting CPU run times shown in table 4.3 , again the results were plotted in Figure 4.5 to observe any trend patterns occurring. As it would be expected for a CPU run time to be significantly affected by the print time (time step) and therefore increase as the print time is decreased. Although the resultant graph shows a steady series of results with minimal change in run time across all print times. This leads to the belief that for this particular set up of the model with an input speed of 100rad/sec and a run time of 3.5 seconds, the print time is not the key limiting factor which is driving the computational run time. This is interesting to note as when progressing to a variable input speed, some speeds

may not be as limited by the print time selected as others, as shown in the previous study input speed controls the run time and therefore at certain speeds it could lead to the print time being less of a key factor. Whilst also potentially supporting the hypothesis that forces tracked within the model are having a significant effect on the run time, with all results within the timestep window tested providing sufficient accuracy to capture the forces in the model.

| Time Step Study, Set Speed 100rad/sec | |
|---|---|
| Print Time | CPU run time |
| Milliseconds | Seconds |
| 150 | 220 |
| 100 | 225 |
| 50 | 220 |
| 10 | 219 |
| 5 | 222 |
| 1 | 221 |

Table 4.3: Print time, CPU run time comparison.

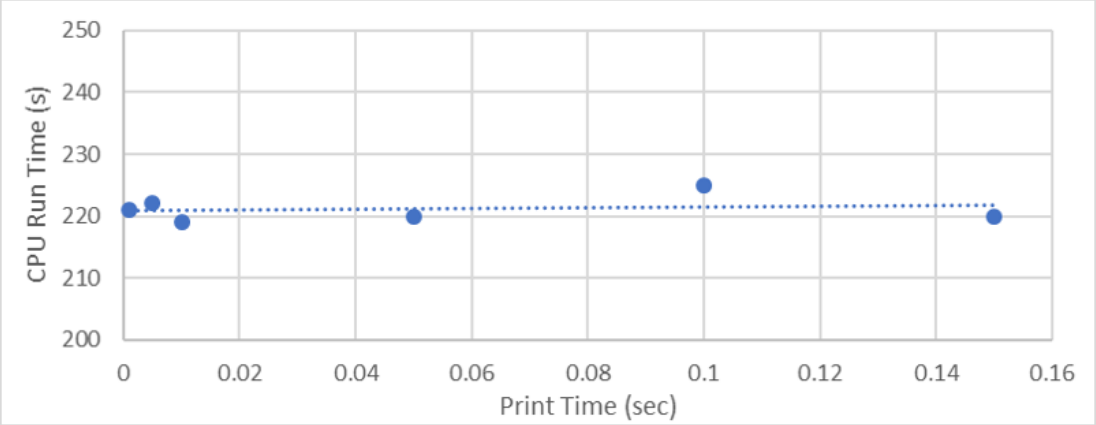



Figure 4.5: Plot of print times effect upon CPU run time.

Although to better understand the print time to run time relationship the same series of print times was tested using the input speed of 10 rad/sec to observe if the same constant result was seen for the run time. The results from this are overlaid on the original graph in Figure 4.6, the orange line representing the 10rad/sec results, show little to no change across this range of print times, confirming at these speeds the print time is having little to no effect on the CPU run time.

### 4.2.2 Initial Model Behaviour

#### 4.2.2.1 Forces and Penetration Depth Overview

The next step in checking the model is functioning appropriately and the methods being utilised are sufficient to continue using, is analysing the max forces and penetration depths. These

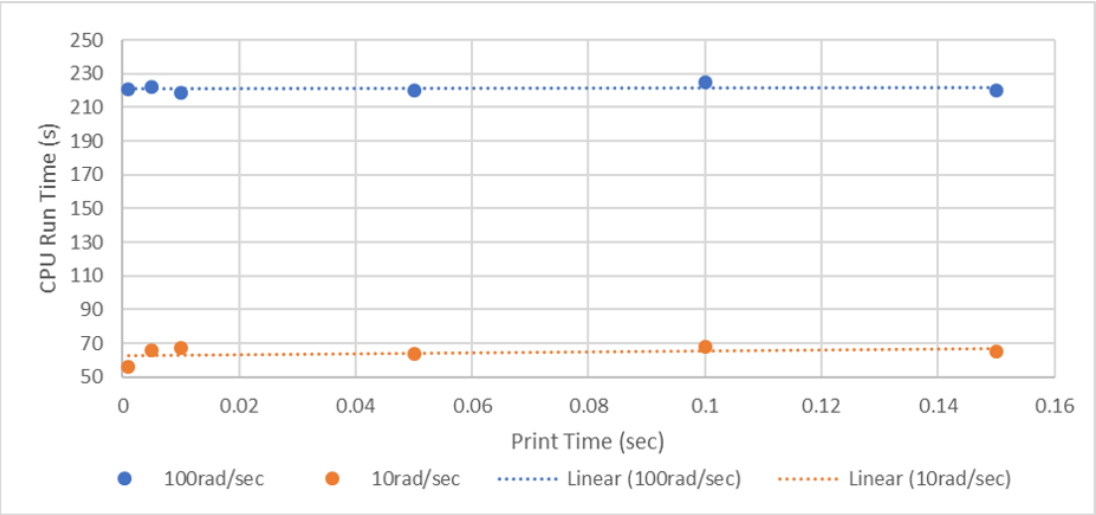



Figure 4.6: Plot of print times effect upon CPU run time, for 10 rad/sec and 100 rad/sec

investigations were to develop an understanding of what was to be expected and to clarify the best techniques to quickly clarify if a model is performing appropriately.

To do this, a series of constant speeds were tested utilising a set print time of 10ms and run time of 3.5 seconds, following each speed being tested the maximum forces seen and maximum penetration depths (PD) observed for the whole simulation were extracted along with the time in which they are observed. The results for the maximum forces seen can be observed in Figure 4.7, all contacts show a clear increase in forces observed as the speed is increased, as to be expected. However, there was a substantial jump at 900 rad/sec to beyond 250N; therefore, to try and examine if this was an anomaly, further sample points were added, these can be seen in the increase in density of sample points between 750 rad/sec and 900 rad/sec. These additional points assisted in proving the problem appeared to be just at 900 rad/sec. The reason for this is not initially clear, although the same issue is observed in Figure 4.8, with the max pds also experiencing a substantial jump at 900 rad/sec before returning back to an expected value at 1000 rad/sec. One thing which is consistent with the 900 rad/sec results, is the forces seen between the latter contacts of the bevel gears, which would be expected to be less than that of the pinion/crown wheel contact, surpass the pinion/crown wheel forces. Overall the forces and max pds do not appear to form a consistent relationship as the speed is increased, exemplified by the 900 rad/sec result, indicating a problem within the model with results spiking by a thousand times that of the previous tested speed. When examining the times at which the maximum forces and pds occur this also highlights inconsistencies, with the majority of the lower speed runs all experiencing their maximum points during the early stages of the run, whereas the higher speed runs exhibit their max values towards the latter stages of the run.

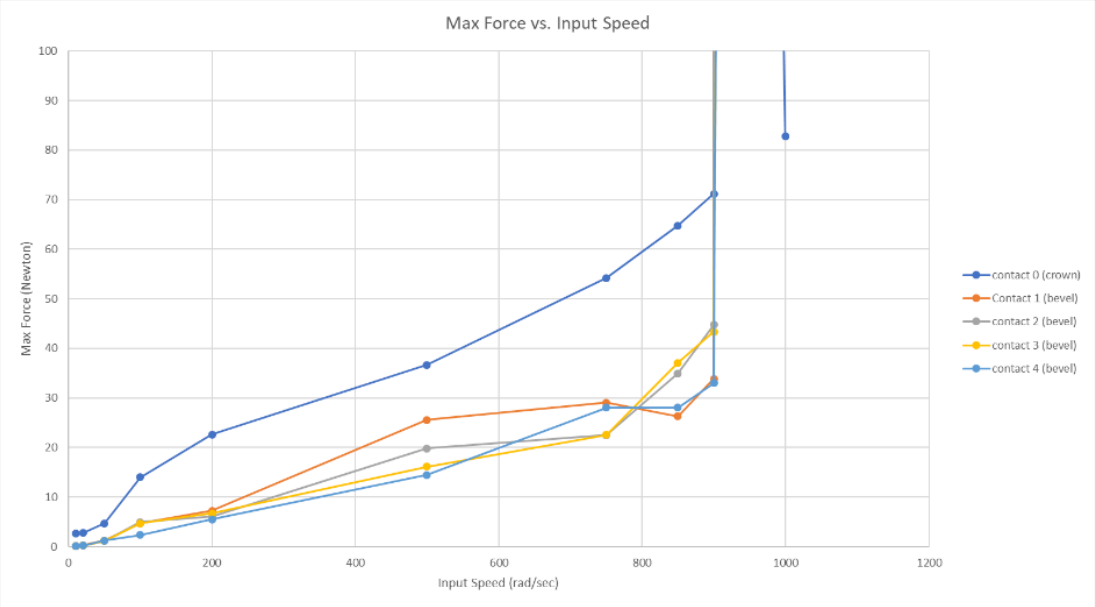



Figure 4.7: Plot of maximum forces observed at various input speeds.

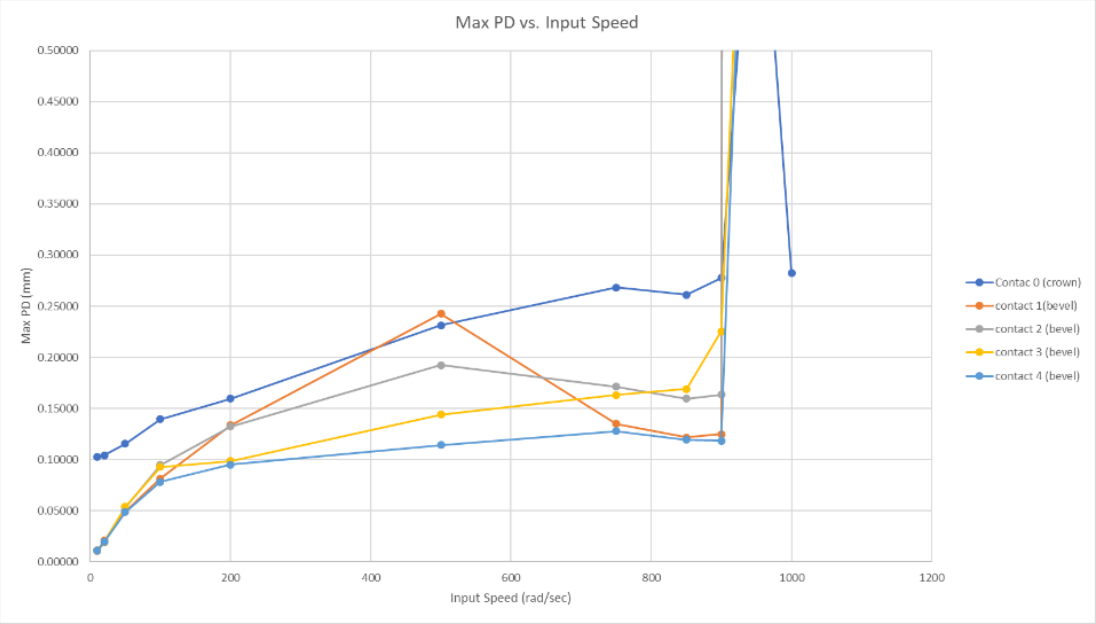



Figure 4.8: Plot of maximum PD's observed at various input speeds.

#### 4.2.2.2 Contact force behaviour

**Complete time frame** Due to a key issue in the model being present, the results were analysed further to try and isolate the cause. Also as the forces should be directly linked to the penetration depths, and the forces were the primary concern for the Motionsolve region of the simulation. These were the focus of the further investigations to identify any issues. Under the assumption that correcting the maximum forces will also result in recording the correct max pds , which can be checked once satisfied with the force results. The starting point for this investigation was to begin with the simplest results e.g. lowest speeds to see if they are behaving as expected. To do this the contact forces were plotted against time for the 5 key contacts within the differential. The graph shown in Figure 4.9 clearly show how the key forces are seen within the pinion/crown wheel contact with the remaining forces on the bevel contacts being comparatively minimal. The forces seen are also relatively consistent throughout, with the frequency of the waves increasing beyond the starting point of the simulation. This is due to the model accelerating up to the prescribed working speed.

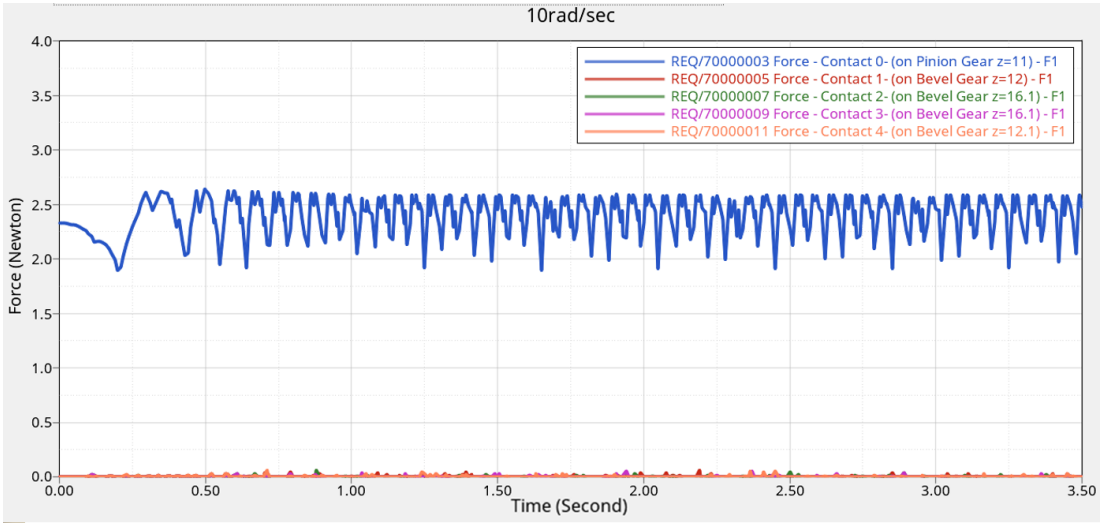



Figure 4.9: Plot of contact forces observed at 10 rad/sec for all gear contacts, throughout 3.5 second analysis.

This method of checking the forces was continued for a 20 rad/sec prescribed speed, which displayed the same behaviour as that seen at 10 rad/sec in Figure 4.9. Although the wavelength has visibly reduced due to doubling of the input speed and there was a slight increase in forces seen for the bevel gear contacts. However, progressing to 50 rad/sec some clear changes are observed, the first of which is a clear rise and fall in forces at the early stages of the simulation, another is occasional spiking in forces during the mid and latter stages. These issues are amplified when progressing to 100rad/sec with the rise and fall in forces remaining at the early stages of the simulation, most likely due to the models acceleration period. However, the spikes

seen thereafter are greatly increased and are the clear maximum force points, the forces for the latter contacts in the system are also seen to begin to spike. The graph showing the force plot at 100rad/sec is seen in Figure 4.10.

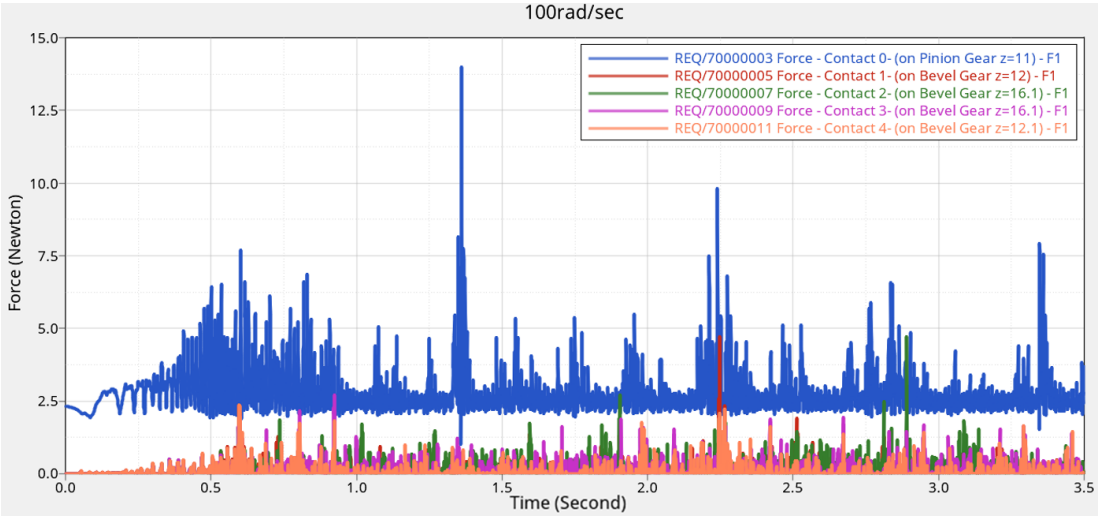



Figure 4.10: Plot of contact forces observed at 100 rad/sec for all gear contacts, throughout 3.5 second analysis.

As the speed continues to increase the spiking forces become more regular and this also begins to distort the initial rise and fall seen at the beginning of the simulation. These fluctuations continue to amplify, as the speed rise up to 950 rad/sec, where the results were examined in Figure 4.11. From this force plot it is apparent that the forces are no longer being captured accurately, with continuous spikes occurring throughout the main pinion/crown wheel contact.

Although the biggest difference seen in comparison to the lower tested speeds, was the contacts expected to experience less significant forces, such as those on the bevel gears are now seen to spike in value to beyond that of the pinion/crown wheel; the primary contact of the system . Some of the spikes are seen to be around 6,000 times larger than any seen in the initial contact. This therefore indicates the current set up of the models, has an inability to cope with any high speeds, with issues occurring in all speeds above 100 rad/sec. Therefore, further investigations were carried out into the behaviours and patterns of the force plots to isolate and correct the problem, to ensure all required speeds can be modelled accurately. However, the knowledge from previous studies does indicate the print time would require reducing to accurately capture the higher speeds, with this addressed in consequent studies.

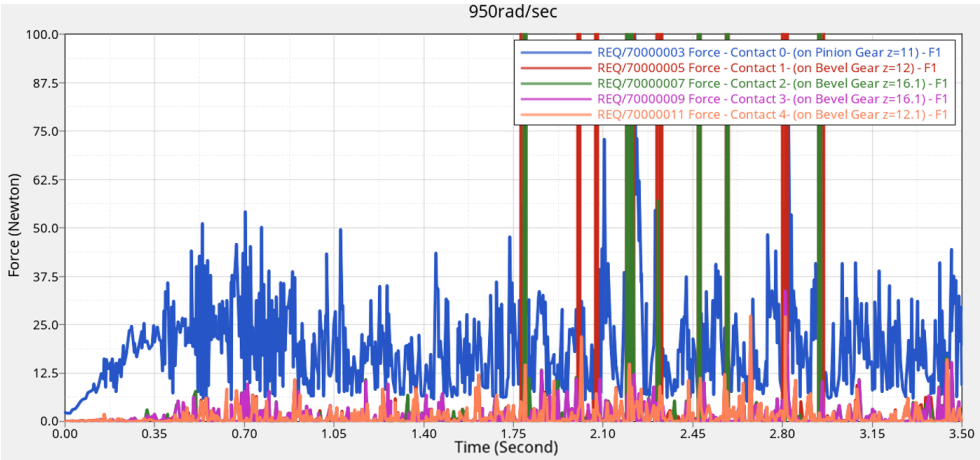



Figure 4.11: Plot of contact forces observed at 950 rad/sec for all gear contacts, throughout 3.5 second analysis.

**Reduced time frame** The next step in checking the accuracy for the results was focusing upon a smaller time frame and analysing just a few force ripples from the plots. Therefore a 0.5 second sample was focussed upon between 1 and 1.5 seconds, and the pinon gear contact was investigated. By focusing in on a shorter range it allowed for each wave to be clearly seen, with each wave in the forces, being due to the passing of a gear tooth. The initial wave utilising a 10 ms print time can be seen in Figure 4.12.The print time was then decreased to examine the effect upon the results. As it was noted at 10ms print time, some waves were distorted and not as smooth as initially desired. Therefore, the print time was adjusted from 10ms to 1ms, this result was then overlaid on the initial plot to compare the accuracy. It is clear in Figure 4.13 that the decreased print time captured the force curve in a much smoother manner, a key note is also each wave pattern appears to be much more uniform with peaks and troughs of very similar values throughout. Due to the clear jump in accuracy from this initial print time reduction, a further decrease was executed. Refining the print time down to 0.1 ms, this however when overlaid with the previous results in Figure 4.14, showed an almost identical pattern to that of 1ms print time. This indicated that their was a cut-off point where the print time will no longer improve the accuracy of the results, but does increase the frequency of data points.

This point was then to be considered when looking at alternative input speeds, as to help determine what the required print time is to achieve the optimal results for each tested speed. However, the change in print time had an effect on another key area of these investigations, this was the CPU run time, with the run times seen to increase from 3minutes to over 15 minutes, as the print time was reduced from 10 ms to 0.1 ms. This effect on the CPU run time, therefore, also required monitoring to ensure an optimum print time can be found for each speed, that delivers a sufficiently accurate and time effective result.

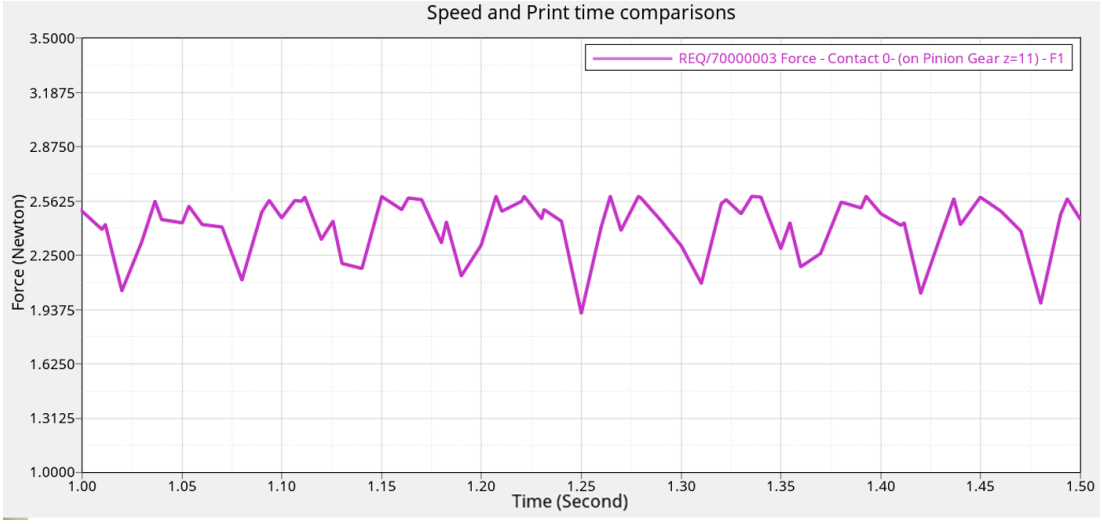



Figure 4.12: Pinion to Crown Wheel Contact Force wave over 0.5 seconds, at 10 ms print time

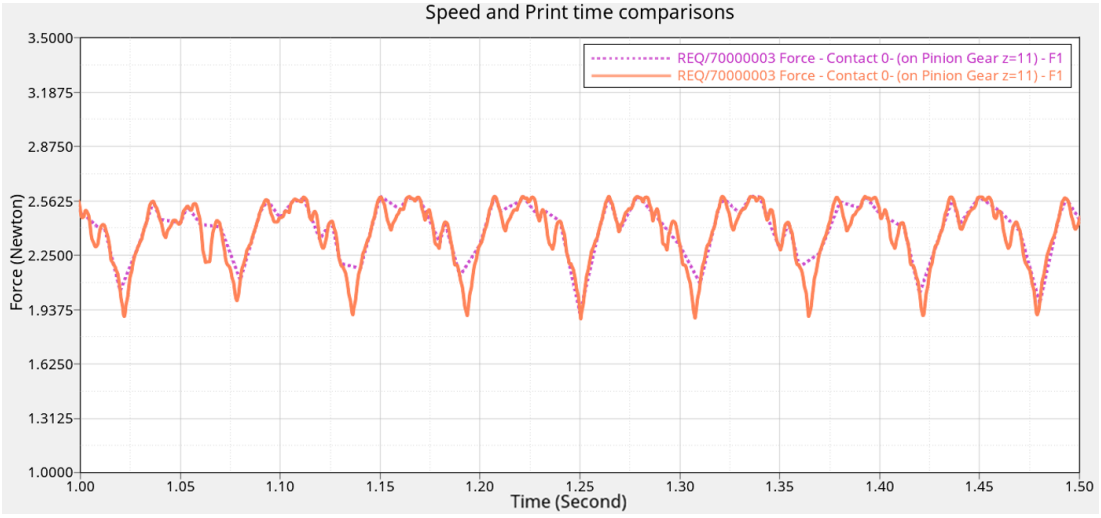



Figure 4.13: Pinion to Crown Wheel Contact Force waves over 0.5 seconds, comparing 10 and 1 ms print times

To continue to check different speeds accuracies 20 rad/sec was also compared at the original 10ms, using 1ms and 0.1 ms print times, 1ms print time again showed a clear increase in accuracy for the force wave for each gear tooth contact, whilst 0.1 ms had minimal effect on the force output. This pattern did not continue at 50 rad/sec though, with again 1 ms providing a more accurate result than 10 ms, although this time the result shown for 0.1 ms proved to provide a further improvement unlike with the other two speeds examined at this stage. This provided further evidence that as the speed increases the print time also required decreasing, to ensure the same level of accuracy. To test the 50rad/sec results further the print time was further reduced by a factor of 10 to 0.01 ms this however led to a significant spike in the computational run time and yielded little to no improvement, as seen previously between 1 ms and 0.1 ms for the lower speeds. All three ideal waves can be seen plotted on the same graph in Figure 4.15,

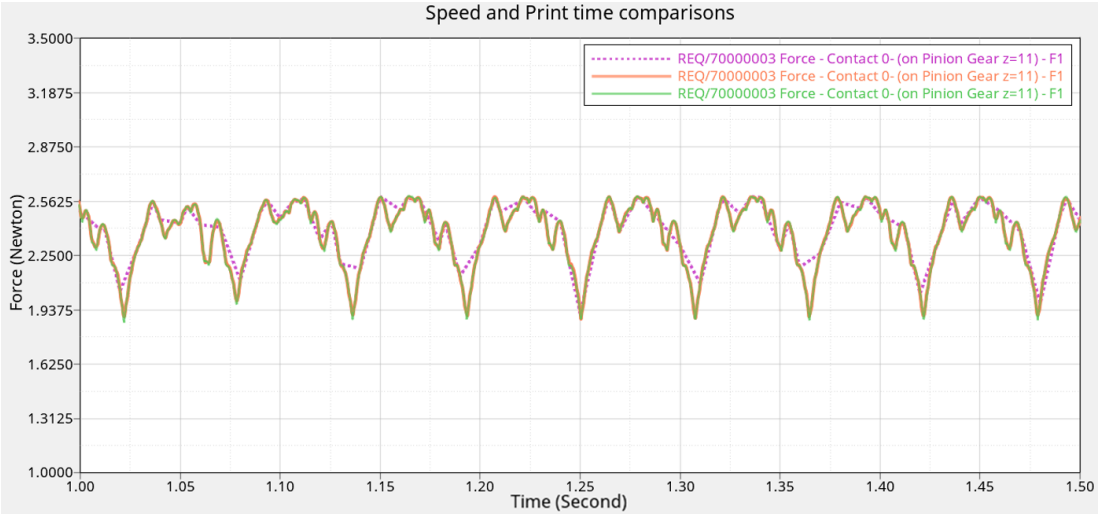



Figure 4.14: Pinion to Crown Wheel Contact Force waves over 0.5 seconds, comparing 10,1 and 0.1 ms print times

the Figure helps to highlight the accurate speed capture of the model with the wavelengths decreasing appropriately in relation to there respective speeds. Another attribute which can be seen is the increase in maximum forces as the speeds are increased, as expected. In addition to this it provides clear learning to what the target wave should like that for all speeds.

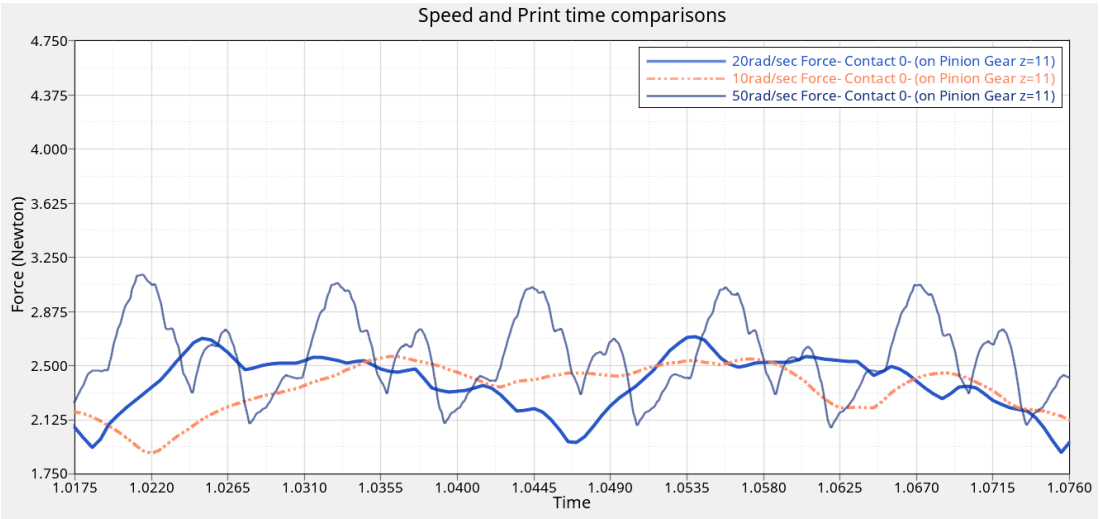



Figure 4.15: Force waves for 10,20 & 50 rad/sec input speeds.

These tests were continued looking at 100 rad/sec and 200 rad/sec motion speed inputs, as mentioned previously at around 100rad/sec results began to become inconsistent with larger fluctuations on the force plots occurring, this is increasingly evident in the plot shown in Figure 4.16 containing 200 rad/sec at 1ms, these large spikes do not appear to be capturing a concise wave for each passing gear tooth as seen with the speeds below it. So as with the speeds tested before, the print time was reduced to 0.1 ms this resulted in the most significant change observed in the plots yet, with the maximum forces seen to half and a concise wave form to be

generated, this improved result is shown in Figure 4.17. This dramatic transition of the orange wave form representing 200 rad/sec input speed seen from Figure4.16 to 4.17, highlights the importance and the effect of adjusting the print time accordingly as the motion speed tested changes.

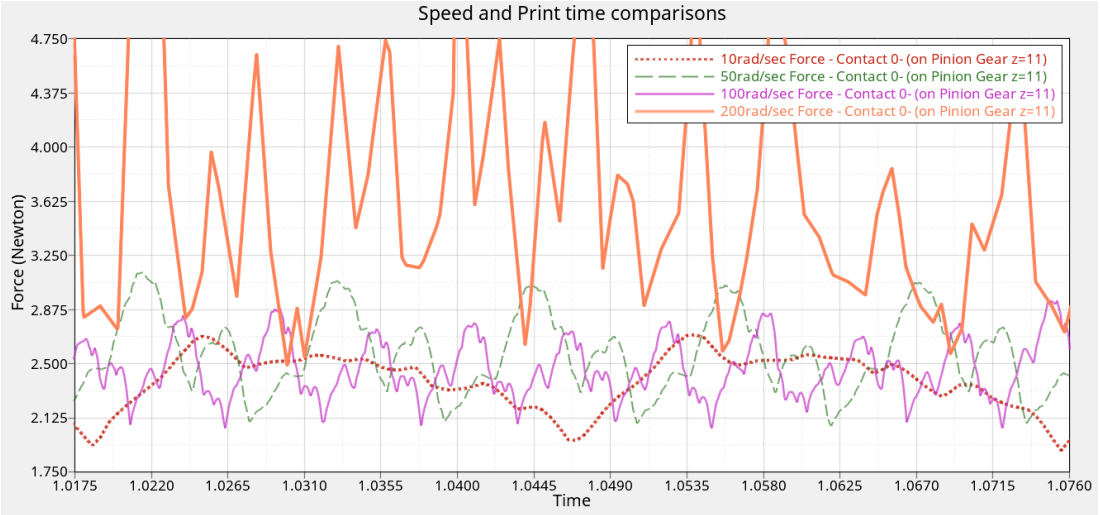



Figure 4.16: Force waves for 10,50,100 & 200 rad/sec input speeds.

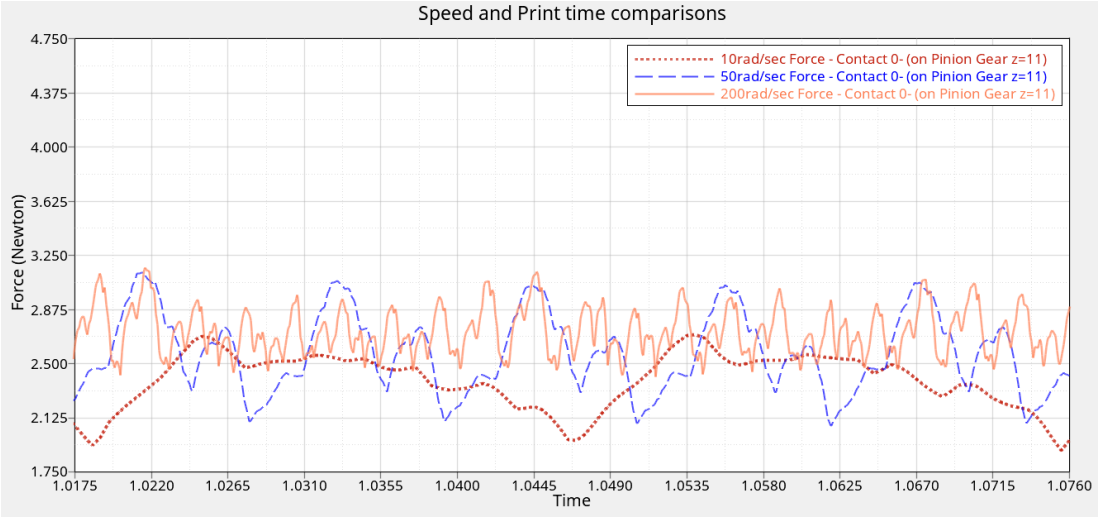



Figure 4.17: Force waves for 10,50 & 200 rad/sec input speeds.

#### 4.2.2.3 Force behaviour reviewed

The change in results following the adjustments of the print times, highlighted already within this section, show how the original set of results, the behaviours were inspected for, were not accurate throughout the full speed range. This was largely due to the fact that the speeds did not have an appropriately sized print time, resulting in loss of accuracy. Therefore, the results were revisited with the newly adjusted print times. Upon examining the forces shown over the full simulation run time, a clear pattern can now be seen, with a clear rise and fall of forces

during the early stages of the simulation before plateauing for the remainder of the set run time. Also, when the velocity of the pinion gear is overlaid, evidence of a clear relationship between the acceleration period and the peak forces can be seen as previously suggested, however previously this behaviour was not as clear and did not present itself across all tested speeds. Figure 4.18, shows the force plots for the full run duration, for a range of input speeds from 10 rad/sec up to 200 rad/sec. Also, overlaid on the graph utilising the second Y-axis is the pinion gear velocity for two of these speeds. This allows the Figure to clearly highlight the relationship between the rise and fall in forces observed up to the one second mark, to the acceleration period of the model. The forces across all speeds tested are then seen to become consistent for the remainder of the run beyond 1second, with readings substantially lower than the peaks observed during the acceleration period.

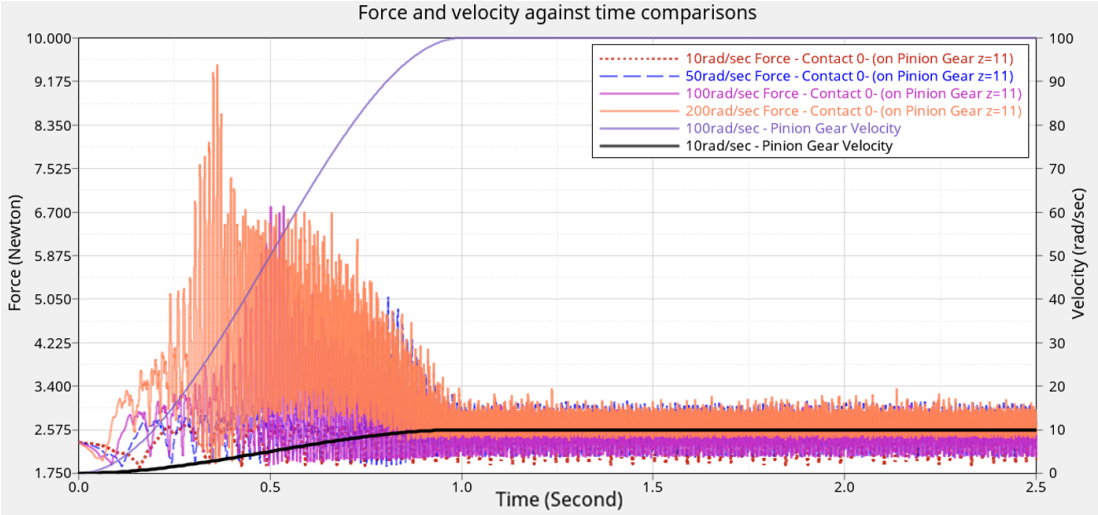



Figure 4.18: Force waves for the full simulation duration, for a range of tested speeds from 10 to 200 rad/sec, supported by the velocity curves of the pinion gear at 10 and 100 rad/sec.

When comparing the force plots for these runs with that seen in Figure 4.10 and 4.11, a clear improvement in the resolution of the results can be seen. These improvements are a result of reducing the print time used in the simulations, due to this the initial study looking at max forces and penetration depths required reinvestigating. To enable a more accurate and representative set of results to be collected. From the investigations within Section 4.2.2.2 and, a new suggested print time of 0.1 ms was given, as this yielded sufficiently accurate results up to 200 rad/sec. Capturing each force wave appropriately and also showing similar behaviours with peak forces during the acceleration period tapering off to a steady set of forces once up to speed. However, the initial study investigated speeds far beyond 200 rad/sec, therefore the effectiveness of a 0.1 ms print time needs to be checked against the highest tested speed of 1,000 rad/sec. The resultant force curves from this simulation can be seen in Figure 4.19, where the pattern seen is consistent with those at lower speeds. Providing evidence that a print time of

0.1 ms is adequate for the max force and penetration depth testing for the desired speed range. Figure 4.19 also includes the speeds of both the pinion gear and bevel gear, showing the effect of the gearing ratio of the differential. Another key feature highlighted by the force plot is the rise and fall of the bevel gear forces which once again coincide with the acceleration period, this rise and fall was not as clear in the lower speeds previously tested, as the forces displayed within the bevel gear secondary contacts are comparatively low.

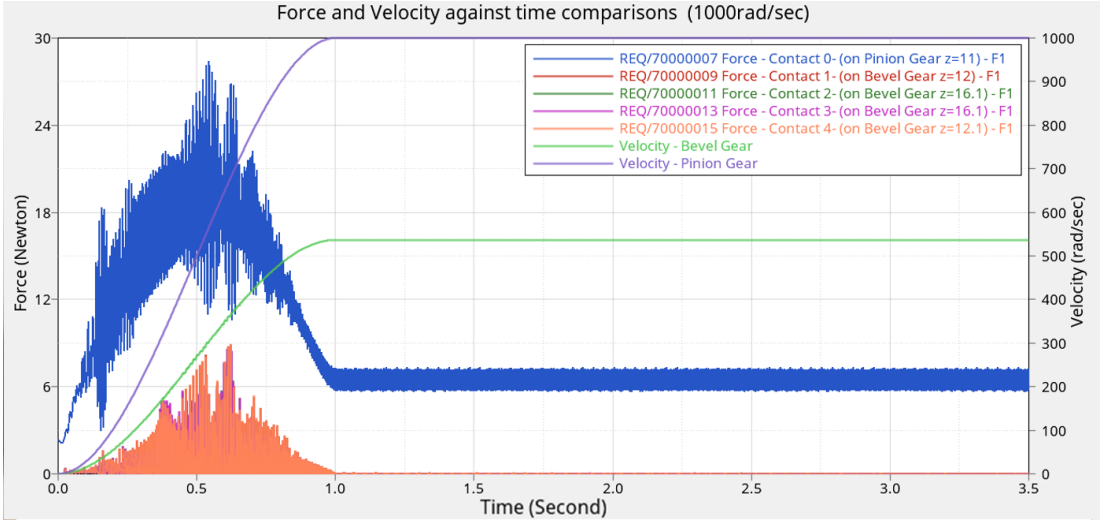



Figure 4.19: Force waves for the full simulation duration, for 1000 rad/sec, supported by the velocity curves of the pinion and bevel gear.

Following confirmation of a 0.1 ms print time, suitability for the full required range of speeds. The maximum force and penetration depths were re-investigated. The simulations were carried out once again and the maximum forces and penetration depths noted. These forces were then plotted against the maximum forces observed when using a 10 ms print time, this can be seen in Figure 4.20. There was a substantial decrease in the maximum forces observed with the decreased print time, with the difference in the two sets of results becoming clearer as the speed increased. The lower speed results remained relatively consistent for both print times, due to the lower speeds the print time was not required to be so small to capture the models behaviour appropriately. The gradient of the trend line is also seen to of decreased with the input speed having less of an effect on the forces observed. The time each maximum is observed has also become a lot more consistent, with the range of times the max force is observed decreasing by over 76.67 %, with all peaks for the 0.2 ms print time occurring within the first second.




Figure 4.20: Plot of maximum forces observed between pinion gear and crown wheel contact at various speeds, for both original and refined print times.

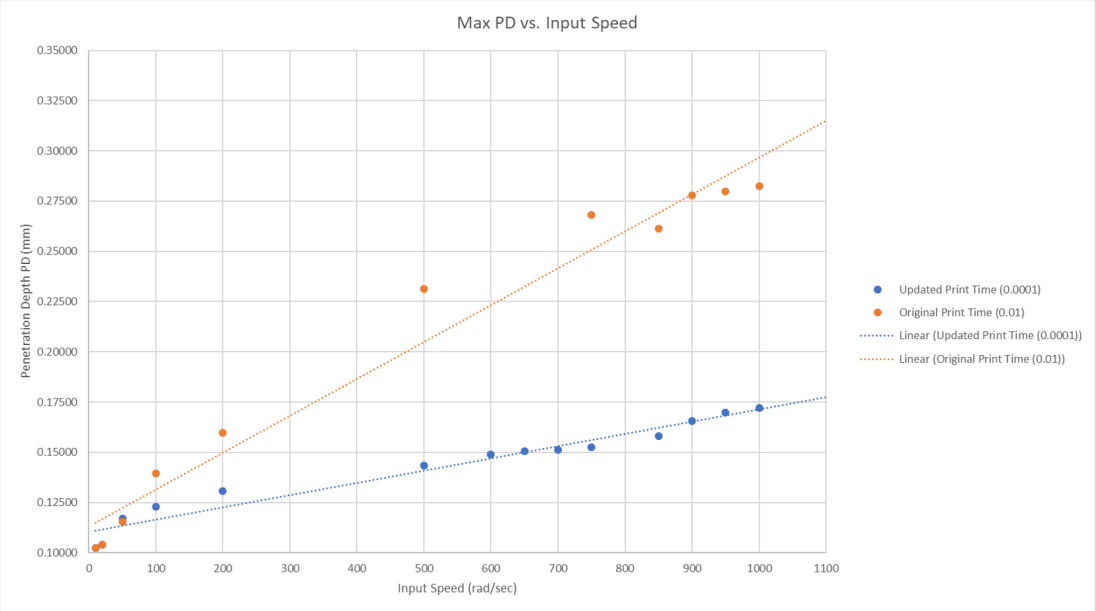



Figure 4.21: Plot of maximum PD's observed between pinion gear and crown wheel contact at various speeds, for both original and refined print times.

The trends seen for the max forces, can also be seen to be repeated in Figure 4.21 displaying the maximum pd's against the various input speeds. Where a substantial decrease in the results is observed, along with a reduction in the gradient of the trend line for the series of results tested with a reduced print time. Also, once again the lower speed points up to 50 rad/sec did not exhibit any significant changes, with the disparity between the two series of results becoming more profound as the input speed is increased as expected.

The most significant improvement from reducing the print time, is seen in the overall capture

of the forces, with a consistent pattern being present for the force plots. In addition to this there is no longer any spiking forces seen in the bevel gear contacts, with all maximum forces for the whole model being present upon the pinion to crown wheel contact. The bevel gear contacts also saw the greatest reduction in forces, the disparity between the two print times results is represented via the trend lines plotted in Figure 4.22. The graph follows a similar pattern to those of the Pinion to crown wheel contact. With the difference in results becoming more distinct as the speed increases, for the same reasons as previously mentioned. The increasing difference drives the trends lines to much steeper gradients than that of its 0.1 ms print time counter parts. However, a couple of points were not utilised to plot the trend lines on the graph, due the fact they were clear anomalies. The points the graph fails to capture include the most severe reduction, at 950 rad/sec with Contact 1 (Bevel Gear z=12 to Bevel Gear z=16) reducing the forces exhibited in the model by 99.99% from 418.9 kN to 13.48 N. Whilst the initial result was incorrect it does highlight how severe of an issue can be caused by not utilising the appropriate time step for the simulation.

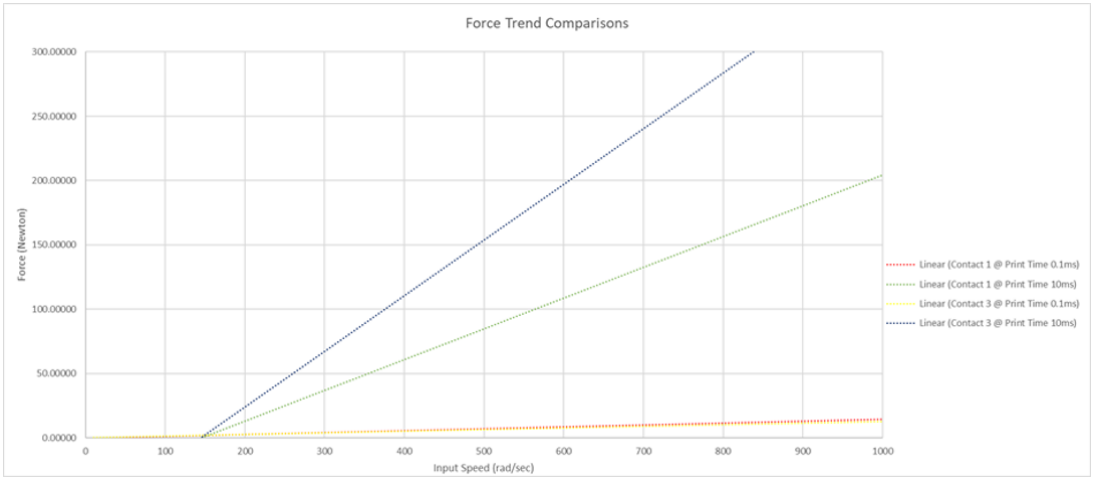



Figure 4.22: Force Trend Comparison for pinion to crown wheel contact (contact 1) and bevel gear contact (contact 3), for 10 ms and 0.1 ms print times.

Concluding these studies, its clear that the maximum forces and penetration depths observed increase as the input speed is increased. The location for these peaks also remains consistent with them occurring during the early acceleration stages of the simulation. This could also be a key factor in the increase in forces as the acceleration period remains consistent across all speeds, therefore leading to a much more severe acceleration for high speeds than those seen for the low speeds. This rise in acceleration for the different speeds is due to the loading method used being a prescribed speed, with the software ramping up to this speed in the shortest time frame possible. An example of the effect of this is the two accelerations speeds for both a 10 rad/sec & 1000 rad/sec speed input, over the one second period, would be 10 rad/sec$^2$ and

1000 rad/sec$^2$. This clearly highlights how large of a factor the acceleration is. One thing that was highlighted from the studies, was that once the acceleration period was over forces became steady, therefore the speed is the main factor controlling these forces. Therefore, these were then investigated to examine if the same level of change was seen when examining the speed differences in isolation, away from the noise generated through the acceleration period.

### 4.2.3 Steady Speed Analysis

As previously highlighted within the maximum forces and penetration depth study, the impact of the speed on the results was clear. However, this coincides with the acceleration period of the models. Due to this the results generated in the previous study were examined further, with the forces exhibited during the steady state region of the simulation being the primary focus. In analysing this region alone, when the speed is constant allowed for a direct impact of motion speed on forces observed to be seen.

As previously highlighted all models tested reach their input speed at approximately one second, this speed then remains constant for the remainder of the simulation. A series of data was extracted for each of the tested speeds, to be able to fully understand how the forces and behaviours observed change as the speed of the model is increased. As the forces for the bevel gear contacts were nominal in comparison to those seen between the pinion gear and crown wheel, denoted as Contact 0 (Pinion Gear z=11 to Crown Wheel z=41, with z denoting the number of gear teeth) was initially monitored for these studies. Within the study four key components of the force waves during their steady speed state were monitored, these consisted of; lowest force, peak force, force wave amplitude and midpoint. The Figures were extracted for a number of tested speeds, with results being generated as an average from results measured from 5 force waves, these can be seen plotted in table 4.4.

A clear spike in the amplitude results can be seen at 750 rad/sec, with the amplitude jumping from 0.69 N to 12.13 N, before returning to 1.32 N at 900 rad/sec. When the force amplitude is plotted against the input speed, its clear that at 750 rad/sec input speed the model is not behaving appropriately and following the general trend laid out by the remaining results. This is seen in Figure 4.23 with the inconsistent result at 750 rad/sec highlighted in red.

| Contact 0 | | | | |
|---|---|---|---|---|
| Pinion to Crown Wheel | | | | |
| Speed | Force Wave Trough Force | Force Wave Peak Force | Force Wave Amplitude | Force Wave Midpoint |
| rad/sec | Newton | Newton | Newton | Newton |
| 10 | 1.87 | 2.60 | 0.73 | 2.24 |
| 20 | 1.89 | 2.70 | 0.81 | 2.30 |
| 50 | 2.06 | 3.08 | 1.02 | 2.57 |
| 100 | 2.03 | 2.91 | 0.88 | 2.47 |
| 200 | 2.41 | 3.08 | 0.67 | 2.75 |
| 500 | 3.58 | 4.27 | 0.69 | 3.93 |
| 750 | 4.64 | 16.77 | 12.13 | 10.71 |
| 900 | 5.32 | 6.64 | 1.32 | 5.98 |
| 950 | 5.47 | 6.88 | 1.41 | 6.175 |
| 1000 | 5.74 | 7.3 | 1.56 | 6.52 |
| 1250 | 6.76 | 8.69 | 1.93 | 7.73 |

Table 4.4: Key features of steady speed force waves for various tested speeds.

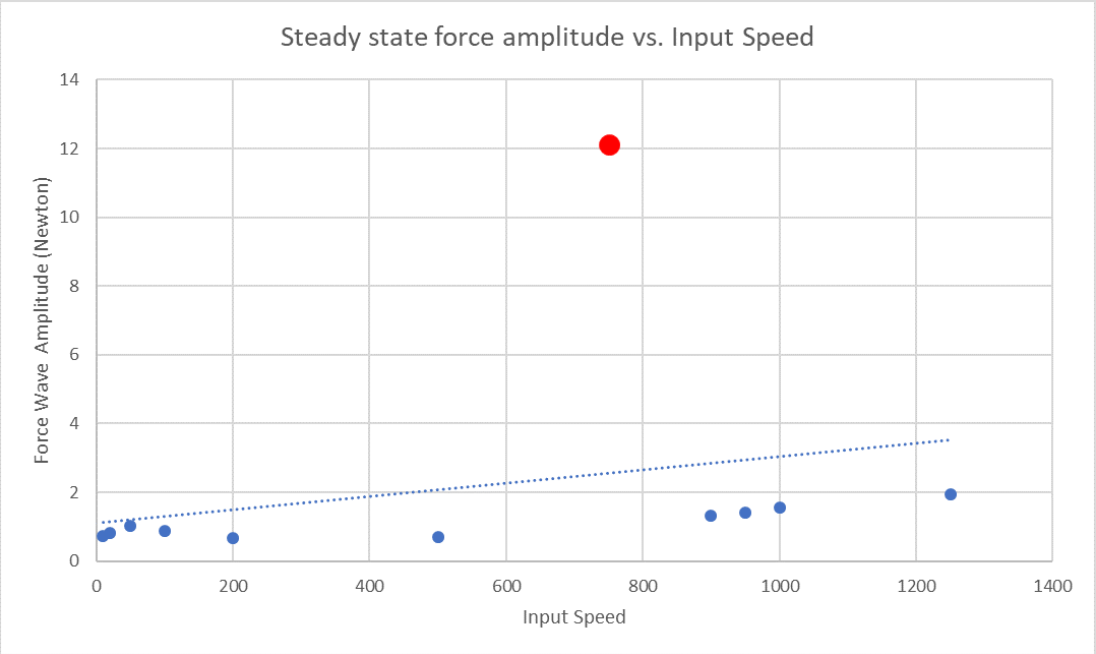



Figure 4.23: Steady state force wave amplitudes, across range of tested speeds. With anomalous result highlighted.

However, when inspecting the 750 rad/sec result for the full simulation duration, it is clear that the behaviours are as expected with a rise and fall during the acceleration period, although unlike the other speeds tested, when the model obtains its prescribed steady speed the forces are comparatively much more significant with a larger amplitude. This difference can be seen in Figure 4.24 , which is comparing the force waves within the steady speed region for a number of the tested input speeds. The figure highlights the issue mentioned with 750 rad/sec force curve being much more prominent than the others. Despite its unexpected increase in amplitude, the wave forms do however remain relatively consistent whilst maintaining the appropriate

wavelength for each passing gear tooth. Figure 4.24 also highlights a clear pattern amongst the other results too, with the midpoint for the force waves becoming higher as the input speed is increased, along with an increase in the force waves amplitude. Providing a clear insight into the models speed affect upon the forces observed within the gear contacts.




Figure 4.24: Force waves for a range of speeds, over a 50ms time frame of the steady speed range.

Whilst these behaviours provide an improved understanding of the effect of the changing operational speed of the differential, they do not provide any indication of what is causing the problem at 750 rad/sec. Therefore, the next step was to conclude if the problem was just an anomaly or affecting a local area of set speeds. As from the results currently obtained it is clear that there are both speeds above and below 750 rad/sec, which are functioning appropriately, under the same conditions. To enable an improved understanding of which speeds are resulting in unexpected results, additional speeds were tested between the two known functioning results of 900 rad/sec and 500 rad/sec. These additional speeds were added to the previous results and can be seen highlighted in table 4.5, the results shown indicate that the problem is not specific to 750 rad/sec, it is acutely covering a range of speeds from 600 rad/sec through to 800 rad/sec, at which point the results are seen to peak before significantly reducing back to follow the same trend as other tested speeds.

| Contact 0 | | | | |
|---|---|---|---|---|
| Pinion to Crown Wheel | | | | |
| Speed | Force Wave Trough Force | Force Wave Peak Force | Force Wave Amplitude | Force Wave Midpoint |
| rad/sec | Newton | Newton | Newton | Newton |
| 10 | 1.87 | 2.60 | 0.73 | 2.24 |
| 20 | 1.89 | 2.70 | 0.81 | 2.30 |
| 50 | 2.06 | 3.08 | 1.02 | 2.57 |
| 100 | 2.03 | 2.91 | 0.88 | 2.47 |
| 200 | 2.41 | 3.08 | 0.67 | 2.75 |
| 500 | 3.58 | 4.27 | 0.69 | 3.93 |
| 550 | 3.78 | 4.57 | 0.79 | 4.175 |
| 600 | 3.89 | 6.74 | 2.85 | 5.315 |
| 650 | 4.16 | 9.25 | 5.09 | 6.705 |
| 700 | 4.25 | 14.25 | 10 | 9.25 |
| 750 | 4.64 | 16.77 | 12.13 | 10.71 |
| 800 | 4.61 | 18.81 | 14.2 | 11.71 |
| 850 | 5.12 | 6.29 | 1.17 | 5.705 |
| 900 | 5.32 | 6.64 | 1.32 | 5.98 |
| 950 | 5.47 | 6.88 | 1.41 | 6.175 |
| 1000 | 5.74 | 7.3 | 1.56 | 6.52 |
| 1250 | 6.76 | 8.69 | 1.93 | 7.73 |

Table 4.5: Key features of steady speed force waves for an extended range of tested speeds.

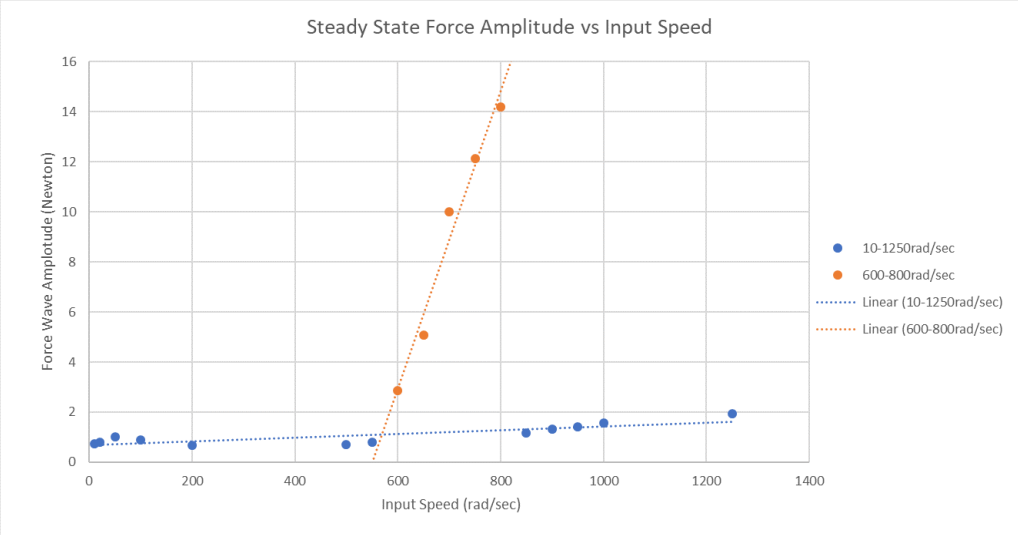



Figure 4.25: Steady speed force wave amplitudes for two series of tested speeds, with corresponding trend lines.

The resultant amplitudes against input speed can be seen plotted upon a graph in Figure 4.25, the results within this graph have been split into two series the first of which is covering all results up to 600 rad/sec and then beyond 800 rad/sec, the second series focussing solely upon the problematic range of 600-800 rad/sec. Both series have their respective trend lines plotted, the trend line for the majority of the results is seen to have a moderate gradient, with the force amplitudes seen increasing as the models speed is increased. The 600-800 speed region however, also displays a prominent consistent trend, with the trend line highlighting a

much more severe gradient. The reasoning for this change in behaviour at the midpoint of the tested speeds is unclear, although it does highlight consistency within the problematic region indicating the problem is not just an anomaly.

To investigate this problem further the remaining bevel gear contacts were further examined across the range of tested input speeds. As a result of the gearing of the system, these gears revolve with an actual speed of approximately 54 % of the input speed. Due to this if the issue is directly speed related then the spike in the results would be expected to shift along, with the new problem range being 1100 rad/sec to 1500 rad/sec (providing 600-800 rad/sec at the bevels.). Which would result in all tested input speeds functioning appropriately apart from 1250 rad/sec. The results were monitored and tracked for each contact, in the same manner as previously carried out for contact 0. They were then plotted upon a graph along with the results from contact 0, the plot is displayed in Figure4.26. From the plot it is clear that the spike in forces remains consistent across all contacts and does not shift as mentioned. This helps to prove that the spike is not directly linked to the speed of the gears. Another feature highlighted by the plot is unlike contact 0, the range between 600 and 800 rad/sec does not show a consistent trend. The forces are instead seen to rise and fall with a less consistent pattern. This lack of continuity is also a feature in the lower speeds with the bevel gear force amplitudes rising and falling, within a much tighter range than that seen between six and eight hundred.

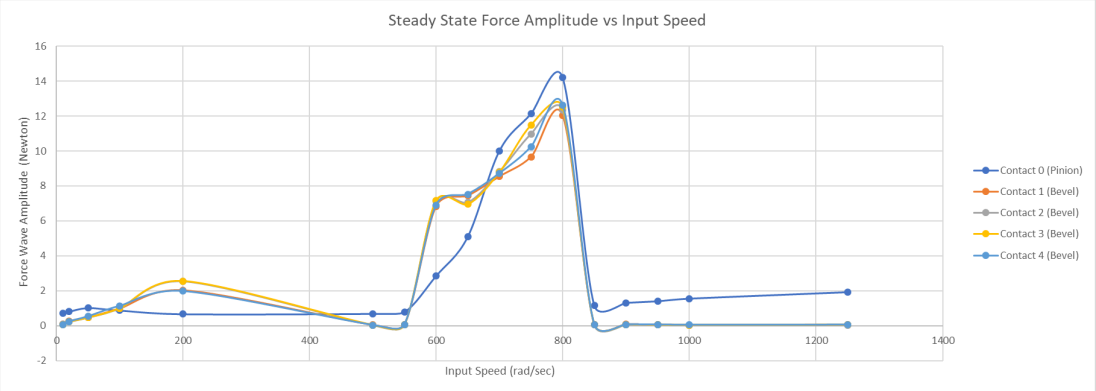



Figure 4.26: Steady speed force wave amplitudes across a wide range of tested speeds, for all gear contacts within the differential.

A final investigation was carried out looking into the steady speed forces, and this was to examine where the mid-point for each speed was and how the input speed affected this feature of the force wave. The investigation was planned to display the same pattern as the amplitude with the input speed increasing the midpoint accordingly. It was also to explore if the average/midpoint forces for speeds between 600 and 800rad/sec, follow the same pattern as the other speeds or continue to amplify across this range. Therefore, confirming whether

it is just the amplitudes of the force waves at these speeds that are inconsistent with the general relationship or other features also. Figure 4.27 displays these results plotted against the operational speed. The spike is seen to occur within the same region as the amplitude results, although the graph does show another clear trend highlighting the input speeds effect on the midpoint for the forces observed under a steady speed loading. Figure 4.28 then shows the series of results split into two portions in the same manner as Figure 4.25, the two trend lines still show a dramatic difference in gradients however the difference is not as significant as that seen when analysing the amplitude of the force wave. This is illustrated by the drop off in value from 800 to 850 rad/sec, the amplitude results decreased by 91.76 %, whereas the midpoint is only seen to decrease by 51.28 %. The remaining bevel contacts when examined also displayed similar behaviours, with all contacts showing a rise in the midpoint of the force waves, the trends however within the secondary bevel contacts is not as clear with a two phase rise seen in Figure 4.26 being exhibited once again. This distortion is most likely a result of the contacts being secondary, therefore not receiving the load in its original smooth state.

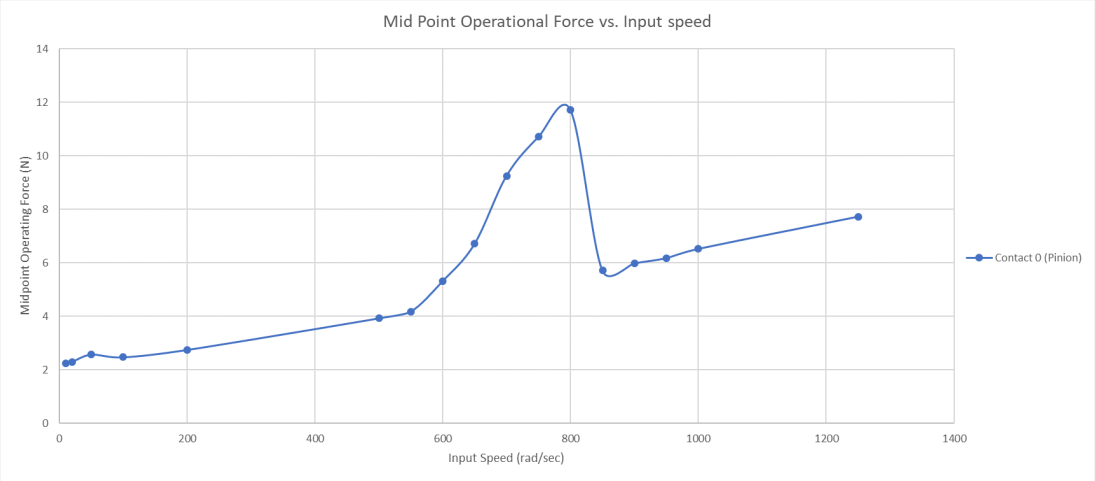



Figure 4.27: Steady speed force wave midpoints across a wide range of tested speeds, for pinion gear to crown wheel contact

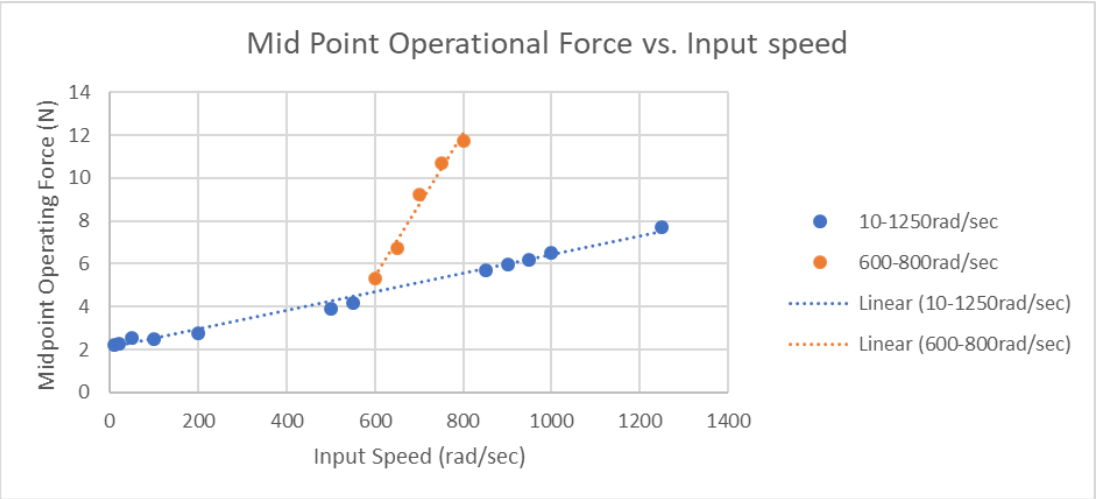



Figure 4.28: Steady speed force wave midpoints for two series of tested speeds, with corresponding trend lines.

Following on from the studies of the steady state speed there is a clear relationship between the speed of the model and the forces it experiences. This relationship is illustrated clearly within Figure 4.29, with the increasing speed moving the average forces observed upwards and increasing the amplitude of the force waves seen. However, the most significant outcome from the studies is highlighting that the speed range of 600-800 rad/sec does not function appropriately. Therefore, this region requires further analysis and investigations to clarify what is causing the spike in the steady speed forces. As the maximum forces from the previous section for these speeds remained consistent with any trends noted.

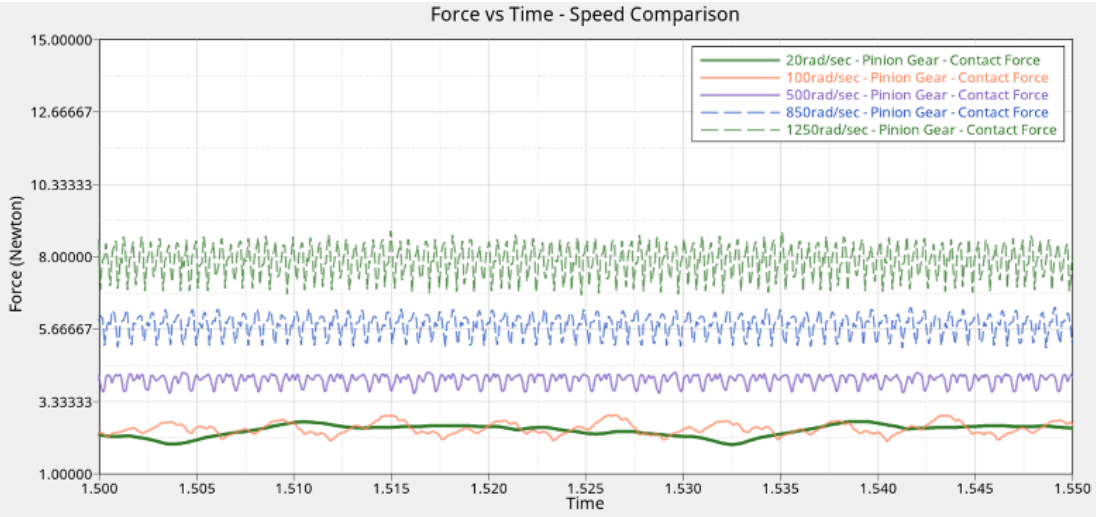



Figure 4.29: Force waves for a range of speeds, over a 50 ms time frame of the steady speed range.

## 4.3 Timing Studies

From the previous investigations and tracking of the models a number of CPU run time factors were seen which were not fully captured when originally investigated. Also, the data collected throughout the runs was not consistent for comparing CPU run times, as whilst the set up and number of threads for each run was consistent, other factors changed. For example, some runs were executed simultaneously which will decrease the available CPU power increasing the run times.

The key areas highlighted for further investigation include;

- The consistency of model run time.
- Input speed effect on CPU run time.
- The print times effect on CPU run time.
- How different inputs and outputs effect the run time.
- CPU powers affect on run time.

#### 4.3.0.1 CPU run time consistency

Starting with an initial investigation to establish the reliability of the CPU run times being recorded throughout these timing studies. This will allow for a percentage error to be calculated, which can be utilised for results going forward. The study utilised a model set up with an input speed of 10 ad/sec with a selected print time of 1 ms. The model was run five times with all run times recorded. This was also repeated for an input of 1000 rad/sec with a print time of 0.1 ms. The results from the repeated runs were then tracked for changes in behaviour and to examine if the results and times remain consistent at both high and low speeds. The timings recorded, along with the key features and variations for the tested speeds can be seen in tables 4.6 through to 4.8. From these it is clear that variations in the CPU run time occur, when carrying out repeat versions of the simulations. Therefore, this variation can be considered in other studies if required. The results from this show a variation in the CPU run times of between 16 and 97 seconds, providing percentage errors of 10 % or lower. The larger percentage error seen for the 10 rad/sec study is due to the comparatively shorter run time. Aside from the timings for these simulations, the results were also checked to ensure the accuracy of the results. When checking these, identical max forces were seen, and visually there was no differentiation in the force waves across the whole simulation for both tested speeds. This leads to the overall conclusion from these runs, being that the current method of running the simulations yields

results which remain consistent throughout, whilst only experiencing mild fluctuations in CPU run time.

| Time Variation Study | |
|---|---|
| Run Number | CPU Run Time |
| Input Speed 10 rad/sec | Seconds |
| 1 | 114.4 |
| 2 | 109.1 |
| 3 | 98.05 |
| 4 | 97.89 |
| 5 | 101.00 |

Table 4.6: Repeat run timings for 10 rad/sec input speed.

| Time Variation Study | |
|---|---|
| Run Number | CPU Run Time |
| Input Speed 1000 rad/sec | Seconds |
| 1 | 1093 |
| 2 | 1108 |
| 3 | 1151 |
| 4 | 1112 |
| 5 | 1054 |

Table 4.7: Repeat run timings for 1000 rad/sec input speed.

| | CPU Time | | | | |
|---|---|---|---|---|---|
| Input Speed | Midpoint | Max Value | Min Value | Variation | Percentage Error |
| Rad/Sec | Seconds | Seconds | Seconds | Seconds | % |
| 10 | 106.15 | 118.40 | 97.89 | 16.51 | 10.03 |
| 1000 | 1102.50 | 1151.00 | 1054.00 | 97.00 | 4.40 |

Table 4.8: Key timings attributes and variations at 10 and 1000 rad/sec

#### 4.3.0.2 Input Speed effect on CPU time.

Speeds effect on the CPU run time has been previously covered within Section 4.3.0.2, however following the latter investigations, the results seen in this earlier section, are now known not to be accurate throughout; due to the print time selected not being suitable for all of the speeds tested. Therefore, an additional series of runs were executed, ensuring all controllable factors

remained consistent, with a print time of 0.1 ms being selected and a run time of 1.75 seconds, with the speed being the only variable. The resultant times can be seen plotted within table 4.9. The result shows a linear change as the speed increases, this is a result of the input speed increasing the forces observed and the larger forces requiring longer for the solver to calculate. This also further emphasises the importance of the print time and its limiting factor on reducing CPU run time for runs including higher speeds. The behaviour seen in the initial Figure from Section , also shows the input speed increasing the CPU time.However, the results from these earlier runs do not accurately capture the forces, with only the lower speeds up to 200 rad/sec from these earlier studies being useable. Therefore, the effect of the input speed on the run time, is dependent on the print time selected, as if the print time is reduced to a low level to aid result accuracy this then becomes the driving factor of the CPU run times.

| Input Speed | CPU Run Time |
|---|---|
| Rad/Sec | Seconds |
| 10 | 152 |
| 20 | 165 |
| 50 | 218 |
| 100 | 204 |
| 200 | 364 |
| 500 | 558 |
| 600 | 612 |
| 700 | 722 |
| 800 | 652 |
| 900 | 782 |
| 1000 | 1108 |

Table 4.9: Input speeds effect on CPU run time, with refined print time of 0.1 ms

#### 4.3.0.3 Print times effect upon CPU run times.

The print times effect on CPU run time, was also initially discussed within Section 4.3.0.2, however the previous investigation into this showed no clear impact on CPU run time from adjusting the print time. This is evident from Figure 4.5. However, in consequent runs a rise in run time was seen as a result of adjusting print time. Also, in the study into speeds effect on CPU time, it was shown that the lower print times required to obtain accurate results becomes the limiting factor for the CPU run time, highlighting their importance. Due to these factors it was clear the initial print time step study didnt go far enough to capture an effect on CPU

time. Therefore, the study was revisited, with all runs being executed again to ensure no other variables are affecting the resultant CPU run time. Print times tested for this version extended the range from 150 ms to 1 ms, down to 0.1 ms. The speed utilised for the study was 100rad/sec with a run time of 3.5 seconds. The selected print times and their corresponding run times can be seen in table 4.10, these results have then been plotted on to a graph shown in Figure 4.30.

| Print Time | CPU Run Time |
|---|---|
| Millisecond | Second |
| 150.0 | 164.3 |
| 100.0 | 173.9 |
| 50.0 | 176.5 |
| 10.0 | 164.0 |
| 5.0 | 164.9 |
| 1.0 | 166.1 |
| 0.8 | 196.7 |
| 0.6 | 216.6 |
| 0.4 | 281.2 |
| 0.2 | 444.8 |
| 0.1 | 847.5 |

Table 4.10: Print Times effect on CPU run time, at set input speed of 100 rad/sec

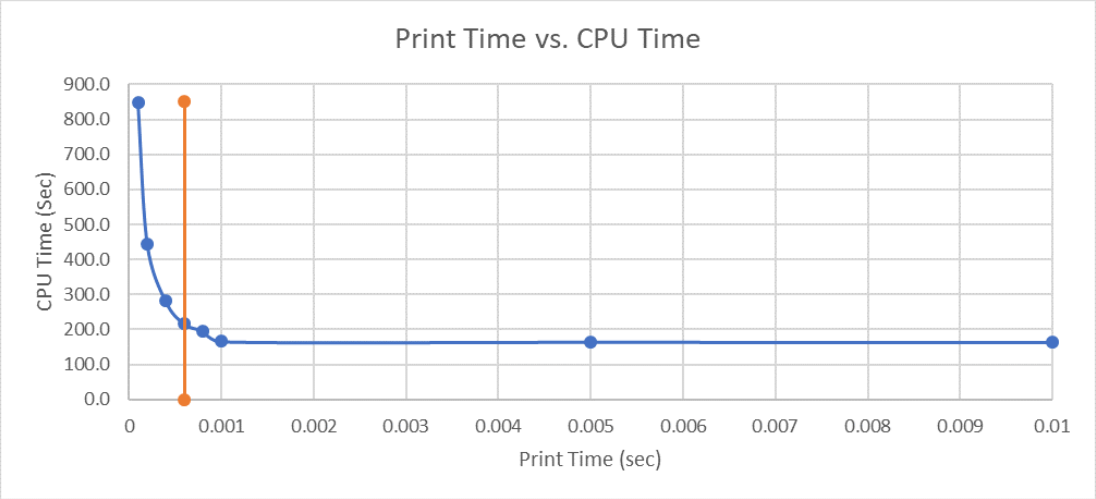



Figure 4.30: Varying print times, plotted against there corresponding CPU times at 100 rad/sec.

The plot in Figure 4.30 shows that throughout the original testing period the results remain constant, with a CPU run time change of less than two seconds. However, when the print time is decreased beyond 1ms, the times are seen to rise exponentially. The exponential increase of

the run time against print time, indicates that during the larger print times ($T_p$>0.001 )the print time is not the limiting factor for the CPU run time, and another aspect of the simulation is capping the run time around the same point. Although beyond this point the CPU run times begin to rise rapidly. Showing how significant of an effect the selected print time has on the run time. Another aspect of this study is to observe at which point the selected print time delivers a desirable sufficiently accurate result, as this will allow a better indication of which region of the curve, accurate usable results sit. If they fall within the sharp rise of the exponential curve, then the selection of the print time will become paramount in achieving a realistic run time for the entire simulation. Therefore, the two key features of the curve being targeted, included, checking for the expected pattern of a rise and fall in forces alongside the acceleration of the model and then the forces tapering to a constant steady range once the model was at speed. Both of which were previously highlighted within Section 4.2.2.3.

When inspecting the force results for these key behaviours at the various print times, it was clear that at 0.6 ms these traits became clear indicating an accurate result. Consequently, with each further decrease in print time the wave pattern observed for each passing gear tooth, became clearer. Although the accuracy displayed at 0.6 ms is sufficient, however due to 0.8ms improved accuracy over 0.6 ms a middle point may be the ideal solution for this particular input speed. The effect of the two print times on accuracy can be seen in Figures 4.31 and 4.32 where they are compared to the most accurate result recorded at 0.1 ms.

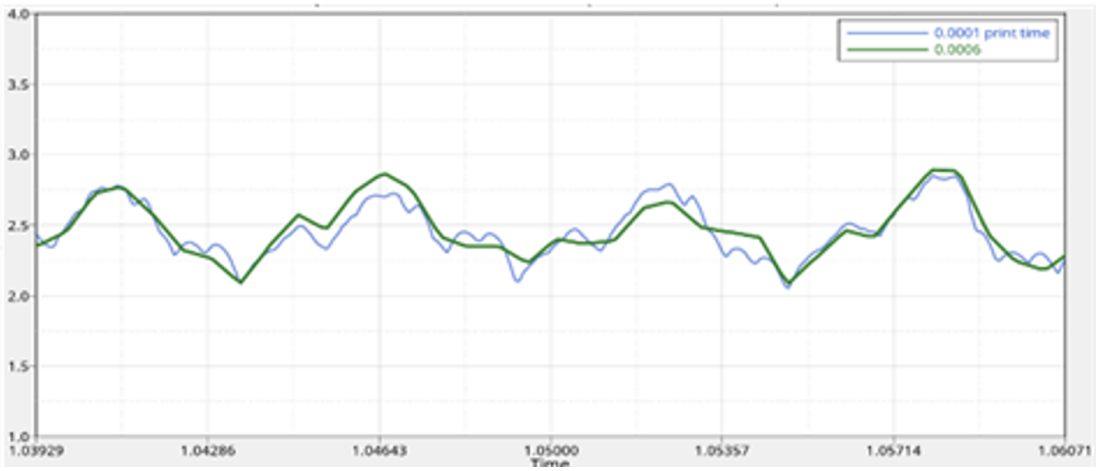



Figure 4.31: Force wave accuracy comparison between force wave generated at 0.6 ms and 0.1 ms print times.

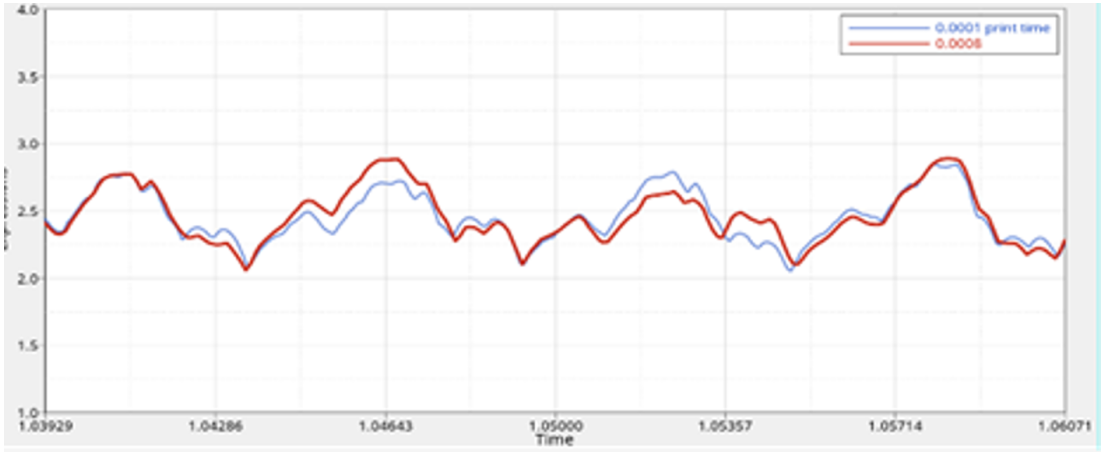



Figure 4.32: Force wave accuracy comparison between force wave generated at 0.8 ms and 0.1 ms print times.

However, when examining the effect on the accuracy in the opposite direction, with the print time increasing. At 0.8 ms the curve observes the expected pattern of rising and falling before becoming constant, although the waves seen begin to become slightly distorted. This issue continues to get worse as the print time increases, with random fluctuations beginning to occur, which would interfere with results when inspecting for fluctuations as a result of the input. This transition in accuracy as a result of the print time is illustrated in Figure 4.33, with the two extremes of the study being compared. It is evident how the higher print time of 150 ms is un-usable for any future work. However, the accurate 0.1 ms result is much more computationally expensive. Illustrating the need to find a mid-point in which both accuracy and time requirements can be satisfied.

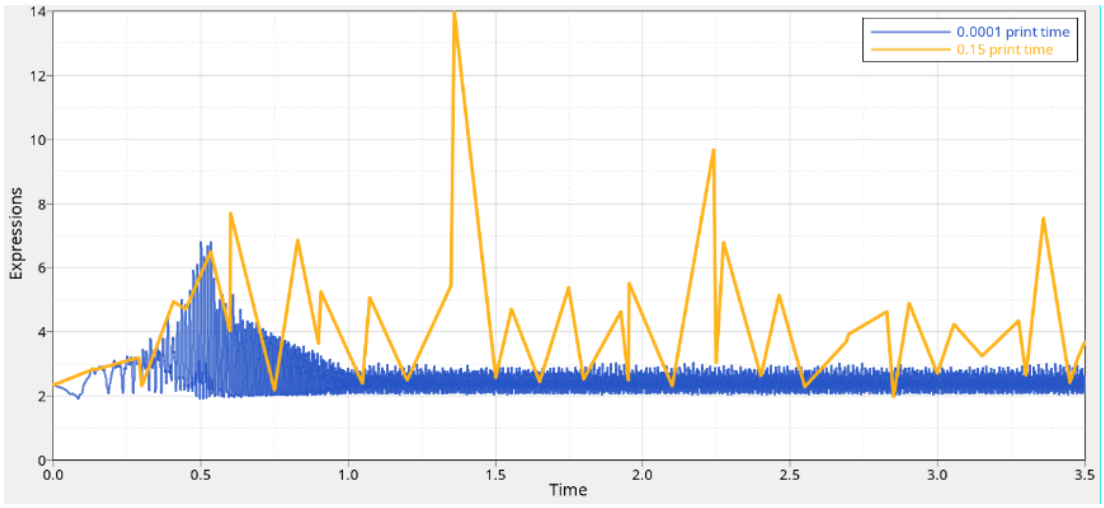



Figure 4.33: Force wave accuracy comparison between force wave generated at 15 ms and 0.1 ms print times. Highlighting disparity in accuracy at tested print time extremities.

From this study it is clear that print times of <0.001, have a significant impact upon the CPU run time of the model. Whereas those greater than this have their CPU run times limited

by other factors. Also, the cut off point for accurate/usable results is highlighted by the red line within Figure 4.30, which sits within the sharp rise of the exponential curve. This highlights the need to ensure the appropriate print time is selected as slight changes of the print time within this region lead to significant CPU run time changes to comparatively small adjustments in the result accuracy.

- How different inputs and outputs effect the run time.
- CPU powers effect on run time

#### 4.3.0.4 Print Time Accuracy Investigations.

As highlighted within the print time step study, the relationship between print time and CPU run time is exponential. Therefore, making the appropriate print time selection is paramount in being able to develop a model which can operate within a reasonable time frame. To begin to understand the results and which print time yields appropriate results for each input speed, the models were ran at a range of print times for each speed, with each result being analysed to examine how accurate the result was and whether it was deemed sufficiently accurate to be utilised in future work. All runs were carried out for a 1.75 second run time, as this will allow enough time for the initial acceleration behaviour to be observed and a period of steady speed to also be checked. The results were inspected in the same manner as the previous Section 4.3.0.3, with the rise and fall being checked, followed by the steady speed force waves. The first two speeds investigated included the original 10 rad/sec and the previously examined 100 rad/sec. The visual evaluation of these results for each print time can be seen in tables 4.11 & 4.12

| Print Time Study,10 rad/sec | | |
|---|---|---|
| Print Time | CPU Run Time | Output Quality |
| MilliSeconds | Second | |
| 10.00 | 67.0 | Bad |
| 8.00 | 67.0 | Acceptable |
| 6.00 | 61.0 | Acceptable |
| 4.00 | 66.0 | Good |
| 2.00 | 55.0 | Good |
| 1.00 | 56.0 | Good |

Table 4.11: CPU run times and corresponding result quality for various tested print times, at 10 rad/sec input speed.

| Print Time Study,100 rad/sec | | |
|---|---|---|
| Print Time | CPU Run Time | Output Quality |
| MilliSeconds | Second | |
| 10.00 | 164.0 | Un-Usable |
| 5.00 | 164.9 | Bad |
| 1.00 | 166.1 | Bad |
| 0.80 | 196.7 | Acceptable |
| 0.60 | 216.6 | Good |
| 0.40 | 281.2 | Good |
| 0.20 | 444.8 | Good |
| 0.10 | 847.5 | Good |

Table 4.12: CPU run times and corresponding result quality for various tested print times, at 100 rad/sec input speed.

From the first two results it is clear that the size of the print time has no significant effect upon the 10 rad/sec timings ,however, as the speed is increased to 100 rad/sec and a reduced print time is required to fully capture the forces occurring within the model, the CPU time is seen to be significantly affected, this is a result of something previously mentioned, in the fact that at the larger print times used for the lower speed, the print time is not the limiting factor. Therefore, the penalty of decreasing the print time to aid accuracy is not present. The investigation was continued over additional speeds to allow for an improved overview of accuracy of results, based on print time selected. Tables 4.13 through to 4.16 contain results for 50,200,500 and 1000 rad/sec input speeds, respectively.

| Print Time Study,50 rad/sec | | |
|---|---|---|
| Print Time | CPU Run Time | Output Quality |
| MilliSeconds | Second | |
| 2.00 | 76.40 | Bad |
| 1.40 | 134.30 | Acceptable |
| 1.20 | 134.00 | Acceptable |
| 1.00 | 85.20 | Good |
| 0.80 | 83.50 | Good |
| 0.60 | 102.20 | Good |
| 0.40 | 153.00 | Good |
| 0.20 | 304.7 | Good |
| 0.10 | 498.00 | Good |

Table 4.13: CPU run times and corresponding result quality for various tested print times, at 50 rad/sec input speed.

| Print Time Study,200 rad/sec | | |
|---|---|---|
| Print Time | CPU Run Time | Output Quality |
| MilliSeconds | Second | |
| 1.00 | 121.00 | Bad |
| 0.80 | 126.00 | Bad |
| 0.60 | 129.00 | Acceptable |
| 0.40 | 170.50 | Good |
| 0.20 | 254.8 | Good |
| 0.10 | 478.30 | Good |

Table 4.14: CPU run times and corresponding result quality for various tested print times, at 200 rad/sec input speed.

| Print Time Study,500 rad/sec | | |
|---|---|---|
| Print Time | CPU Run Time | Output Quality |
| MilliSeconds | Second | |
| 1.00 | 217.00 | Un-Usable |
| 0.80 | 214.00 | Un-Usable |
| 0.60 | 207.00 | Un-Usable |
| 0.40 | 197.00 | Bad |
| 0.20 | 324.00 | Acceptable |
| 0.18 | 403.40 | Good |
| 0.16 | 442.80 | Good |
| 0.14 | 479.20 | Good |
| 0.12 | 542.00 | Good |
| 0.10 | 612.10 | Good |

Table 4.15: CPU run times and corresponding result quality for various tested print times, at 500 rad/sec input speed.

| Print Time Study,1000 rad/sec | | |
|---|---|---|
| Print Time | CPU Run Time | Output Quality |
| MilliSeconds | Second | |
| 0.40 | 323.20 | Un-Usable |
| 0.35 | 273.40 | Un-Usable |
| 0.30 | 285.00 | Bad |
| 0.25 | 312.60 | Acceptable |
| 0.20 | 367.50 | Good |
| 0.15 | 442.00 | Good |
| 0.10 | 594.30 | Good |
| 0.08 | 979.20 | Good |
| 0.06 | 1060.00 | Good |

Table 4.16: CPU run times and corresponding result quality for various tested print times, at 1000 rad/sec input speed.

The times seen in all tables show a sharp rise in CPU time as the decreases. Although a couple of behaviours can be seen in all results. The first of which is there are no significant changes seen to the CPU run time occurring with print times above 0.5 ms, the results indicate that until the print time is reduced below this point the CPU run time is relatively unaffected

by its changes. This sharp rise in CPU run times beyond 0.5 ms print time was also seen in Figure 4.30. The second behaviour which appears primarily in the higher speed tests, where the vast majority of print times tested are below 0.5 ms. Is a slight rise in CPU run time for the higher print times which yield un-usable results. This is most likely a result of the un-usable result containing larger spiking forces which are more computationally complex to solve, hence the slight rise in time.

From the results particularly the higher speed versions, the judgement on the accuracy of the results was split into two sections, with the first stage being the general pattern of the contact forces, the second part was the accuracy of the individual force waves for each passing tooth, naturally the larger forces across a shorter wave length seen for the higher speeds require a much lower print time to generate the same number of points per force wave, to deliver the same perceived level of accuracy. Due to this a set of theoretical work was also carried out to help select print times for specific input speeds, this data will then be usable to develop a print time expression, which can adapt to the input speed when utilising a variable input to try to ensure an optimum CPU run time, as opposed to using a blanket print time selected from the highest test speed. Which will in turn drive the entire run time up substantially in areas where that particular level of accuracy is not required or beneficial. Another consideration that must be made when selecting an appropriate print time or developing an expression is the fact that the forces seen during the lower speeds are comparatively small and will most likely not be the key areas of concern in the consequent stages of the e-axle investigation.

To begin the theoretical calculations, calculations were carried out based on the number of recorded output points for each passing gear tooth. So, continuing to focus on the contact between the pinion and the crown wheel. The number of teeth on the pinion gear is known to be 11. The input speed then required converting from rad/sec to the number of revolutions per second. This was done using equation 4.2 below. Equation 4.3 was then utilised to establish the force wavelength when at constant speed, from the known data, with the wavelength being representative of each passing gear tooth.

$$\frac{V_{rad/sec}}{2/\pi} = V_{rev/sec} \tag{4.2}$$

$\lambda -$ Force Wavelength, $N_t -$ Number of teeth on pinion gear, $V -$ Input Speed (rev/sec)

$$\lambda = \frac{1}{N_t * V} \tag{4.3}$$

With the wavelength now calculated it can be used to explore the relationship between the

number of sample points per force wave/passing gear tooth and the print time selected.

$$T_p - \text{Print Time} \qquad N_s - \text{Sample Number}$$
$$T_p = \frac{\lambda}{N_s} \tag{4.4}$$

The aim is to find a sample number ($N_s$) that can be utilised as a constant value for all different speeds, to ensure all force curves recorded have the same number of points and therefore the same level of accuracy. Therefore equation 4.4 can then be simply used to provide a suggested print time based on the input velocity. This method was trialled to examine the outcome and compare the results from this theoretical method with that of the visual inspections of the results. The initial trial run was executed based upon the 10 rad/sec example. As the visually inspected suggested print time for this input speed was 4ms. Therefore, by utilising the above equations a suggested sample number ($N_s$ ) could be found, and in turn used to generate theoretical optimum print times for other input speeds.

$$\frac{1}{N_t * \frac{V}{2\pi}} = \frac{1}{11} * \frac{10}{2\pi} = 57.12ms$$
$$N_s = \frac{\lambda}{T_p} = \frac{57.12e^{-3}}{4e^{-3}} = 14.28 \tag{4.5}$$

The sample number for an input speed of 10rad/sec with a print time of 4ms is found to be 14.28. The maths to calculate this can be seen above in equations 4.5. Although to draw a comparison on suggested sample numbers, the same calculation was carried out based on the best visually selected print time at 100 rad/sec, which was 0.7ms. In the hope that a comparable sample number would be highlighted, giving evidence that the theoretical method would function based on a predefined sample number ($N_s$).

$$\frac{1}{N_t * \frac{V}{2\pi}} = \frac{1}{11} * \frac{10}{2\pi} = 57.12ms$$
$$N_s = \frac{\lambda}{T_p} = \frac{57.12e^{-3}}{4e^{-3}} = 14.28 \tag{4.6}$$

The resultant sample number from the calculation shown in equation 4.6, equated to 8.16, which is considerably different to the value suggested by inspecting the 10rad/sec result. This is most likely due to the fact that sample points have a more visible effect upon the longer wavelengths at lower speeds and may not actually be required for overall accuracy, also as mentioned previously the larger range in forces seen for the higher speeds in combination with the decreased force wave length, will also cause imperfections due to a lower sample number to be less apparent.

The suggested number of sample points ($N_s$) were then used to calculate a suggested print times, with the 10rad/sec 14.28 sample point resulting in a print time of 0.4 ms for 100 rad/sec.

Which when referring to the results in table 4.12, display a more accurate result than that previously selected at 0.7ms, however the run time is 281.2 seconds approximately 40% longer than the visually selected optimum. In the opposite direction using the 100rad/sec suggested sample number ($N_s$) of 8.16 to calculate an equivalent print time for 10 rad/sec. The print time would be 7ms, which when checked in table 4.11 falls within the Acceptable region showing a moderate level of accuracy. Continuing to inspect the suggested print time values for an extended range of input speeds, using the two initially calculated sample point numbers ($N_s$), results in suggested print times shown in table4.17, when using the 10 rad/sec, $N_s$-14.28, with table 4.18 displaying suggested print times when using the 100 rad/sec, $N_s$-8.16.

| Force wave desired sample number - 14.28 | |
|---|---|
| Input Speed (rad/sec) | Suggested Print Times (Milliseconds) |
| 10 | 4.00 |
| 50 | 0.80 |
| 100 | 0.40 |
| 200 | 0.20 |
| 500 | 0.08 |
| 1000 | 0.04 |

Table 4.17: Suggested print times at various input speeds, for set number of sample points per force wave, determined from 10 rad/sec inspected result.

| Force wave desired sample number - 8.16 | |
|---|---|
| Input Speed (rad/sec) | Suggested Print Times (Milliseconds) |
| 10 | 7.00 |
| 50 | 1.40 |
| 100 | 0.70 |
| 200 | 0.35 |
| 500 | 0.14 |
| 1000 | 0.07 |

Table 4.18: Suggested print times at various input speeds, for set number of sample points per force wave, determined from 100 rad/sec inspected result.

Immediately from the suggested print times, it is clear that a sample number as high as 14.28, equates to, a print time that is too low at higher speeds, to yield time efficient results. With a suggested value of 0.04 ms for 1000 rad/sec, this will sit within the sharpest rise of the exponential curve of the print time against CPU time and from the already known results

and timings, this will take in excess of 1060 seconds. In addition from the results already visually inspected a value of 0.2 ms is suggested to provide sufficient accuracy, whilst also saving approximately 65 % CPU run time over 0.06 ms. As a result of the discovery that the two initially selected sample points lead to such low print times for higher speeds, and therefore increased CPU run times. The visual results for 10 rad/sec input speed were re-analysed, as a result of this a new suggested print time for 10 rad/sec was obtained. With a new value of 8ms suggested, as opposed to the original 4ms. The visual force wave results when compared in Figure 4.34, still result in the same peaks and troughs with the general wave form consistent, although the 4 ms version naturally captured additional details for each wave. Satisfied with the result seen from 8ms print time at 10rad/sec, a new suggested sample number of 7.14 was calculated within equation 4.7.

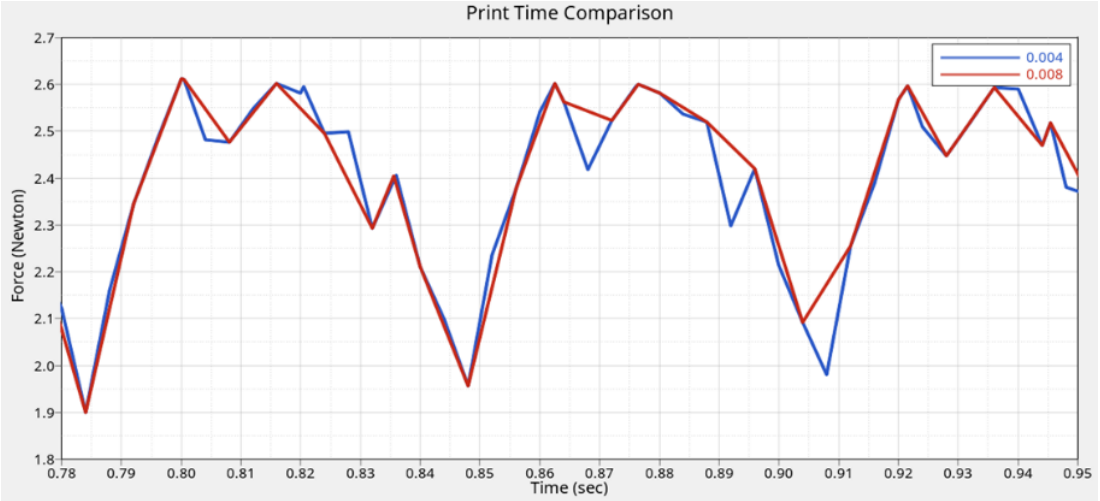



Figure 4.34: Force wave accuracy comparison between force wave generated at 0.8 ms and 0.4 ms print times, for 10 rad/sec input speed.

$$\begin{aligned} \frac{1}{N_t * \frac{V}{2\pi}} &= \frac{1}{11} * \frac{10}{2\pi} = 57.12ms \\ N_s = \frac{\lambda}{T_p} &= \frac{57.12e^{-3}}{8e^{-3}} = 7.14 \end{aligned} \tag{4.7}$$

The approach of utilising the suggested visual result from the top speed tested, to suggest print times for lower speeds was previously mentione; Whereby if the accuracy is satisfactory at the highest speed, where the forces are more significant then this would be a good indication of the sample number needed, and therefore the print times required for other speeds. Also this would enable comparisons between the sample numbers of 10,100 and 1000 rad/sec. The 1000 rad/sec with a visually selected print time of 0.1 ms, resulted in a sample number of 5.712, which was calculated within equation 4.8.

$$\frac{1}{N_t * \frac{V}{2\pi}} = \frac{1}{11} * \frac{1000}{2\pi} = 0.5712ms$$
$$N_s = \frac{\lambda}{T_p} = \frac{5.712e^{-4}}{1e^{-4}} = 5.712 \tag{4.8}$$

Input speed 1000 rad/sec calculated sample number of 5.712, results in the revised 10 rad/sec value being located between the 100 and 1000 suggested points. Therefore, it was hoped to deliver a good level of accuracy whilst maintaining a workable run time for the vast majority of speeds. Although it is important to consider a high run time will always be expected at high speed, due to the fact any of the suggested print times where its results are seen to be accurate, require a print time within the sharp rise of the exponential curve relationship between print time and CPU time.

The additional two suggested print times from 1000 rad/sec and 10 rad/sec (revisited), were used to calculate theoretical print times. Which are seen within tables 4.19 and 4.20. All of the suggested print times from all fours sample number were then compared against the visually inspected results to understand whether they are increasing or decreasing the computational expense, along with the consequent effect upon the accuracy of the results observed.

| Force wave desired sample number - 7.14 | |
|---|---|
| Input Speed (rad/sec) | Suggested Print Times (Milliseconds) |
| 10 | 8.00 |
| 50 | 1.60 |
| 100 | 0.80 |
| 200 | 0.40 |
| 500 | 0.16 |
| 1000 | 0.08 |

Table 4.19: Suggested print times at various input speeds, for set number of sample points per force wave, determined from 10 rad/sec revisited result, utilising a larger print time.

| Force wave desired sample number - 5.712 | |
|---|---|
| Input Speed (rad/sec) | Suggested Print Times (Milliseconds) |
| 10 | 10.00 |
| 50 | 2.00 |
| 100 | 1.00 |
| 200 | 0.50 |
| 500 | 0.20 |
| 1000 | 0.10 |

Table 4.20: Suggested print times at various input speeds, for set number of sample points per force wave, determined from 1000 rad/sec inspected result.

A summary of the suggested print times along with their visual accuracy and CPU times, can be seen in table 4.21. It is clear from comparing the results, that the higher sample number originally suggested when taking an inspection point from a low speed run, results in accurate results for all speeds being tested. However, this accuracy for the majority of speeds is above the perceived necessary requirements. Also when as previously mentioned when print times drop below 0.5 ms the CPU run times are seen to begin to rise, which for this set of results is 66.67 % of the tested runs. Additionally, when examining the higher speed region the print times are seen to drop so low the CPU run times become substantial, with the 1000 rad/sec 1.75 sec run taking over 1300seconds to compute. This significant jump, whilst being currently feasible during the Motionsolve extraction of load forces stage, will become a more profound problem when analysing the stresses and movements as a result of these forces, due to its vast increase in input points.

However, when analysing the opposing end of the spectrum with the suggested print times derived from the 1000rad/sec suggested sample number. A significant drop in CPU run times is seen with the cumulative total from all 6 runs taking half the time of those executed with the original 10 rad/sec suggested sample number. Although the time saving comes at a cost of accuracy with some of the lower speed visually inspected results, being perceived to have poor levels of accuracy. As expected, the 100 rad/sec suggested print times yield results within the middle ground of both options, with the majority of results showing a good level of accuracy and not being overly computationally expensive. Although this is not the case for the top end speeds again which due to the exponential nature of the CPU run time and print time relationship, end up experiencing a sharp rise in CPU run time. In turn this results in the average time saving from the 10 rad/sec versions to 32.71 %, with only a minor loss of accuracy across all results.

However, when revisiting the visual accuracies of the results, to determine an alternative ideal print time for a 10 rad/sec input speed. The print time was doubled from 4ms to 8 ms, resulting in a sample number per force wave, that when used to suggest print times for the remaining tested speeds, delivered print times which provided accurate force results throughout all tested speeds. With the lowest print time observed across the range at 1000 rad/sec being 0.08 ms. In turn capping the maximum CPU run time at 979.00 seconds, which is 64 % longer than the visually selected 0.1 ms option. From the studies it is clear from table4.21 and table4.20 that no matter which usable print time is used, at this high of an input speed the print time required to deliver an adequate force output comes with a high computational demand, due to sitting within the sharp end of the exponential relationship of print time to CPU run time. This factor is a key issue in reducing the overall run times for the models being used, with high speed loading, particularly when the high speed is for a prolonged period of time, ensuring the print time required is low for this duration also. Therefore, due to the fact high speeds will allways result in increased CPU times, the accuracy of the lower speeds should not be readily compromised by using a low force wave sample number in an effort, to aid in reducing the run time at these higher speeds.

Following on from the behaviours observed within this section and the effects of the selected print times, and appropriate number of sample points per force wave. It is clear that the sample number selected needs to provide a print time that provides accurate results at both speed extremities. Therefore the sample number can be re-assessed based upon these extremities for each selected load case. The loading proposed for the e-axle system being investigated results in a calculated maximum input speed for the differential of 628 rad/sec, based upon the maximum e-motor speed of 18,000 rpm (1,884 rad/sec) , and the proposed 3 to1 gearing ratio. This lower top end speed, would therefore not require the print time to be reduced as low to obtain the same level of accuracy, whilst also eradicating the most computationally expensive region of the print time investigations.

Potential to revisit at 600 rad/sec suggested peak point as this will be the top input speed used, and therefore the limit for the accuracy required.

| Suggested Print Times | | | Results | |
|---|---|---|---|---|
| Sample Number ($N_s$) | Input Speed | Print Time ($T_p$) | Output Quality | CPU Run Time |
| 14.28 (10rad/sec) | 10 | 4.00 | Good | 66.00 |
| 14.28 | 50 | 0.80 | Good | 83.50 |
| 14.28 | 100 | 0.40 | Good | 281.00 |
| 14.28 | 200 | 0.20 | Good | 255.00 |
| 14.28 | 500 | 0.08 | Good | 334.45 |
| 14.28 | 1000 | 0.04 | Good | 383.20 |
| 8.16 (100rad/sec) | 10 | 7.00 | Acceptable | 62.00 |
| 8.16 | 50 | 1.40 | Acceptable | 135.00 |
| 8.16 | 100 | 0.70 | Good | 200.00 |
| 8.16 | 200 | 0.35 | Good | 205.00 |
| 8.16 | 500 | 0.14 | Good | 479.00 |
| 8.16 | 1000 | 0.07 | Good | 1000.00 |
| 7.14 (10rad/sec,V2) | 10 | 8.00 | Acceptable | 67.00 |
| 7.14 | 50 | 1.60 | Acceptable | 148.00 |
| 7.14 | 100 | 0.80 | Acceptable | 196.70 |
| 7.14 | 200 | 0.40 | Good | 170.50 |
| 7.14 | 500 | 0.16 | Good | 442.00 |
| 7.14 | 1000 | 0.08 | Good | 979.00 |
| 5.712 (1000rad/sec) | 10 | 10.00 | Bad | 67.00 |
| 5.712 | 50 | 2.00 | Acceptable | 76.00 |
| 5.712 | 100 | 1.00 | Acceptable | 166.10 |
| 5.712 | 200 | 0.50 | Good | 240.00 |
| 5.712 | 500 | 0.20 | Good | 324.00 |
| 5.712 | 1000 | 0.10 | Good | 594.00 |

Table 4.21: Summary of the suggested print times for various input speeds, derived from the four tested number of sample points per force wave. With there respective result quality and CPU run times.

#### 4.3.0.5 Loading Methods

There are three key methods for applying a load within the Motionsolve software. These are linear loading, expression loading and curve loading. Each of the three methods were tested to understand their effect upon the simulation and any key difference in the models behaviour or timing. The linear loading option provides a clear linear load throughout the simulation at a set speed. However, due to the model always being stationary initially this method results in a significant spike at the beginning of the simulation as the model rapidly accelerates to the desired speed. This period is seen across a range of tested speeds to take approximately 50 ms, leading to some un-realistic acceleration Figures. However, if the aim is to observe the steady speed forces of a model then this loading option is ideal, as it allows the velocity to be reached in the shortest possible time frame, allowing the user to reduce the overall run of the model. An example of the results seen using a linear loading method can be seen in Figure4.35, where an initial input of 200 rad/sec was prescribed as a linear load. This method resulted in a spike as expected, where the forces are seen to be in excess of 6000 N, which when compared with the results shown in Figure 4.36 utilising the same speed and print time, but utilising an expression to disperse the acceleration period over 1second. This option results in a peak force of only 10 N, approximately 600 times less, with an acceleration reduction from 2,800 rad/sec$^2$ to 200 rad/sec$^2$ which is 14 times less. Therefore this method of abrupt loading is not appropriate when wishing to examine the models acceleration and transitions between speeds, as the acceleration is to abrupt. The Figures however do show that despite which approach is taken in getting the model to achieve the desired velocity, once it obtains the set speed the forces seen are the same. However, there is one key difference, as the waves are not in phase due to the differing points in when the desired velocity is achieved.

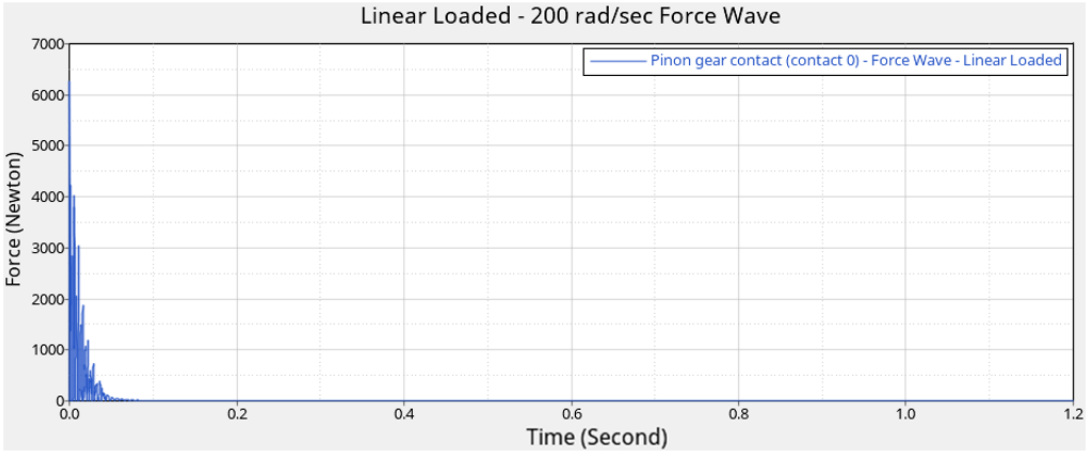



Figure 4.35: Force wave for 200 rad/sec input speed, using the linear loading option, with a significant rise in forces seen over a short time frame at the beginning of the simulation.

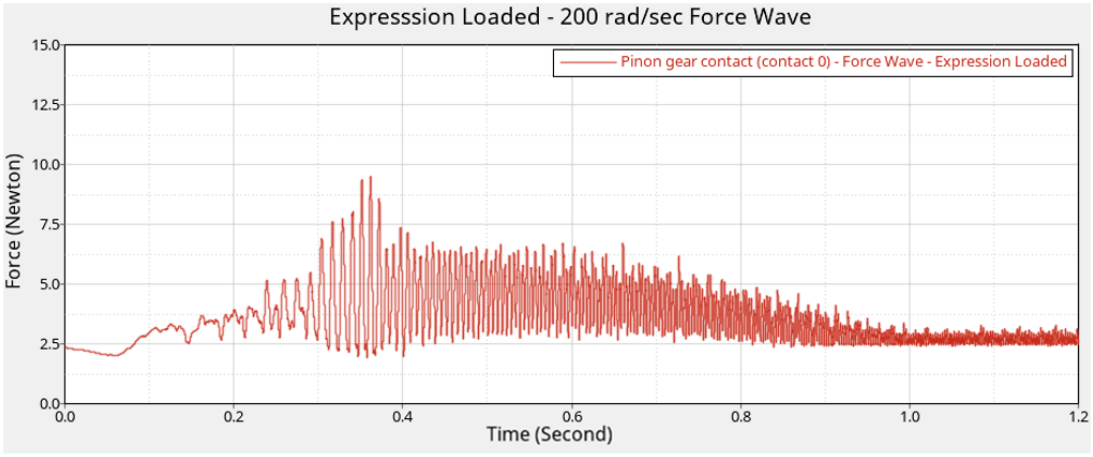



Figure 4.36: Force wave for 200 rad/sec input speed, using the expression loading option, with the acceleration of the model over one second.

The expression option is the default method used for the work, that has been executed within the Motionsolve platform. The reason for this selection is, it enables the user to adjust the loading method in a variety of ways, via different expressions. The formulation of the expression can be seen in equation 4.9, followed by the expression being utilised within these investigations in equation4.10, with an example included for the expression loading of zero to 200 rad/sec from zero to one second.

The expression allows the user to allocate a desired speed for the system. This approach allows an additional level of control over the linear loading method. This expression also allows the user to depict a time period for the acceleration to take place over. This method can therefore be implemented as a way of examining the effects of the acceleration on the forces seen within the model or as a more accurate way of observing initial results, as the acceleration period can be set to eradicate any excessive spikes in forces, as a result of unrealistic acceleration Figures, such as those seen when using a linear loading method in Figure 4.35.

$$\begin{aligned} &\text{Step}(x, t_0, v_0, t_1, v_1) \\ &x - \text{The Independent variable} \\ &t_0 - \text{A real variable that specifies the v value at which the step function begins.} \\ &t_1 - \text{A real variable that specifies the v value at which the step function ends.} \\ &v_0 - \text{The initial value of the step.} \\ &v_1 - \text{The final value of the step.} \end{aligned} \tag{4.9}$$

$$\text{Step}(time, t_0, v_0, t1, v1)$$

$time$ – The selected independent variable.

$t_0$ – A time value that specifies the velocity value at which the step function begins.

$t_1$ – A time value that specifies the velocity value at which the step function ends. (4.10)

$v_0$ – The initial velocity value for the step.

$v_1$ – The final velocity value for the step.

$$\text{Step}(time, 0, 0, 1, 200)$$

The third loading option, which is key to the development of the e-axle model the paper is focussed upon, is curve loading. This method allows the user to input transient loadings into the system, via a loading curve. The loading curve can be loaded from an external source, where typically the desired speed is plotted against time. A trial series was executed using a simple loading curve to understand its effects on the models output as well as any effects on the computational intensity of the model. The load curve utilised for the initial trial run is shown in Figure 4.37, the curve was generated within the Motionsolve platform, by using a .csv file containing two columns of numbers. The first representing the times at 0.01 second intervals, the second the corresponding input speeds, in rads/sec. This curve entity is then selected as the input motion of the model. This loading was then teamed with a 0.1 ms print time and executed to examine it's behaviours. The model was seen to function appropriately by monitoring the speed of the pinion gear in the actual simulation, this was seen to be consistent with that of the input curve.

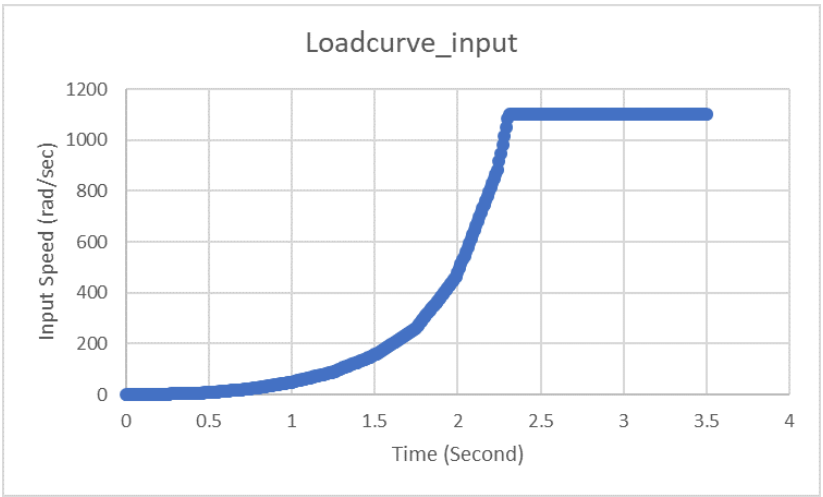



Figure 4.37: Visualisation of the loading Curve utilised, to initially observe effect of curve loading the differential model.

To continue to inspect the models response to various curves, a further curve was initially tested. This can be seen in Figure 4.38,the curve was generated and implemented in the same method as the previous test. However, the aim of this curve was to examine how the model decelerates. The results showed an instant drop off in speed as the input speed dropped to zero, this resulted in a spike in forces similarly to those previously seen under the sharp acceleration of linear loading. This behaviour shows that the model instantly reacts to any changes in input, which means with the current model set up no residual torque remains within the system, due to this for any natural wind down of the system to be observed this would also have to be accounted for within the load curve input. This is a key current limitation when progressing to a full transient load input, as any decelerations will have to be accurately considered, particularly sharp decelerations within the system, as a result of any regenerative braking, which is commonly implemented within electric drive systems.

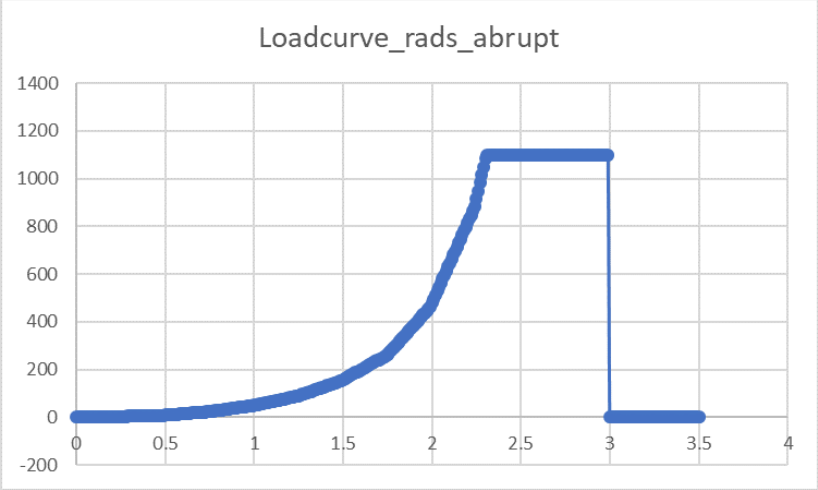



Figure 4.38: Visualisation of the loading Curve utilised, to observe the effect of an abrupt drop in the curve loading input.

Following the initial investigations using curve loads, to check the models behaviour via its observed speeds. Additional testing was carried out to compare the force results seen between a curve loading application and one generated using one of the already established methods, in this case the load expression application. The benchmark model was set up using the expression previously discussed, with the acceleration period set over two seconds and the desired speed 500 rad/sec, with a print time selected of 0.1 ms. The output speed curve of the pinion gear from this model was then extracted, to allow for an identical acceleration and loading to be applied via the curve method. The data points were utilised to generate the loading curve, which was then run under the same conditions as the expression version.

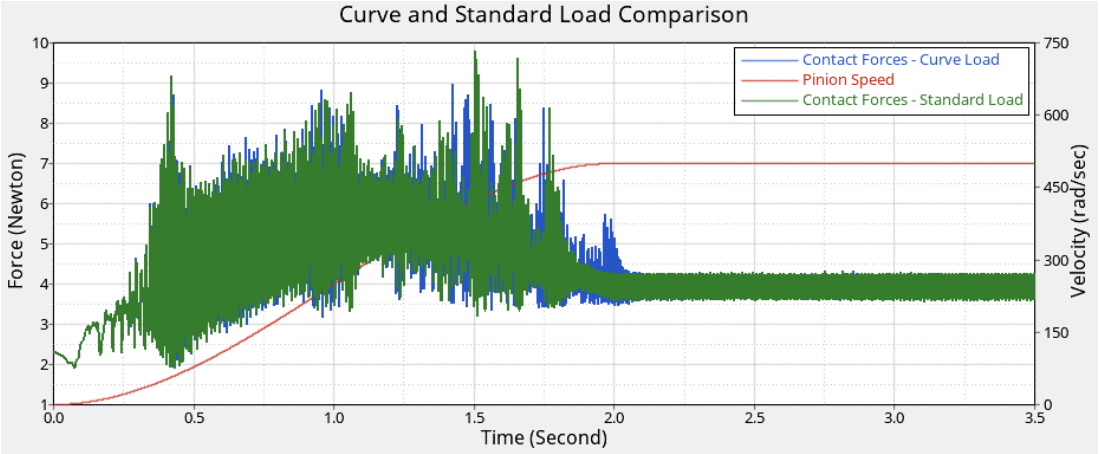



Figure 4.39: Comparison of force wave outputs for pinion gear contact, using both curve and standard loading methods.

The two output results can be seen plotted in Figure 4.39, Visually it can be seen that the two different loading methods yield similar results. Both pinion speeds as expected were seen to be identical. Whilst the contact forces observed, followed the same pattern with a rise and fall occurring in the forces during the acceleration period, followed by a series of steady force waves, once the target speed was achieved. However, the forces seen for the curve load option, take approximately 0.2 seconds longer before settling to a steady state. There was also occasional spikes to slightly different amplitudes during the acceleration period. The slight fluctuations during the acceleration period could be a result of the curve not forming a continuous load path. As each time intervals speed forms, a marginal step in the velocity curve not initially observed. These slight steps of sharp acceleration, are seen to manifest as force spikes. Which in turn would be the cause for the delay in the curve loaded option achieving steady state, as it is still experiencing high acceleration periods over very small time frames, as opposed to the expression version which is seen to gradually and most importantly smoothly reducing its acceleration to zero.

The forces during the steady state period are seen to be consistent as the inputted curve data has fewer data points, when no speed changes are observed. This leads to a smooth line. Therefore, a further investigation was carried out to examine the effect of adjusting the curve to have fewer sample points which will lead to smoother linear acceleration between the points. Whilst this will reduce the overall accuracy of the curve capture, it will eradicate the large number of sharp rises. The data was sampled at a rate of one point every 50 ms. This sampled data was used to create the secondary load curve, where the resultant force output can be seen in Figure 4.40. Due to the points being taken at larger intervals the transition acceleration points which were leading to spiking forces are no longer present. This is particularly evident during the final stages of the acceleration period, where the forces are seen to reduce and become more

consistent 0.30 seconds earlier than the previous curve run. Although a fluctuation is seen at the latter end of the simulation, where the speed prescribed should remain constant, resulting in a steady force wave. However, upon closer inspection a slight rise and fall in the speed can be seen which is the most probable cause for the deviation observed. The difference in the two speed for this steady speed time period, can be seen in Figure 4.41

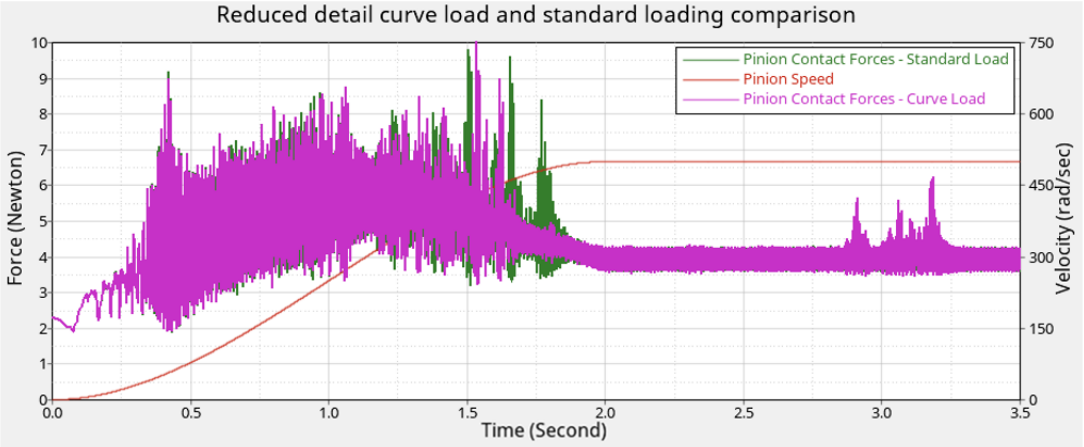



Figure 4.40: Comparison of force wave outputs for pinion gear contact, using both curve and standard loading methods, with the curve load taking loading inputs every 50 ms as opposed to Figure 4.39 which is every 0.1 ms.

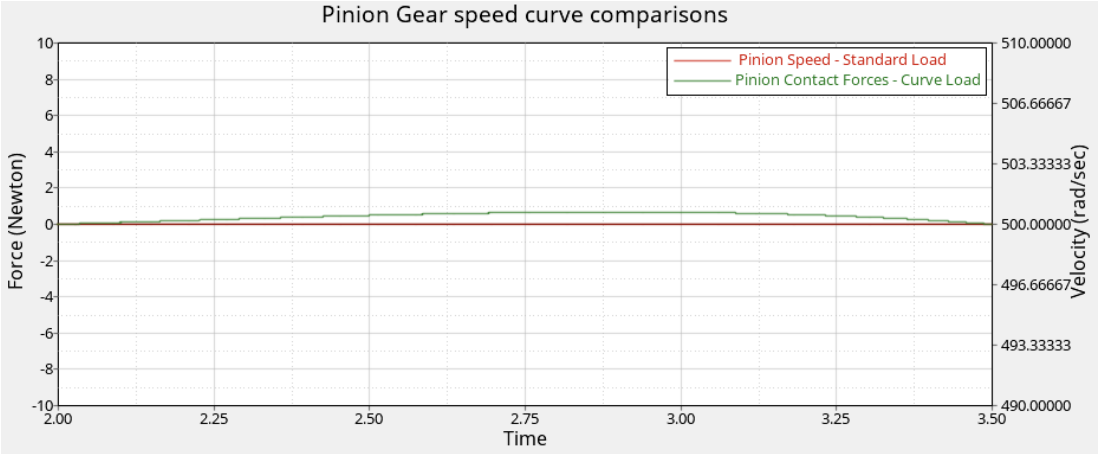



Figure 4.41: Closer inspection of the pinion gear speed during the designated steady state region, comparing the standard expression loaded output with the curve loaded output.

With regards to the computational run times seen from the executed investigations, the resultant times varied by approximately 20 %. With the more detailed curve plot taking approximately 20 % longer than the standard expression and the reduced detail curve taking roughly 20 % less. The variation in the timings seen show no significant changes from using the different loading methods, which allows for confidence progressing with a transient load curve, knowing it will not have a severe detrimental effect upon the CPU run time.

Overall from the following investigations, it was concluded that using a curve to define the

load input of the model is feasible and supplies suitably accurate results. However, it is key to note that the current method does not supply a smooth curve and slight steps are observed between the inserted data points, which result in minor changes to the forces observed, as opposed to reality. Although the investigations supply sufficient data to allow for the future works to be executed using a load curve as the input and for the user to obtain accurate usable results, whilst understanding any limitations. Whilst the end result will be utilising a curve load, it is vital to of develop the understanding of the other loading options. As the series of investigations has highlighted areas in which each one can be used in developing an understanding, of how best to control the run times of the simulations, and explore areas to reduce the models computational run time.

#### 4.3.0.6 Acceleration Investigations

Progressing from the previous seen results, from the various studies already executed within this chapter. The acceleration has presented its self as a clear contributing factor in the magnitude of the contact forces observed, within the model. Therefore, several additional investigations were executed to improve the understanding of the changing acceleration rates.

#### 4.3.0.7 Acceleration rates effect upon forces.

In previous tests it has been seen that the larger acceleration rates naturally result in larger contact forces. This was particularly evident within Section 4.3.0.5, where the transition to a linear loading option, resulted in a significant spike in forces as a result of unrealistically large acceleration Figures. However, due to the Figures in this extreme case being so large no clear relationship could be observed. Therefore, a series of more realistic acceleration rates were tested to examine the effect upon the contact forces seen. For this study the forces at contact 0 between the Pinion gear and the crown wheel were focussed upon. The model was set up utilising a print time of 0.14 ms, with the input speed defined via the expression method to allow for a consistent method of altering the acceleration rates via altering the expressions acceleration time period. The rates initially tested covered a range from 250 rad/sec$^2$ to 1000 rad/sec$^2$ , the corresponding acceleration time periods are seen within table 4.22. The acceleration rates have been calculated based upon an initial target test speed of 500 rad/sec, calculating the time period required for each of the various acceleration rates being targetted for testing by dividing the test speed by the targetted acceleration rate.

| Target Acceleration Rate | Utilised Acceleration Period | Equivalent Acceleration Rate |
|---|---|---|
| Rad/Sec$^2$ | Seconds | Rad/Sec$^2$ |
| 1000 | 0.5000 | 1000.000 |
| 900 | 0.5555 | 900.099 |
| 800 | 0.6250 | 800.000 |
| 700 | 0.7143 | 699.986 |
| 600 | 0.8333 | 600.024 |
| 500 | 1.0000 | 500.000 |
| 400 | 1.2500 | 400.000 |
| 300 | 1.6666 | 300.012 |
| 250 | 2.0000 | 250.000 |

Table 4.22: Tested acceleration rates, and corresponding acceleration periods.

The maximum forces observed were collated and plotted within Figure 4.42 against the acceleration rates. It is clear from the results that there is a linear relationship between the rate of acceleration and the forces seen. In addition to this all forces generated using the tested rates yield reasonable force results, as opposed to those previously seen with the linear input speed method.

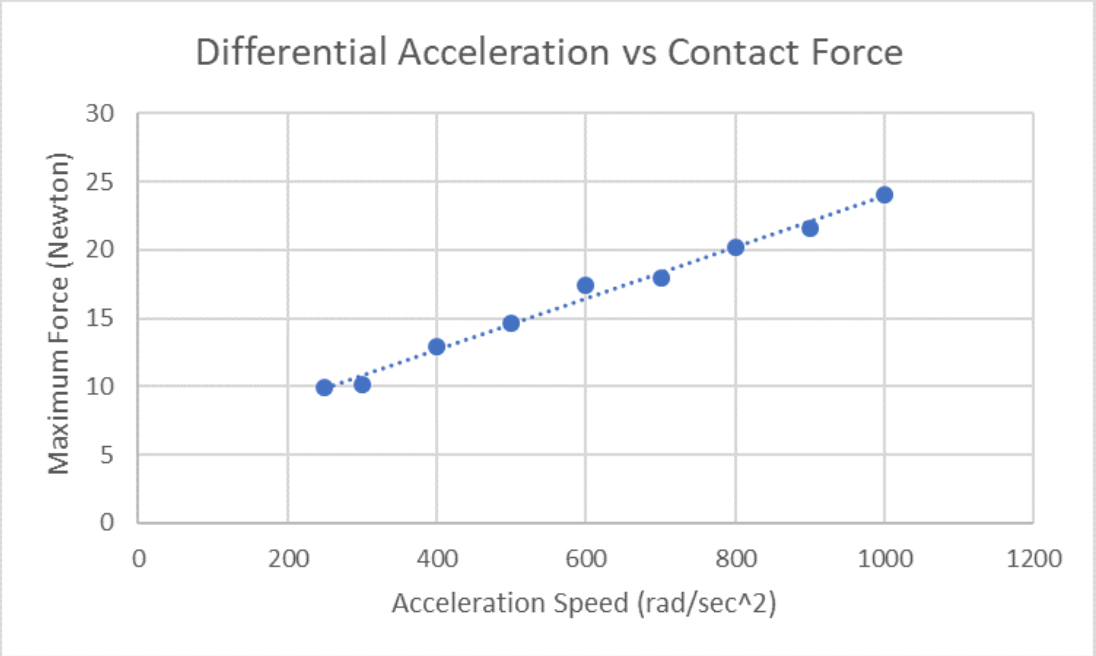



Figure 4.42: Plot of maximum contact forces observed within differential model, for varying tested acceleration rates.

To ensure the behaviours observed are accurate and not just local to the tested region, the tested range of acceleration rates was increased up to 8000rad/sec$^2$. From this extension once again it was seen that even when utilising an acceleration rate beyond the capabilities of the e-motor, the relationship remains linear with no sharp rise in forces as the acceleration rate is increased. Although when examining the two gradients it is seen that the gradient increases from 0.019 to 0.031, this slight increase is not significant enough to cause concern over such a large range of tested rates. With the gradient increasing by just 63 %, in comparison to the testing range increasing by over 10 times. The force curves for a number of the tested acceleration rates can be seen plotted in Figure 4.43, where the change in acceleration can also be clearly seen.

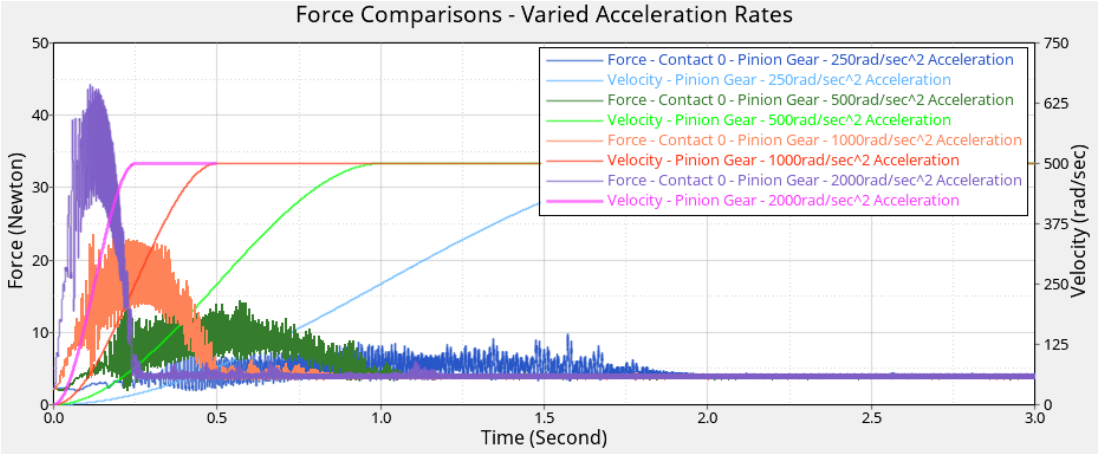



Figure 4.43: Plot of contact force plots for pinion gear/crown wheel contact, at varying acceleration rates. Supported by the tracked speed of the pinion gear for the corresponding rates.

From this graphic it is clear that a clear rise and fall in forces is seen despite the acceleration rate used. This rise and fall is a result of the way the acceleration is plotted using the expression. The acceleration seen is not a constant linear acceleration up to the desired speed. The acceleration rate rises and then falls again, forming a curve in the acceleration rate, which is emulated within the force patterns observed. To clarify the severity of this rise and fall, and to illustrate the connection to the force patterns seen, the acceleration rates were extracted from the listed 1000 rad/sec$^2$ version, at 25 ms intervals. The acceleration rates are listed within table 4.23 with their corresponding time periods. They were then plotted against each other and can be seen in Figure 4.44.

| Time Point | Acceleration Rate |
|---|---|
| Seconds | Rad/Sec$^2$ |
| 0.000 | 0.00 |
| 0.025 | 282.50 |
| 0.050 | 540.00 |
| 0.075 | 765.00 |
| 0.100 | 960.00 |
| 0.125 | 1125.00 |
| 0.150 | 1260.00 |
| 0.175 | 1365.00 |
| 0.200 | 1440.00 |
| 0.225 | 1485.00 |
| 0.250 | 1500,00 |

Table 4.23: Extracted acceleration rates for the 1000rad/sec$^2$ run, with corresponding time stamps.

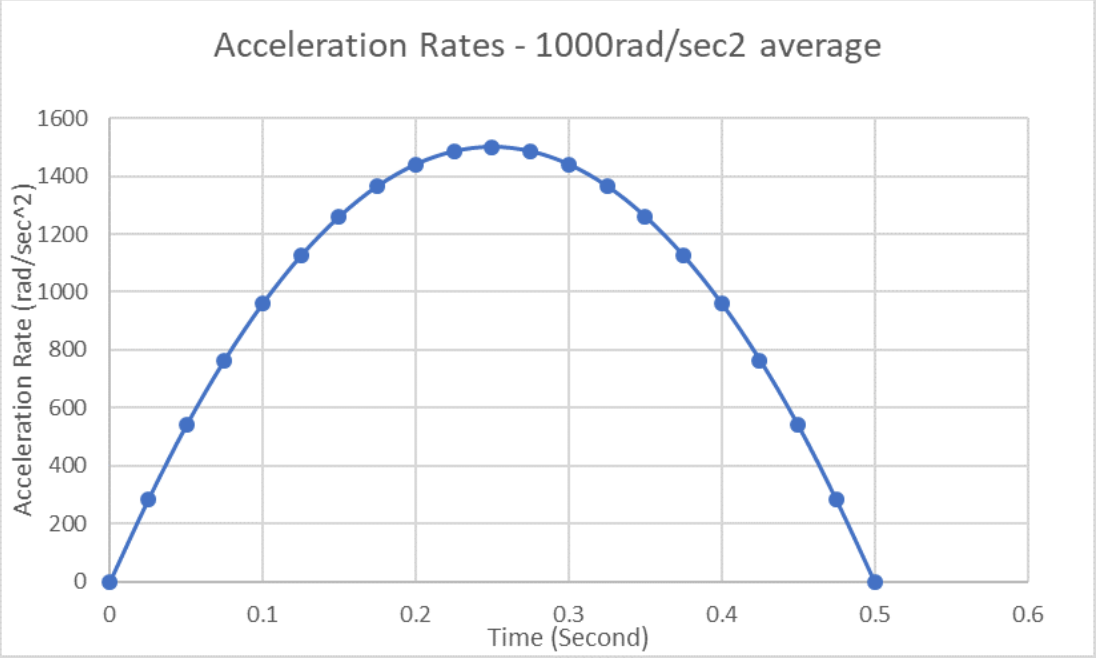



Figure 4.44: Visualisation of results in table 4.23

The Figure provides supporting evidence that the pattern observed in all of the forces is a result of a similar pattern being portrayed in the loading process. The results also highlight that the forces seen in the previously tested results are not entirely accurate as the acceleration rate is seen to peak at almost 50 % above the desired rate, in turn resulting in larger forces at these

points, than the values which would be expected for a linear acceleration. Figure 4.45 shows the tracked acceleration on the actual model over a two second time period, for the model with its motion defined via the expression method, resulting in a 1000 rad/sec$^2$ average acceleration rate. From this the curve again is clearly visible, however, spikes can also be seen upon the main rise and fall of the acceleration rate which is depicted in Figure 4.45, the acceleration rate is seen to peak at a maximum of 1636 rad/sec$^2$ at a time of 0.19 seconds. Despite this the maximum force still occurs as the model reaches the half way point at approximately 1500 rad/sec$^2$, the reason for the spike not resulting in a maximum observed force is due to it not being sustained for a period long enough to have a noticeable effect upon the forces. In addition to this feature being observed, the steady state region once the acceleration is expected to of tended to zero shows clear spikes throughout. A closer look at these spikes in Figure 4.46, shows the majority of ripples around 17 rad/sec$^2$ with sporadic spikes in value in excess of 55rad/sec$^2$. These shifts in acceleration are the most probable cause for the fluctuations observed in models during their steady state region. The cause for the accelerations are most likely the loss of contact with each passing gear tooth, resulting in minor fluctuations.

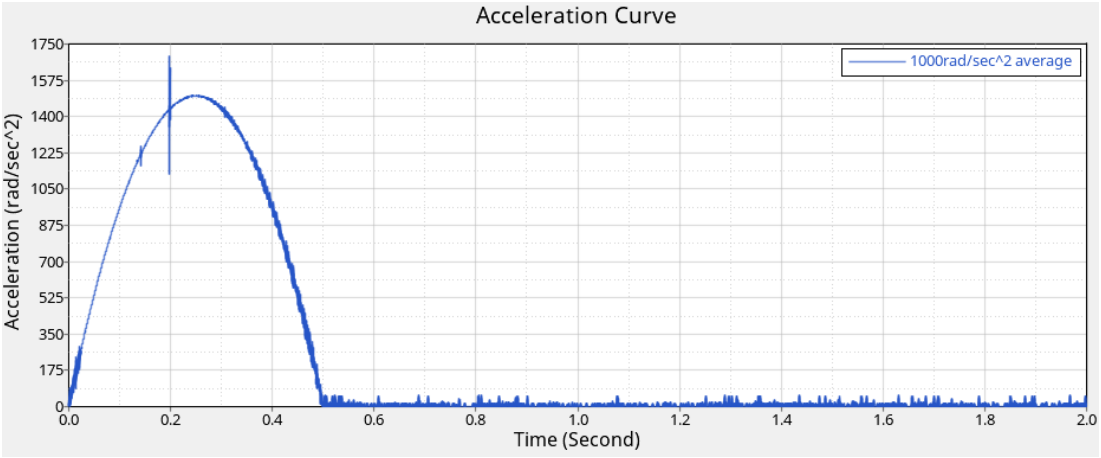



Figure 4.45: Plot of acceleration rate against time, for the 1000 rad/sec$^2$ expression generated model.

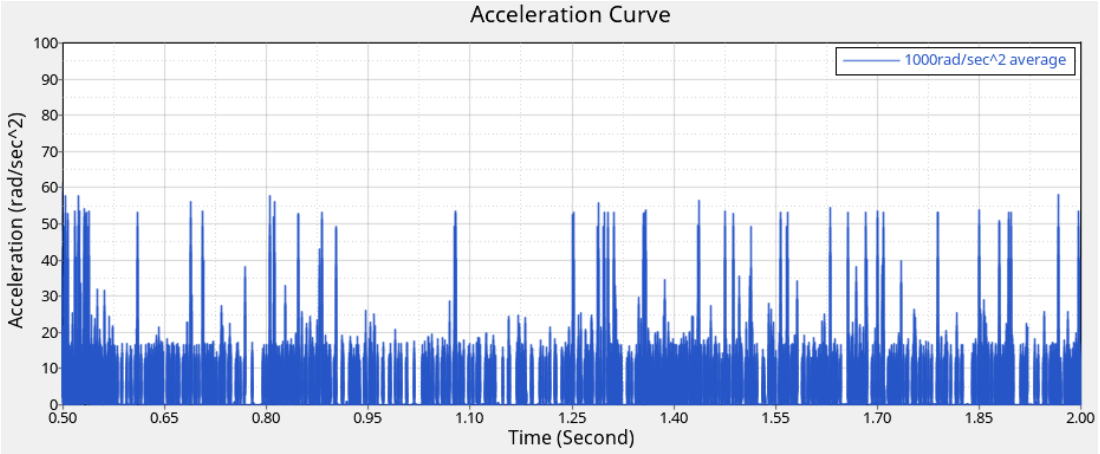



Figure 4.46: Inspection of acceleration rates during steady speed region of the model displayed in Figure 4.45

**Linear Acceleration Comparison** To examine where the actual maximum forces for the tested rates would be, a linear acceleration was utilised and the previously tested acceleration rates revisited. However, this time using a curve to define the input speed path to ensure a constant acceleration period.

When generating the curve a shortened approach was taken hoping to use fewer points to generate the curve, used to define the input speed. Initially a simple to step approach was taken providing the initial conditions of zero speed at zero seconds, followed by the desired speed of 500 rad/sec at 0.5 seconds, to ensure a linear 1000 rad/sec$^2$ acceleration rate. The resultant loading was seen to generate the loading as expected, with the models speed accelerating at a constant rate of 1000 rad/sec$^2$ up to 500 rad/sec at the 0.5 second point. However, the model then continues to accelerate at this rate for the remainder of the simulation as seen in Figure 4.47, this is due to an insufficient amount of data used to generate the curve. This feature of the software continuing a loading path until adjusted is key for generating load curves, for future investigations. Also in Figure 4.47 you can clearly see the difference in the speeds of the model from the standard expression defined acceleration and the curve. With the speed of the expression option initially being below the linear acceleration version, before surpassing it at the half way point and tailing off to obtain the desired speed at the same time point. This change in acceleration rates clearly affects the forces with the difference in the force values being evident within the graph. With the forces for the linear option being much more consistent across the entire acceleration period and beyond. As opposed to the forces which are seen to peak at almost 50 % higher during the mid-stages of the expression version. This approximate 50% increase is supported by the Figures in table 4.23 , with the acceleration rate at 0.25 seconds being 50 % higher at 1500rad/sec$^2$.

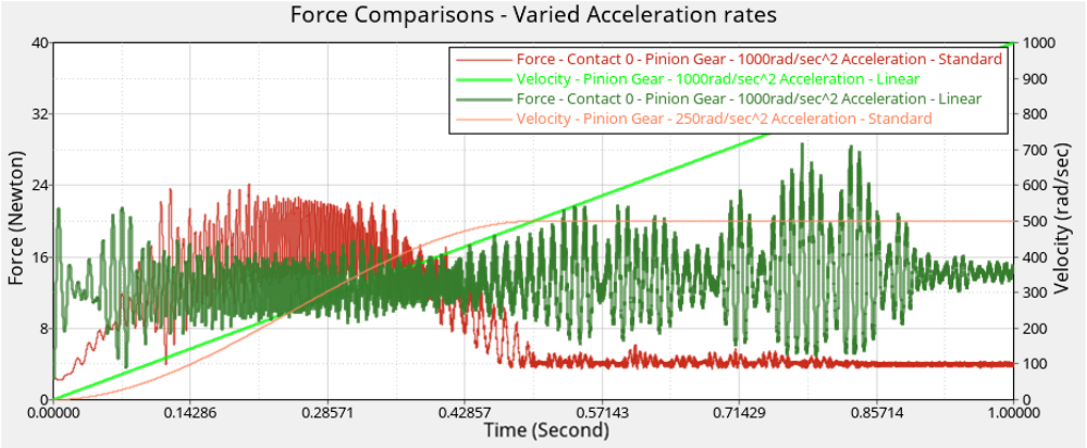



Figure 4.47: Visualisation of forces for a linear acceleration at a rate of 1000 rad/sec$^2$, with reference plot of equivalent expression generated version.

To correct the model and examine any change in forces as a result, the curve was edited to ensure the acceleration ceased once the desired speed of 500 rad/sec was achieved. The resultant forces for this version can be seen in Figure 4.48. overlaid with the results previously examined in Figure 4.47. The significant change in the result is the immediate drop off in forces once the acceleration rate drops to zero, the initial force wave is seen to be identical to the initial curve result with constant acceleration throughout the entire run. This significant drop also highlights how significant acceleration rate is in the contact forces observed within the model. With the forces decreasing on average by over 50 %, despite the input speed being at its peak. In addition to the drop off in forces, once the model is at a steady speed, during this period the forces are seen to be much more consistent in comparison to the same region when using the standard expression to define the input speed. With the red force wave of the expression version, fluctuating at points of the steady speed region. The difference in the two results during this steady speed region could be a result of the curve loading having no additional points to reiterate the desired speed value over this 0.5 second region. Also as they are seen to no longer be present beyond 0.8 seconds for the expression version, they could be a consequence of the gradual decrease in acceleration rate to 0 rad/sec$^2$. With the model still having a marginal fluctuation in input speed for the consequent 0.3seconds following the 0.5 second acceleration window.

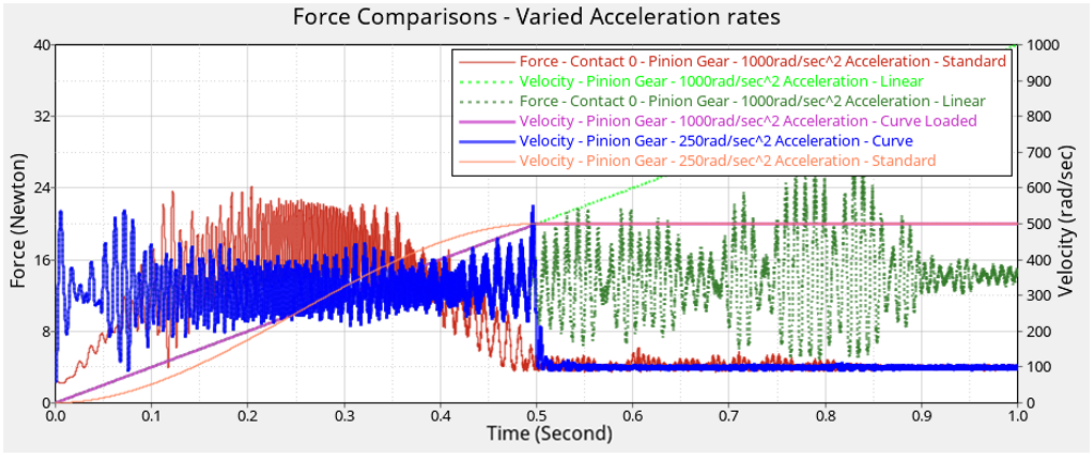



Figure 4.48: Visualisation of forces for a capped linear acceleration at a rate of 1000 rad/sec$^2$ up to a speed of 500 rad/sec, with reference plot of equivalent expression generated version and previous linear version.

Following the successfully preliminary investigation into the difference in the forces when using a linear acceleration, generated via a loading curve. This method was applied to all tested acceleration rates from 250 through to 2000 rad/sec$^2$. The resultant maximum forces for each tested acceleration rate can be seen plotted in Figure 4.49, alongside the maximum forces for the same acceleration rates, when using an expression to define the loads.

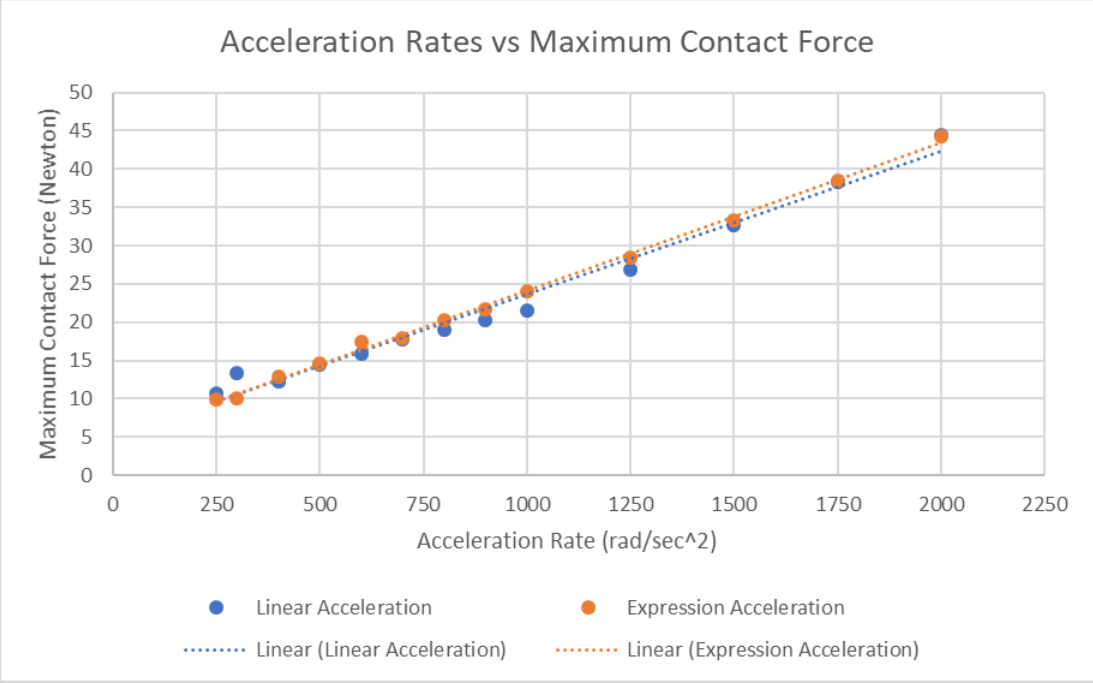



Figure 4.49: Comparison of maximum forces observed at various acceleration rates when using a linear accelertion and a expression derived curved acceleration.

It is clear from the Figure that the maximum forces observed are very similar, which was not expected, due to the findings indicating that the expression versions have peak acceleration rates at around 50 % higher than the average. Therefore, the results for the linear loads were

expected to be lower than the expression options. Although upon further inspections a number of different factors were noted. First of which was when comparing the two force outputs for contact 0, (pinion to crown wheel) during the acceleration period, the forces overall were seen to show a more consistent value throughout as opposed to a clear rise and fall. Although as a result of two spikes of similar value the overall maximum for all tested forces, ended up being almost identical. Also each of the spikes seen for the linear results occurred at a comparative distance before and after the half way point of the acceleration. Due to this trait the tracked acceleration Figure when using a linear load was observed, with an example from the 400 rad/sec$^2$ model being shown in Figure 4.50. The Figure shows a different curve to that which was expected to be flat throughout the acceleration period before tending to zero for the remainder of the simulation. With fluctuations occurring at random intervals throughout the acceleration period, one of these minor spikes is seen to match the point in which the maximum force is recorded. However, it remains unclear as to why the larger spikes in acceleration rate are not resulting in even more significant force spikes. The current theory for this is the potential slippage between gears at these points causing spiking acceleration rates, but having no effect upon the contact force.

An additional trait which is also seen in the acceleration wave, was the increasing amplitude of the acceleration of the wave as the speed of the model increased. This increase in wave amplitude for higher speeds was also observed within Section 4.2.3 when observing the input speeds effect upon the contact forces. In addition when revisiting Figure 4.45 a rise in the amplitude can be seen toward the latter end of the acceleration curve when utilising the expression to define the input motion. This provides key information when later examining ripples within the contact forces, to ensure consideration is given to the cause of the fluctuation as its clear both speed and acceleration also give rise to these ripples and larger amplitudes.

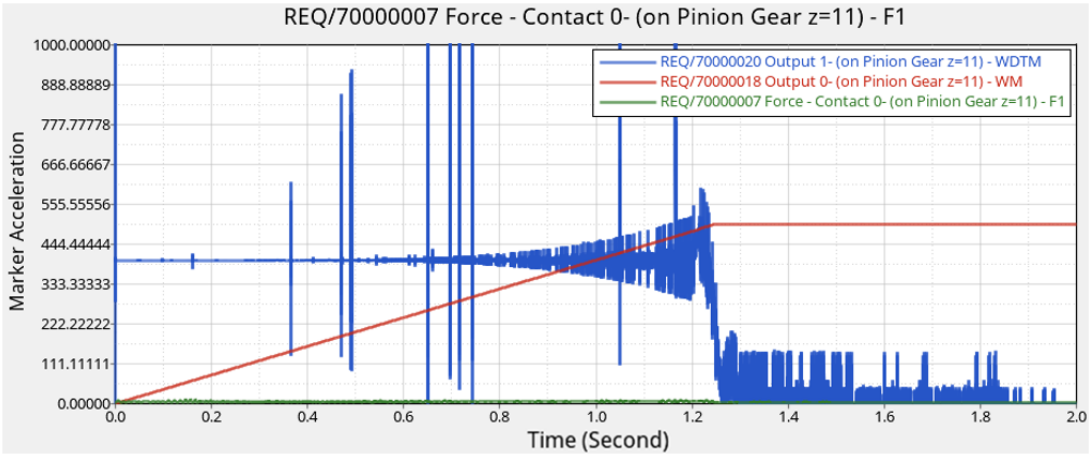



Figure 4.50: Acceleration rates plotted for 1000 rad/sec$^2$ linear acceleration up to 500 rad/sec.

Following investigations into both a linear acceleration and the accelerations observed when utilising an expression, connections can be made with regards to the forces observed at specific acceleration rates. Whilst Figure 4.49 showing the maximum contact forces observed for both methods at various selected acceleration rates, shows minimal difference. Which was unexpected due to the actual acceleration rates observed when using an expression, peaking at 50 % greater than the targeted value. However, with the knowledge of the maximum recorded forces coming as a result of spiking forces a more representative conclusion can be drawn when looking at the average force at the mid points of the two acceleration types. A series of results were extracted and can be seen collated in table 4.24, these results clearly show that at the half way point of the acceleration period the acceleration rate is significantly higher for the expression option, as is the forces observed. The peaks for the expression option are around 50 % higher as expected and when compared to the equivalent linear acceleration rate, the force is seen to be very similar with an average difference of 4 %. This proves that the acceleration rate is having a clear affect on the forces observed, and despite the graphic within Figure 4.49, overall the forces seen are reflective of the acceleration rate differences observed.

| Average Acceleration Rate | Linear Acceleration | | Expression Acceleration | |
|---|---|---|---|---|
| | Acceleration Rate | Force Value | Acceleration Rate | Force Value |
| rad/sec$^2$ | rad/sec$^2$ | Second | rad/sec$^2$ | Second |
| 400.00 | 400.00 | 6.598 | 598.97 | 7.97 |
| 600.00 | 600.00 | 8.722 | 880.62 | 12.30 |
| 900.00 | 900.00 | 12.45 | 1348.45 | 19.80 |
| 1000.00 | 1000.00 | 15.202 | 1500.00 | 22.30 |
| 1500.00 | 1500.00 | 22.346 | 2235.68 | 28.57 |

Table 4.24: Forces extracted at the midpoint of various acceleration periods, for a number of acceleration rates and both application methods.

**Acceleration rates effect upon CPU run time.** To ensure a full understanding of any behaviours which could affect the CPU run time, the run times for the various tested acceleration rates were also monitored throughout. From previous studies it is expected that the larger acceleration rates, which provided the larger forces will in turn require a longer computational run time. As seen with the extreme case runs previously seen with exceptionally high acceleration rates, resulting in spiking forces and longer CPU run times. However, from plotting the run times and examining the results within Table 4.25, the CPU run times are seen to be relatively unaffected by the changing acceleration rate. The slight fluctuations are not beyond the region of variation expected when running the simulations locally as highlighted

in Section 4.3.0.1. This in turn supplies confidence that the run times will remain relatively consistent and will be mostly driven by the print time selected, which as previously mentioned is partially determined by the speed of the model to ensure accurate capture of the force waves are maintained.

| Acceleration Rate | CPU Run Time | |
|---|---|---|
| | Application Method | |
| | Expression | Linear |
| rad/sec$^2$ | Second | Second |
| 250 | 813.10 | 1232.00 |
| 300 | 850.90 | 1360.00 |
| 400 | 775.40 | 1304.00 |
| 500 | 775.90 | 970.00 |
| 600 | 758.70 | 1156.00 |
| 700 | 824.30 | 1102.00 |
| 800 | 762.40 | 1292.00 |
| 900 | 820.70 | 1133.00 |
| 1000 | 812.90 | 985.00 |
| 1250 | 1290.00 | 1038.00 |
| 1500 | 1140.00 | 1110.00 |
| 1750 | 1295.00 | 1018.00 |
| 2000 | 1368.00 | 822.60 |
| 4000 | 1374.00 | NA |
| 8000 | 1473.00 | NA |

Table 4.25: CPU run times, for a series of acceleration rates for both tested application methods.

However, when comparing the CPU run times for the two applied methods, linear accelerations and the expression generated curve, a relatively uniform difference is observed in the run times. This indicates that the method of application is effecting the CPU run times but the various acceleration rates are not. Therefore, reassuring the fact that despite the method of application the different rates do not affect CPU time, and in turn are not an area for investigation for reducing the computational intensity of the model when progressing to longer more complex transient loadings.

To combine the above conclusions of the higher the acceleration rate the larger the contacts forces exhibited are, and also the fact that despite the acceleration rate the CPU run time will remain relatively unaffected. A simulation was created to support these theories, using a curve

load with an increasing acceleration rate every 0.1 seconds from 120 rad/sec$^2$ to 3840 rad/sec$^2$ with a print time of 0.14 ms and a run time of 3.5 seconds. The resultant forces for the first 1 second can be seen in Figure 4.51, where the forces can clearly be seen to increase at each 0.1 second interval, before dropping to a steady value once the acceleration rate drop to zero. This Figure whilst illustrating the increasing forces alongside the increasing acceleration rate, also reinforces the lack of effect the acceleration rate has upon the CPU run time, with the model completing its run in 1395 seconds, which is comparative to timings listed within table 4.25, when using a curve to define the load case.

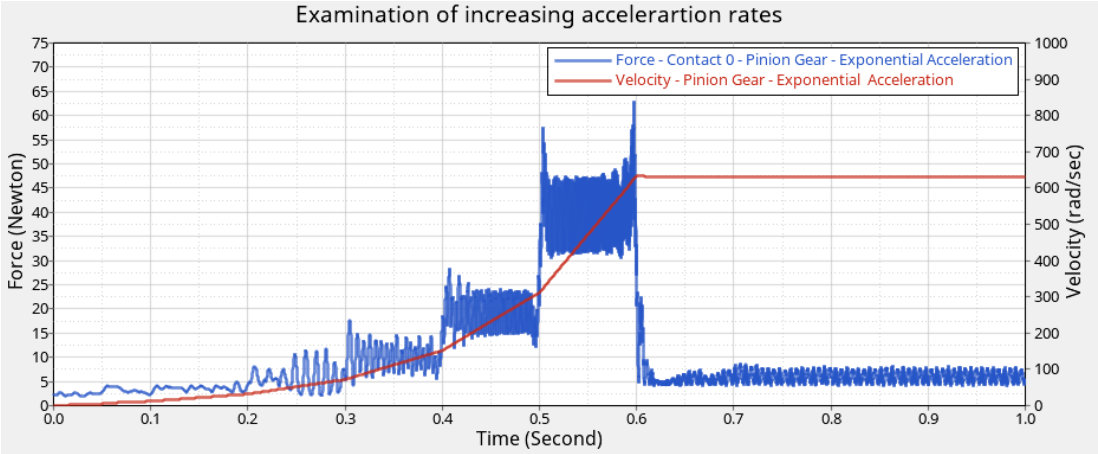



Figure 4.51: Forces plotted alongside pinion gear speed, for an exponentially increasing acceleration rate curve.

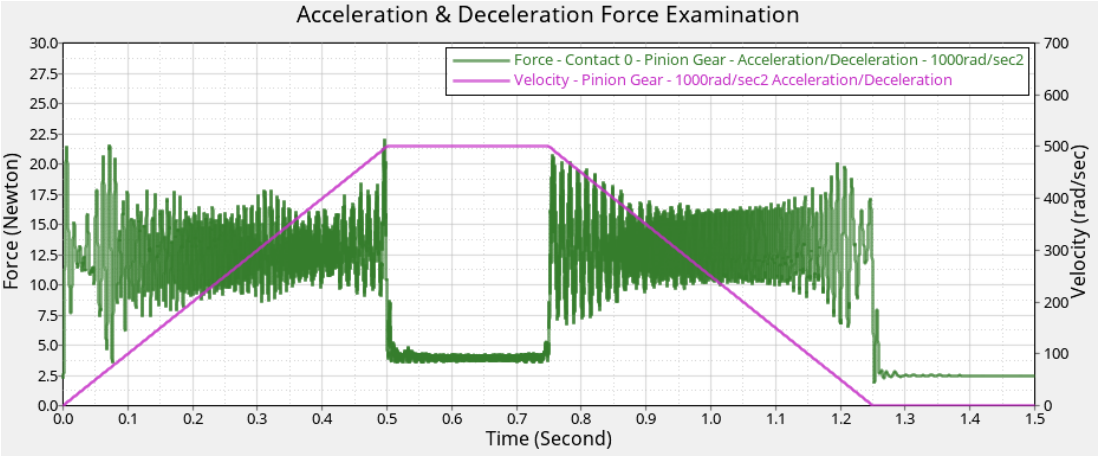



Figure 4.52: Forces plotted alongside pinion gear speed, for a model accelerating up to 500rad/sec and then decelerating back to zero, both at a rate of 1000 rad/sec$^2$

**Deceleration Comparison** Following on from the acceleration studies a final study within this area was desired, to round out the understanding of the acceleration affects upon the model. The investigations in question were to note the effect of deceleration rates and to compare the forces seen during these to that of the equivalent accelerations. Testing at two

acceleration/deceleration rates was executed, the two rates consisted of 1000 rad/sec$^2$ and 2000 rad/sec$^2$ up to 500 rad/sec. Figure 4.52 displays the speed of the pinion gear and the forces of contact 0 throughout. It is clear from this initial visual inspection that the forces throughout the deceleration period are comparable to that of the acceleration period. To obtain a better understanding two runs were set up to allow the acceleration and deceleration to overlap as seen in Figure 4.53, displaying the speed of the pinion gear and the forces of contact 0 for both acceleration and deceleration of 1000 rad/sec$^2$ overlaid, with the respective accelerations taking commencing at the 0.75 second mark. It is clear from the initial visual inspection that the forces follow an almost identical path. With a mirror of the forces being displayed, this can be seen with the slight peak at 0.825 seconds (0.075seconds from the beginning) for the acceleration and 1.20 seconds (0.05 seconds from the end) for the deceleration.

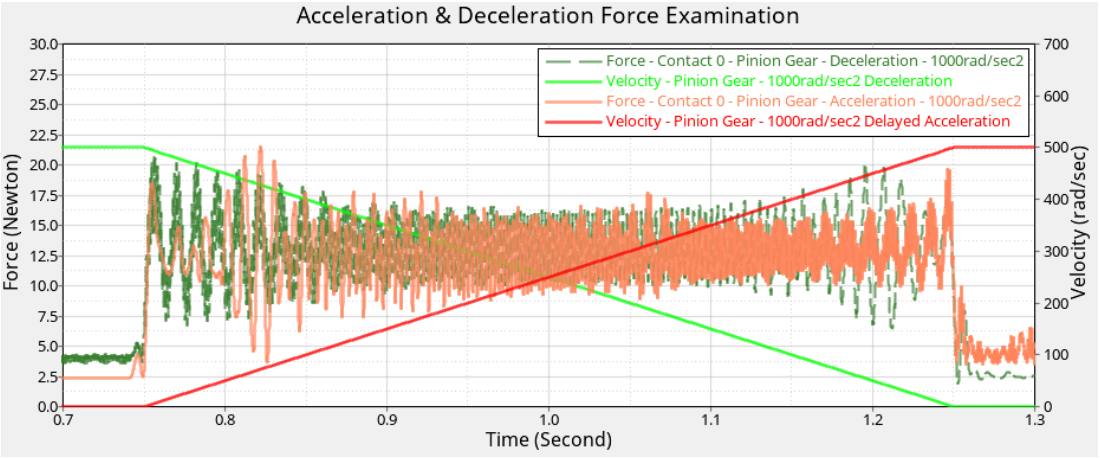



Figure 4.53: Forces and pinion gear speed, overlaid for two separate models one accelerating up to 500 rad/sec and the other decelerating from 500 rad/sec both at a rate of 1000 rad/sec$^2$

The same two Figures utilising an acceleration rate of 2000 rad/sec$^2$ can be seen in Figures 4.54 and 4.55. Once again the results show a clear comparative result for the acceleration to deceleration. This therefore consolidates the fact, that whether the model is accelerating or decelerating the rate of the acceleration will result in almost identical contact forces. Therefore, the decelerations which are likely to be higher, will result in the peak forces.

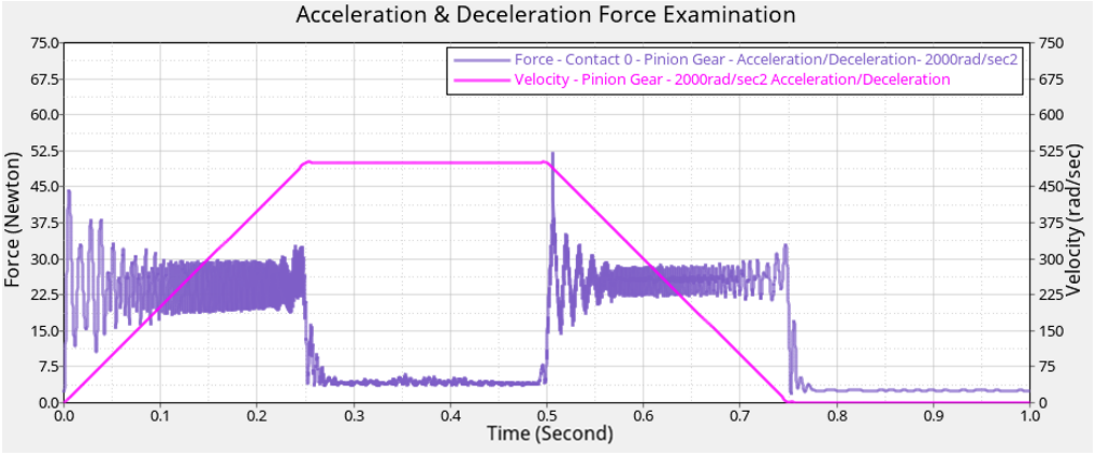



Figure 4.54: Forces plotted alongside pinion gear speed, for a model accelerating up to 500 rad/sec and then decelerating back to zero, both at a rate of 2000 rad/sec$^2$

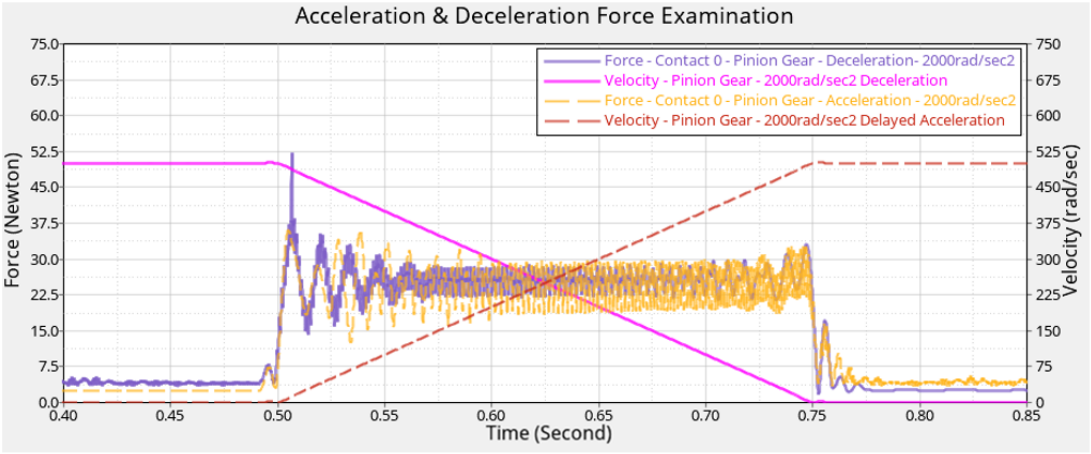



Figure 4.55: Forces and pinion gear speed, overlaid for two separate models one accelerating up to 500 rad/sec and the other decelerating from 500 rad/sec both at a rate of 2000 rad/sec$^2$

#### 4.3.0.8 Print Time Expression

Following on from the print time accuracy studies in Section 4.3.0.4, it is clear how the ideal print time is not consistent for all speeds. As a print time which is suited to the higher end speeds will in turn result in an overly computational expensive simulation for all lower speeds, likewise a print time set from the lower speeds will not provide the accuracy required for higher input speeds. As a result of this it was apparent that a speed dependent variable print time was required, this is achievable within the Motionsolve platform via the use of an expression driven print time.

Firstly, to establish any differences between the use of expression print times and set prescribed print times, two comparative runs were executed. The runs utilised an input speed of 200 rad/sec with a print time of 0.4ms. The first run utilised the standard method of prescribing the desired print time. However, the resultant force curve generated by this result had issues,

as whilst the force waves accuracy was to a good level and the overall behaviour of the forces in the model were captured, a number of spikes were seen in the result, which were increasingly apparent during the steady speed state of the model. Figure 4.56 shows the result overlaid with the 0.1 ms print time version. From this it is clear that the spiking forces are not a feature of this particular speed, but in fact they are an error due to the print time selection being to large. Errors occurring such as these spikes are a clear indication of how imperative, having confidence in the print time selected or the expression utilised to select the print time is. As if spikes such as these were to occur, during the latter stages of the investigation it would be hard to distinguish which spikes are a result of the print time and which are a result of torque ripples from the motors and other parts of the e-axle assembly.

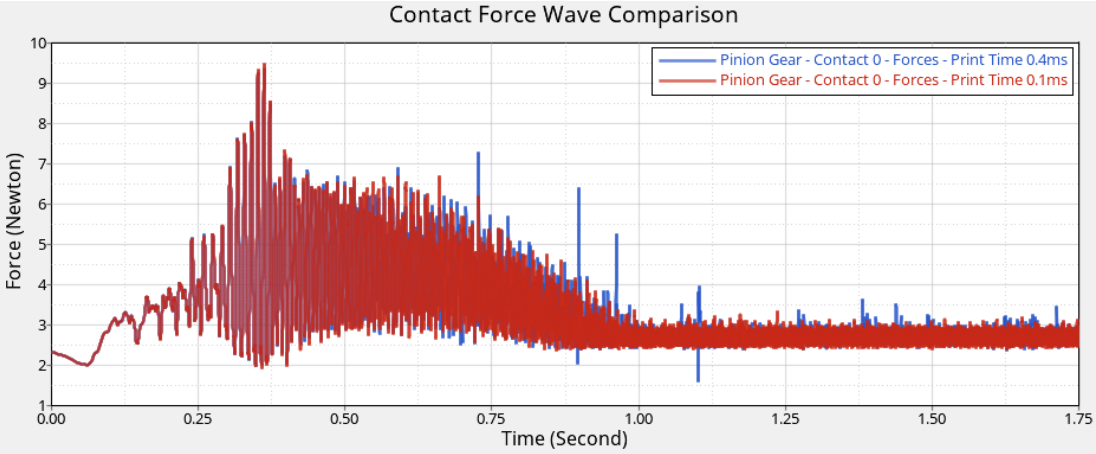



Figure 4.56: Closer inspection of the pinion gear speed during the designated steady state region, comparing the standard expression loaded output with the curve loaded output.

Following the discovery of the spiking force readings at print time 0.4 ms. Further work was carried out to settle upon a print time to execute the print time application comparisons. The model was ran again using a standard print time from 0.2 ms where it was known to function appropriately, up to 0.4 ms at 0.05 ms intervals. From this study it was seen that the spikes in the force results began to occur at 0.3 ms with these becoming progressively larger and more frequent as the print time was increased further, upwards towards 0.4 ms. As a result of this investigation a new print time was suggested for the print time application comparison of 0.2 ms or 0.25 ms. The 0.2 ms print time at 200 rad/sec falls in line with the originally suggested Figure from 10 rad/sec. Providing further indication that a sample number per force wave of approximately 14 may be needed for lower speed runs. However, when comparing the run times the drop down from 0.4 ms to 0.2 ms print time comes at a computational cost with the run time increasing by almost 50 %, although due to both Figures being in the lower region of the exponential curve, the 50% increase only equates to an 84.3 second rise.

With the print time refined to 0.2 ms at 200 rad/sec input speed, the comparison study

was resumed with the first model being ran with a standard prescribed print time. The second utilising an abbreviated equation based upon equations 4.4 and 4.3, seen within Section 4.3.0.3. This abbreviated version seen in equation 4.11, allowed the print time to be controlled by the user, by adjusting the prescribed sample number and utilising the defined input velocity defined for the model. For this particular example with the input velocity defined elsewhere as 200 rad/sec, the equivalent print time equated to $1.99 \cdot e^{-4}$seconds. The slight decrease in print time is due to the accuracy prescribed to the value of Pi within the software. However, the 99.99 % accuracy is assumed to be satisfactory to progress the comparison with.

$$\begin{aligned} T_p &= \frac{2\pi}{11 * N_s * V} \\ N_s &= 14.28 \\ T_p &= \frac{2\pi}{11 * 14.28 * V} \\ T_p &= \frac{6.28318}{157.08 * V} \end{aligned} \tag{4.11}$$

However, issues occurred when attempting to enable the print time expression on the current model. These were due to the fact the motions; initial velocity is set via the expression previously shown in equation 4.9, where the acceleration period and speed can both be adjusted, along with the initial acceleration point. Therefore, 'V' is not a constant causing the print time expression to fail.

This issue can be easily rectified for this initial comparison by adjusting the initial velocity input method, to a linear option. However when previously investigated within Section 4.3.0.5, this results in a significant spike in forces during the initial region of the simulation as the model accelerates up to full velocity in approximately 50 ms. This change allows the print time expression to utilise a distinct velocity value within its calculation, as opposed to it originally calling upon an expression. The change to linear loading was made for both the expression and pre-prescribed print time versions, to allow for the appropriate comparisons to be made. The resultant outputs can be seen within Figure 4.57, with both results yielding identical visual force wave results. The maximum forces and pd results show minimal difference, with a 1.50 % average difference across all contacts, with the maximum pinion forces for both methods result in the same value occurring at identical time points. However, from Figure 4.57 it is clear that the force waves of the pinion gear contact do spike higher when utilising the expression version. In addition the waves during the steady state are not in phase, this is likely due to the linear loading option not defining an acceleration period. Overall the capture of this 'unrealistically' aggressive acceleration period is of a good standard, and provides confidence in the expression contained in equation 4.11. Knowing that it functions appropriately utilising the

input velocity to determine the corresponding print time and yield accurate results, the main differences exhibited in this region are believed to be a consequence of using the linear loading method and a moderately high speed, resulting in an exceptionally sharp acceleration period.

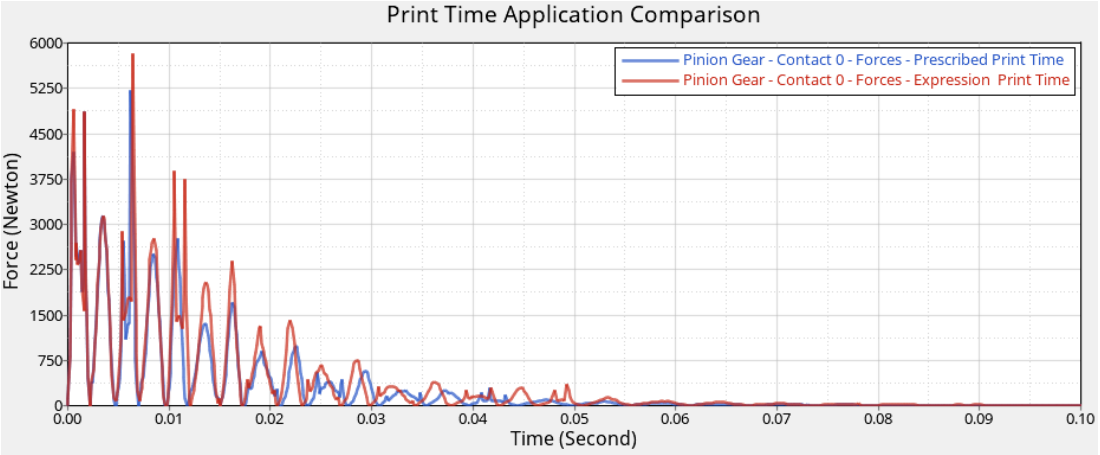



Figure 4.57: Comparison of force wave results during initial sharp acceleration period, for standard and expression print time application methods for a 200 rad/sec input speed.

Progressing from the 200 rad/sec test, the input speed was reduced to 10 rad/sec. This was to ensure the expression adapts the print time appropriately, also by reducing the speed the acceleration will not be as aggressive, which should result in a more trackable result. With the speed adjusted the print time expression should now equate to 4ms, although due to the use aforementioned issues with the level of accuracy of Pi within the system the expression results in a print time of 3.99$\dot{}$ms. The automatic altering of the print time also provides the evidence required; that the expression is accurately tracking any changes to the velocity which will be key when progressing. The simulation was also executed with the print time prescribed at 4 ms, to once again compare outputs when utilising different methods of defining the print time. Figure 4.58 displays both resultant outputs focussing upon the early stage of the simulation where the forces are seen to be more significant, due to the sharp acceleration. The results are focussed over a time frame of 50 ms to help highlight any differences between the two methods. It is seen from this that the two results visually differ slightly. Although the key element of maximum forces are consistent with the peaks observed, occurring at identical points. This is reinforced when examining the max forces output for all the contacts, with zero difference observed between any of the peak forces. Ensuring the key peak forces are correctly observed under both print time application methods.

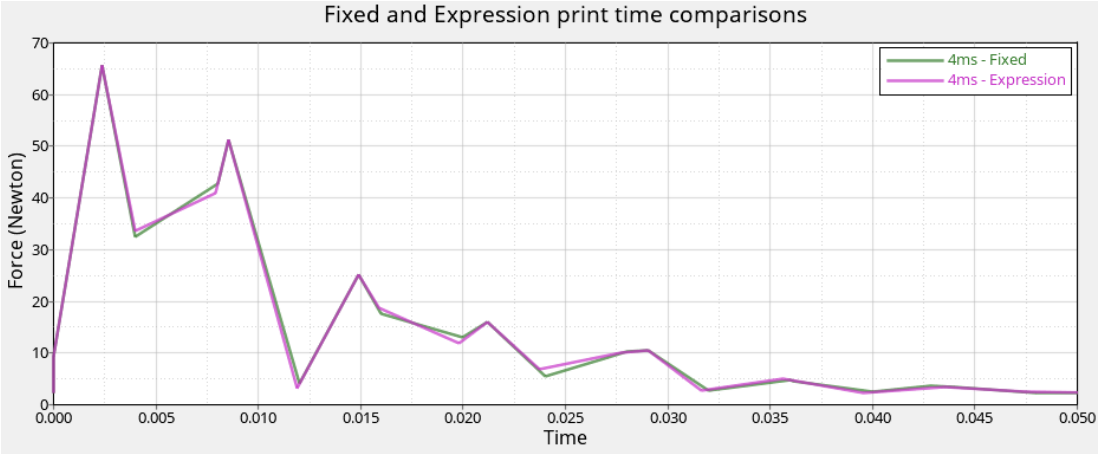



Figure 4.58: Comparison of force wave results during initial sharp acceleration period, for standard and expression print time application methods for a 10 rad/sec input speed.

However due to the slight discrepancies in the two print time application methods seen at 4ms, the print time was reduced to 2ms to observe if this effected the difference between the two methods in either way. Reducing the print time to 2 ms required the sample number, to be adjusted within the equation to match the increased level of accuracy and ensure the same result capture quality. As the print time was halved, the sample number was therefore doubled to 28.56, once again making this change within the print time expression resulted in the print time being set at 1.99·ms. The correlation between both methods is visibly improved throughout, at this lower print time. This is clearly seen in Figure 4.59, where both methods forces are plotted on the same graph. Once again, the results examined were over the initial 50ms of the run, due to its higher forces. The result correlation as mentioned is improved, although some slight variations can be seen at different points although this is most likely a result of the slight variation caused by the constants used within the expression. The maximum forces for all contacts this time showed 0 % difference and this is also seen in the visual representation with both force plots peaking at identical points.

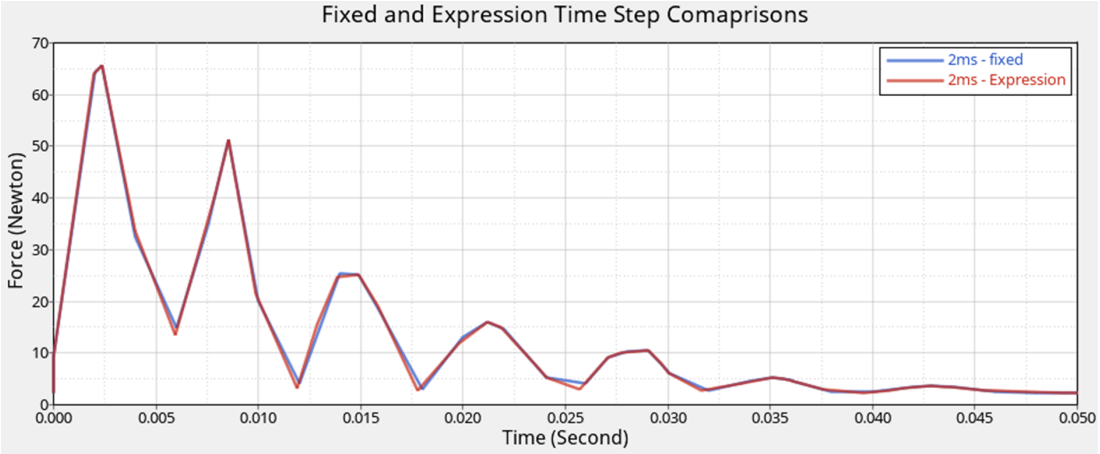



Figure 4.59: Comparison of force wave results during initial sharp acceleration period, for standard and expression print time application methods for a 10 rad/sec input speed, with a reduced print time of 2.00 ms.

In addition to the accuracy being compared between the two print time application techniques, the effect on the CPU run time was also monitored in case of any adjustments. However, no timing difference were observed beyond the region of error highlighted in Section 4.3.0.1. This teamed with the results observed within this section, indicate that the use of the expression in equation 4.11, is just as efficient and accurate as when prescribing the print time value. As the expression adjusts the print time accordingly as the input velocity is adjusted. The behaviour capture also remains consistent at ranging print times, and various tested speeds. The testing at various speeds and print times supplies sufficient evidence the expression functions appropriately under a range of conditions. Despite this there are still issues to be resolved for this expression to function appropriately within a varied loading simulation. As it has already proven to not function when an expression is utilised for the input velocity as well. Trials have also been excited , using a load curve as the input velocity. However again the current limitations in the software do not allow for a varied loading to be called upon within the expression due to the fact the print time is currently required to be constant.

This is therefore an area to be investigated to develop the software further, as their could also be the option to utilised the load curve to generate a time dependent set of print time results, which can be introduced into the simulation, to ensure the appropriate print time is used for each specific speed region. At this stage some areas to be investigated with regards to this would be to implement operating windows for each speeds set print time, as opposed to it being directly driven by the operational speed. As during acceleration periods this will be changing constantly, and therefore a varying print time could lead to further complications. However, this is something which could be investigated further with appropriate future software development.

## 4.4 Chapter Summary

This chapter covered an in depth dive of the modelling aspects for an e-axle system, to allow for accurate loadings to be captured from real life dynamic events. A key outcome from this work covered the modelling of the e-axle system for obtaining loads accurately. However, limitations to the current proposed modelling technique were covered with solutions proposed, some of which requiring further software development. With a continually varying time step required to obtain an accurate model within a timely manner, as simply applying the lowest required print time to the whole simulation duration will not deliver a result in a timely manner. With the studies highlighting how a print time expression is better suited to this application over a consistent time step. Whilst the time duration for the simplified models used in this chapter are short and therefore, allow for a lower constant time step to maintain accuracy. Longer run times would benefit from the decreased time step, such as those required to support an extended full dynamic simulation such as that of a track lap, where ensuring an optimal model is imperative.

The understanding of what drives the forces seen in the model has also been greatly improved. Highlighting the sharpest forces can be observed during the acceleration and deceleration periods as opposed to steady state. Therefore, a large dynamic plot could also be broken down to isolate these key events, for examining within the dynamic model.

# Chapter 5

# Utilisation of low fidelity models in crash scenarios to extract loadings for component and sub-system analysis.

## 5.1 Chapter introduction

The design and lightweighting of components within vehicles has always been a key target for the majority of OEMs. However, with the movement to BEVs and the increasing vehicle size keeping component weight to a minimal and ensuring parts aren't over engineered is vital. As such generating the appropriate loads for component design is key. Although this can be a challenge depending on what prior knowledge is available at the time of component design. For example a vehicle undergoing a mid-cycle refresh has a large amount of data available from both previous physical tests and FEA DFEM models, in addition to full detailed CAD of the vehicle to allow for DFEM models to be created if not already available. However, when generating a completely new vehicle model/platform such as those which have had to be generated with OEMs creating there first BEVs, data available is much more limited.

Whilst previous vehicle data is not available, generating appropriate loadings for component design such as those within the Electric drivetrain and ESS is more of a challenge. OEMs and component suppliers do have access to a series of component level testing requirements from regulatory bodies. However, as discussed within this thesis' literature review these can often be contradictory of other standards and also excessive; with some prescribed loadings in component

level testing of ESS's being un-feasible. The scope of this research is not constrained to such regulatory standards, so whilst OEMs utilise these forces and tests to aid in component design, despite knowledge that they are often excessive when compared to vehicle level testing and real world forces that may be observed, this thesis doesn't not have to. As such it is intended in this chapter to investigate and extract loadings on components from low fidelity CAE models, which could be used in place of those from regulatory standards and testing. With the expectation that these loadings will be more representative to drive component and sub-assembly design, whilst also being lower than those extracted from standards. In turn offering greater design and weight reduction opportunities.

### 5.1.1 Modelling

To enable the type of CAE assessments necessary the modelling method selected is crucial, with DFEM models naturally supplying detailed outputs. Although these do require correlation to physical tests for user confidence. Although as highlighted within the introduction for developing new vehicles, this detail is not yet available. However, designs and guidance can come from vehicle force schemes and low fidelity models. With the use of low fidelity models being the focus of this chapter. A low fidelity version of a DFEM model can provide assessments of large vehicle level models in a fraction of the CPU run time. Typically taking models from days to hours on a comparative number of cores.

A methodology which is leveraged within this chapter is Altairs C123 process, which takes a model from a conceptual design to validated dfem model. Figure 5.1 highlights the key steps within the process;

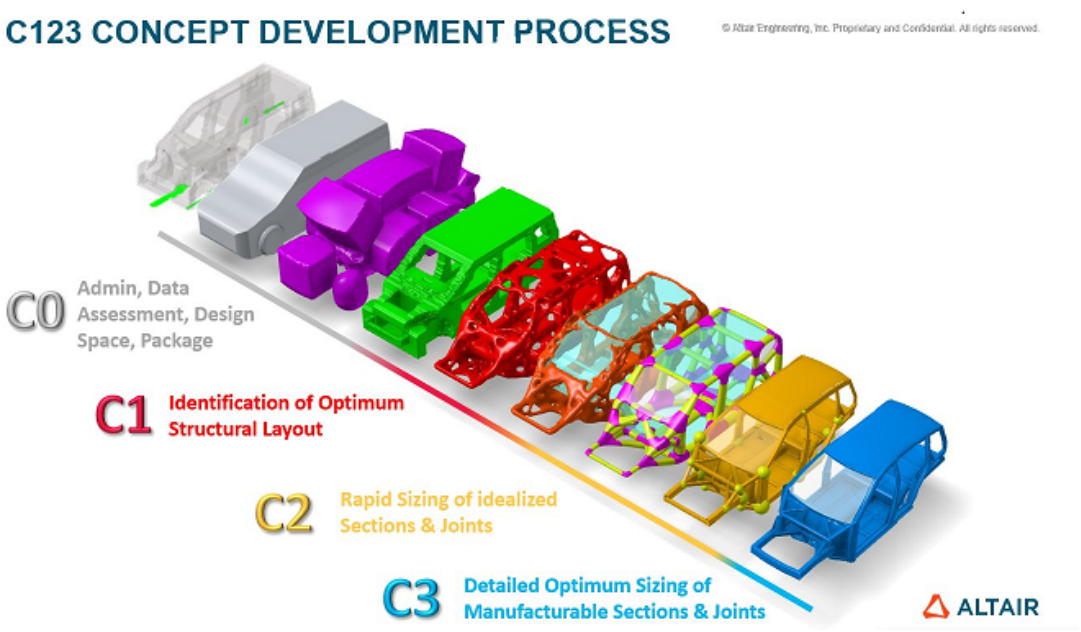



Figure 5.1: Key steps of Altairs C123 process

- **C0** Focusses upon defining of design spaces. Including items such as defining vehicle A Space, overall objective of the design, items such as tyre envelopes and ground lines can be used to ensure generated designs do not foul these pre-defined constraints.
- **C1** Conceptual design; Static analyses can be performed using loading such as crash and NVH equivalent static loadings (ESL) upon the C0 design space. This step helps provide indicative guidance of key structural load paths. With multiple loads from various performance testing disciplines being able to be examined concurrently.
- **C2** has two areas; one is rapid optimum sizing of idealized sections and joints using low fidelity models. These models can then be used to carry out further dynamic and static assessments. Alternatively when working from an original dfem (C3) the same methodology can be applied converting the dfem to model to a low fidelity representation for rapid assessment.
- **C3** Detailed optimum sizing of manufacturable sections and joints using high fidelity modelling.

The C2 region will be utilised to extract the required loadings from the crash models, utilising a C3 to C2 route, with thought to developing an adequate library to aid in approaching from C0.

### 5.1.2 Component Selection

The work carried out within the section was centralised around ESS, with the aim of being able to extract loadings from vehicle models for component or sub-assembly assessment. Unfortunately, due to restraints and access issues no feasible battery pack models were available to the research at the time of the work being executed. As such the ESS selected was that of an ICE vehicle, as the prove out of the theory of testing for loadings on the ICE fuel tank remain the same in principle as those which was aimed towards FCEV. Two main vehicle models were selected, both being that of an ICE vehicle where a DFEM is available. However, only partial visuals of one of the models are contained to maintain the model and results are protected. The other is that of an open source Ford Taurus model used primarily to allow for publishing requirements.

### 5.1.3 Dynamic Load Selection

From literature and existing knowledge of the crash scenarios, a selection for which load cases would be most appropriate to focus this section upon were made. For this work a non standard test was implemented, to generate a worst case loading condition; Whereby both the rear and side impacts were selected, as the most aggressive loadings for a rear mounted fuel tank, which is observed in the donor model for this work. The rear impact whilst typically one of the lesser crash tests, in terms of maximum forces observed, provides the x loadings into the fuel tank. These loads in conjunction with a relocated side trolley crash test, which provides direct impact to the fuel tank from the y direction. Figure 5.2 displays the xy plane of the underside of the crash, with both tests being applied simultaneously. Whilst Side Pole is a known challenging load case for BEV vehicles, it was not selected for this instance as the tank is rearward in the vehicle and if the pole is moved beyond it's regulatory provided locations to impact in line with the tank the force is less severe due to dissipation of the vehicle pivoting around the small diameter. When located centrally nearer to the cars COG it is seen to cause greater damage, as force is not lost in the rotational force of the car pivoting around the pole.

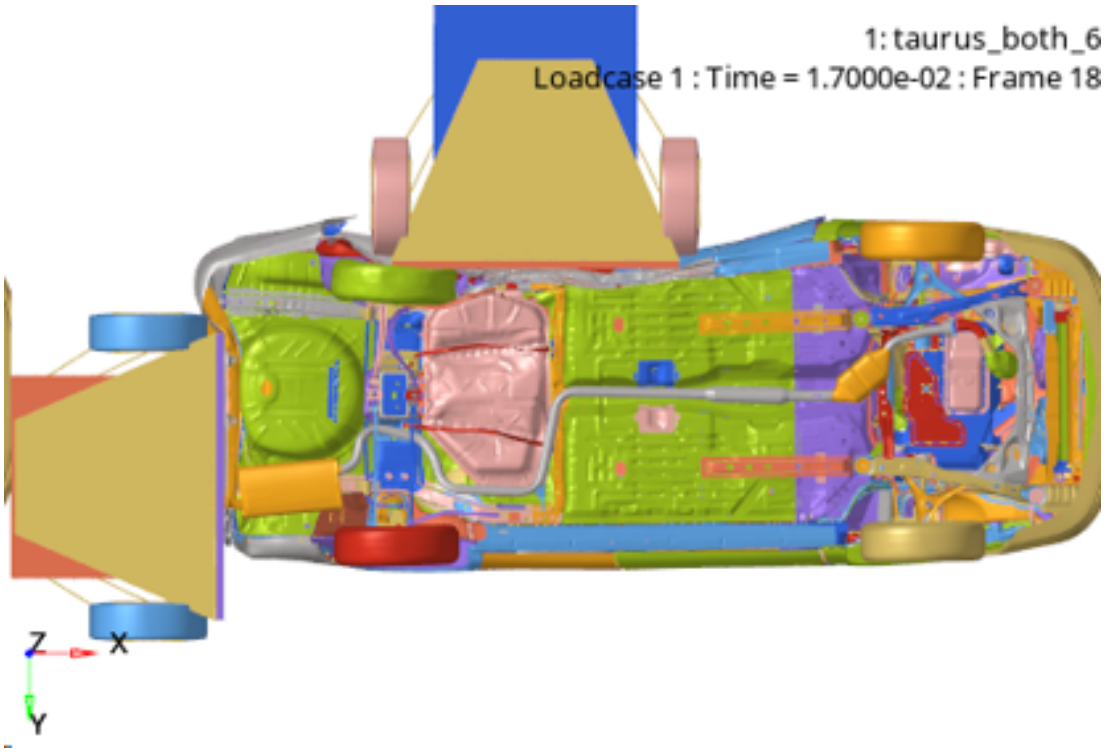



Figure 5.2: Visual of the double crash scenario being assessed upon the Taurus model.

## 5.2 ESL Method

ESL is a method whereby the solver creates the same response field as that of a dynamic non-linear analysis for a given time step. However, this method when not taking continuous assessments results in a loss of detail over a dynamic assessment. With two key equations underpinning the generation of these forces, Equation 5.1 & 5.2. An assessment of using these equations to evaluate the fuel tank in a static simulation is carried out. To allow for this the relevant parameters included in the equations must be extracted.

$$(M\ddot{u} + C\dot{u} + Ku = f)$$

$M -$ Mass matrix

$C -$ Damping Matrix

$K -$ Stiffness Matrix - These matrices are derived using finite elements. (5.1)

$f -$ The vector describes the external loads.

$u -$ Displacement vector. The dots describe the derivatives with respect to time.

$$
\begin{aligned}
(F_{eq} = f - Ma - Cv) \\
F_{eq} - \text{ESL} \\
u - \text{Deformation} \\
a - \text{Acceleration} \\
v - \text{Velocity} \\
f - \text{External Load}
\end{aligned}
\tag{5.2}
$$

A key aspect of utilising this method is the accurate extraction of deformations from the dfem dynamic models. To extract local deformations, two options were evaluated; First of which took key points where contact is made between the vehicle frame and the fuel tank, and extracted both displacements. With them then deducted from each other to provide the local deformation on the tank, with the frames deformation providing an account for the vehicles overall movement within the crash instance. Figure 5.3 displays an example point, to allow for the ESL approach to be tested.

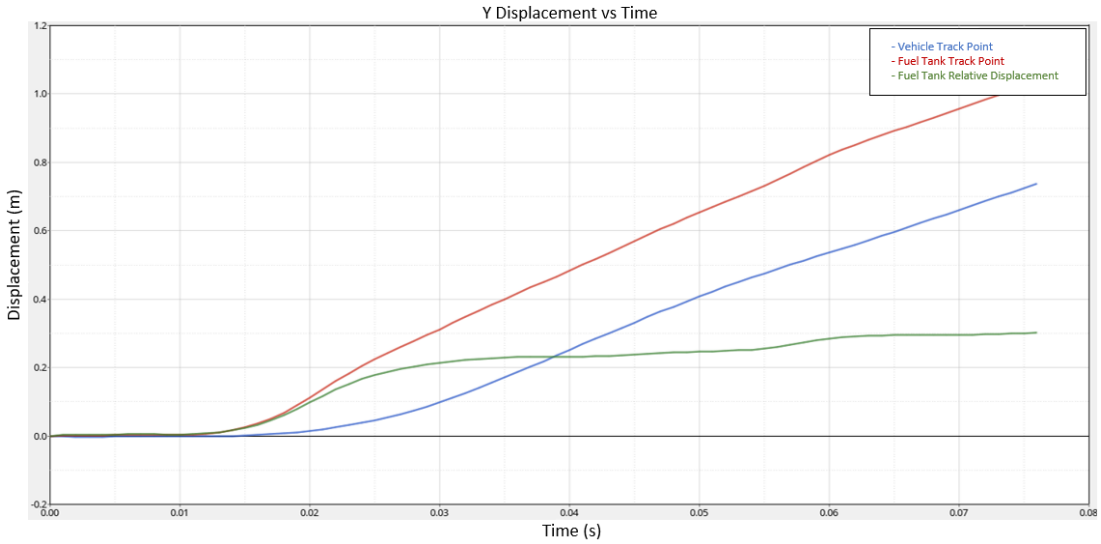



Figure 5.3: Graph tracking body and tank displacements, with relative displacement calculated.

Alternatively local co-ordinate systems can be used on the tank under load and vehicle to extract movements for all three axis. Results showed an initial offset of 0.048 m between the tank and vehicle body. With the vehicle body displacing by 1.104 m at the end of the dynamic run, and fuel tank 0.821 m. With resultant displacements of x -0.0008 m, y 0.2897 m, 0.12908 m & 0.317 m vector. The y-axis displacement matching the value extracted in Figure 5.3 however, the value only being the final displacement as opposed to the graph providing time based data. As such the original extraction method was the one utilised.

To accompany the extracted displacements for a static assessment the stiffness of the compo-

nent being tested was required, this was carried out using a modal static analysis of the tank, global modes seen in Figure 5.4. This resulted in a global stiffness for the tank as opposed to local stiffnesses across the component. Approximations such as this one could result in a disparity in the end static result when compared to the dynamic.

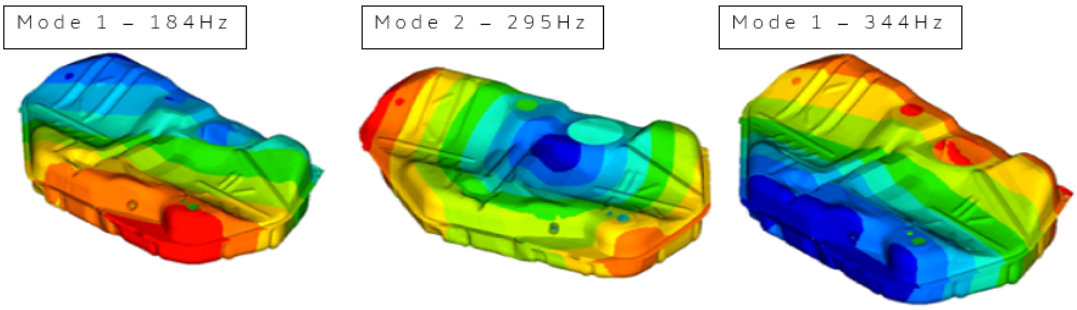



Figure 5.4: Modal Assesment of the fuel tank,global modes depicted.

Utilising the data extracted the ESL was calculated and applied in the Y axis to the fuel tank, with a load applied to the contacting face from the dynamic model and the opposing edge constrained in 6 dof as seen in Figure 5.5, with the resultant displacement contour plot in Figure 5.6. The run time for the static model was under 60 seconds, when compared with the crash run time of circa 36 hours; with the max resultant displacement in the y-axis being 0.197 m in comparison to the dynamic result of 0.221 m an 11 % derivation. However, it was noted that the initial set-up to establish the ESL results was sub-optimal, with the load location being away from the primary deformation zone observed in the dynamic tests. Also, it applied a uniform load, which is not representative of the varying displacements seen across the contacting faces of the fuel tank.



Figure 5.5: Basic model set up for ESL assesment.

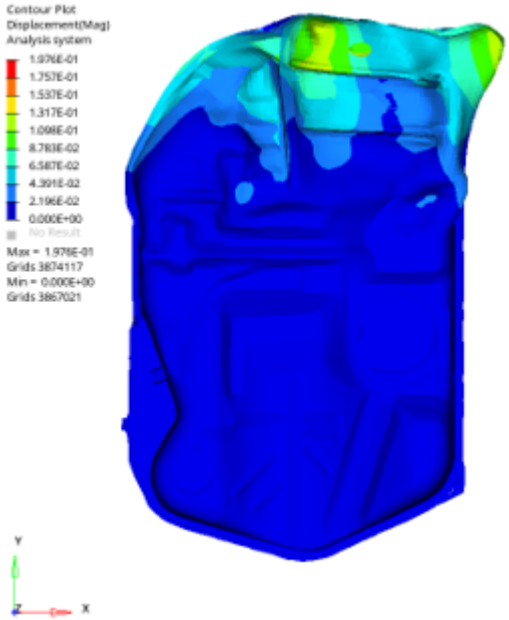



Figure 5.6: Displacement contour plot for initial ESL assesment of the fuel tank.

Following on, with confidence in the ESL assessments ability to represent the dynamic loads further detail was targeted, by the extraction of displacements for multiple regions of the fuel tanks contacting faces. The displacements were taken for three Y sections, being led by the

side impact with three sections for capturing X deformation from the rear impact. With 6 points evenly spaced within each of the zones and the average displacement per zone taken. As it is clearly observed on the end deformed fuel tank from the dynamic assessments that the deformations vary significantly across the contacting lengths of the tank. With primary areas of deformation being all three Y sections and X1 highlighted in Figure 5.7.

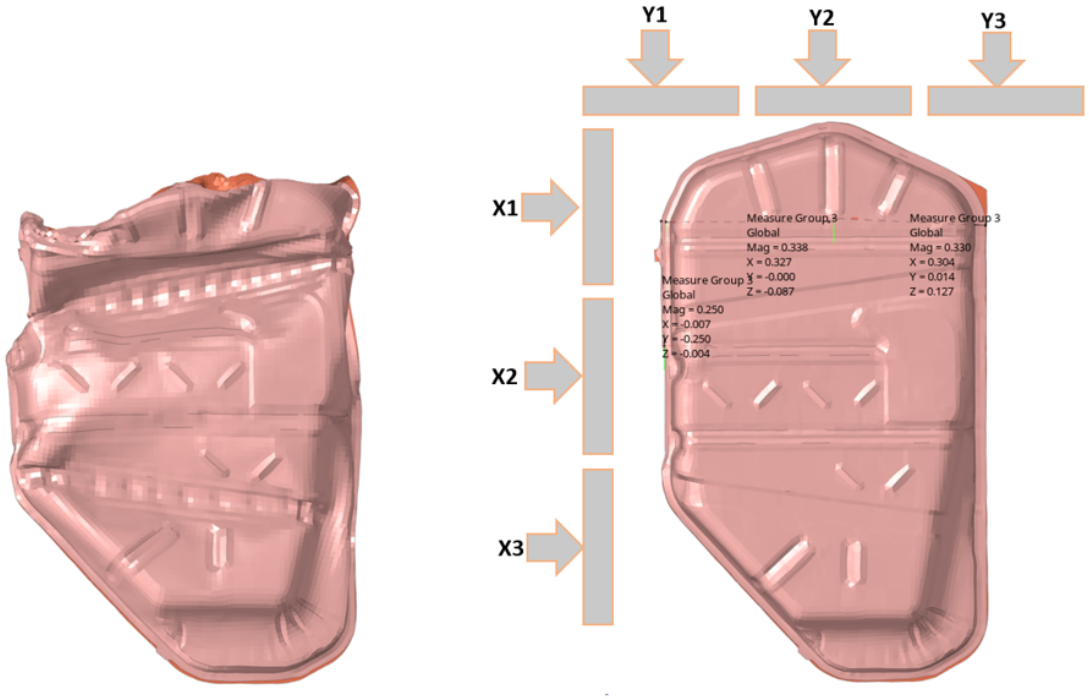



Figure 5.7: Left; Displaying deformed fuel tank post dynamic simulations. Right; Highlighted regions for individual ESL loading.

Figure 5.8 displays the results from the improved application of ESL loads with 6 varying loads being applied. Visually an improved correlation between the two results can be seen and this is supported by the max displacement value for the static assessment increasing to 0.232 m from the previous 0.197 m, bringing the result to within 5 % of the dynamic result of 0.221 m. As mentioned this could be partially due to the ESL force being calculated using the fuel tanks overall global stiffness and not capturing local stiffnesses. However, the result does display the ability to emulate a dynamic event at a component level with good accuracy which would in turn allow a designer to continue to optimise the design based upon the ESL loadings with rapid feedback, as opposed to iteratively designing and waiting in excess of a day for the dynamic result to provide feedback.

The ESL set-up however still offers the opportunity for further refinement, whether through an increased break down of the loads applied or through the improvement of the constraints utilised. As in the dynamic model energy is dissipated through the movement of the whole vehicle, with forces being transferred through and around the fuel tank. As such limited dof

constraints could further aid in the accuracy of the ESL model or a factor reduction in the loadings applied in the ESL model to compensated for the rigidity of the constraints.

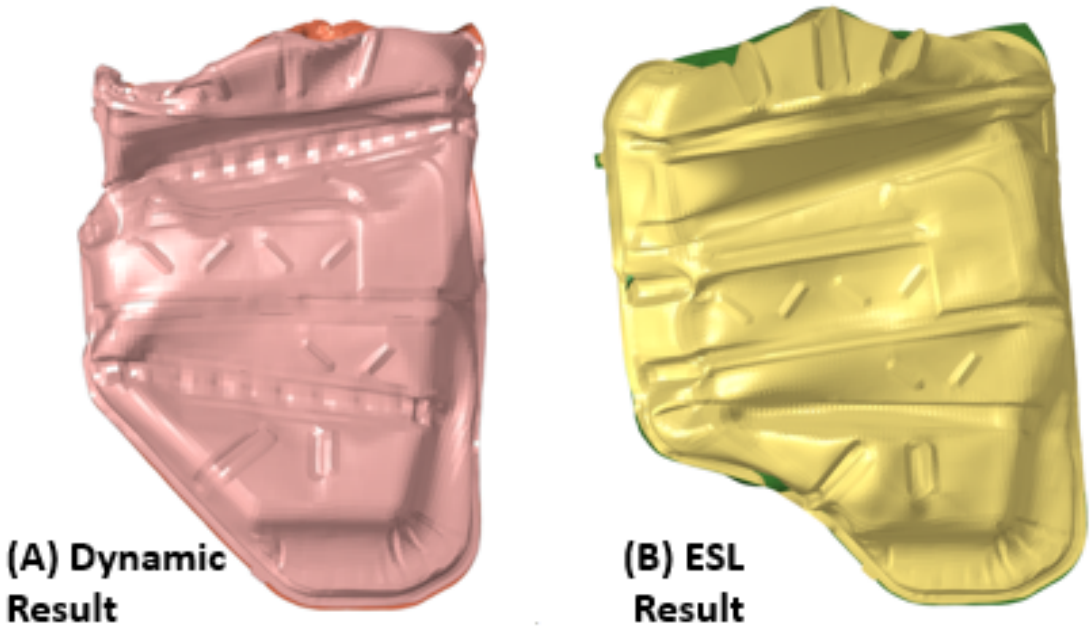



Figure 5.8: (A) End deformed fuel tank, post dynamic test. (B) End deformed fuel tank post ESL test.

## 5.3 Acceleration Method

Attempting to make the loading more representative, and adding back a level of complexity with the ESL force method, considering accelerations. Taking accelerations from the dynamic model in a similar fashion to that of the displacement extraction for ESL, however utilising a dynamic reduced sub-assembly model to obtain guidance on run time and potentially improved loadings over a purely linear static model.

This method uses similar principals to that of the Section 5.2 , the initial assessment takes the fuel tank and a rigid wall along the xz plane and accelerates the fuel tank into it. This simplified test was used to ascertain an approximate time frame for the sub-model assessment and initial result guidance. As if the run time was unfeasible for iterative design then further detailed evaluation would be redundant. Initial assessments provided a run time of 20minutes, and maximum displacements in the fuel tank of 0.182 m, an 18.2 % difference from those seen in the dynamic model. However, the key concern regarding CPU run time was satisfied.

As such, the model was built up further with the suggestion of using a similar method as that seen on the right of Figure 5.7 whereby a cage esque set-up could be formed around the fuel tank or any component which the user wishes to assess. With the metaphorical cage being

broken down into sections which can have individual loads applied to them to represent those observed in the dynamic events. This principal is preferable over the ESL method as it utilises the loadings of the body regardless of the ESS that would be housed within, meaning once successfully set up the user can substitute any ESS wishing to be assessed within the cage.

The 'cage' was set up using rigid walls for each of the previously highlighted sections, with relevant accelerations applied to each of the walls. With constraints then applied to the far end of the fuel tank in a similar fashion to that seen in the ESL assessments. Figure 5.9 shows the deformed result with stresses plotted, whilst deformations in x and y are well captured the overall behaviour of this model is not as desired. With the tank buckling along the centre line where the pressed indentations for fixings to the vehicle would be located. These regions instead are acting as initiators when the fuel tank is under load in isolation. Whilst this behaviour can be seen happening on the indentation nearest the impact site on the dynamic model, it has moved to the indent further from the site on this version. Reinforcing these regions was considered and tested, although this in turn resulted in over strengthening of the fuel tank and unrepresentative results.

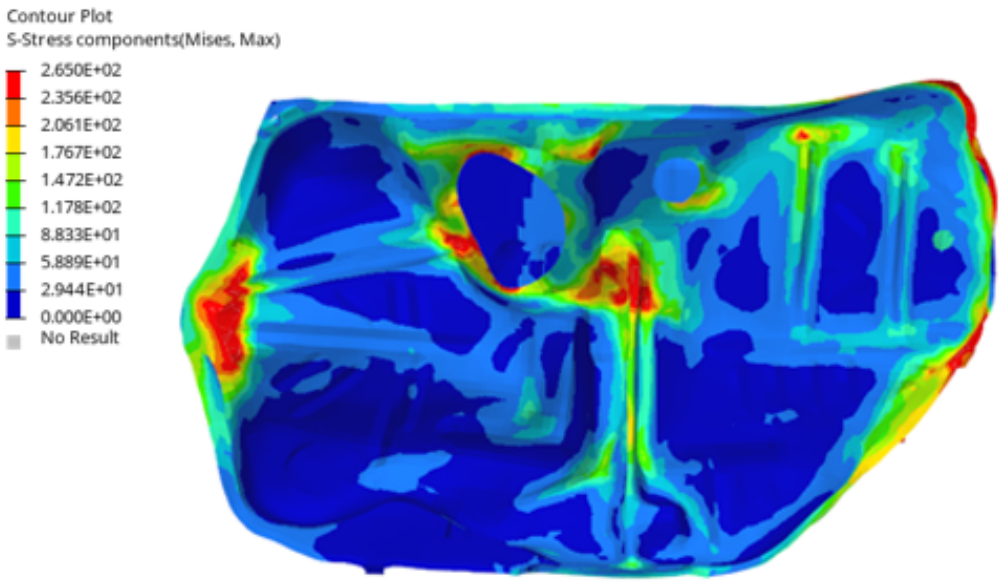



Figure 5.9: Stress contour plot of the fuel tank post assessment.

Another aspect which was considered to not be aiding in these undesirable outputs was that the rigid walls offered zero compliance when crushing the tank. Whereas the actual test would see both the tank and the sill deform in combination. Therefore, the substitution of the rigid walls for 1D members was considered, where the 1D members could be mapped with the relevant extrusion sections.

### 5.3.1 1D crush

Testing the crushing ability and interaction between the shell components and the 1D beams is key. Therefore, an initial assessment was made with a 1D beam with a box section profile applied to it, which was set with a imposed deformation to impact a simplified ESS substitute. Figure 5.10 showing the basic setup along with the deformed result, with the output displaying the 1D beam and the shell represented ESS substitute interacted appropriately. In continuation of this, the originally assessed fuel tank was subbed into the model, with the methodology continuing to function.

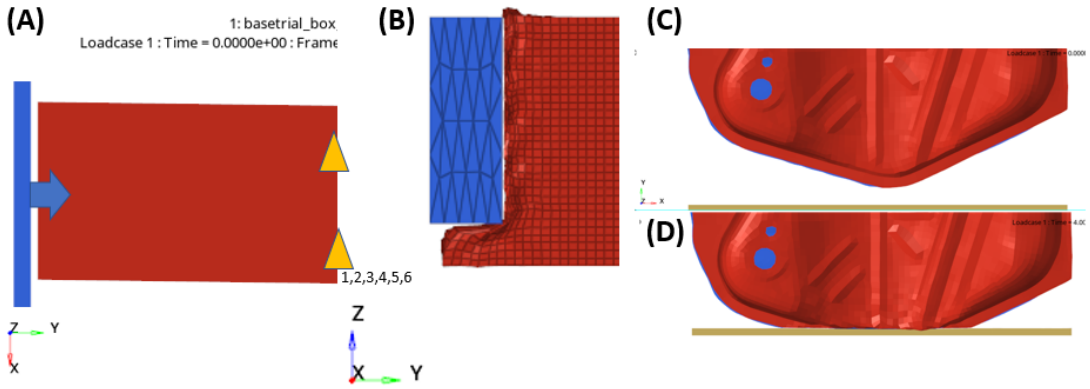



Figure 5.10: (A) Schematic of the initial 1D crush set-up. (B) Deformed result with 2D represented 1D beam. (C) Fuel tank 1D assessment pre-loading 3D mesh. (D) Fuel tank 1D assessment post-loading 3D meshed tank.

Progressing the model, to the original 'cage' suggestion was then carried out. With a sill section applied to the 1D beam and the deformations previously seen in Figure 5.3 applied to the 1D beams with a transient loading taken from the graph displayed. However, with these updates an issue was seen to occur with some of the 1D elements, interactions with the shell meshed fuel tank. The errors arising were based around the seam of the fuel tank whereby the 2D elements within this region failed. This is a well documented error, which occurs where 2D elements are not being axially loaded, previously in Figure 5.10 (B) the elements were loaded axially and as such no problems were noted.

The adjustment of the mesh to 3D, displayed a positive result with the tank being crushed by the surrounding 1D members as planned. This in turn had a negative effect on run time increasing it from 20 minutes to over 37 minutes. Whilst still an acceptable time frame when compared to the dfem this still poses almost a 100 % rise from the previous assessment and thousand fold over the ESL assessment.

## 5.4 C2 Model Development

Alternatively and following on from the issues raised by 1D beam interactions with 2D elements, a third option is to be considered and is relevant at both sub-model like above and vehicle level. That is the leveraging of C2 models for dynamic assessments. With a C2 model able to reduce run times to sub one hour for the full vehicle assessment.

### 5.4.1 Full vehicle C2.

The C2 frame model was built from the pre-existing DFEM for initial validation against the DFEM. The DFEM was broken down with ancillaries removed to allow for just the body to be assessed in a low fidelity c2 format, providing a base model to have various alternative ESS systems into it. The C2 skeleton generated can be seen in Figure 5.11 with the 2D represented sections adjacent. The reduced C2 model was assessed against the DFEM with additional masses added to the model to ensure a close representation to the DFEM; Good correlation was observed in Figure 5.12 with discrepancies due to the loss of load paths such as the ICE engine which in the DFEM reacts the load and transmits it to the tunnel region of the vehicle, with the C2 model having no ancillaries included the tunnel can not assist in reacting the loads from the front impact causing an increased buckle in the subframe members. Most notably with regards to this thesis' the run time was seen to reduce, with CPU run times varying between 15-30 mins, compared to 36 hours (2,160 mins) for the DFEM. Bringing it below the running time of the sub-assembly model within Section 5.3.

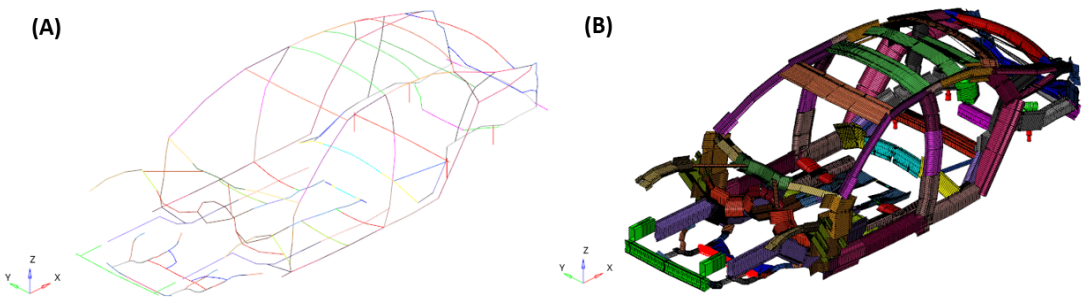



Figure 5.11: (A) C2 skeleton from DFEM (B) 2D realised sections of C2 skeleton.

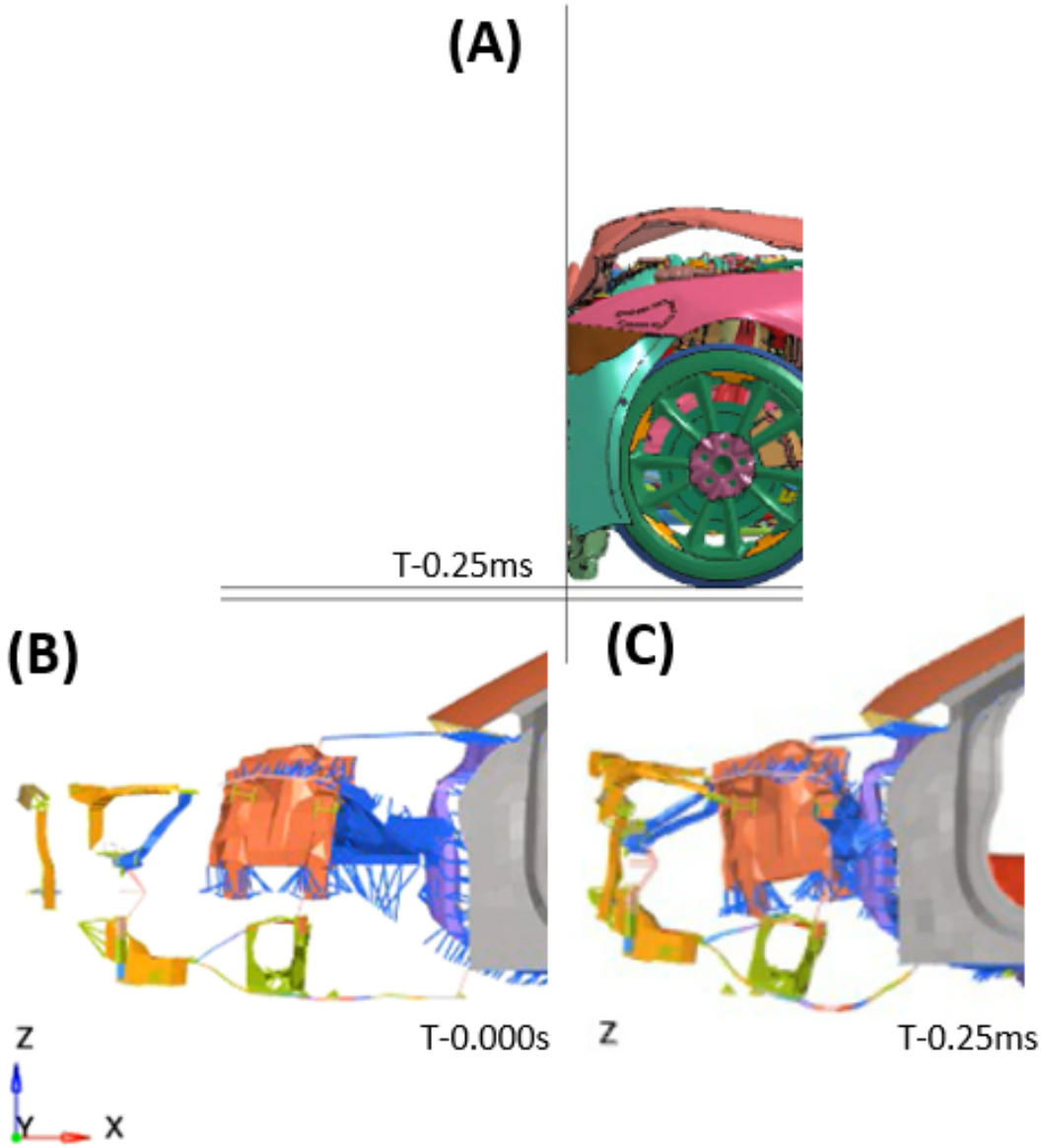



Figure 5.12: (A) Front rigid crash DFEM T=0.25 ms (B) Front rigid crash reduced C2 T=0.0 ms(C)Front rigid crash reduced C2 T=0.25 ms

### 5.4.2 Localised C2 vehicle assessment.

Progressing from the studies carried out previously and with evidence of the potential time frame of vehicle level C2 models, along with the noted negatives in loss of detail from using 1D elements in critical areas displacements and forces wish to be observed. The suggestion of a hybrid C2 model arose, as following the trends from FEA in the past as computing power has increased over time, so has the demand upon it. In turn resulting in a net zero time gain. For example a model of three hundred thousand elements previously taking 36 hours to run due to computing power, when power was increased reducing this time window as opposed to accepting the time saving more detail was demanded of models upping them to millions of elements and back to the original CPU time frame window. This trend indicates that users

demand for detail within there simulations surpasses that of the need for quicker results.

Continuing with this in mind, detail is evidently key as such if you were to combine both DFEM and low fidelity C2 you could reduced time and still deliver the comparative results. As within the frontal impact assessment carried out on the C2 model whereby all ancillaries had been removed, providing the appropriate masses were added to the model and COG etc. maintained the performance observed remained comparative to that of the DFEM. In the same manner that within the DFEM the refining of the mesh and detail of components to the rear of the vehicle away from the assessed region bring no further detail to the results. However, they will continue to add to the computational cost of analysis the problem.

As such, the reduction of fidelity for the C2 models away from the primary areas of investigation is suggested. With this in turn reduced the run time from the DFEM down to approximately six hours whilst showing almost identical results to those seen upon the DFEM.

## 5.5 Chapter Summary

From the above section various loading methods were discussed, each of which could potentially be leveraged in improving component design. ESL was the simplest method proposed and proved to be effective, although it has the draw back of not being able to be assessed without input from DFEM or physical test. It could be used on future vehicles where no pre-existing data is available but would then have to based on previous existing knowledge or high level preliminary intrusion targets and also planned component stiffnesses. Although if a previous model had already been assessed in this manner, the new ESS could be substituted into the static model with forces adjusted to correspond to the proposed ESS global stiffnesses.

The ESL method in addition to be the quickest of those reviewed, allows the most significant opportunities for design optimisation. With the quick solving linear model being able to carry out various optimisations upon the ESS system such as gauge, shape or even topology. The C2 hybrid approach could be used in conjunction to ESL, by being used to generate the inputs for the ESL studies, or as a more refined method of assessing newly generated designs within a lighter model than the full dfem. With the full dfem remaining desirable for final verification and assessment. The C2 'cage' method also offers users the ability to perform quick dynamic non-linear assessments upon ESS design which can help highlight any dynamic behaviours which may not be picked up with static linear loadings, through its inclusion of time dependent loading and more advanced material cards.

# Chapter 6

# Conclusion

sectionProject outcomes The work covered within this thesis' covered a broad range of topics all aiming to improve loadings at component level design and extracting these inputs in a computationally efficient manner.

Firstly example optimisation of an e-drive component was demonstrated, with careful consideration to the constraints to prevent gear misalignment. With the conventional design offering 6.222 kg weight saving, and a further 3.426 kg reduction being offered by un-constraining the design to truly maximise the mass savings. Providing guidance on the level in which e-axle components can be mass reduced if given the appropriate level of attention. Whilst also raising the question of how much further mass reduction could be taken with loadings from dynamic real world events taken.

The exploration of torque ripples and the accurate capture of the forces generated between gear contacts within an e-axle system were explored, with the conclusion of a print time expression suggestion to accurately capture the outputs for a range of motor speeds which would be observed in real world loadings. Whilst also highlighting, which events cause the most significant spikes in the forces observed, with this being the acceleration of the motor, which is a particular problem within some e-axle set ups due to the instant torque and rapid accelerating motors.

The final outcome was proving out the ability to set an ESL load case from a pre-existing dfem model, to allow for rapid assessment of various ESS design options. With the investigation into utilising low fidelity models to replace the dfem to allow quicker extraction of the input to support the ESL studies. The opportunity to leverage both of these methods in combination and with any proposed future ESS type the user may desire, providing an appropriate baseline is configured from pre-existing knowledge or pre-defined targets.

Whilst the end results may in some instances not yet be feasible with accessible code,

it does provide promise for the future design options and tools. Whilst also displaying the ability to extract these key loads in substitution for loads covered within the literature review from regulatory bodies which can be contradictory to other bodies and appear to be excessive. Therefore, not conducive to creating the most optimal vehicle to fulfil the industries alternatively fuelled future. These methods may not in the first instance save users time, but the intention of building these sub-models for component assessment would be able to be leveraged for multiple instances in conjunction with a growing data library to allow for rapid assessments in the future.

## 6.1 Future Work

Following on from the research carried out within this project, there is further scope for future work in two main areas; one being the investigations into the use of low fidelity models to improve other non covered vehicle performance challenges and the second the leveraging of the results from the studies to offer component optimisation opportunities. As mentioned, this work opened up more ideas for leveraging dynamic solvers to aid component design and optimisation. With a consideration that the low-fidelity model use, highlighted in this thesis for crash loadings. Could take a similar approach and also be applied to the NVH inputs, biased towards providing guidance for reducing or mitigating structural borne noises generated by e-axle components, through the ability to rapidly assess there effect on the entire vehicle system as opposed to in isolation.

With this thesis' focussing primarily on the extraction of loads from dynamic models and reducing the fidelity of them to allow for quicker result extraction and evaluation. The application of these extracted loads and comparisons to prescribed loads from standards would also offer further insight into the theoretical advantage the utilisation of these techniques may offer. Allowing a potentially more economical future FCEV design through unlocking substantial light weighting by deviating from regulatory standards and reducing loadings where proven to be appropriate.

# Bibliography


[1] R. Wohlecker and M. Funcke, "EGVI Expert Workshop on Testing of Electric Vehicle Performance and Safety Battery Safety and Electric Vehicle Benchmarking Agenda Introduction Battery Safety Requirements Testing Simulation Electric Vehicle Benchmarking Summary," no. 1, 2014.

[2] N. Lutsey, "Review of Technical Literature and Trends Related to Automobile Mass-Reduction Technology May 2010," no. Mayl, 2010.

[3] A. Chernoff, "A reinvented industry - The skateboard platform impact - A 20 year journey."

[4] U. D. of Energy, "Alternative Fuels Data Center: How Do Gasoline Cars Work?," 2009.

[5] U. D. of Energy, "Alternative Fuels Data Center: How Do Hybrid Electric Cars Work?," 2009.

[6] U. D. of Energy, "Alternative Fuels Data Center: How Do Plug-In Hybrid Electric Cars Work?," 2009.

[7] U. D. of Energy, "Alternative Fuels Data Center: How Do All-Electric Cars Work?," 2009.

[8] U. D. of Energy, "Alternative Fuels Data Center: How Do Fuel Cell Electric Vehicles Work Using Hydrogen?," 2009.

[9] E. C. Sherbrooke, N. M. Patrikalakis, and E. Brisson, "An algorithm for the medial axis transform of 3D polyhedral solids," *IEEE Transactions on Visualization and Computer Graphics*, vol. 2, no. 1, pp. 44–61, 1996.

[10] T. N. H. S. Agency, "Crash Simulation Vehicle Models," 2001.

[11] CECA and CSTE, "Assessment requirements for forerunner standard - Electric vehicles traction batteries," tech. rep., 2021.

[12] J. Kukreja, T. Nguyen, T. Siegmund, W. Chen, W. Tsutsui, K. Balakrishnan, H. Liao, and N. Parab, "Crash analysis of a conceptual electric vehicle with a damage tolerant battery pack," *Extreme Mechanics Letters*, vol. 9, pp. 371–378, 2016.

[13] M. de Podesta, "ICE vs BEV vs FC," 2021.

[14] J. Meschke, J. Tölle, and L. Berger, "Multi-material Concept for a Battery Electric Vehicle," *ATZ worldwide*, vol. 119, no. 11, pp. 48–53, 2017.

[15] F. Hao, X. Lu, Y. Qiao, and X. Chen, "Crashworthiness Analysis of Electric Vehicle with Energy-Absorbing Battery Modules," *Journal of Engineering Materials and Technology, Transactions of the ASME*, vol. 139, no. 2, pp. 1–4, 2017.

[16] I. A. E. P. Ltd., "A Guide to Differential Parts and Their Uses," 2024.

[17] R. D. Ali, "Design and Development of a Chassis Concept for an Autonomous Airport Shuttle," 2020.

[18] R. T. Sataloff, M. M. Johns, and K. M. Kost, "Package of Implementation measures for the EU's objectives on climate change and renewable energy for 2020," 2008.

[19] Unkown, "Number of registered passenger cars in Europe (EU-28) from 1990 to 2017," 2019.

[20] European Automobile Manufacturers Association, "The Automobile Industry Pocket Guide," tech. rep., ACEA, 2020.

[21] S. Hawkins, A. Holmes, D. Ames, K. Rahman, and R. Malone, "Design Optimization, Development and Manufacturing of General Motors New Battery Electric Vehicle Drive Unit (1ET35)," *SAE International Journal of Alternative Powertrains*, vol. 3, no. 2, pp. 213–221, 2014.

[22] JATO, "In September 2020, for the first time in European history, registrations for electrified vehicles overtook diesel.," Tech. Rep. September 2019, JATO, 2020.

[23] ACEA, "Fuel types of new passenger cars in the EU," 2022.

[24] Department for Transport, "Outcome and response to ending the sale of new petrol, diesel and hybrid cars and vans.," tech. rep., UK Government, 2021.

[25] R. B. Farrington, R. Anderson, D. M. Blake, and S. D. Burch, "Challenges and Potential Solutions for Reducing Climate Control Loads in Conventional and Hybrid Electric Vehicles," pp. 2–4, 1999.

[26] J. Dumortier, S. Siddiki, S. Carley, J. Cisney, R. M. Krause, B. W. Lane, J. A. Rupp, and J. D. Graham, "Effects of Life Cycle Cost Information Disclosure on the Purchase Decision of Hybrid and Plug-In Vehicles E ff ects of Life Cycle Cost Information Disclosure on the Purchase Decision of Hybrid and Plug-In Vehicles," no. February, 2015.

[27] M. Yugo and A. Soler, "A look into the role of e-fuels in the transport system in Europe (2030-2050)," vol. 28, no. 1, pp. 4–22, 2019.

[28] E. Yurday, "Average MPG for Cars UK 2020," 2020.

[29] E. Yurday, "Average Electric Car Range in the UK 2020," 2020.

[30] UKPIA, "UKPIA - Statistical Review," tech. rep., UKPIA, 2019.

[31] A. B. Balaji, C. Rudd, and X. Liu, "Recycled Carbon Fibers ( rCF ) in Automobiles : Towards Circular Economy," 2020.

[32] P. J. Frey and P.-l. George, "Mesh Generation: Application to Finite Elements: Second Edition," *Mesh Generation: Application to Finite Elements: Second Edition*, 2008.

[33] T. Zheng and T. Ji, "Equivalent representations of beams with periodically variable cross-sections," *Engineering Structures*, vol. 33, no. 3, pp. 706–719, 2011.

[34] Altair, "1D Elements," pp. 1–20.

[35] H. Blum, "A Transformation For Extracting New Descriptors of Shape," pp. 362–380, 1967.

[36] T. K. H. Tam and C. G. Armstrong, "2D finite element mesh generation by medial axis subdivision," *Advances in Engineering Software and Workstations*, vol. 13, no. 5, pp. 313–324, 1991.

[37] Altair and M. Goelke, "3D Meshing ," *Practical Finite Element Anlaysis*, vol. 1, pp. 1–34, 2008.

[38] W. Frei, "Meshing Your Geometry: When to Use the Various Element Types," 2013.

[39] M. Viceconti, L. Bellingeri, L. Cristofolini, and A. Toni, "A comparative study on different methods of automatic mesh generation of human femurs," *Medical Engineering & Physics*, vol. 20, pp. 1–10, apr 1998.

[40] Altair Engineering, *Practical Aspects of Finite Element Simulation.* No. Study Guide, 2016.

[41] Q. Fang and D. A. Boas, "Tetrahedral mesh generation from volumetric binary and grayscale images," in *2009 IEEE International Symposium on Biomedical Imaging: From Nano to Macro*, pp. 1142–1145, jun 2009.

[42] Altair Engineering and R. Ponginan, "Tetra Meshing Introduction Tetrameshing : Standard Tetrameshing," 2016.

[43] A. M. Shahhosseini, G. Prater, G. M. Osborne, E. Y. Kuo, and P. R. Mehta, "Major compliance joint modelling survey for automotive body structures," *International Journal of Vehicle Systems Modelling and Testing*, vol. 5, no. 1, pp. 1–17, 2010.

[44] G. Georgiou and T. Zeguer, "On the assessment of the macro-element methodology for full vehicle crashworthiness analysis," *International Journal of Crashworthiness*, vol. 23, no. 3, pp. 336–353, 2017.

[45] T. Wierzbicki and W. Abramowicz, "On the Crushing Mechanics of Thin-Walled Structures," *Journal of Applied Mechanics*, vol. 50, pp. 727–734, dec 1983.

[46] W. Abramowicz and T. Wierzbicki, "Axial Crushing of Multicorner Sheet Metal Columns," *Journal of Applied Mechanics*, vol. 56, pp. 113–120, mar 1989.

[47] S. Bates, P. Rousseau, G. Georgiou, and T. Zeguer, "Build, Verify & Optimise a Body-in-White Structure in a Working Day," in *Altair Technology Conference*, 2019.

[48] P. D. Bois, C. C. Chou, B. B. Fileta, A. I. King, and H. F. Mahmood, "VEHICLE AND OCCUPANT PROTECTION," tech. rep., Automotive Applications Committee; American Iron and Steel Institute, 2004.

[49] I. Fallon and D. O'Neill, "The world's first automobile fatality," *Accident Analysis and Prevention*, vol. 37, no. 4, pp. 601–603, 2005.

[50] I. Roberts, "Reducing road traffic," *British Medical Journal*, vol. 316, no. January, pp. 242–243, 1998.

[51] J. Hughes, "The history of car safety testing - how cars came to be rigorously tested - John Hughes," 2018.

[52] Department for Transport, "Road Use Statistics Great Britain 2016," Tech. Rep. 6, 2016.

[53] Euro-NCAP, "The Ratings Explained."

[54] T. Gilles, *Automotive Chassis: Brakes, Suspension, and Steering*. Thomson Delmar Learning, 2005.

[55] Euro-NCAP, "EUROPEAN NEW CAR ASSESSMENT PROGRAMME ( Euro NCAP ) FRONTAL IMPACT," no. October, p. 52, 2013.

[56] EuroNCAP, "European New Car Assessment Programme L7e Side Impact," no. June, p. 52, 2014.

[57] Euro-NCAP, *EUROPEAN NEW CAR ASSESSMENT PROGRAMME ( Euro NCAP ) THE DYNAMIC ASSESSMENT OF CAR SEATS FO R NECK INJURY PROTECTIO N TESTING PROTOCOL.* No. June, Euro-NCAP, 2011.

[58] T. Ambati, K. Srikanth, and P. Veeraraju, "Simulation of vehicular frontal crashtest," *International Journal of Applied Research in Mechanical Engineering (IJARME)*, vol. 2, no. 1, pp. 37–42, 2012.

[59] K. Komeilizadeh, R. Hefele, and F. Duddeck, "A Multifidelity Approach Using Physical and Mathematical Surrogates for Crash Optimization," *Pamm*, vol. 18, no. 1, pp. 20–21, 2018.

[60] R. Thornhill, *Exploration of Midmeshing technologies for efficient crash analysis and BIW design.* PhD thesis, Swansea University, 2018.

[61] L. Wech, R. Richter, R. Justen, and R. Schöneburg, "Crash Safety Aspects of HV Batteries for Vehicles," *22nd ESV Conference Proceedings*, no. Table 1, pp. 1–8, 2011.

[62] R. Justen and R. Schöneburg, "Crash safety of hybrid-and battery electric vehicles," *22th ESV-Conference*, pp. 1–9, 2011.

[63] R. Justen, A. Lamm, R. Schöneburg, and D. Scheuner, "Crash safety of lithium-ion batteries in hybrid vehicles," in *FIVE Fires in Vehicles*, (Gothenburg, Sweden), 2010.

[64] V. Ruiz, A. Pfrang, A. Kriston, N. Omar, P. Van den Bossche, and L. Boon-Brett, "A review of international abuse testing standards and regulations for lithium ion batteries in electric and hybrid electric vehicles," *Renewable and Sustainable Energy Reviews*, vol. 81, no. May, pp. 1427–1452, 2018.

[65] DVLA, "Driving Licence Categories."

[66] Q. Liu, Y. Lin, Z. Zong, G. Sun, and Q. Li, "Lightweight design of carbon twill weave fabric composite body structure for electric vehicle," *Composite Structures*, vol. 97, pp. 231–238, 2013.

[67] M. Schäffer, M. Münster, R. Sturm, and H. E. Friedrich, "Development of an optimised side crash concept for the battery - electric vehicle concept Urban Modular Vehicle," no. October, 2016.

[68] T. Hofman and C. H. Dai, "Energy efficiency analysis and comparison of transmission technologies for an electric vehicle," *2010 IEEE Vehicle Power and Propulsion Conference, VPPC 2010*, 2010.

[69] S. Nakakuki, "NII-Electronic Library Service," *Chemical and Pharmaceutical Bulletin*, vol. 34, no. 1, pp. 430 – 433, 1986.

[70] J. Wang, H. Wang, and L. Guo, "Analysis of effect of random perturbation on dynamic response of gear transmission system," *Chaos, Solitons and Fractals*, vol. 68, pp. 78–88, 2014.

[71] E. Sato, S. Sasaki, J. K. Kaisha, F. Application, P. Data, P. Examiner, and T. Lewis, "( 12 ) United States Patent," vol. 2, no. 12, 2006.

[72] S. Du, R. B. Randall, and D. W. Kelly, "Modelling of spur gear mesh stiffness and static transmission error," *Proceedings of the Institution of Mechanical Engineers, Part C: Journal of Mechanical Engineering Science*, vol. 212, no. 4, pp. 287–297, 1998.

[73] J. Lin and R. G. Parker, "Planetary gear parametric instability caused by mesh stiffness variation," *Journal of Sound and Vibration*, vol. 249, no. 1, pp. 129–145, 2002.

Appendix

# .1 Misalignment Tables

## .1.1 Steel Benchmark Misalignments

| Misalignment (mrad) | Steel Original Version | | | | | | | | | | | |
|---|---|---|---|---|---|---|---|---|---|---|---|---|
| Angle (deg) | 0.00 | 30.00 | 60.00 | 90.00 | 120.00 | 150.00 | 180.00 | 210.00 | 240.00 | 270.00 | 300.00 | 330.00 |
| PLL1 | | | | | | | | | | | | |
| Pin 1 | 0.342 | 0.374 | 0.393 | 0.398 | 0.379 | 0.348 | 0.306 | 0.253 | 0.199 | 0.179 | 0.22 | 0.291 |
| Pin 2 | 0.221 | 0.259 | 0.306 | 0.36 | 0.398 | 0.413 | 0.407 | 0.374 | 0.309 | 0.24 | 0.199 | 0.199 |
| Pin 3 | 0.294 | 0.259 | 0.233 | 0.232 | 0.257 | 0.295 | 0.332 | 0.356 | 0.354 | 0.338 | 0.331 | 0.323 |
| Pinion | 0.329 | 0.337 | 0.337 | 0.343 | 0.359 | 0.374 | 0.378 | 0.36 | 0.334 | 0.313 | 0.309 | 0.32 |
| PLL2 | | | | | | | | | | | | |
| Pin 1 | 0.32 | 0.337 | 0.336 | 0.321 | 0.292 | 0.253 | 0.198 | 0.145 | 0.141 | 0.192 | 0.248 | 0.292 |
| Pin 2 | 0.228 | 0.277 | 0.315 | 0.34 | 0.35 | 0.339 | 0.3 | 0.243 | 0.185 | 0.152 | 0.155 | 0.185 |
| Pin 3 | 0.203 | 0.188 | 0.194 | 0.222 | 0.26 | 0.289 | 0.296 | 0.286 | 0.276 | 0.268 | 0.255 | 0.231 |
| Pinion | 0.26 | 0.269 | 0.277 | 0.291 | 0.303 | 0.3 | 0.281 | 0.253 | 0.237 | 0.238 | 0.249 | 0.257 |

## .1.2 Titanium Benchmark Misalignments

| Misalignment (mrad) | Titanium Original Version | | | | | | | | | | | |
|---|---|---|---|---|---|---|---|---|---|---|---|---|
| Angle (deg) | 0.00 | 30.00 | 60.00 | 90.00 | 120.00 | 150.00 | 180.00 | 210.00 | 240.00 | 270.00 | 300.00 | 330.00 |
| PLL1 | | | | | | | | | | | | |
| Pin 1 | 0.323 | 0.353 | 0.372 | 0.376 | 0.359 | 0.329 | 0.288 | 0.238 | 0.186 | 0.168 | 0.209 | 0.275 |
| Pin 2 | 0.208 | 0.244 | 0.289 | 0.34 | 0.375 | 0.389 | 0.384 | 0.353 | 0.292 | 0.227 | 0.188 | 0.187 |
| Pin 3 | 0.278 | 0.245 | 0.22 | 0.218 | 0.242 | 0.278 | 0.314 | 0.336 | 0.335 | 0.319 | 0.313 | 0.306 |
| Pinion | 0.311 | 0.318 | 0.317 | 0.323 | 0.339 | 0.353 | 0.356 | 0.34 | 0.315 | 0.295 | 0.292 | 0.302 |
| PLL2 | | | | | | | | | | | | |
| Pin 1 | 0.303 | 0.318 | 0.318 | 0.304 | 0.278 | 0.239 | 0.193 | 0.137 | 0.133 | 0.183 | 0.236 | 0.276 |
| Pin 2 | 0.216 | 0.263 | 0.298 | 0.321 | 0.331 | 0.32 | 0.284 | 0.23 | 0.176 | 0.144 | 0.146 | 0.174 |
| Pin 3 | 0.193 | 0.178 | 0.182 | 0.21 | 0.246 | 0.274 | 0.28 | 0.271 | 0.261 | 0.254 | 0.242 | 0.22 |
| Pinion | 0.248 | 0.254 | 0.262 | 0.275 | 0.287 | 0.284 | 0.266 | 0.239 | 0.225 | 0.226 | 0.236 | 0.243 |

### .1.3 Misalignments for V4 steel castable model.

| Misalignment (mrad) | Steel Castable V4 | | | | | | | | | | | |
|---|---|---|---|---|---|---|---|---|---|---|---|---|
| Angle (deg) | 0.00 | 30.00 | 60.00 | 90.00 | 120.00 | 150.00 | 180.00 | 210.00 | 240.00 | 270.00 | 300.00 | 330.00 |
| Loadcase 1 | | | | | | | | | | | | |
| Pin 1 | 0.55 | 0.599 | 0.602 | 0.561 | 0.478 | 0.362 | 0.225 | 0.08 | 0.068 | 0.215 | 0.443 | 0.529 |
| Pin 2 | 0.144 | 0.291 | 0.803 | 0.524 | 0.591 | 0.613 | 0.59 | 0.525 | 0.424 | 0.298 | 0.154 | 0.009 |
| Pin 3 | 0.402 | 0.28 | 0.144 | 0.028 | 0.139 | 0.273 | 0.396 | 0.495 | 0.561 | 0.584 | 0.562 | 0.5 |
| Pinion | 0.247 | 0.262 | 0.274 | 0.282 | 0.286 | 0.281 | 0.273 | 0.261 | 0.254 | 0.248 | 0.244 | 0.244 |
| Loadcase 2 | | | | | | | | | | | | |
| Pin 1 | 0.539 | 0.54 | 0.499 | 0.422 | 0.317 | 0.195 | 0.071 | 0.099 | 0.228 | 0.348 | 0.443 | 0.507 |
| Pin 2 | 0.296 | 0.416 | 0.491 | 0.536 | 0.546 | 0.524 | 0.465 | 0.372 | 0.258 | 0.133 | 0.057 | 0.167 |
| Pin 3 | 0.237 | 0.114 | 0.026 | 0.15 | 0.273 | 0.381 | 0.461 | 0.505 | 0.517 | 0.496 | 0.438 | 0.349 |
| Pinion | 0.206 | 0.221 | 0.227 | 0.228 | 0.224 | 0.214 | 0.205 | 0.195 | 0.19 | 0.187 | 0.188 | 0.195 |

### .1.4 Table displaying misalignments for v4 steel castable model with the park lock removed.

| Misalignment (mrad) | Steel Castable V4, with no park lock wheel | | | | | | | | | | | |
|---|---|---|---|---|---|---|---|---|---|---|---|---|
| Angle (deg) | 0.00 | 30.00 | 60.00 | 90.00 | 120.00 | 150.00 | 180.00 | 210.00 | 240.00 | 270.00 | 300.00 | 330.00 |
| Loadcase 1 | | | | | | | | | | | | |
| Pin 1 | 0.554 | 0.621 | 0.607 | 0.565 | 0.481 | 0.364 | 0.226 | 0.081 | 0.068 | 0.215 | 0.353 | 0.469 |
| Pin 2 | 0.139 | 0.292 | 0.423 | 0.528 | 0.595 | 0.618 | 0.593 | 0.528 | 0.427 | 0.299 | 0.154 | 0.011 |
| Pin 3 | 0.404 | 0.28 | 0.144 | 0.026 | 0.139 | 0.273 | 0.398 | 0.498 | 0.565 | 0.588 | 0.566 | 0.504 |
| Pinion | 0.248 | 0.263 | 0.275 | 0.283 | 0.287 | 0.282 | 0.274 | 0.262 | 0.254 | 0.249 | 0.245 | 0.245 |
| Loadcase 2 | | | | | | | | | | | | |
| Pin 1 | 0.544 | 0.544 | 0.503 | 0.424 | 0.319 | 0.197 | 0.073 | 0.101 | 0.23 | 0.35 | 0.446 | 0.511 |
| Pin 2 | 0.298 | 0.412 | 0.494 | 0.54 | 0.55 | 0.528 | 0.468 | 0.375 | 0.259 | 0.134 | 0.059 | 0.168 |
| Pin 3 | 0.238 | 0.115 | 0.027 | 0.15 | 0.275 | 0.383 | 0.464 | 0.509 | 0.521 | 0.5 | 0.441 | 0.351 |
| Pinion | 0.206 | 0.222 | 0.228 | 0.229 | 0.224 | 0.215 | 0.206 | 0.196 | 0.19 | 0.188 | 0.189 | 0.196 |

### .1.5 Table displaying misalignments for adjusted v4 steel model, for no park lock instances.

| Misalignment (mrad) | Steel Castable V4, redesign for no park lock instances | | | | | | | | | | | |
|---|---|---|---|---|---|---|---|---|---|---|---|---|
| Angle (deg) | 0.00 | 30.00 | 60.00 | 90.00 | 120.00 | 150.00 | 180.00 | 210.00 | 240.00 | 270.00 | 300.00 | 330.00 |
| Loadcase 1 | | | | | | | | | | | | |
| Pin 1 | 0.586 | 0.632 | 0.632 | 0.588 | 0.499 | 0.376 | 0.234 | 0.089 | 0.064 | 0.221 | 0.372 | 0.499 |
| Pin 2 | 0.142 | 0.293 | 0.434 | 0.549 | 0.623 | 0.647 | 0.625 | 0.559 | 0.451 | 0.314 | 0.163 | 0.018 |
| Pin 3 | 0.436 | 0.302 | 0.154 | 0.013 | 0.136 | 0.279 | 0.417 | 0.529 | 0.602 | 0.626 | 0.605 | 0.542 |
| Pinion | 0.257 | 0.27 | 0.279 | 0.286 | 0.292 | 0.286 | 0.284 | 0.27 | 0.26 | 0.255 | 0.253 | 0.253 |
| Loadcase 2 | | | | | | | | | | | | |
| Pin 1 | 0.572 | 0.568 | 0.521 | 0.436 | 0.325 | 0.201 | 0.077 | 0.109 | 0.245 | 0.374 | 0.474 | 0.541 |
| Pin 2 | 0.31 | 0.43 | 0.517 | 0.568 | 0.581 | 0.558 | 0.494 | 0.393 | 0.27 | 0.141 | 0.067 | 0.176 |
| Pin 3 | 0.255 | 0.126 | 0.044 | 0.162 | 0.294 | 0.41 | 0.496 | 0.546 | 0.56 | 0.538 | 0.475 | 0.376 |
| Pinion | 0.212 | 0.224 | 0.231 | 0.234 | 0.232 | 0.223 | 0.213 | 0.2 | 0.195 | 0.194 | 0.197 | 0.204 |

### .1.6 Table displaying misalignments for titanium version of v4

| Misalignment (mrad) | Titanium Castable Version 1 | | | | | | | | | | | |
|---|---|---|---|---|---|---|---|---|---|---|---|---|
| Angle (deg) | 0.00 | 30.00 | 60.00 | 90.00 | 120.00 | 150.00 | 180.00 | 210.00 | 240.00 | 270.00 | 300.00 | 330.00 |
| PLL1 | | | | | | | | | | | | |
| Pin 1 | 0.519 | 0.566 | 0.569 | 0.529 | 0.451 | 0.342 | 0.212 | 0.075 | 0.065 | 0.204 | 0.332 | 0.44 |
| Pin 2 | 0.138 | 0.276 | 0.398 | 0.495 | 0.558 | 0.579 | 0.557 | 0.495 | 0.4 | 0.28 | 0.145 | 0.009 |
| Pin 3 | 0.379 | 0.263 | 0.135 | 0.025 | 0.132 | 0.258 | 0.436 | 0.468 | 0.53 | 0.552 | 0.53 | 0.472 |
| Pinion | 0.233 | 0.246 | 0.258 | 0.266 | 0.27 | 0.265 | 0.257 | 0.246 | 0.239 | 0.234 | 0.228 | 0.238 |
| PLL2 | | | | | | | | | | | | |
| Pin 1 | 0.51 | 0.51 | 0.472 | 0.399 | 0.3 | 0.184 | 0.067 | 0.094 | 0.216 | 0.33 | 0.419 | 0.479 |
| Pin 2 | 0.28 | 0.388 | 0.464 | 0.507 | 0.516 | 0.495 | 0.439 | 0.352 | 0.244 | 0.125 | 0.054 | 0.158 |
| Pin 3 | 0.224 | 0.108 | 0.024 | 0.142 | 0.259 | 0.361 | 0.375 | 0.478 | 0.489 | 0.469 | 0.415 | 0.33 |
| Pinion | 0.194 | 0.209 | 0.215 | 0.215 | 0.211 | 0.202 | 0.194 | 0.184 | 0.179 | 0.177 | 0.178 | 0.172 |

### .1.7 Table displaying misalignments for v5 steel additive manufacture model.

| Misalignment (mrad) | Steel Additive Manfacture Version | | | | | | | | | | | |
|---|---|---|---|---|---|---|---|---|---|---|---|---|
| Angle (deg) | 0.00 | 30.00 | 60.00 | 90.00 | 120.00 | 150.00 | 180.00 | 210.00 | 240.00 | 270.00 | 300.00 | 330.00 |
| PLL1 | | | | | | | | | | | | |
| Pin 1 | 1.112 | 1.119 | 1.212 | 1.123 | 0.933 | 0.697 | 0.445 | 0.215 | 0.114 | 0.368 | 0.654 | 0.929 |
| Pin 2 | 0.269 | 0.548 | 0.827 | 1.087 | 1.236 | 1.25 | 1.18 | 1.025 | 0.79 | 0.527 | 0.26 | 0.078 |
| Pin 3 | 0.757 | 0.5 | 0.247 | 0.128 | 0.301 | 0.553 | 0.813 | 1.05 | 1.184 | 1.193 | 1.13 | 0.986 |
| Pinion | 0.706 | 0.748 | 0.779 | 0.8 | 0.816 | 0.816 | 0.792 | 0.746 | 0.715 | 0.7 | 0.689 | 0.688 |
| PLL2 | | | | | | | | | | | | |
| Pin 1 | 1.035 | 1.035 | 0.955 | 0.8 | 0.593 | 0.374 | 0.14 | 0.12 | 0.391 | 0.654 | 0.853 | 0.977 |
| Pin 2 | 0.565 | 0.817 | 0.987 | 1.064 | 1.062 | 0.999 | 0.868 | 0.672 | 0.437 | 0.201 | 0.044 | 0.301 |
| Pin 3 | 0.402 | 0.175 | 0.07 | 0.309 | 0.558 | 0.789 | 0.945 | 1.01 | 1.007 | 0.949 | 0.824 | 0.634 |
| Pinion | 0.59 | 0.628 | 0.652 | 0.659 | 0.649 | 0.623 | 0.591 | 0.555 | 0.534 | 0.529 | 0.539 | 0.561 |

### .1.8 Table displaying misalignments for titanium additive manufacture model.

| Misalignment (mrad) | Titanium Additive Manufactured Version | | | | | | | | | | | |
|---|---|---|---|---|---|---|---|---|---|---|---|---|
| Angle (deg) | 0.00 | 30.00 | 60.00 | 90.00 | 120.00 | 150.00 | 180.00 | 210.00 | 240.00 | 270.00 | 300.00 | 330.00 |
| PLL1 | | | | | | | | | | | | |
| Pin 1 | 0.624 | 0.693 | 0.706 | 0.64 | 0.515 | 0.382 | 0.261 | 0.161 | 0.085 | 0.164 | 0.321 | 0.495 |
| Pin 2 | 0.152 | 0.278 | 0.428 | 0.589 | 0.696 | 0.723 | 0.689 | 0.584 | 0.428 | 0.28 | 0.143 | 0.091 |
| Pin 3 | 0.407 | 0.261 | 0.153 | 0.129 | 0.176 | 0.278 | 0.413 | 0.56 | 0.658 | 0.683 | 0.653 | 0.555 |
| Pinion | 0.408 | 0.436 | 0.455 | 0.459 | 0.465 | 0.47 | 0.463 | 0.432 | 0.412 | 0.409 | 0.399 | 0.399 |
| PLL2 | | | | | | | | | | | | |
| Pin 1 | 0.604 | 0.605 | 0.549 | 0.45 | 0.331 | 0.222 | 0.115 | 0.047 | 0.182 | 0.337 | 0.463 | 0.554 |
| Pin 2 | 0.293 | 0.437 | 0.541 | 0.602 | 0.618 | 0.586 | 0.5 | 0.37 | 0.227 | 0.105 | 0.044 | 0.154 |
| Pin 3 | 0.21 | 0.109 | 0.081 | 0.163 | 0.285 | 0.413 | 0.508 | 0.563 | 0.579 | 0.549 | 0.467 | 0.344 |
| Pinion | 0.343 | 0.364 | 0.375 | 0.379 | 0.386 | 0.36 | 0.344 | 0.324 | 0.312 | 0.31 | 0.315 | 0.327 |

### .1.9 Table displaying misalignments for version four of titanium additive manufacture model.

| Misalignment (mrad) | Titanium Additive Manufactured Version 3 | | | | | | | | | | | |
|---|---|---|---|---|---|---|---|---|---|---|---|---|
| Angle (deg) | 0.00 | 30.00 | 60.00 | 90.00 | 120.00 | 150.00 | 180.00 | 210.00 | 240.00 | 270.00 | 300.00 | 330.00 |
| PLL1 | | | | | | | | | | | | |
| Pin 1 | 0.763 | 0.83 | 0.843 | 0.795 | 0.677 | 0.517 | 0.349 | 0.209 | 0.162 | 0.292 | 0.475 | 0.645 |
| Pin 2 | 0.232 | 0.407 | 0.591 | 0.747 | 0.84 | 0.86 | 0.823 | 0.734 | 0.588 | 0.408 | 0.234 | 0.145 |
| Pin 3 | 0.558 | 0.393 | 0.249 | 0.196 | 0.262 | 0.404 | 0.57 | 0.713 | 0.797 | 0.814 | 0.78 | 0.697 |
| Pinion | 0.447 | 0.473 | 0.495 | 0.509 | 0.515 | 0.511 | 0.499 | 0.478 | 0.46 | 0.447 | 0.439 | 0.438 |
| PLL2 | | | | | | | | | | | | |
| Pin 1 | 0.719 | 0.723 | 0.673 | 0.568 | 0.427 | 0.275 | 0.125 | 0.119 | 0.287 | 0.457 | 0.588 | 0.676 |
| Pin 2 | 0.403 | 0.566 | 0.677 | 0.732 | 0.736 | 0.699 | 0.615 | 0.483 | 0.322 | 0.159 | 0.073 | 0.224 |
| Pin 3 | 0.303 | 0.171 | 0.123 | 0.235 | 0.391 | 0.536 | 0.638 | 0.687 | 0.69 | 0.655 | 0.575 | 0.452 |
| Pinion | 0.375 | 0.401 | 0.413 | 0.414 | 0.408 | 0.395 | 0.378 | 0.356 | 0.342 | 0.338 | 0.342 | 0.355 |

# .2 Costing

## .2.1 Table displaying estimated costs for various model options.

| Costing: | |
|---|---|
| Original Cast | 4.336kg |
| Tool | $ 10,000.00 |
| Material | $ 9.76 |
| Casting | $ 52.03 |
| Unit Cost: | $ 65.95 |
| Total | $ 158,291.20 |

| Costing: | |
|---|---|
| Steel Cast | 2.64kg |
| Tool | $ 10,000.00 |
| Material | $ 5.94 |
| Casting | $ 31.68 |
| Unit Cost: | $ 41.79 |
| Total | $ 100,288.00 |

| Costing: | |
|---|---|
| Steel Cast/Adapted | 2.64kg/2.262kg |
| Tool | $ 10,000.00 |
| Material | $ 5.94 |
| Casting | $ 31.68 |
| Machining for no PL | $ 14.57 |
| Unit Cost Adapted: | $ 56.36 |
| Total | $ 123,604.48 |

| Costing: | |
|---|---|
| Steel AM | 1.629kg |
| Tool | $ - |
| Material | $ 162.90 |
| AM | $ 1,612.71 |
| Unit Cost: | $ 1,775.61 |
| Total | $ 4,261,464.00 |

| Costing: | |
|---|---|
| Original Cast Ti | 2.486kg |
| Tool | $ 10,000.00 |
| Material | $ 54.69 |
| Casting | $ 36.30 |
| Unit Cost: | $ 95.15 |
| Total | $ 228,370.24 |

| Costing: | |
|---|---|
| Ti Cast | 1.514kg |
| Tool | $ 10,000.00 |
| Material | $ 33.31 |
| Casting | $ 22.10 |
| Unit Cost: | $ 59.58 |
| Total | $ 142,989.76 |

| Costing: | |
|---|---|
| Ti AM | 1.12kg |
| Tool | $ - |
| Material | $ 448.00 |
| Casting | $ 1,349.04 |
| Unit Cost: | $ 1,797.04 |
| Total | $ 4,312,896.00 |